



universität  
wien

# DISSERTATION

Titel der Dissertation

Quantum opto-mechanics with micromirrors:  
combining nano-mechanics with quantum optics

angestrebter akademischer Grad  
Doktor der Naturwissenschaften

Verfasser: Mag. Simon Gröblacher  
Matrikelnummer: 9909402  
Dissertationsgebiet: Physik  
Betreuer: o. Univ.-Prof. Dr. DDr. h.c. Anton Zeilinger

Wien, im Dezember 2010



*für Erwin*



# Contents

<b>Contents</b>	<b>5</b>
<b>1 Abstract</b>	<b>7</b>
<b>2 Zusammenfassung</b>	<b>9</b>
<b>3 Theory</b>	<b>11</b>
3.1 A classical mechanical harmonic oscillator . . . . .	11
3.1.1 Normal modes of coupled harmonic oscillators . . . . .	14
3.2 A quantum mechanical harmonic oscillator . . . . .	16
3.2.1 Quantum states . . . . .	18
3.2.2 Phase-space distribution . . . . .	19
3.3 Radiation pressure . . . . .	20
3.3.1 Classical analysis . . . . .	22
3.3.2 Quantum analysis . . . . .	24
3.3.3 Quantum opto-mechanics . . . . .	28
3.3.4 SQL + Backaction . . . . .	28
3.3.5 Strong coupling . . . . .	29
3.3.6 Optomechanical entanglement . . . . .	32
<b>4 Experimental techniques</b>	<b>37</b>
4.1 Fiber-Interferometer . . . . .	37
4.2 Optical resonators . . . . .	37
4.2.1 Fabry-Pérot cavity . . . . .	38
4.2.2 Ring cavity . . . . .	42
4.3 Locking techniques . . . . .	43
4.3.1 Pound-Drever-Hall . . . . .	43
4.3.2 Tilt Locking . . . . .	46
4.3.3 Experimental Locking . . . . .	48
4.4 Experimental setup . . . . .	52
4.4.1 Two-color setup . . . . .	52
4.4.2 Laser systems . . . . .	54
4.4.3 Cavities . . . . .	55
4.4.4 Imaging & miscellaneous . . . . .	57
4.5 Acousto-optic modulator . . . . .	58
4.6 Homodyne detection . . . . .	60
4.7 Data Acquisition . . . . .	66
4.8 Data Analysis . . . . .	68
4.9 Calibration . . . . .	68
4.10 Effective mass . . . . .	70

4.11	Cryogenic operation of an optical cavity . . . . .	71
4.11.1	Continuous-flow $^4\text{He}$ cryostat . . . . .	72
4.11.2	Closed-cycle $^4\text{He}$ cryostat . . . . .	73
4.11.3	Dilution refrigerator . . . . .	74
<b>5</b>	<b>High-reflectivity, high-Q mechanical resonators</b>	<b>79</b>
5.1	$\text{Ta}_2\text{O}_5/\text{SiO}_2$ Distributed Bragg reflector resonators . . . . .	80
5.2	$\text{Si}_3\text{N}_4 + \text{Ta}_2\text{O}_5/\text{SiO}_2$ resonators . . . . .	82
5.3	$\text{Si} + \text{Ta}_2\text{O}_5/\text{SiO}_2$ resonators . . . . .	88
5.4	$\text{Al}_x\text{Ga}_{1-x}\text{As}$ resonators . . . . .	88
5.5	FEM simulations . . . . .	93
<b>6</b>	<b>Mechanical laser cooling in cryogenic cavities</b>	<b>95</b>
6.1	Radiation-pressure self-cooling of a micromirror in a cryogenic environment . . . . .	95
6.2	Demonstration of an ultracold micro-optomechanical oscillator in a cryogenic cavity . . . . .	101
<b>7</b>	<b>Opto-mechanics in the strong coupling regime</b>	<b>111</b>
<b>8</b>	<b>Optomechanical down-conversion</b>	<b>121</b>
<b>9</b>	<b>Conclusions &amp; Outlook</b>	<b>125</b>
<b>10</b>	<b>Bibliography</b>	<b>127</b>
	<b>Acknowledgements</b>	<b>139</b>
	<b>Curriculum Vitae</b>	<b>141</b>

# 1 Abstract

This work describes more than four years of research on the effects of the radiation-pressure force of light on macroscopic mechanical structures. The basic system studied here is a mechanical oscillator that is highly reflective and part of an optical resonator. It interacts with the optical cavity mode via the radiation-pressure force. Both the dynamics of the mechanical oscillation and the properties of the light field are modified through this interaction. In our experiments we use quantum optical tools (such as homodyning and down-conversion) with the goal of ultimately showing quantum behavior of the mechanical center of mass motion. In this thesis we present several experiments that pave the way towards this goal and when combined should allow the demonstration of the envisioned quantum phenomena, including entanglement, teleportation and Schrödinger cat states. The study of quantum behavior of truly macroscopic systems is a long outstanding goal, which will help to answer some of the most fundamental questions in quantum physics today: Why is the world around us classical and not quantum? Is there a size- or mass-limit to systems for them to behave according to quantum mechanics? Is quantum theory complete or do we have to extend it to include mechanisms such as decoherence? Can we use the quantum nature of macroscopic objects to, for example, improve the measurement precision of classical apparatuses?

The experiments discussed in this thesis include the very first passive radiation-pressure cooling of a mechanical oscillator in a cryogenic optical resonator, as well as the experimental demonstration of radiation-pressure cooling close to the mechanical quantum ground state. Cooling of the mechanical motion is an important pre-condition for observing quantum effects of the mechanical oscillator.

In another experiment, we have demonstrated that we are able to enter the strong-coupling regime of the optomechanical system a regime where coherent energy exchange between the optical and the mechanical subsystems is possible, as their coupling rate is bigger than their individual decoherence rates. This experiment is an important milestone in showing macroscopic mechanical quantum behavior.

Finally, we have performed an experiment where we have measured the optomechanical correlations. The correlations are used for probing radiation-pressure based down-conversion and such an experiment will ultimately allow the generation and detection of entanglement between the optical and the mechanical system.





## 2 Zusammenfassung

Diese Arbeit beschreibt mehr als vier Jahre an Forschung über die Effekte von Strahlungsdruck von Licht auf makroskopische, mechanische Strukturen. Das System das hier erforscht wird ist ein mechanischer Oszillator der gleichzeitig ein hochreflektierender Spiegel ist und als Teil eines optischen Resonators verwendet wird. Die mechanische Struktur wechselwirkt mit der optischen Mode in der Kavität über die Strahlungsdruckkraft des Lichtes. Sowohl die Dynamik der mechanischen Oszillation als auch die Eigenschaften des Lichtes werden durch diese Wechselwirkung beeinflusst. In unseren Experimenten verwenden wir Werkzeuge der Quantenoptik (wie Homodyndetektion und parametrische Fluoreszenz (= down-conversion)) mit dem Ziel Quantenverhalten der mechanischen Schwerpunktsbewegung zu zeigen. In dieser Dissertation präsentieren wir mehrere Experimente die den Weg zu diesem Ziel ebnen und, wenn gemeinsam durchgeführt, zu der gewünschten Demonstration der makroskopischen, mechanischen Quantenphänomene führen sollten, wie Verschränkung, Teleportation und nicht-klassische Zustände (Stichwort "Schrödingers Katze"). Das Studium des Quantenverhaltens von makroskopischen Systemen ist ein seit langer Zeit verfolgtes Ziel welches dabei helfen wird einige der zentralen offenen Fragen der modernen Quantenphysik zu beantworten: Warum ist die Welt wie wir sie wahrnehmen klassisch und nicht quantenmechanisch? Gibt es eine Beschränkung in der Größe oder der Masse für Objekte oberhalb der sie sich nicht mehr nach den Gesetzen der Quantenmechanik verhalten können? Ist die Quantentheorie vollständig oder müssen wir sie mit einem Mechanismus wie der Dekohärenz erweitern? Können wir die Quantennatur von makroskopischen Objekten nutzen um zum Beispiel die Messgenauigkeit von klassischen Apparaten zu verbessern?

Die Experimente die in dieser Arbeit diskutiert werden inkludieren das erste passive Kühlen eines mechanischen Oszillators mit Hilfe von Strahlungsdruck in einem kryogenen optischen Resonator überhaupt. Weiters konnten wir ein Experiment durchführen in welchem wir die mechanische Struktur in die Nähe ihres quantenmechanischen Grundzustandes gekühlt haben. Das Kühlen der mechanischen Bewegung ist eine wichtige Voraussetzung um Quantenphänomene des mechanischen Oszillators zu beobachten.

In einem anderen Experiment haben wir gezeigt, dass wir im Bereich der starken Wechselwirkung des opto-mechanischen Systems arbeiten können. In diesem Bereich ist ein kohärenter Energieaustausch zwischen dem optischen und dem mechanischen System möglich da ihre Wechselwirkungsrate größer ist als ihre individuellen Dekohärenzraten. Dieses Experiment ist ein wichtiger Meilenstein um makroskopisches, mechanisches Quantenverhalten zu zeigen.

Zuletzt haben wir in einem Experiment die opto-mechanischen Korrelationen gemessen. Mit Hilfe dieser Korrelationen kann man die aufgrund des Strahlungsdruckes auftretende parametrische Fluoreszenz untersuchen. Dieses Experiment ist

so konzipiert, dass man damit in Zukunft Verschränkung zwischen dem optischen und dem mechanischen System sowohl erzeugen, als auch auslesen wird können.

## 3 Theory

### 3.1 A classical mechanical harmonic oscillator

The harmonic oscillator is a prominent, basic textbook example of a classical mechanical system. While we do not want to discuss it in great detail as it can be found in any introductory physics textbook (see for example [1]), we would like to briefly review its features and introduce some of the nomenclature that will be used throughout this thesis.

Mechanical oscillations are a widespread form of motion in nature, for example, it can be found in almost any kind of physical system – from microscopic objects such as molecules up to the biggest found in our universe including neutron stars or more familiarly in systems like clocks, engines or musical instruments. The concept is always the same: an oscillation is the repetitive variation of some parameter around a central value. For example, a system at an initial position  $x_0$  experiences a restoring force  $F$  that is proportional to its position  $x$ , returns to its point of origin and subsequently moves back to  $x_0$ . As long as the system stays decoupled from its environment it continues with this oscillatory movement. According to Newton's second law, the system is described by

$$F = m\ddot{x} = -kx, \quad (3.1)$$

where  $F$  is a force,  $m$  is the mass of the harmonic oscillator,  $\ddot{x}$  is the second derivative of its position with respect to time and  $k$  is a positive constant, usually referred to as the spring constant. This is a simple differential equation and one easily sees that the equation of motion is given by

$$x(t) = A \sin(\omega_m t + \varphi). \quad (3.2)$$

Here  $A$  is the amplitude, which is determined by the initial conditions and  $\omega_m = 2\pi f_m$  is the oscillator's eigenfrequency. The phase  $\varphi$  is the position of the oscillator relative to the point of origin at  $t = 0$  and is also determined by the initial conditions. In fact  $A$  and  $\varphi$  are given by [1]

$$A = \sqrt{\frac{\dot{x}^2(0)}{\omega_m^2} + x^2(0)}, \quad (3.3)$$

$$\varphi = \arctan\left(\omega_m \frac{x(0)}{\dot{x}(0)}\right). \quad (3.4)$$

The eigenfrequency of the system is

$$\omega_m = \frac{2\pi}{\tau_m} = \sqrt{\frac{k}{m}}, \quad (3.5)$$

with  $\tau_m$  being the oscillation period. The total energy  $E_{tot}$  of the system is conserved and only its kinetic  $E_k$  and potential  $E_p$  components vary over time

$$E_k(t) = \frac{m}{2}\dot{x}^2 = \frac{k}{2}A^2 \cos^2(\omega_m t + \varphi) \quad (3.6)$$

$$E_p(t) = \frac{k}{2}x^2 = \frac{k}{2}A^2 \sin^2(\omega_m t + \varphi). \quad (3.7)$$

As a result the total energy is

$$E_{tot} = E_k + E_p = \frac{m}{2}\omega_m^2 A^2. \quad (3.8)$$

Any real harmonic oscillator, however, experiences some kind of friction as it interacts with its environment and therefore we have to include a damping term in the differential equation describing the system:

$$\ddot{x} + \gamma_m \dot{x} + \omega_m^2 x = 0. \quad (3.9)$$

Here  $\gamma_m$  is the damping rate and it determines how fast the oscillation decays. Again, the equation of motion can be easily solved and is given by [1]

$$x(t) = A_d e^{-\frac{\gamma_m}{2}t} \sin \left[ \sqrt{\omega_m^2 - \left(\frac{\gamma_m}{2}\right)^2} t + \varphi_d \right]. \quad (3.10)$$

A very useful quantity for a damped harmonic oscillator is its quality factor  $Q$ , which is a measure of how many oscillations it undergoes before its amplitude decays by a factor of  $e$ :

$$Q := \frac{\omega_m}{\gamma_m}. \quad (3.11)$$

The quality factor determines the behavior of the damped harmonic oscillator and the three different alternatives are:

- $Q > \frac{1}{2}$ : The underdamped oscillator is a system that oscillates at a slightly different frequency than the free harmonic oscillator and gradually decays to zero.
- $Q = \frac{1}{2}$ : The critically damped oscillator attempts to return to its equilibrium position as quickly as possible and does this without oscillating at all.
- $Q < \frac{1}{2}$ : The overdamped oscillator also returns to its equilibrium position without oscillations but takes longer than in the critically damped case – the smaller  $Q$  becomes, the longer it takes.

Often harmonic oscillators are not only damped but they are also coupled to an external bath that drives their motion. The differential equation describing such a damped, driven harmonic oscillator reads

$$\ddot{x} + \gamma_m \dot{x} + \omega_m^2 x = \frac{F(t)}{m}, \quad (3.12)$$

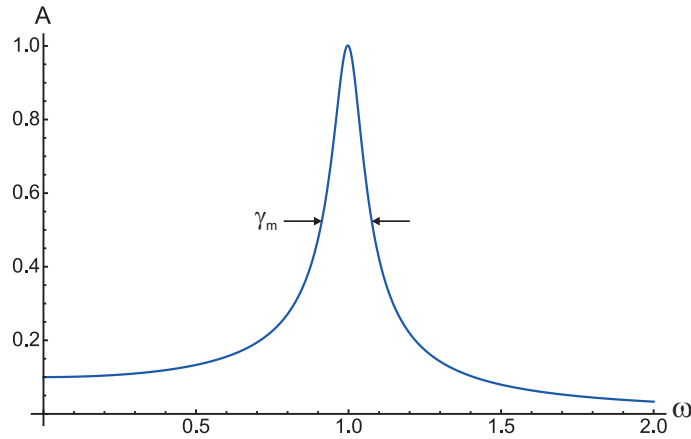


Figure 3.1: The amplitude response  $A$  of a damped, driven harmonic oscillator described by (3.13) as a function of frequency  $\omega$ . In this example the unperturbed frequency  $\omega_m = 1$  and the damping  $\gamma_m = 0.1 \cdot \omega_m$ , which is defined as the full width at half maximum (FWHM) of the resonance.

where  $F(t)$  in the simplest case is a harmonic driving force of the form  $F(t) = F_0 \sin(\omega t)$  but can in general take the form of any arbitrary external force. We can again take an Ansatz of the form  $x(t) = A \sin(\omega t + \varphi)$  (if we neglect the initial transient behavior of the system [2]) and after some simple calculations we obtain

$$A = \frac{F_0/m}{\sqrt{(\omega_m^2 - \omega^2)^2 + \omega^2 \gamma_m^2}} \quad (3.13)$$

for the amplitude of the motion of the oscillator, while the phase evolves according to

$$\varphi = \arctan \frac{-\omega \gamma_m}{\omega_m^2 - \omega^2}. \quad (3.14)$$

The response of the damped, driven harmonic oscillator is similar to a Lorentzian and has its resonance close to the natural frequency of the oscillator. It is given by

$$\omega_{res} = \omega_m \sqrt{1 - \frac{\gamma_m^2}{2\omega_m^2}}. \quad (3.15)$$

The general form of  $x(t)$  in its Fourier space is [2]

$$\tilde{x}(\omega) = \frac{\tilde{F}(\omega)}{m} \cdot \frac{1}{\omega_m^2 - \omega^2 + i\omega \gamma_m}, \quad (3.16)$$

where  $\tilde{F}(\omega)$  is the Fourier transform of an external driving force  $F(t)$ . For an oscillator subject to Brownian noise, i.e. coupled to a thermal bath at temperature  $T$ , the bath can be described as an infinite sum of harmonic oscillators exerting a force of equal amplitude, i.e.  $F_{th}(t) = \sum_i F_{ext}^i$ . Its power spectrum  $S_{xx}(\omega) = \langle \tilde{x}(\omega) \tilde{x}^*(\omega) \rangle$  is given by

$$S_{xx}(\omega) = \frac{\tilde{F}_{th}}{m^2} \cdot \frac{1}{(\omega_m^2 - \omega^2)^2 + \omega^2 \gamma_m^2}, \quad (3.17)$$

where  $\tilde{F}_{th}$  is constant in frequency for the Brownian bath. Throughout this thesis  $\gamma_m$  is defined as the full width at half maximum (FWHM). The Wiener-Khinchin theorem states that the power spectral density of a wide-sense stationary random process, i.e. a stochastic process with a constant mean (here  $x(t)$ ), is equal to the Fourier transform of its autocorrelation function [3]:

$$S_{xx}(\omega) = \int_{-\infty}^{+\infty} \langle x(t)x^*(t-\tau) \rangle e^{-i\omega\tau} d\tau, \quad (3.18)$$

or equivalently for  $\tau = 0$

$$\langle x^2 \rangle = \int_{-\infty}^{+\infty} S_{xx}(\omega) d\omega = \frac{F_{th}}{m^2} \cdot \frac{\pi}{\omega_m^2 \gamma_m}. \quad (3.19)$$

Here the solution of the integral for Brownian noise is taken from [4], where the integral is done from 0 to  $\infty$  and therefore differs by a factor of 2. This result is very important for this work – it connects the measured power spectrum of a harmonic oscillator to its temperature. This can be seen by using the equipartition theorem: for a 1-dimensional oscillator in thermal equilibrium the total average energy  $\langle E \rangle$  is equally distributed between the kinetic  $E_k$  and the potential energy  $E_p$  of the system

$$\langle E \rangle = \langle E_k \rangle + \langle E_p \rangle = \frac{1}{2}k_B T + \frac{1}{2}k_B T = k_B T, \quad (3.20)$$

where  $k_B$  is the Boltzmann constant and  $T$  the oscillators temperature. Therefore, using (3.7) and (3.20) we obtain  $m \omega_m^2 \langle x^2 \rangle = k_B T$ . Given that (3.19) holds

$$F_{th} = \frac{m \gamma_m \cdot k_B T}{\pi}. \quad (3.21)$$

The power spectrum for a damped harmonic oscillator, driven by Brownian noise is finally given by

$$S_{xx}(\omega) = \frac{\gamma_m \cdot k_B T}{\pi m} \cdot \frac{1}{(\omega_m^2 - \omega^2)^2 + \omega^2 \gamma_m^2}. \quad (3.22)$$

### 3.1.1 Normal modes of coupled harmonic oscillators

An interesting effect occurs if two harmonic oscillators are coupled together (see figure 3.2) – for sufficiently strong coupling the two oscillators can be described as one single system oscillating at frequencies that are determined by their coupling strength. The differential equations for two simple harmonic oscillators that are coupled by a spring with spring constant  $k_j$  are

$$\begin{aligned} m\ddot{x}_1 &= -kx_1 + k_j(x_2 - x_1), \\ m\ddot{x}_2 &= -kx_2 + k_j(x_1 - x_2). \end{aligned} \quad (3.23)$$

For simplicity, here the oscillators have the same mass  $m$  and spring constant  $k$ . Taking the Ansatz  $x_1(t) = A \sin(\omega t + \varphi)$  and  $x_2(t) = B \sin(\omega t + \varphi)$  and substituting

into (3.23) we find

$$\begin{aligned}(k + k_j - m\omega^2)A - k_j B &= 0, \\ -k_j A + (k + k_j - m\omega^2)B &= 0.\end{aligned}\tag{3.24}$$

For the equation to have a non-trivial solution the determinant of the system of equations must be singular, i.e. zero:

$$(k + k_j - m\omega^2)^2 - k_j^2 = 0.\tag{3.25}$$

This is a simple quadratic equation in  $\omega$  and assuming that  $\omega \geq 0$  we obtain

$$\omega_1 = \sqrt{\frac{k + 2k_j}{m}},\tag{3.26}$$

$$\omega_2 = \sqrt{\frac{k}{m}}.\tag{3.27}$$

Substituting back into (3.24) we find  $A = B \equiv A_1$  and  $A = -B \equiv A_2$  for the two frequencies, respectively. The most general equations of motions now are

$$\begin{aligned}x_1(t) &= A_1 \sin(\omega_1 t + \varphi_1) + A_2 \sin(\omega_2 t + \varphi_2), \\ x_2(t) &= -A_1 \sin(\omega_1 t + \varphi_1) + A_2 \sin(\omega_2 t + \varphi_2).\end{aligned}\tag{3.28}$$

The amplitudes  $A_{1,2}$  and the phases  $\varphi_{1,2}$  are determined by the initial conditions of  $x_{1,2}(0)$  and  $\dot{x}_{1,2}(0)$ . The motion of the oscillators can therefore be decomposed into two normal modes with frequencies  $\omega_{1,2}$  and amplitudes  $A_{1,2}$ , which are non-degenerate for  $k_j \neq 0$ . This is true for arbitrarily small  $k_j$  as the damping  $\gamma_m$  is zero.

The system becomes even more interesting for two damped (and driven) oscillators. Their uncoupled equations of motions are given by (3.12)

$$\begin{aligned}\ddot{x}_1 + \gamma_m \dot{x}_1 + \omega_m^2 x_1 - \frac{k_j}{m}(x_2 - x_1) &= 0, \\ \ddot{x}_2 + \gamma_m \dot{x}_2 + \omega_m^2 x_2 - \frac{k_j}{m}(x_1 - x_2) &= \frac{F(t)}{m}.\end{aligned}\tag{3.29}$$

For simplicity we have assumed that the damping rates  $\gamma_m$ , the masses  $m$  and the frequencies  $\omega_m$  of the oscillators are the same, while only one oscillator is externally driven by a force  $F(t)$ . These differential equations are solved by (if we neglect the transient terms) [5]

$$\begin{aligned}q_1(t) &= A_1 \sin(\omega t + \varphi_1), \\ q_2(t) &= A_2 \sin(\omega t + \varphi_2),\end{aligned}\tag{3.30}$$

where we have introduced the normal mode coordinates  $q_1 = x_1 + x_2$  and  $q_2 = x_2 - x_1$ . The frequencies of the normal modes are given by

$$\begin{aligned}\omega_1 &= \sqrt{\frac{k + 2k_j}{m - \gamma_m^2/4}}, \\ \omega_2 &= \sqrt{\frac{k}{m - \gamma_m^2/4}},\end{aligned}\tag{3.31}$$

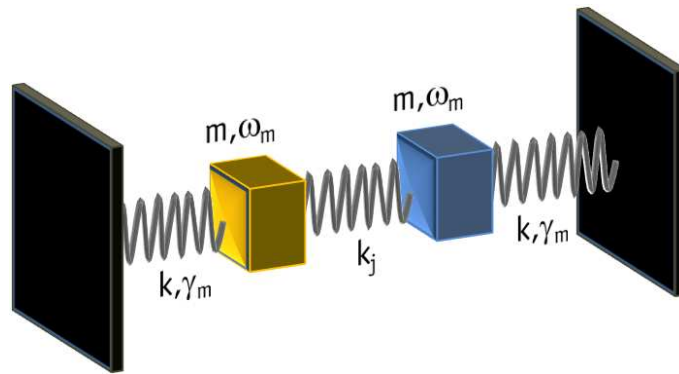


Figure 3.2: Coupled harmonic oscillators. Two oscillators with masses  $m$  and frequencies  $\omega_m$  are each coupled to an environment via a spring with a spring constant  $k$  and a damping rate  $\gamma_m$ . In addition, they are coupled to each other via a joint spring with a spring constant  $k_j$ . In chapter 7 we present an experiment where the two oscillators are a mechanical resonator and an optical field that are strongly coupled to each other.

and their respective amplitudes

$$A_i = \frac{F_0/m}{\sqrt{(\omega_i^2 - \omega^2)^2 + \omega^2\gamma_m^2}}, \quad (3.32)$$

with  $i = 1, 2$ . If we now look at the spectrum of the normal modes (figure 3.3) we see that the modes are degenerate as long as the coupling strength between the oscillators is small, i.e.  $k_j < \gamma_m$ . A splitting of the spectrum only occurs if the coupling is stronger than the damping to the environment. In chapter 7 we use this condition to demonstrate that we enter the strong coupling regime of an optomechanical system.

## 3.2 A quantum mechanical harmonic oscillator

In quantum mechanics the harmonic oscillator is one of the simplest examples that is analytically solvable. But already this simple system shows some of the peculiar quantum features that make it so distinct from classical mechanics. The usual starting point is the classical Hamiltonian function, i.e. the total energy of the system (3.8). If one replaces the classical variables with their corresponding quantum operators, i.e.  $x \rightarrow x$  and  $m\dot{x} = p \rightarrow -i\hbar\frac{d}{dx}$  one obtains the quantum mechanical Hamiltonian operator

$$H = -\frac{\hbar^2}{2m} \frac{d^2}{dx^2} + \frac{m\omega^2 x^2}{2}, \quad (3.33)$$



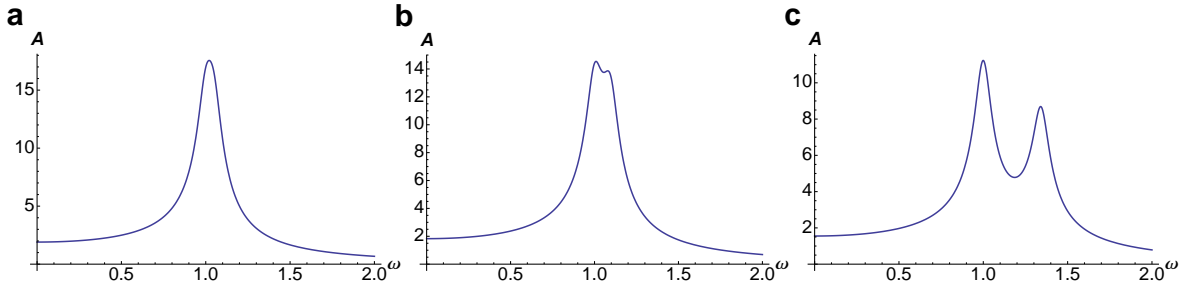


Figure 3.3: Normal mode splitting of coupled damped harmonic oscillators. The spectrum of two coupled oscillators (equation (3.32)) is shown for different coupling constants  $k_j$ . The parameters of the oscillators are chosen to be  $F(t) = m = k = \omega_m = 1$  and  $\gamma_m = 0.1 \cdot \omega_m$ . **a** For a coupling  $k_j = 0.5 \cdot \gamma_m$  the normal modes are still degenerate, while for  $k_j = \gamma_m$  the splitting can already be observed **b**. **c** When increasing the coupling further to  $k_j = 4 \cdot \gamma_m$  the modes become very distinct.

with  $\hbar$  being the reduced Planck constant. One can rewrite the operators  $x$  and  $p$  in terms of the creation  $a^\dagger$  and annihilation  $a$  operators

$$\begin{aligned} x &= \sqrt{\frac{\hbar}{2m\omega}} (a + a^\dagger), \\ p &= \sqrt{\frac{m\omega\hbar}{2}} (a - a^\dagger). \end{aligned} \quad (3.34)$$

As  $x$  and  $p$  fulfill the commutation relation  $[x, p] = i\hbar$ ,  $a$  and  $a^\dagger$  obey the following relations

$$[a, a^\dagger] = 1 \text{ and } [a, a] = [a^\dagger, a^\dagger] = 0. \quad (3.35)$$

Hence the Hamiltonian can be expressed as

$$H = \hbar\omega \left( a^\dagger a + \frac{1}{2} \right), \quad (3.36)$$

and the corresponding Schrödinger equation reads

$$a^\dagger a \psi = \left( \frac{E}{\hbar\omega} - \frac{1}{2} \right) \psi. \quad (3.37)$$

This is an eigenvalue equation for the so-called number operator  $a^\dagger a$ , which obeys the commutation relations  $[a^\dagger a, a^\dagger] = a^\dagger$  and  $[a^\dagger a, a] = -a$ . The eigenfunctions of the eigenvalue equation are solutions of the Schrödinger equation. The lowest eigenfunction  $\psi_0$  is the ground state of the harmonic oscillator, which we can calculate using  $a \psi_0 = 0$

$$\psi_0(x) = \left( \frac{m\omega}{2\hbar} \right)^{1/4} \exp\left(-\frac{m\omega}{2\hbar} x^2\right). \quad (3.38)$$

The eigenfunction for the  $n^{\text{th}}$  energy eigenstate then is

$$\psi_n(x) = \sqrt{\frac{1}{n!}} (a^\dagger)^n \psi_0(x). \quad (3.39)$$

It is now easy to find the energy spectrum for the harmonic oscillator by simply writing down the eigenvalue equation for the Hamiltonian defined in equation (3.36), which is discrete and the energy levels are equidistant:

$$E_n = \hbar\omega \left( n + \frac{1}{2} \right). \quad (3.40)$$

We can now also calculate the expectation value for the position operator  $x$  and the position operator squared  $x^2$  and find

$$\langle x \rangle = \langle \psi_n | x | \psi_n \rangle = 0, \quad (3.41)$$

$$\langle x^2 \rangle = \langle \psi_n | x^2 | \psi_n \rangle = \frac{\hbar}{m\omega} \left( n + \frac{1}{2} \right). \quad (3.42)$$

The ground state of a quantum mechanical oscillator therefore has non-zero energy and an associated extension

$$E_0 = \frac{1}{2}\hbar\omega, \quad (3.43)$$

$$x_{zp} = \sqrt{\langle x^2 \rangle_0 - \langle x \rangle_0^2} = \sqrt{\frac{\hbar}{2m\omega}}.$$

This so-called zero-point energy is the minimal energy compatible with the Heisenberg uncertainty principle. Another widely used definition of the zero-point extension is the half width at half maximum of the associated wavepacket (3.38) of the oscillator, which differs by a factor  $\sqrt{2}$  from how  $x_{zp}$  is defined here.

### 3.2.1 Quantum states

The quantum state that most closely resembles a classical harmonic oscillator is the so-called coherent state, which was first described by Schrödinger in 1926 [6], while the term itself was introduced by Glauber [7]. It is defined as

$$|\alpha\rangle = e^{-\frac{1}{2}|\alpha|^2} \sum_{n=0}^{\infty} \frac{\alpha^n}{\sqrt{n!}} |n\rangle, \quad (3.44)$$

where  $|n\rangle$  are the number or Fock states and the average occupation number of the state is given by  $\bar{n} = |\alpha|^2$ . The variance then is  $\Delta n = \sqrt{\bar{n}} = |\alpha|$ . The probability  $P_\alpha(n)$  of finding an oscillator described by the coherent state in its  $n^{\text{th}}$  state is given by a Poissonian distribution

$$P_\alpha(n) = e^{-|\alpha|^2} \frac{|\alpha|^{2n}}{n!}. \quad (3.45)$$

Often the coherent state is also defined as a displaced vacuum state [7]

$$|\alpha\rangle = D(\alpha)|0\rangle, \quad (3.46)$$

where  $|0\rangle$  is the vacuum state and  $D(\alpha) = \exp(\alpha a^\dagger - \alpha^* a)$  the displacement operator. As  $D(\alpha)$  is unitary, it is relatively easy to see (cf. [7]) that the coherent state is an

eigenfunction of the annihilation operator, i.e.  $a|\alpha\rangle = \alpha|\alpha\rangle$ . The output field of a laser, for example, is well described by a coherent state. The phase of such a coherent state has an uncertainty of  $\Delta\phi = 1/2\sqrt{\bar{n}}$  (see e.g. [3]) for  $\alpha \gg 1$  and hence the coherent state obeys the uncertainty relation  $\Delta\phi \cdot \Delta n = \frac{1}{2}$ . In other words, the coherent state has an equally spread uncertainty in phase-space with a width of  $1/2$ . It approaches the case of a classical oscillator that has no uncertainty with increasing  $\alpha$  as the uncertainty becomes less significant.

A harmonic oscillator in thermal equilibrium with a bath at temperature  $T$  must be described as a mixture of pure states, i.e. it is in a thermal state (see for example [8])

$$\rho = \sum_{n=0}^{\infty} \frac{\bar{n}^n}{(1 + \bar{n})^{n+1}} |n\rangle\langle n|, \quad (3.47)$$

where  $\bar{n} = (\exp\{\hbar\omega/k_B T\} - 1)^{-1}$  is the oscillator's mean occupation number following the Bose-Einstein statistics. In the large temperature limit, i.e.  $k_B T \gg \hbar\omega$ , the mean thermal occupation  $\bar{n}$  due the equipartition of energies is

$$\bar{n} \approx \frac{k_B T}{\hbar\omega} - \frac{1}{2}. \quad (3.48)$$

Only close to the ground state, i.e. for  $\bar{n} = \mathcal{O}(1)$ , this approximation does not hold and one has to use the full Bose-Einstein statistics. Here we have used the density matrix representation of the state in the Fock basis, which is defined as

$$\rho = \sum_{m,n} c_{m,n} |m\rangle\langle n|, \quad (3.49)$$

with  $c_{m,n} = \langle m|\rho|n\rangle$ .

### 3.2.2 Phase-space distribution

A classical particle has well defined position  $x$  and momentum  $p$ . For an ensemble of such particles one can define a probability distribution, which gives the probability of finding a particle for a given  $x$  and  $p$  in phase space. In the quantum domain there is no exact analogue due to the Heisenberg uncertainty principle, but nonetheless a quasi-probability distribution can be defined, the Wigner function [9]. If one takes the marginal of the Wigner function, i.e. the projection onto the vertical plane defined by for example the  $x$ -axis, one recovers the distribution obtained by measurements of (in this example) the  $x$ -quadrature of an ensemble of equally prepared quantum systems. This is completely analogous to the classical case. The Wigner function has many properties of a classical probability distribution, e.g. it is real and normalized. However, it can also have negative values, which is the reason why it is called a quasi-probabilistic distribution. The negativity is often taken to determine whether a state is non-classical or not – while this is a sufficient condition, it is not a necessary one. Often states that have a fully positive Wigner distribution, such as the vacuum state or a squeezed coherent state (in fact this is the case for all Gaussian states), are still considered to be quantum (for a more detailed discussion

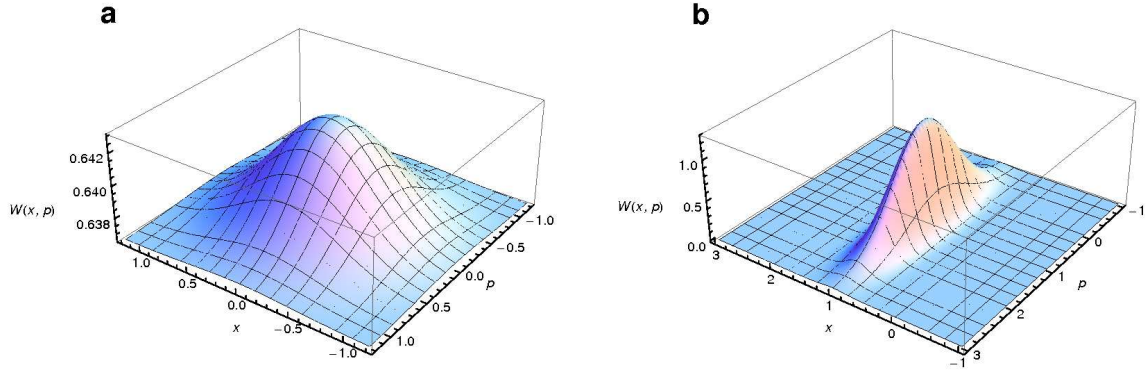


Figure 3.4: **a** shows the Wigner function  $W(x, p)$  of a thermal state. The state has no phase and its mean occupation  $\bar{n}$  follows the Bose-Einstein statistics. **b** in contrast, is the Wigner function of a squeezed coherent state, where squeezing of approximately 6 dB in the  $x$ -quadrature is shown. All axes are in arbitrary units.

see for example [10]). The Wigner function is defined as [11]

$$W(x, p) = \frac{1}{\pi\hbar} \int_{-\infty}^{+\infty} e^{2ipy/\hbar} \langle x-y | \rho | x+y \rangle dy, \quad (3.50)$$

where  $\rho$  is the density matrix of a general mixed state. The marginals for example for  $x$  and  $p$  are

$$\begin{aligned} \int_{-\infty}^{+\infty} dx W(x, p) &= \langle x | \rho | x \rangle = |\psi(x)|^2, \\ \int_{-\infty}^{+\infty} dp W(x, p) &= \langle p | \rho | p \rangle. \end{aligned} \quad (3.51)$$

And as it is normalized  $\int dx \int dp W(x, p) = \text{Tr}(\rho) = 1$ , where  $\text{Tr}$  is the trace. The Wigner function for the thermal state (3.49) and a squeezed coherent state are shown in figure 3.4. More details on Wigner functions can be found in [4].

### 3.3 Radiation pressure

Radiation-pressure effects, i.e. forces acting solely due to the momentum of light, have been discussed as early as the 17<sup>th</sup> century when Johannes Kepler suspected that the inclination of the tails of comets could be due to a mechanical force exerted by the sun [12, 13]. In fact, the tails of a comet are due to the solar radiation that vaporizes particles on the surface of the comet. Radiation pressure from the sun then exerts a force on the coma of the comet (white tail), while the force of the solar wind creates the ionized (blue) tail. In the early 20<sup>th</sup> century, experiments by

Lebedev [14] and Nichols and Hull [15] first verified unambiguously predictions by Maxwell [16] and Bartoli [17] on the strength of the radiation-pressure force.

In the 1960s and 70s, Braginsky and colleagues studied radiation-pressure effects in the context of gravitational wave antennae – they experimentally and theoretically analyzed the sensitivity limits due to the quantum nature of light [18, 19]. Braginsky also predicted that the radiation pressure inside a cavity with finite decay time would give rise to dynamic backaction, the underlying mechanism to the parametric instabilities and cooling of a mechanical oscillator, which will be discussed later in this section [20]. In the 1980s, also Caves [21] and Meystre et al. [22] analyzed the radiation-pressure noise in interferometers. First experiments on radiation-pressure effects in cavities with macroscopic mechanical oscillators were performed in the 1980s [23]. Subsequently, several theoretical proposals for quantum optics experiments in a cavity using radiation-pressure effects were published, such as the generation of squeezed light [24, 25], quantum non-demolition measurements of photon numbers [26, 27], feedback-cooling of the mechanical motion [28] (which was experimentally realized in [29]), entanglement between the optical and the mechanical mode [30–32], and the quantum-state transfer from the light field to the mechanical oscillator [33]. However, first experiments were only realized in recent years (except for [23]): measurements of the motion of a mechanical oscillator [34–36], parametric amplification of the mechanical motion [37], cavity cooling of the mechanical resonator [38–41], cryogenic cavity cooling [42–45] and strongly coupled opto-mechanics [46]. For a more detailed historic overview of radiation-pressure forces up to the early 20<sup>th</sup> century see [14, 47] and for the more recent developments see for example [48–53]. It is important to note that experiments involving nanomechanical oscillators and microwave cavities have achieved similar results [54–57] and that in experiments with microscopic mechanical oscillators quantum effects have already been observed [58].

The system studied throughout this thesis is a Fabry-Pérot cavity, in which one of the end-mirrors is suspended, i.e. it can be described as a damped harmonic oscillator with a resonance frequency  $\omega_m$  and a mass  $m$ , subject to an external thermal bath and coupled to the light inside the cavity via the radiation-pressure force (figure 3.5). The interaction between the mechanical and the optical system can be understood qualitatively as follows: light with a wavelength  $\lambda$  impinges on the moving mirror and each photon transfers momentum of  $2\hbar k$  onto the mechanics, where  $k = 2\pi/\lambda$  is the wavenumber of the light. A quasi-static displacement of the mirror due to the light force changes the length of the cavity and hence the phase of the light field. In a cavity detuned from resonance, the sensitivity of the intra-cavity intensity strongly depends on the length of the cavity and even the typically very small displacement of the suspended end-mirror can modify the light fields' amplitude and phase significantly (see section 4.2.1 for details). In turn, the mechanical displacement is modified by the momentum transfer of the radiation-pressure force. This interaction hence generates an intensity dependent phase shift of the light incident onto the cavity, which is equivalent to the optical or AC Kerr effect [59]. Also, the frequency of the photons hitting the mirrors is changed due to a Doppler-shift from the oscillating mirror, resulting in frequency sidebands in the optical field that are spaced by  $\omega_m$ .

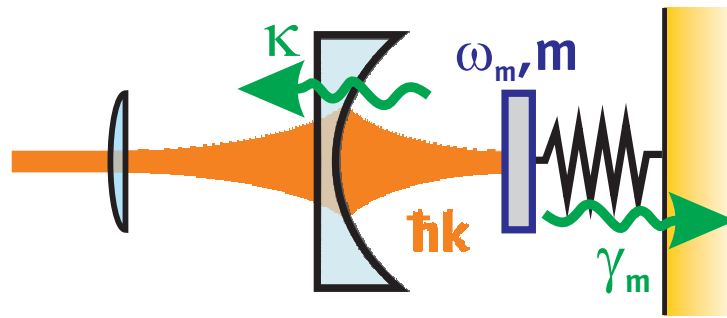


Figure 3.5: Sketch of the radiation-pressure interaction: light is coupled through a rigid input mirror into an optical resonator with a movable back-mirror of frequency  $\omega_m$  and mass  $m$ . The photons inside the cavity each transfer momentum of  $2\hbar k$  onto the movable mirror, displace it and hence acquire a phase shift, depending on its position. The intensity of the light field inside the cavity strongly depends on the relative distance between the mirrors, as well as on their reflectivities – the amplitude cavity decay rate is given by  $\kappa$ . The movable mirror couples to its environment at a rate  $\gamma_m$ .

The radiation-pressure interaction can now be exploited to modify the dynamics of the mechanical oscillator, which is described in detail in the following subsections. One particularly interesting effect is the possibility to damp, i.e. cool, the mechanical motion with the help of the radiation-pressure force. In a very intuitive picture, in close analogy to the sideband cooling of atoms [60], the sidebands in the light field are created due to an energy exchange between the optical and the mechanical mode, where the creation of a photon at the frequency  $\omega_c + \omega_m$  ( $\omega_c$  is the cavity frequency) results in the annihilation of a phonon in the mechanical oscillator, while the optical sideband at  $\omega_c - \omega_m$  comes from the creation of a phonon. If we now detune the cavity resonance with respect to the incoming laser, or vice versa, an imbalance between the two first-order sidebands is created resulting in an effective cooling of the mechanical mode or a net heating, depending on the sign of the detuning (cf. figure 3.6). The latter case also gives rise to entanglement between the optical and the mechanical mode, a true optomechanical feature. The detailed physical mechanisms behind the cooling, the entanglement and the modification of the dynamics in general, both in a classical and a quantum framework, are derived in the following sections.

### 3.3.1 Classical analysis

The radiation-pressure force  $F_{rp}$  inside a Fabry-Pérot cavity is proportional to the intra-cavity light intensity  $I$  (see section 4.2.1), which in turn is a function of the length of the cavity (and of the detuning of the laser with respect to the cavity resonance) and hence  $F_{rp} = F_{rp}(x)$ . If a damped harmonic oscillator is now not only driven by Brownian noise but in addition by an external radiation-pressure force, the differential equation (3.12) is modified to

$$\ddot{x} + \gamma_m \dot{x} + \omega_m^2 x = \frac{F_{th}(t) + F_{rp}(x(t))}{m}. \quad (3.52)$$

The equation of motion for such an oscillator in thermal equilibrium can be expressed in terms of its susceptibility, which is simply the response of the system to an applied force, i.e.  $\chi(\omega) = \tilde{x}(\omega)/F(\omega)$ , or for our case

$$\tilde{x}(\omega) = \chi(\omega) \left( \tilde{F}_{th} + \tilde{F}_{rp}(\omega) \right). \quad (3.53)$$

For a damped harmonic oscillator driven by Brownian noise we know from (3.16) that the susceptibility is given by

$$\chi(\omega) = \frac{1}{m \cdot (\omega_m^2 - \omega^2 + i\omega \gamma_m)}. \quad (3.54)$$

The radiation-pressure force modifies the dynamics of the oscillator and therefore the susceptibility can be rewritten as an effective susceptibility, with an effective frequency  $\omega_{eff}$  and an effective oscillator damping  $\gamma_{eff}$

$$\chi_{eff}(\omega) = \frac{1}{m \cdot (\omega_{eff}^2 - \omega^2 + i\omega \gamma_{eff})}, \quad (3.55)$$

where, in the limit of  $Q \gg 1$ , the modified frequency and damping rate are given by [39]

$$\omega_{eff}(\omega) = \omega_m \left( 1 + M \cdot \left[ 1 - \frac{\omega^2 + \Delta_0^2}{\kappa^2} \right]^{-1} \right), \quad (3.56)$$

$$\gamma_{eff}(\omega) = \gamma_m \left( 1 + M \cdot \frac{Q\kappa}{\omega} \right). \quad (3.57)$$

Here  $M = \frac{4\pi\Delta_0 \cdot I}{\lambda \cdot \kappa^2 \cdot L \cdot m\omega_m^2}$  and  $\kappa = \frac{\pi c}{2L \cdot F}$  is the cavity amplitude decay rate, with  $L$  being the cavity length,  $c$  the speed of light and  $F$  the finesse, while  $\Delta_0 = \omega_c - \omega_l$  is the cavity detuning (modulo  $[2\pi \cdot FSR]$ ), with the free spectral range  $FSR = c/2L$  and the laser frequency  $\omega_l$ . The dynamics can be modified by choosing the sign of the detuning, which will be explained in more detail later. We can now write down the spectral response of the oscillator

$$S_{xx}(\omega) = \frac{\gamma_m \cdot k_B T}{\pi m} \cdot \frac{1}{(\omega_{eff}^2 - \omega^2)^2 + \omega^2 \gamma_{eff}^2}. \quad (3.58)$$

It is interesting to note that the radiation-pressure force is completely contained in the effective frequency and damping rate and that only the Brownian noise force appears in the equation of motion  $\tilde{x}(\omega)$ . According to the fluctuation-dissipation theorem the coupling to the thermal bath at temperature  $T$  is uniquely described by  $\gamma_m$  [3, 61]. In analogy to the damped harmonic oscillator subject to a thermal Brownian driving force we use the Wiener-Khinchin theorem and find

$$m\omega_{eff}^2 \langle x^2 \rangle = m\omega_{eff}^2 \int_{-\infty}^{+\infty} \tilde{x}(\omega) d\omega = k_B T \cdot \frac{\gamma_m}{\gamma_{eff}} = k_B T_{eff}, \quad (3.59)$$

here we have introduced an effective temperature  $T_{eff} = T \frac{\gamma_m}{\gamma_{eff}}$ , which again satisfies the equipartition theorem for the harmonic oscillator. For an experiment where the

parameters are chosen such that  $\gamma_{eff}$  is increased, the radiation-pressure interaction allows for cooling of the mechanical mode.

In our optomechanical system the mass in the radiation-pressure interaction is not the actual mass  $m$  of the oscillating mirror but rather a quantity that takes the finite overlap of the optical and the mechanical mode into account, the effective mass  $m_{eff}$ . An extensive theoretical analysis of the matter can be found in [62], while the experimental procedure to determine the effective mass is described in section 4.10.

### 3.3.2 Quantum analysis

In this section we will analyze the radiation-pressure interaction between an optical cavity mode and a mechanical oscillator in a quantum framework. The derivation closely follows [63, 64] and assumes that we detect a single mechanical mode only, that the individual mechanical modes do not couple to each other and that we only have to consider a single cavity mode, i.e.  $\omega_m \ll c/2L$ . The full Hamiltonian of the system at hand is [65]

$$H = \hbar\omega_c a^\dagger a + \frac{1}{2}\hbar\omega_m (p_m^2 + x_m^2) - \hbar g_0 a^\dagger a x_m + i\hbar E (a^\dagger e^{-i\omega_l t} - a e^{i\omega_l t}). \quad (3.60)$$

Here  $\omega_c$  is the cavity frequency,  $a$  and  $a^\dagger$  are the annihilation and creation operators of the cavity field, with  $[a, a^\dagger] = 1$ ,  $p_m$  and  $x_m$  are the dimensionless versions of the momentum and position operators of the mechanical oscillator defined in equation (3.34), i.e.  $[x_m, p_m] = i$  and their creation and annihilation operators are  $b$  and  $b^\dagger$ , respectively,  $g_0$  is the frequency shift of the cavity due to the displacement of the mechanical oscillator by a single-photon,  $E$  related to the input laser power  $P$  by  $|E| = \sqrt{2P\kappa/\hbar\omega_l}$  and  $\omega_l$  the laser frequency. The optomechanical coupling rate  $g_0$  is a measure for the frequency shift of the cavity when the mechanics is displaced by  $x_{zp}$  and is defined as  $g_0 = \frac{\partial\omega_c}{\partial x} \cdot x_{zp}$ . For a Fabry-Pérot cavity  $g_0$  is given by

$$g_0 = \frac{\omega_c}{L} \sqrt{\frac{\hbar}{m_{eff} \cdot \omega_m}}, \quad (3.61)$$

as  $\omega_c = \frac{2\pi c}{\lambda} = \frac{2\pi c \cdot n}{L}$ , with  $n \in \mathbb{N}$ , where  $L$  is the cavity length. The first term of the Hamiltonian is the energy of the cavity field, while the second term is the corresponding quantity for the mechanical mode. The third term is the optomechanical interaction Hamiltonian  $H_{rp}$  on which we will concentrate in the following and the last term describes the coupling of the laser to the cavity mode.

In order to obtain the dynamics of the optomechanical system, one usually finds the Langevin equations of the system – they are stochastic differential equations describing the time evolution of a subset of degrees of freedom, where the mean value of the system slowly varies and is treated dynamically, while the small fluctuations around the mean value are treated probabilistically. Paul Langevin initially considered the Brownian motion of particles [66] and assumed that such a particle is subject to a systematic force, i.e. a viscous drag, and a rapidly fluctuating force, which comes from surrounding particles randomly impacting on the system under investigation with a mean amplitude of zero, i.e. the net force is zero on average. He treated this rapid force statistically, assuming that it was independent from the



viscous drag and arrived at an expression for the mean motion of the particle (for an introduction to Langevin equations see for example [67]). In general, the Langevin equations for an operator  $\hat{O}$  are given by  $\partial\hat{O}/\partial t = (i/\hbar) [H, \hat{O}] + \hat{N}$ , where  $\hat{N}$  is the corresponding noise operator of  $\hat{O}$ . The quantum Langevin equations for the optomechanical system therefore are

$$\begin{aligned}\dot{x}_m &= \omega_m p_m, \\ \dot{p}_m &= -\omega_m x_m - \gamma_m p_m + g_0 a^\dagger a + \xi, \\ \dot{a} &= -(\kappa + i\Delta_0) a + ig_0 a x_m + E + \sqrt{2\kappa} a^{in},\end{aligned}\tag{3.62}$$

where  $\gamma_m$  is the damping of the viscous force that acts on the mechanical mode and  $\xi$  is the Brownian stochastic force with zero mean amplitude. We have also introduced the cavity detuning  $\Delta_0 = \omega_c - \omega_l$  and the optical vacuum input noise  $a^{in}$ . In order to simplify the problem we can take a semi-classical approach by assuming a strong intra-cavity field amplitude  $|\alpha_s| \gg 1$ , which allows us to write down a steady state amplitude for each operator with small zero-mean fluctuations, i.e. for the generic operator  $\hat{O} = \hat{O}_s + \delta\hat{O}$ , where  $\hat{O}_s$  now is the mean value with the fluctuation operator  $\delta\hat{O}$ . We first find the steady state values by setting the time derivatives in (3.62) to zero

$$x_s = \frac{g_0 |\alpha_s|^2}{\omega_m},\tag{3.63}$$

$$\alpha_s = \frac{E}{\kappa + i\Delta}.\tag{3.64}$$

Due to the bright light field inside the cavity the mechanical oscillator is displaced by  $x'_s = x_s \cdot x_{zsp}$  into a new equilibrium position. Here  $\Delta$  is the detuning of the cavity including radiation-pressure effects

$$\Delta = \Delta_0 - \frac{g_0^2 |\alpha_s|^2}{\omega_m}.\tag{3.65}$$

The nonlinear equation for  $\Delta$  can be solved analytically but gives a rather lengthy expression which will not be shown here.<sup>1</sup> The Langevin equations can now be rewritten for the fluctuation operators, while neglecting their higher order terms:

$$\begin{aligned}\delta\dot{x}_m &= \omega_m \delta p_m, \\ \delta\dot{p}_m &= -\omega_m \delta x_m - \gamma_m \delta p_m + g\delta X + \xi, \\ \delta\dot{X} &= -\kappa\delta X + \Delta\delta Y + \sqrt{2\kappa} X^{in}, \\ \delta\dot{Y} &= -\kappa\delta Y - \Delta\delta X + g\delta x_m + \sqrt{2\kappa} Y^{in}.\end{aligned}\tag{3.66}$$

---

<sup>1</sup>Note that the detuning of the laser to the cavity in an experiment equals the detuning for an empty cavity, if the laser frequency is kept on resonance with the cavity and only part of it is detuned and used for radiation-pressure coupling, i.e.  $\Delta = \Delta_0$  for our experimental situation (cf. chapters 6 and 7). This of course does not imply  $\frac{g_0^2 |\alpha_s|^2}{\omega_m} = 0$  in (3.65).

We have introduced the cavity field quadratures  $\delta X = (\delta a + \delta a^\dagger) / \sqrt{2}$  and  $\delta Y = (\delta a - \delta a^\dagger) / i\sqrt{2}$ , as well as the corresponding Hermitian input noise operators  $X^{in} = (a^{in} + a^{in,\dagger}) / \sqrt{2}$  and  $Y^{in} = (a^{in} - a^{in,\dagger}) / i\sqrt{2}$ . The effective optomechanical coupling rate in the linearized quantum Langevin equations is

$$g = \alpha_s \cdot g_0 = \frac{2\omega_c}{L} \sqrt{\frac{P\kappa}{m_{eff}\omega_m\omega_l(\kappa^2 + \Delta^2)}}. \quad (3.67)$$

In an actual experiment the cavity is never perfectly single-sided, i.e. it is not possible for a mirror to have unity reflectivity, and therefore leakage of the field through the second mirror needs to be taken into account

$$g = \frac{2\omega_c}{L} \sqrt{\frac{P\kappa'}{m_{eff}\omega_m\omega_l((\kappa' + \bar{\kappa})^2 + \Delta^2)}}, \quad (3.68)$$

where we have introduced the amplitude cavity decay rate for the first  $\kappa'$  and the second mirror  $\bar{\kappa}$ . They are defined as  $\kappa_i = \frac{c}{4L} \cdot \varrho_i$ , where  $\varrho_i$  are the losses associated with the respective mirror and  $\kappa = \sum_i \kappa_i$ .

By linearizing the problem we have lost the non-linear interaction character in equation (3.60), which would be accessible for example by single photons. However, we have gained significantly in the achievable interaction strength by simply increasing the intra-cavity field. When solving the linearized Langevin equations according to [63, 64] we finally obtain the effective susceptibility for the mechanical oscillator interacting with the cavity mode via radiation pressure

$$\chi_{eff}(\omega) = \frac{\omega_m}{\omega_m^2 - \omega^2 - i\omega\gamma_m - \frac{g^2\Delta\omega_m}{(\kappa - i\omega)^2 + \Delta^2}}. \quad (3.69)$$

The effective mechanical frequency and damping rate are given by

$$\omega_{eff}(\omega) = \left( \omega_m^2 - \frac{2g^2\Delta\omega_m(\kappa^2 - \omega^2 + \Delta^2)}{[\kappa^2 + (\omega - \Delta)^2][\kappa^2 + (\omega + \Delta)^2]} \right)^{1/2}, \quad (3.70)$$

$$\gamma_{eff}(\omega) = \gamma_m + \frac{g^2\Delta\omega_m\kappa}{[\kappa^2 + (\omega - \Delta)^2][\kappa^2 + (\omega + \Delta)^2]}. \quad (3.71)$$

The modification of the mechanical oscillation frequency is called the optical spring effect, as the spring constant of the resonator is effectively modified. This effect has first been observed experimentally in [68] and subsequently been confirmed in several experiments [69–71]. In extreme cases this effect can change the resonance frequency by almost two orders of magnitude [72]. The change in the damping rate can be used to heat or cool the mechanical resonator – when choosing the detuning  $\Delta$  between the laser and the cavity to be negative the mechanical system is excited by radiation pressure and therefore parametrically driven [37]. However, if  $\Delta > 0$  the mechanical motion is damped, which corresponds to an effective cooling of the mode as long as the laser noise is small compared to the thermal noise [73, 74]. The thermal mean occupation of such a damped oscillator is given by the Bose-Einstein statistics  $\bar{n} = (\exp\{\hbar\omega_m/k_B T_{eff}\} - 1)^{-1}$ , where the temperature now is an

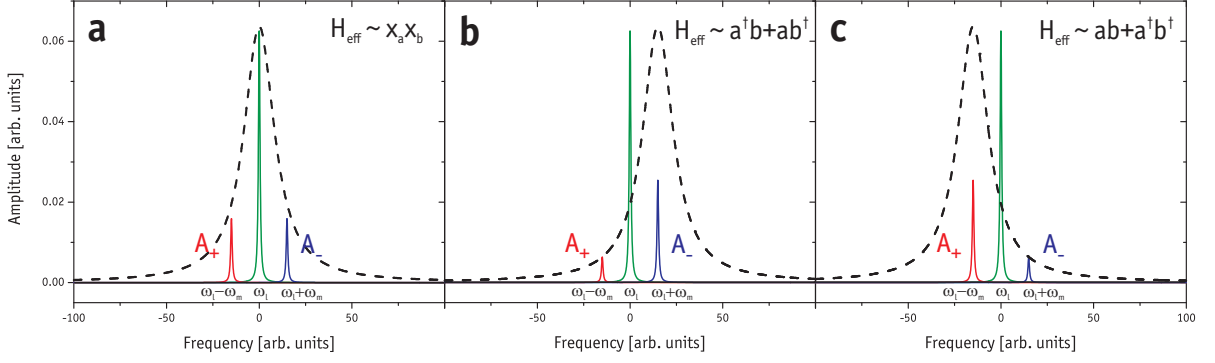


Figure 3.6: **a** A laser field (green) with frequency  $\omega_l$  drives the optomechanical cavity (dashed black line) on resonance. Due to the radiation-pressure interaction frequency sidebands are created at  $\omega_l - \omega_m$  (red) and  $\omega_l + \omega_m$  (blue) with rates  $A_{\pm}$ , respectively, given by equation (3.72). The rates  $A_{\pm}$  are equal and this configuration allows for example to perform quantum non-demolition measurements as proposed in [26, 27]. **b** The situation becomes quite different if the cavity is detuned with respect to the laser by  $\Delta = \omega_m$ . The rates become unbalanced and  $A_- > A_+$ , which results in cooling of the mechanical mode. This can be intuitively understood as the sideband with higher energy (which is created by extracting phonons from the mechanical resonator), the anti-Stokes sideband, becomes stronger than lower energy Stokes sideband. The corresponding effective interaction Hamiltonian is  $\propto a^\dagger b + ab^\dagger$  (see section 3.3.3). **c** When detuning the cavity by  $\Delta = -\omega_m$  the effective interaction Hamiltonian becomes a two-mode squeezer, i.e. is  $\propto ab + a^\dagger b^\dagger$ , which can be used for creating optomechanical entanglement (see section 3.3.6 and chapter 8). The effective interactions in **b** and **c** are valid in the rotating wave approximation (RWA), i.e. for weak coupling and sideband resolved operation ( $\omega_m > \kappa$ ).

effective mode temperature  $T_{eff}$ . It has been theoretically shown that this technique in principle allows for cooling the mechanical mode into its quantum ground state if operating in the sideband-resolved regime, i.e.  $\omega_m > \kappa$  [64, 75, 76]. The first experimental demonstrations of such a passive mechanical cavity-cooling have been realized by [38–41, 77], with similar experiments in the microwave regime [54, 56, 57], however no experiment to date has shown ground state cooling using this technique. Another interesting quantity for such cooling experiments is the scattering rate  $A_{\pm}$  of laser photons into the Stokes (+) and anti-Stokes (-) sideband, where for positive detuning an imbalance between the sidebands of the form  $A_- > A_+$  results in the desired cooling

$$A_{\pm} = \frac{g^2 \kappa}{8 [\kappa^2 + (\Delta \pm \omega_m)^2]}. \quad (3.72)$$

### 3.3.3 Quantum opto-mechanics

The Hamiltonian (3.60) can be rewritten in the interaction picture, i.e. we make a basis change into the frame rotating at the laser frequency  $\omega_l$ . The corresponding unitary transformation is  $U(t) = \exp(i\omega_l t a^\dagger a)$  and we can first transform the Schrödinger equation

$$i\hbar \frac{d}{dt} |\psi\rangle = H |\psi\rangle \rightarrow i\hbar \frac{d}{dt} \left( U^\dagger |\tilde{\psi}\rangle \right) = H U^\dagger |\tilde{\psi}\rangle, \quad (3.73)$$

where  $|\tilde{\psi}\rangle = U |\psi\rangle$ . After some simple algebra we get  $i\hbar \frac{d}{dt} |\tilde{\psi}\rangle = \tilde{H} |\tilde{\psi}\rangle$ , with

$$\tilde{H} = U \left( H - i\hbar \frac{d}{dt} \right) U^\dagger = \hbar \Delta a^\dagger a + \frac{1}{2} \hbar \omega_m (p_m^2 + x_m^2) - \hbar g_0 a^\dagger a x_m + \hbar E (a^\dagger + a). \quad (3.74)$$

Another way of qualitatively describing the cooling is to analyze the interaction term  $H_{rp}$  of the Hamiltonian. By assuming  $\alpha_s \gg 1$  one can write  $a \rightarrow \alpha_s + a$ , where  $a$  now is the associated fluctuation operator and  $a^\dagger \rightarrow \alpha_s + a^\dagger$ . By factorizing  $H_{rp}$  and neglecting higher order terms in the fluctuation operators we obtain

$$H_{rp} \approx \hbar \alpha_s g_0 (a + a^\dagger) \cdot (b + b^\dagger), \quad (3.75)$$

where we have used the definition for  $x_m$  and omitted a static mirror displacement of  $\mathcal{O}(\alpha^2 x_m)$ , which is defined by (3.63). If we go into another rotating frame by using the unitary operator  $U'(t) = \exp(i(\Delta a^\dagger a + \omega_m b^\dagger b)t)$  we obtain for the linearized interaction Hamiltonian

$$\begin{aligned} \tilde{H}'_{rp} &= \hbar g (a e^{-i\Delta t} + a^\dagger e^{i\Delta t}) \cdot (b e^{-i\omega_m t} + b^\dagger e^{i\omega_m t}) \\ &= \hbar g (a b e^{-i(\Delta + \omega_m)t} + a^\dagger b^\dagger e^{i(\Delta + \omega_m)t}) + \hbar g (a^\dagger b e^{i(\Delta - \omega_m)t} + a b^\dagger e^{-i(\Delta - \omega_m)t}). \end{aligned} \quad (3.76)$$

The first term is  $\propto ab + a^\dagger b^\dagger$ , which is a two-mode squeezing (TMS) operation and hence can be used to entangle the optical with the mechanical mode (see section 3.3.6). The second term  $\propto a^\dagger b + ab^\dagger$  in turn is simply a beamsplitter (BS) interaction, which results in the cooling described above. If the detuning  $\Delta$  is chosen to be  $+\omega_m$  the phase of the BS vanishes, while the TMS oscillates at a frequency of  $2\omega_m$ . By performing a perturbation expansion we can see that for this case the TMS term only contributes on the order of  $\frac{g}{\omega_m}$  and the BS dominates for small  $g$  and sideband resolution ( $\omega_m > \kappa$ ), which corresponds to the so-called rotating wave approximation (RWA). The inverse is true for  $\Delta = -\omega_m$ .

### 3.3.4 SQL + Backaction

Due to the quantum nature of light, measurements of the motion of a mechanical oscillator as described in this thesis are fundamentally limited in sensitivity. In general, the uncertainty principle poses a limit on how well one can continuously measure a certain quantity. The phase and the photon number (amplitude) of a light field, for example, are connected by the uncertainty relation  $\Delta\phi \cdot \Delta n \geq 1/2$  (for a coherent state this actually becomes an equality if  $\alpha$  is large, as shown in

section 3.2.1). In order to determine the displacement of the mechanical oscillator we measure the phase shift the movement imparts on a probing light field. The field itself however has a phase uncertainty of  $\Delta\phi = 1/(2\sqrt{\bar{n}})$ , which is due to the shot-noise of the laser and for small  $\bar{n}$  makes the measurement noisy. This can be overcome by increasing the read-out intensity. However, increasing the laser power also increases another noise source, namely the shot-noise induced backaction of the laser, which is just the uncertainty in the photon number  $\Delta n = \sqrt{\bar{n}}$  of the laser. This results in random “kicks” of the mechanical oscillator, which is proportional to  $2\hbar k\sqrt{\bar{n}}$ , and commonly called backaction noise. When increasing the read-out power the noise is first dominated by the phase uncertainty, while the backaction dominates at large powers. The point where the two contributions are of equal size is the so-called standard quantum limit (SQL), which for a position measurement of an oscillator with mass  $m$  and frequency  $\omega_m$  is given by [78, 79]

$$\Delta x_{SQL} = \sqrt{\frac{\hbar}{2m\omega_m}}. \quad (3.77)$$

In all optomechanical experiments to date either the phase noise or the thermal noise dominate the backaction noise, and therefore it remains an outstanding goal to observe the backaction effects of radiation pressure (for a review on the quantum noise in measurements see [3]). Note that several schemes exist to circumvent this measurement limit by, for example, measuring only one quadrature of the resonator in a backaction evading scheme [80–82].<sup>2</sup>

### 3.3.5 Strong coupling

In our experimental arrangement, the optomechanical system comprises two harmonic oscillators in the linearized regime, namely the light field and the mechanical resonator. In section 3.1.1 we have seen that two coupled oscillators exhibit normal modes, which are non-degenerate in energy if their coupling exceeds the damping rates of the individual systems. This so-called strong coupling regime is interesting for optomechanical systems as coherent quantum control of the mechanical oscillator requires an energy exchange between the optical and the mechanical part that is faster than the dissipation rates of the two systems into their local environments, i.e.  $g \gtrsim \kappa, \gamma_m$ . This condition is also known from cavity QED [83] and solid state qubits coupled to photons [84, 85]. The normal mode splitting can be used as unambiguous evidence that the system actually is in the strong coupling regime, while the modes stay degenerate if  $g$  is small. As we have seen in section 3.3.2 the optomechanical coupling can be increased by increasing the intra-cavity amplitude  $\alpha_s$ , which experimentally corresponds to increasing the input laser power  $P$ .

In this section we will use a quantum approach to briefly derive the normal modes for the coupled optomechanical system and show that the splitting can only be observed when entering the strong coupling regime. The derivation is taken from [46]. We start by defining  $\vec{R}^T = (x_c, p_c, x_m, p_m)$ , where  $x$  and  $p$  are the amplitude (position) and phase (momentum) operators for the cavity field (the mechanical mode),

<sup>2</sup>Note that in the experiment presented in section 6.2 we have achieved sub-SQL measurement precision [3].

respectively, and express the linearized Hamiltonian as  $H = \frac{\hbar}{2} \vec{R}^T M \vec{R}$  where

$$M = \begin{pmatrix} \Delta & 0 & g & 0 \\ 0 & \Delta & 0 & 0 \\ g & 0 & \omega_m & 0 \\ 0 & 0 & 0 & \omega_m \end{pmatrix}.$$

The transformation to normal modes  $\vec{R}^{NM} = (x_+, p_+, x_-, p_-)$  is achieved with a linear transformation  $\vec{R}^{NM} = S \vec{R}$ , where  $S$  fulfills  $M = S^T \text{diag}(\omega_+, \omega_+, \omega_-, \omega_-) S$  and is symplectic, i.e. it obeys  $J = S J S^T$  where

$$J = \begin{pmatrix} 0 & 1 & 0 & 0 \\ -1 & 0 & 0 & 0 \\ 0 & 0 & 0 & 1 \\ 0 & 0 & -1 & 0 \end{pmatrix}.$$

The latter property guarantees that canonical commutation relations are conserved, i.e.  $[\vec{R}_i, \vec{R}_j] = [\vec{R}_i^{NM}, \vec{R}_j^{NM}] = i J_{ij}$ . The explicit form of  $S$  can in principle be determined, but is quite involved and does not give much insight. As will become clear in a moment, the normal mode frequencies  $\omega_{\pm}$  can be easily calculated without constructing  $S$  and are (in the absence of damping) given by

$$\omega_{\pm}^2 = \frac{1}{2} \left( \Delta^2 + \omega_m^2 \pm \sqrt{(\Delta^2 - \omega_m^2)^2 + 4g^2 \omega_m \Delta} \right). \quad (3.78)$$

The canonical operators evolve according to

$$\dot{\vec{R}}(t) = i[H, \vec{R}(t)] - D \vec{R}(t) - \sqrt{2D} \vec{R}_{in}(t) = (JM - D) \vec{R}(t) - \sqrt{2D} \vec{R}_{in}(t), \quad (3.79)$$

where we included damping of the cavity field and the mechanical resonator with  $D = \text{diag}(\kappa, \kappa, \gamma_m, \gamma_m)$  and Langevin forces  $\vec{R}_{in}(t) = (x_{in}, p_{in}, f_{x_m}, f_{p_m})$ . For white vacuum noise input to the cavity and a thermal white noise bath coupling to the mechanical system, all first moments vanish  $\langle \vec{R}(t) \rangle \equiv 0$  and the only non-zero time correlation functions are

$$\begin{aligned} \langle x_{in}(t) x_{in}(t') \rangle &= \langle p_{in}(t) p_{in}(t') \rangle = \frac{1}{2} \delta(t - t'), \\ \langle f_{x_m}(t) f_{x_m}(t') \rangle &= \langle f_{p_m}(t) f_{p_m}(t') \rangle = \left( \bar{n} + \frac{1}{2} \right) \delta(t - t'), \end{aligned} \quad (3.80)$$

where  $\bar{n} \approx \frac{k_B T}{\hbar \omega_m}$ .

From (3.79) it is clear that eigenfrequencies and effective damping rates of the system are given by, respectively, the imaginary and real parts of the eigenvalues of  $i(JM - D)$ . The eigenvalues occur in complex conjugate pairs and the imaginary parts of the ones in the upper half plane determine eigenfrequencies. For the undamped system,  $D = 0$ , the eigenvalues are purely complex and one arrives at expression (3.78) for the normal mode frequencies. For the damped system,  $D \neq 0$ , the eigenvalues of  $i(JM - D)$  will in general be complex and thus determine normal mode frequencies  $\omega_{\pm}$  and effective damping rates  $\gamma_{\pm}$  of normal modes, as exemplified

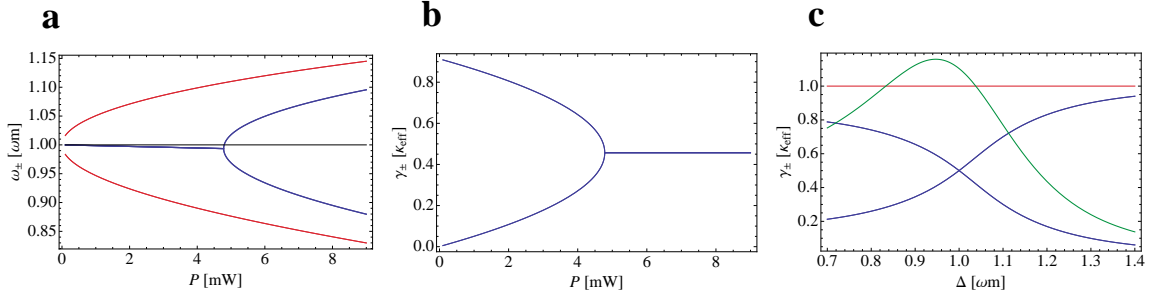


Figure 3.7: **a** Normal mode frequencies  $\omega_{\pm}$  for an undamped (red) and a damped system (blue) for varying power of the driving laser. **b** Same for effective normal mode damping  $\gamma_{\pm}$ . **c** Effective damping rates of normal modes (blue), cavity amplitude decay rate  $\kappa$  (red) and effective mechanical decay rate  $\gamma_{eff}$  (green) for varying detuning. Not shown is the natural mechanical damping rate as  $\gamma_m/\kappa \simeq 10^{-3}$ . Parameters are as in chapter 7,  $\omega_m = 2\pi \times 947$  kHz,  $\gamma_m = 2\pi \times 140$  Hz,  $m_{eff} = 145$  ng,  $L = 25$  mm,  $\omega_c = 1.77 \times 10^{15}$  Hz,  $\kappa' = 2\pi \times 172$  kHz and  $\bar{\kappa} = 2\pi \times 43$  kHz. In **a** and **b**  $\Delta = \omega_m$  and in **c**  $P = 10.7$  mW. Thanks to Klemens Hammerer for providing the plots.

in Fig. 3.7. While normal mode splitting (NMS) occurs for any non-zero coupling  $g$  in an undamped, a threshold of  $g \gtrsim \kappa$  must be surpassed to observe NMS in a damped system [76, 86]. The effective damping rates behave complementary and merge above the same threshold. Comparison of the normal mode damping rates  $\gamma_{\pm}$  to the effective mechanical damping rate (3.71) shows that the condition for resolving the normal mode peaks is  $g \gg \kappa, \gamma_m$ .

In terms of normal mode operators the full linearized Hamiltonian (3.75) is given by  $H = \frac{\hbar\omega_+}{2}(x_+^2 + p_+^2) + \frac{\hbar\omega_-}{2}(x_-^2 + p_-^2)$ . It can be expressed also in terms of creation and annihilation operators  $a_{\pm} = (x_{\pm} + ip_{\pm})/\sqrt{2}$  as  $H = \hbar\omega_+ \left( a_+^{\dagger} a_+ + \frac{1}{2} \right) + \hbar\omega_- \left( a_-^{\dagger} a_- + \frac{1}{2} \right)$ . The Eigenstates and -energies are thus  $H|n, m\rangle = E_{n,m}|n, m\rangle$ , where

$$|n, m\rangle = \frac{1}{\sqrt{n!m!}} (a_+^{\dagger})^n (a_-^{\dagger})^m |0, 0\rangle,$$

$$E_{n,m} = \hbar\omega_+ \left( n + \frac{1}{2} \right) + \hbar\omega_- \left( m + \frac{1}{2} \right). \quad (3.81)$$

Emission of a cavity photon is in general accompanied by a transition of the optomechanical system from one eigenstate to another by changing a single excitation,  $|n, m\rangle \leftrightarrow |n-1, m\rangle$  and  $|n, m\rangle \leftrightarrow |n, m-1\rangle$ . In order for such a transition to be allowed, the matrix element  $\langle k, l | a_c | n, m \rangle$  must be non-zero, where  $a_c = (x_c + ip_c)/\sqrt{2}$  is the annihilation operator for a cavity photon. From the linear relation  $\vec{R} = S^{-1} \vec{R}^{NM}$  it is clear that  $a_c$  can be related to the normal mode creation and annihilation operators via a Bogoliubov transformation  $a_c = \eta_1 a_+ + \eta_2 a_+^{\dagger} + \eta_3 a_- + \eta_4 a_-^{\dagger}$  where  $\eta_i$  are complex numbers. The energy splitting between these states is  $E_{n,m} - E_{n-1,m} = \hbar\omega_+$

and  $E_{n,m} - E_{n,m-1} = \hbar\omega_-$  respectively. Photons emitted from the cavity have to carry away this energy excess/deficiency relative to the incoming laser photons of frequency  $\omega_l$ , i.e. they have to have frequencies  $\omega_l \pm \omega_+$  or  $\omega_l \pm \omega_-$ .

The power spectral density of light emitted by the cavity is explicitly determined as follows: In frequency space  $[\vec{R}(\omega) = \int d\omega \vec{R}(t) \exp(i\omega t)/\sqrt{2\pi}]$  the steady state solutions to the equations of motion (3.79) are

$$\vec{R}(\omega) = \frac{1}{i\omega + JM - D} \sqrt{2D} \vec{R}_{in}(\omega). \quad (3.82)$$

With the quantum optical cavity input-output relations (see for example [87, 88]) it follows that

$$\vec{R}_{out}(\omega) = \sqrt{2D} \vec{R}(\omega) + \vec{R}_{in}(\omega) = \left( \sqrt{2D} \frac{1}{i\omega + JM - D} \sqrt{2D} + 1 \right) \vec{R}_{in}(\omega),$$

where  $\vec{R}_{out}(\omega) = (x_{out}, p_{out}, f_{x_{m,out}}, f_{p_{m,out}})$ .  $(x_{out}, p_{out})$  are quadratures for the cavity output field which are subject to homodyne detection (see section 4.6). In order to calculate their stationary properties we formally introduce also "phononic output fields"  $(f_{x_{m,out}}, f_{p_{m,out}})$ . The spectral correlation functions can be collected in a Hermitian spectral  $4 \times 4$  correlation matrix  $\gamma_{ij}^{out}(\omega, \omega') = \langle (\vec{R}_{out}(\omega'))_i (\vec{R}_{out}(\omega))_j \rangle$ . Straight forward calculation yields  $\gamma^{out}(\omega, \omega') = \delta(\omega + \omega') \Gamma(\omega)$  where

$$\Gamma(\omega) = \left( \sqrt{2D} \frac{1}{i\omega + JM - D} \sqrt{2D} + 1 \right) N \left( \sqrt{2D} \frac{1}{-i\omega + JM - D} \sqrt{2D} + 1 \right)^T$$

and  $N = \text{diag} \left( \frac{1}{2}, \frac{1}{2}, \bar{n} + \frac{1}{2}, \bar{n} + \frac{1}{2} \right)$ . The generalization of  $\Gamma(\omega)$  where a lossy second mirror with an associated  $\bar{\kappa}$  is taken into account can be found in [46]. Finally, the spectral density  $S(\omega)$  is defined as  $S(\omega) \delta(\omega + \omega') = \langle a_{out}^\dagger(\omega') a_{out}(\omega) \rangle$  where the amplitude operator for the cavity output field is  $a_{out}(\omega) = (x_{out}(\omega) + ip_{out}(\omega)) \sqrt{2}$ . It follows from the definition of the spectral correlation matrix given above that

$$S(\omega) = \frac{1}{2} [\Gamma_{11}(\omega) + \Gamma_{22}(\omega) + i(\Gamma_{12}(\omega) - \Gamma_{21}(\omega))].$$

This expression gives the spectral density of sideband modes at a frequency  $\omega_l + \omega$ . In homodyne detection of sideband modes we do not distinguish sideband frequencies  $\omega_l \pm \omega$  and extract only the overall noise power spectrum at a sideband frequency  $|\omega|$ , which is given by  $S_{NPS}(\omega) = \sqrt{S(\omega)^2 + S(-\omega)^2}$ . The calculated positions of the spectral peaks are in excellent agreement with measured data presented in chapter 7.

### 3.3.6 Optomechanical entanglement

The generation of entanglement between an optical light field and a mechanical oscillator is a major outstanding goal in the field of quantum opto-mechanics. Showing quantum entanglement with a massive macroscopic object is a sufficient condition for unambiguously demonstrating that quantum physics remains valid even for macroscopic systems. Besides the purely academic benefit of generating optomechanical entanglement and using it for generating non-classical mechanical states [31, 89], it



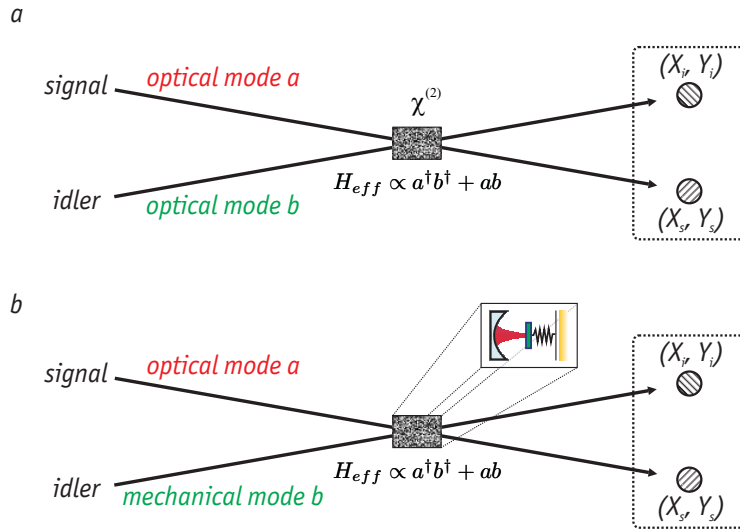


Figure 3.8: **a** Down-conversion in continuous variable quantum optics. Two optical fields (signal and idler) interact in a nonlinear  $\chi^{(2)}$  medium generating a 2-mode squeezed output state. The quadratures  $X_{s,i}$  and  $Y_{s,i}$  of the fields become non-classically correlated (figure adapted from Ou et al. [92]). **b** The optomechanical analogue to down-conversion – here the signal is an optical field non-linearly interacting with the vibrations of a mechanical resonator inside a properly detuned optical cavity. The effective interaction Hamiltonians of both **a** and **b** are equivalent. For properly chosen parameters (see text and figure 3.9) the optomechanical system becomes entangled and hence also exhibits non-classical correlations.

is also at the heart of several applications in quantum information processing, such as quantum teleportation [90, 91].

In quantum optics the generation of entangled states between two optical modes can nowadays be routinely achieved both for continuous variables [92] and discrete quantum systems [93]. The most commonly used technique to create an entangled state is to use down-conversion in a nonlinear medium. It is interesting to note, that the interaction of an optical field with the mechanical motion of an oscillator inside an optical cavity is also of a nonlinear nature, in fact part of it is the exact analogue to the down-conversion interaction in quantum optics. In the quantum optical continuous variable approach the resulting quantum states of the down-conversion process are 2-mode squeezed fields – exactly the same is produced if we pump the optical cavity in the optomechanical setup with a blue-detuned beam, only this time 2-mode squeezing between an optical and a mechanical continuous variable system is generated. For large squeezing the 2-mode squeezed states approximate the perfect correlations between conjugate observables as are required for an entangled state of the type described in the seminal paper by Einstein, Podolsky and Rosen (EPR) [94].

Let us first recall the situation for two optical modes. In simple conceptual terms the down-conversion (2-mode squeezing) interaction in a non-linear medium couples

two previously uncorrelated modes via a Hamiltonian

$$H_{dc} = -i\hbar\chi(a_1^\dagger a_2^\dagger - a_1 a_2), \quad (3.83)$$

where  $\chi \propto |\alpha_p|^2$  is the coupling strength between the optical modes 1, 2 and  $\alpha_p$  is the amplitude of the optical pump field [92, 95, 96]. The main action of this interaction is to correlate one pair of quadratures between the outgoing modes, say the amplitude quadratures  $x_{1,2} = (a_{1,2} + a_{1,2}^\dagger)/\sqrt{2}$ , and anti-correlate the conjugate pair of quadratures, here the phase quadratures  $p_{1,2} = (a_{1,2} - a_{1,2}^\dagger)/\sqrt{2}i$ . With increasing interaction strength the uncertainty in the sum (difference) between the quadratures decreases,  $\Delta(x_1 - x_2)^2$ ,  $\Delta(p_1 + p_2)^2 \rightarrow 0$ , whereas the uncertainty in the individual quadrature increases. In the limiting case of infinite squeezing of these variances the two modes will eventually approximate the entangled state underlying the famous EPR argument [94],  $|\Psi\rangle = \int dx|x, x\rangle = \int dp|p, -p\rangle = \sum_n |n, n\rangle$  (written here in position, momentum and number state representation, respectively). Realizations of sources for EPR entangled light, such as an optical parametric oscillator, typically require a cavity containing the nonlinear medium and supporting both modes 1 and 2. The EPR correlations between the modes can then be observed by performing two independent homodyne detections of light coupled out of these two cavities. The respective photocurrents for a given local oscillator phase  $\phi_j$  ( $j = 1, 2$ ) essentially provide a measurement of  $x_j(\phi_j) = (a_j e^{i\phi_j} + \text{h.c.})/\sqrt{2}$ . Cross correlating the two photocurrents thus constitutes a measurement of the correlations  $\langle x_1(\phi_1)x_2(\phi_2) \rangle$ , and scanning the local oscillator phases  $\phi_j$  gives direct access to the quadrature correlations and anti-correlations characteristic of an EPR state. This way it was possible to realize the EPR paradox [92] and to use this entanglement for quantum teleportation [97].

Let us now draw the direct analogy to the optomechanical case. The radiation-pressure interaction between a mechanical oscillator with resonance frequency  $\omega_m$  and an optical cavity field can effectively be described by (3.75)

$$H_{rp} = \hbar g(ab^\dagger + a^\dagger b) + \hbar g(ab + a^\dagger b^\dagger), \quad (3.84)$$

where the full Hamiltonian of the system is  $H = H_0 + H_{rp}$  given by (3.60). The first term in the interaction  $H_{rp}$  describes the exchange of energy between the mechanical oscillator and the cavity field. As long as photons can leave the cavity this leads to (optical) cooling of the mechanical mode [38–40, 99]. The second term is the 2-mode squeezing, or down-conversion interaction, and stands for creation and annihilation of phonons and photons in pairs. Up to a change in phase it is equivalent to  $H_{dc}$  in Eq. (3.83). By choosing the detuning  $\Delta$  of the laser from cavity resonance to be either  $+\omega_m$  or  $-\omega_m$  the first or the second process becomes resonant, respectively. The latter case resembles the desired down-conversion interaction  $H_{dc}$  between an optical cavity mode and a mechanical resonator mode, cf. figure 3.8b.

We focus on the situation where  $\Delta \approx \omega_m$ . In this case the so-called co-rotating (cooling) terms  $ab^\dagger + a^\dagger b$  dominate the interaction while the so-called counter-rotating (down-conversion) terms  $ab + a^\dagger b^\dagger$  contribute on the order of  $\frac{g}{\omega_m}$ , as can be directly seen from first-order perturbation theory. As long as the coupling strength is small, i.e. for  $g \ll \omega_m$ , one can neglect the counter-rotating terms and obtains the rotating wave approximation where only co-rotating terms are kept in the Hamiltonian [100]. This means that only cooling of the mechanical mode occurs (whose

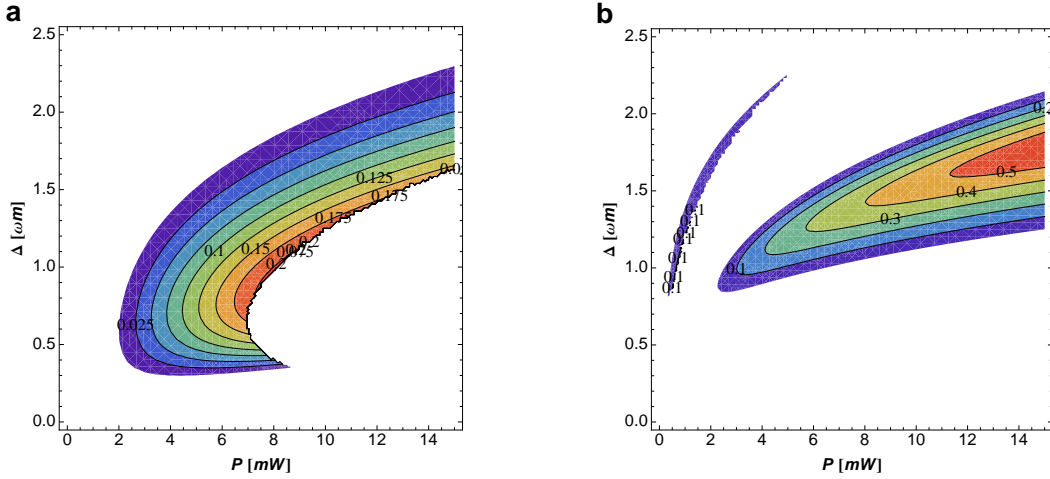


Figure 3.9: Optomechanical entanglement. The entanglement measure plotted here is the logarithmic negativity  $E_N$  (for a definition see for example [98]) as a function of optical detuning  $\Delta$  and input power  $P$ . Positive values of  $E_N$  mean that the optical and the mechanical systems are entangled. **a** The parameters are  $\omega_m = 950$  kHz,  $m_{eff} = 50$  ng,  $Q = 30,000$ ,  $L = 10$  mm,  $F = 7,000$  and  $T = 100$  mK. The maximal value of  $E_N$  is 0.2. **b** For this plot we chose  $\omega_m = 360$  kHz,  $m_{eff} = 50$  ng,  $Q = 63,000$ ,  $L = 25$  mm,  $F = 14,000$  and  $T = 100$  mK. We find a maximal  $E_N$  of 0.5. Note that the color coding of the contour plots is different for **a** and **b**. White areas mean that no entanglement is present. Thanks to Sebastian Hofer for providing the plots.

quantum limit is ultimately given exactly by the effects of counter-rotating terms). For increasing coupling strength, however, i.e. for  $\frac{g}{\omega_m} \approx \mathcal{O}(1)$ , this approximation is no longer valid and the regime beyond the rotating wave approximation becomes accessible. Specifically, while the co-rotating interaction increases its cooling action and hence prepares a mechanical input state of increasingly higher purity (i.e. smaller entropy), the strength of the counter-rotating interaction also increases and enables optomechanical down-conversion to take place. Note that in the realm of atomic physics the rotating wave approximation is so good that there are only few demonstrations of physical effects that are due to counter-rotating terms [101]. In our experiment (see chapter 8) it is the explicit breakdown of the rotating wave approximation that will allow us to combine state preparation with the desired nonlinear 2-mode interaction in a simple way.



## 4 Experimental techniques

### 4.1 Fiber-Interferometer

In order to have a testing station for our mechanical devices, we built a simple, fiber-based interferometer. It had several advantages over the actual Fabry-Pérot setup – it was easy to use, i.e. it did not require any active stabilization, the chips with the mechanical resonators could be easily swapped, the travel on the piezo-stage was larger and hence allowed for measuring a full chip at once and most importantly, in contrast to the actual setup, the radiation-pressure backaction was negligible and hence it did not have to be taken into account when determining the mechanical frequency and  $Q$ . The working principle is to use a cleaved fiber, put it above the chip with the mechanical devices, and measure the interference between the light that is directly reflected off the fiber-tip (which is approx. 4%) and the light being reflected by the mechanical device, which imparts a phase modulation due to its mechanical motion (see figure 4.1). This simple scheme allowed us to measure the mechanical properties at room temperature in a vacuum chamber, with the drawback that the devices had to be resonantly driven to increase the interference to a level where it was detectable. For a review see [102, 103]. Recently, several upgrades to the first design have been made and the current fiber interferometer is built in a continuous flow  $^4\text{He}$  cryostat, which allows for measurements down to 20 K. In addition, the read-out was replaced by a fiber-based homodyne detection scheme (see section 4.6), which can directly measure the phase modulation of the mechanical motion in the light field, and the fiber tip has been replaced with a fiber lens [104] to allow for automated mode tomography.

### 4.2 Optical resonators

An optical resonator, often referred to as an optical cavity, confines light between two or more mirrors. They are extensively used in lasers, where they surround the gain medium and provide feedback of the laser light. Only light with a certain phase shift upon reflection off the mirrors can be stored in the cavity, which makes it a frequency filter for light. It also acts as a spatial filter and produces either a standing or a traveling wave inside the resonator. The detailed properties of a cavity will be discussed in the following section.

In our experiments there are two main applications for a cavity - first, for the optomechanical interaction we use a Fabry-Pérot type cavity, i.e. a linear cavity with end mirrors, which enhances the interaction strength between the light field and the mechanical motion and also allows us to cool and eventually entangle the mechanical mirror (see chapter 3). And secondly, triangular cavities are used to spatially and spectrally filter the laser [105].

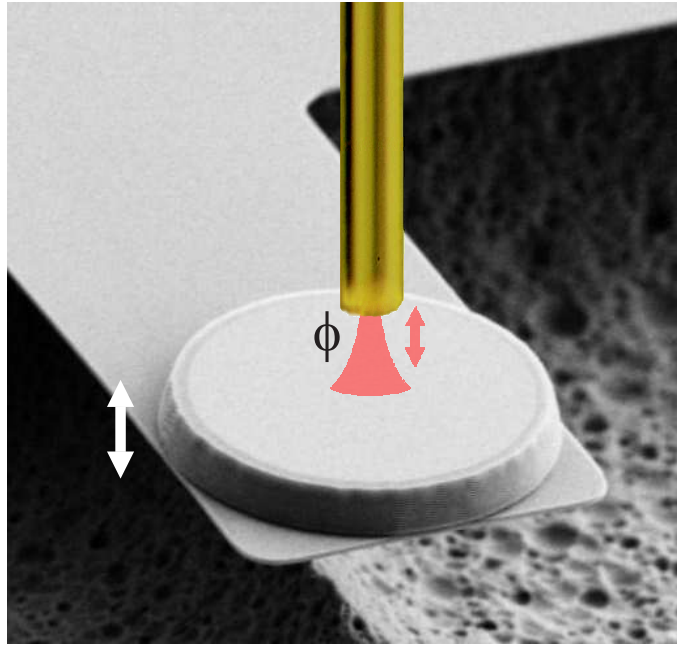


Figure 4.1: Working principle of the fiber interferometer. A fiber tip is positioned above the mechanical resonator, which modulates the phase  $\phi$  of the light field upon back-reflection into the fiber. The modulation can either be detected by observing the amplitude of the beam, as the fiber tip partially reflects light (around 4%), which then interferes with the signal reflected off the resonator, or by performing a homodyne measurement.

### 4.2.1 Fabry-Pérot cavity

The simplest kind of an optical resonator is a planar-mirror cavity. The basic design is made of two flat mirrors that face each other at a distance  $L$ . The wave function of an incident monochromatic field of frequency  $\omega = 2\pi \cdot f$  can be written as

$$E(\mathbf{r}, t) = A(\mathbf{r})e^{i\omega t}. \quad (4.1)$$

The complex amplitude  $A(\mathbf{r})$  satisfies the Helmholtz equation, i.e.  $\nabla^2 A(\mathbf{r}) + k^2 A(\mathbf{r}) = 0$ , where  $k = \omega/c$  is the wavenumber and  $c = c_0/n$  is the speed of light in the medium, with  $c_0$  being the vacuum speed of light and  $n$  the refractive index of the medium. The modes of the optical resonators are the solutions of the Helmholtz equation with the boundary conditions set by the two mirrors, i.e. the wave has to vanish at  $z = 0$  and  $z = L$ . Here  $z$  is the longitudinal propagation direction of the beam. A solution satisfying these conditions is a standing wave of the form  $A(\mathbf{r}) = A \sin(kz)$ , given that  $kL = q\pi$ , with  $q$  being an integer. The general solution for the resonator mode can therefore be written as

$$A(\mathbf{r}) = \sum_q A_q \sin(k_q z), \quad (4.2)$$

where  $A_q$  are constants and  $k_q = q\frac{\pi}{L}$ , with  $q = 1, 2, \dots$ . The spacing between two adjacent resonator modes is called the free spectral range (FSR) of the cavity and

is given by

$$FSR = \frac{c}{2L}, \quad (4.3)$$

as the wavelengths of each mode are  $\lambda_q = 2L/q$ . The phase shift  $\varphi$  of a resonant wave has to be an integer multiple of itself after one roundtrip, i.e.  $\varphi = q2\pi$ . So far we have considered equal mirrors with perfect (intensity) reflectivity  $R = 1$ . For partially reflecting mirrors however, the amplitude of the wave changes with each roundtrip by a complex factor  $h = \sqrt{R}e^{-i\varphi}$ , as  $\sqrt{R} \neq 1$  now is an amplitude attenuation factor. The amplitude after  $n$  roundtrips is therefore

$$A = \sum_n h^n A_0 = \frac{A_0}{1-h}, \quad (4.4)$$

for  $n \rightarrow \infty$ . The intensity of the light inside the optical resonator as a function of the optical frequency  $f$  is hence given by

$$I = |A|^2 = \frac{I_0}{(1 - \sqrt{R})^2 (1 + (2F/\pi)^2 \sin^2(\pi f / FSR))}, \quad (4.5)$$

where  $I_0 = |A_0|^2$  and  $F$  the finesse of the cavity, which is a measure of the quality of the cavity [106]

$$F := \frac{\pi\sqrt{\sqrt{R}}}{1 - \sqrt{R}}. \quad (4.6)$$

In a real experiment the cavity is in general not impedance matched, i.e. the reflectivities of the mirrors are not equal,  $R_1 \neq R_2$ . Also any real cavity will have some losses that cannot be attributed to the transmission losses of the mirrors, for example absorption or scattering – both in the mirror and in the cavity medium. Those losses together with the partial intensity transmission of the mirrors  $T_1, T_2$  are the overall losses  $\varrho$ , which degrade the quality of the cavity and therefore the finesse. In its most general form it is given by [107]

$$F = \frac{\pi}{2 \arcsin\left(\frac{1-\sqrt{\rho}}{2\sqrt[4]{\rho}}\right)}, \quad (4.7)$$

with  $\rho = R_1 + R_2 - \varrho - 1$ . For large finesse  $F \gg 1$  the width of the cavity resonance  $\kappa$  is given by

$$\frac{\kappa}{2\pi} = \frac{FSR}{2F} = \frac{c}{4LF}, \quad (4.8)$$

which makes it easy to determine the finesse of a cavity in practice, by simply measuring  $FSR$  and  $\kappa$  on an oscilloscope. Note that  $\kappa$  is the amplitude cavity decay rate and hence corresponds to the half width at half maximum (HWHM) of the resonance. Also, the finesse can be estimated to be  $F \approx 2\pi/\varrho$  for large finesse. The incident power  $I_0$  is enhanced inside the cavity and the circulating power (on resonance) is given by [108]

$$I_{circ} = I_0 \frac{\sqrt{T_1 T_2}}{(\sqrt{R_1 R_2} - \rho)^2}, \quad (4.9)$$

which for a high-finesse cavity can be many times the incident power.

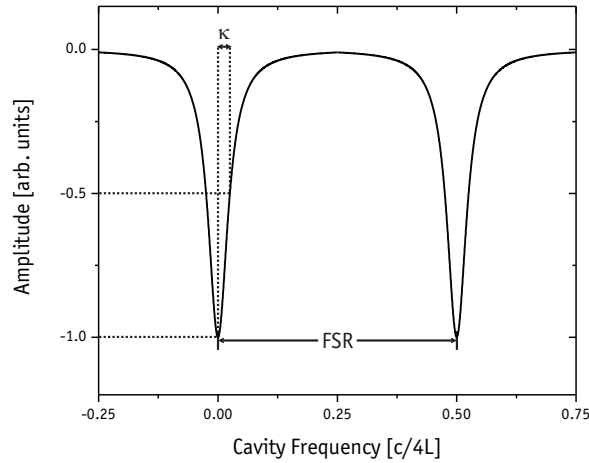


Figure 4.2: When scanning the length of a cavity its amplitude response shows resonances when the input laser field matches a resonator mode. For a single-mode field, adjacent resonances are spaced by the free spectral range (FSR) given by equation (4.3). The half width at half maximum of a resonance is the amplitude cavity decay rate  $\kappa$ .

It is typically unfavorable to make a high-performance cavity out of planar mirrors. Instead one uses spherical mirrors, as planar mirrors would have to be perfectly parallel, as well as the input field would have to be a perfectly aligned planar wave. Any deviation from this ideal case causes the light to escape the optical resonator. Therefore, it is common to build cavities from spherical mirrors, making the alignment less sensitive and making it possible to build a variety of different cavities. The condition for a cavity to be stable, i.e. to confine the light without the size of the beam continuously growing with every reflection, is [106]

$$0 \leq g_1 g_2 \leq 1. \quad (4.10)$$

Here  $g_{1,2}$  are defined as  $g_{1,2} = 1 + L/C_{1,2}$ , where  $C_{1,2}$  are the radii of curvature of the mirrors. Planar mirrors have a curvature  $C = \infty$ , concave mirrors  $C < 0$  and convex mirrors  $C > 0$ . The most common stable cavity designs are the confocal ( $C_1 = C_2 = L$ ), the concentric or spherical ( $C_1 = C_2 = L/2$ ), the hemispherical ( $C_1 = L, C_2 = \infty$ ) and the concave-convex ( $C_1 > L, C_2 = L - C_1$ ) cavity. Throughout this thesis the optomechanical Fabry-Pérot cavity is a hemispherical cavity, while other designs were tested, e.g.  $C_1 \gg L$  and  $C_2 = \infty$ , however never used in an actual experiment.

In most experiments the laser has a Gaussian profile and therefore Gaussian beam optics should be used to adequately describe the system. While most of the cavity description obtained so far remains valid, a few properties of a Gaussian beam in a



cavity will now be discussed. The electric field of a Gaussian beam is given by [106]

$$E(x, y, z) = E_0 \frac{W_0}{W(z)} \exp\left(-\frac{x^2 + y^2}{W^2(z)}\right) \exp\left(-ikz - ik\frac{x^2 + y^2}{2R(z)} + i\zeta(z)\right), \quad (4.11)$$

where  $W_0$  is the waist size (the waist radius at  $z = 0$ ),  $W(z) = W_0 \sqrt{1 + \left(\frac{z}{z_R}\right)^2}$  the waist as a function of  $z$ ,  $R(z) = z \left[1 + \left(\frac{z}{z_R}\right)^2\right]$  the radius of curvature of the wavefront,  $\zeta(z) = \tan^{-1} \frac{z}{z_R}$  the Gouy phase and  $z_R = \frac{\pi W_0^2}{\lambda}$  the Rayleigh range at which  $W_0$  increases by a factor of  $\sqrt{2}$ . In order for a Gaussian beam to be resonant with a cavity its wavefront radius of curvature must match the radius of curvature of the mirrors. This condition, together with the length of the cavity  $L = z_2 - z_1$  lets us define a unique Rayleigh range for the cavity:

$$z_R = \frac{\sqrt{g_1 g_2 (1 - g_1 g_2)}}{g_1 + g_2 - 2g_1 g_2} L. \quad (4.12)$$

The position of mirror 1 can also be calculated to be

$$z_1 = \frac{g_2(1 - g_1)}{g_1 + g_2 - 2g_1 g_2} L, \quad (4.13)$$

while  $z_2$  is identical, just with swapped indices. The optical resonator is stable if (4.10) is fulfilled. In addition, the waist radius of the beam on mirror 1 is given by

$$W_1^2 = \frac{L\lambda}{\pi} \sqrt{\frac{g_2}{g_1(1 - g_1 g_2)}} \quad (4.14)$$

and vice versa for mirror 2. The waist size is defined as

$$W_0^2 = \frac{L\lambda}{\pi} \frac{\sqrt{g_1 g_2 (1 - g_1 g_2)}}{|g_1 + g_2 - 2g_1 g_2|}. \quad (4.15)$$

The phase of a Gaussian beam is given by

$$\varphi(x, y, z) = kz - \zeta(z) + \frac{k(x^2 + y^2)}{2R(z)}. \quad (4.16)$$

The phase retardation on the optical axis with respect to a plane wave is therefore the Gouy phase  $\zeta(z)$  and the phase change per roundtrip is  $\Delta\varphi = 2kL - 2(\zeta(z_2) - \zeta(z_1))$ , which again must be a multiple of  $2\pi$ . Going from simple plane waves to Gaussian waves therefore does not change the free spectral range but only the absolute resonance frequency, which is shifted by  $\frac{\Delta\zeta}{\pi} FSR$ . This is also the reason why different modes have different resonance frequencies.

Several conditions have to be fulfilled for a real cavity with a Gaussian input beam to work properly. For example, the mode of the input field has to match the mode of the resonant field. In order to achieve the best possible mode matching the incoming beam is typically collimated, adjusted in size with a telescope and finally focused by a properly chosen mode-matching lens. If this is done carefully almost all of the incident laser power can go into the desired cavity mode.

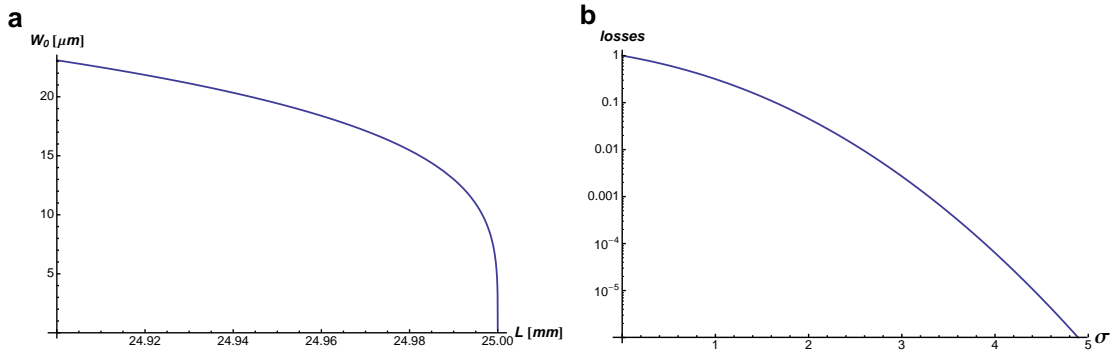


Figure 4.3: **a** Optical waist size  $W_0$  (in  $\mu\text{m}$ ) as a function of the cavity length  $L$  for a hemispherical cavity on the flat mirror. The more  $L$  approaches the radius of curvature of the input mirror (here chosen to be 25 mm), the steeper the change in  $W_0$ . **b** Diffraction losses as a function of mode size.  $\sigma$  is defined as the ratio of  $W_0$  to the mirror size. – For a  $50 \mu\text{m}$  mirror of reflectivity 99.99%  $\sigma$  needs to be greater than 3.9 for the diffraction losses to be smaller than the mirror losses, corresponding to  $W_0 \leq 6.4 \mu\text{m}$ . This requires alignment precision of the cavity length on the sub- $\mu\text{m}$  scale.

In our experiments it is crucial that the mode size on the second mirror is as small as possible, as the diffraction losses on the micromirror have to be minimized, while the mirror should be as small as possible to reduce the effective mass (see section 4.10) and hence maximize the optomechanical coupling strength  $g$  (3.67). The best way to achieve this is to use a hemispherical cavity design, where the micromirror has a radius of curvature of  $C_{MM} = \infty$ , while choosing the length of the cavity to be as close to the radius of curvature of the input mirror as possible (see figure 4.3). This is achieved by mounting the chip with the mechanical resonator on a xyz-piezo stage (see chapter 4.4 for details), with a typical step size of a few nanometers.

Another important requirement for our Fabry-Pérot cavity is that the amount of light transmitted through the cavity should be as small as possible. The reason for that is manifold - for one, if operated in a cryostat we do not want the power to be dissipated in the cryostat as this adds an additional heat load. The other main reason is that when eventually operating in the quantum regime, any quantum features, for example entanglement, created inside the cavity should leave the cavity through only one mirror. Any light exiting through the transmitted port is lost and the fidelity of the quantum state is reduced by the ratio of the losses to the detected light (see section 4.6). Therefore we try to make the micromirror as highly reflective as possible (currently limited to  $R_{MM} \approx 99.991\%$  by the coating design, however better reflectivities should be achievable if necessary) and choose the input coupler's reflectivity  $R_{IC}$  such that we obtain the finesse needed for the experiment, while still retaining a high ratio of  $R_{MM}/R_{IC}$ .

## 4.2.2 Ring cavity

The second cavity design that we use in our experiments is a ring resonator that is made of three instead of two mirrors. The input mode is incident onto the first,

flat mirror under an angle of slightly more than  $45^\circ$ . The optical mode entering the cavity now runs between a second flat mirror, the output mirror, tilted under the same angle as the input mirror and a curved mirror (2 m radius of curvature) that is mounted on a piezo-electric stack for stabilizing the cavity (see section 4.3.3 for details). The filter cavities were designed by Hannes Böhm and they are described in detail in his PhD thesis [105]. The physics of such a ring cavity is essentially the same as for a Fabry-Pérot cavity, with only a small difference, namely that the mode spacing is given by

$$FSR_o = \frac{c}{L}. \quad (4.17)$$

The reason for that is, that the cavity can be seen as half a FP cavity, only folded and the optical mode is not reflected onto itself but rather propagates around the cavity.

## 4.3 Locking techniques

Obtaining a fixed frequency relation between the pump laser and the cavity is a very crucial requirement for operating an optical resonator. The accuracy one has to achieve is determined by the length of the cavity and its finesse - it should not vary by more than a fraction of the cavity linewidth  $\kappa$ . This can be achieved by building a very rigid, stable cavity, which for high-finesse cavities is normally not sufficient, as the stability needs to be typically better than  $\Delta\lambda_q/F$  ( $\Delta\lambda_q$  is the difference in wavelength for two adjacent cavity modes), which is around a few femtometers for our parameter regime. Alternatively, the relative distance can be stabilized, i.e. locked, with an active feedback on, for example, a piezo (on which one of the mirrors is mounted) or by actively tuning the laser frequency - the laser can be kept resonant despite the actual distance between the mirrors being unstable. For any of the stabilization schemes typically used in optics experiments, an error-signal has to be generated, which contains information on the relative distance between the mirrors. The simplest example is to detect the transmission (or equivalently the reflection) curve of the laser through the cavity. This method is however only sensitive to whether the cavity is out of resonance but not if it is too long or too short. This is the reason why it is not possible to use this signal to stabilize the cavity on resonance but only off resonance - in general, locking requires an error-signal with a linear slope at the desired lock-point, i.e. the derivative of the signal should be large and not zero. Therefore, several methods exist which allow the generation of an error-signal for resonant locking of a cavity. The ones that were used in this thesis will be described in the following sections.

### 4.3.1 Pound-Drever-Hall

Originally devised in the early 1980s [109] based on work used in microwave applications in the 1940s [110], this technique relies on the interference of frequency sidebands with the main laser carrier to generate an error-signal for cavity stabilization. To generate the sidebands one typically uses an electro-optical modulator (EOM), which produces a phase modulation on an input laser beam. Given a laser

field  $E_{in}$  with an amplitude  $A$  and a frequency  $\omega$ , i.e.  $E_{in} = Ae^{i\omega t}$ , a phase modulator generates a field

$$E_{in,EOM} = Ae^{i\omega t + i\beta \sin \Omega t}, \quad (4.18)$$

where  $\beta$  is the modulation depth of the EOM and  $\Omega$  the modulation frequency. In the limit of small  $\beta$  we can do a Taylor expansion and by neglecting higher than first order terms we obtain

$$E_{in,EOM} = A \left( e^{i\omega t} + \frac{\beta}{2} e^{i(\omega+\Omega)t} - \frac{\beta}{2} e^{i(\omega-\Omega)t} \right). \quad (4.19)$$

It is easy to see that the generated field contains three different frequencies, where the amplitude of the sidebands is determined by  $\beta$ . The expansion can also be done using Bessel functions

$$\begin{aligned} E_{in,EOM} &= Ae^{i\omega t} \left( J_0(\beta) + \sum_{n=1}^{\infty} J_n(\beta) e^{in\Omega t} + \sum_{n=1}^{\infty} (-1)^n J_n(\beta) e^{-in\Omega t} \right) \\ &\approx Ae^{i\omega t} (J_0(\beta) + J_1(\beta) e^{i\Omega t} - J_1(\beta) e^{-i\Omega t}), \end{aligned} \quad (4.20)$$

where the Bessel functions are defined as

$$J_a(x) = \sum_{n=0}^{\infty} \frac{(-1)^n}{n!(n+a)!} \left(\frac{x}{2}\right)^{2n+a}. \quad (4.21)$$

The relative powers in the carrier and the upper and lower sidebands are  $P_c = J_0^2(\beta)P_0$ ,  $P_{\pm} = J_1^2(\beta)P_0$ , respectively. Here  $P_0 = |A|^2$  is the absolute power in the laser. The reflection coefficient  $R(\omega)$  for a Fabry-Pérot cavity is simply the ratio of the incident laser to the reflected field and in general given by [111]

$$R(\omega) = \frac{-r_1 + r_2(r_1^2 + t_1^2) \exp\{i\omega/FSR\}}{1 - r_1 r_2 \exp\{i\omega/FSR\}}. \quad (4.22)$$

Here  $r_1 = \sqrt{R_1}$  ( $t_1 = \sqrt{T_1}$ ) is the amplitude reflection (transmission) coefficient of the input mirror and  $r_2 = \sqrt{R_2}$  of the end mirror of the cavity. The field reflected off the cavity then reads

$$E_{ref} = Ae^{i\omega t} (R(\omega)J_0(\beta) + R(\omega + \Omega)J_1(\beta)e^{i\Omega t} - R(\omega - \Omega)J_1(\beta)e^{-i\Omega t}). \quad (4.23)$$

In an experiment what is actually measured is the power on the photodetector, which is given by

$$\begin{aligned} P_{det} &= |E_{ref}|^2 = P_c |R(\omega)|^2 + P_{\pm} [|R(\omega + \Omega)|^2 + |R(\omega - \Omega)|^2] + \\ &\quad + \sqrt{P_c P_{\pm}} [R(\omega)R^*(\omega + \Omega)e^{-i\Omega t} - R(\omega)R^*(\omega - \Omega)e^{i\Omega t} + \\ &\quad + R^*(\omega)R(\omega + \Omega)e^{i\Omega t} - R^*(\omega)R(\omega - \Omega)e^{-i\Omega t}] + \mathcal{O}(2\Omega). \end{aligned} \quad (4.24)$$

The first three terms give rise to a DC signal on the photodiode, while the next order terms oscillate at  $\Omega$ . Those are the parts of the signal we are actually interested in, as they come from the interference of the carrier with the sidebands, which gives direct

access to the phase response of the cavity. For  $\kappa \ll \Omega$  and  $\omega$  being sufficiently close to the cavity resonance, the sidebands created in the EOM are directly reflected off the cavity, i.e.  $R(\omega \pm \Omega) \approx -1$ , and the carrier acquires a phase inside the cavity. This is the regime we work in in all our experiments. In our setup the terms oscillating at  $\Omega$  can be isolated by mixing the photodetector output signal with the same frequency the EOM is modulated with and low-pass filtering that signal. More quantitatively, the mixing of two sinusoidal signals with frequencies  $\Omega$  and  $\Omega'$  results in

$$\sin(\Omega t) \sin(\Omega' t) = \frac{1}{2} \{ \cos [(\Omega - \Omega')t] - \cos [(\Omega + \Omega')t] \}, \quad (4.25)$$

and hence the first term is 1/2 for  $\Omega = \Omega'$ , while the second term can be neglected if a low-pass filter with a cut-off frequency that is smaller than  $\Omega$  is used. It is important to note that

$$\sin(\Omega t) \cos(\Omega' t) = \frac{1}{2} \{ \sin [(\Omega - \Omega')t] - \sin [(\Omega + \Omega')t] \}, \quad (4.26)$$

and hence the signal for  $\Omega = \Omega'$  would vanish at DC. Therefore, the phase between the signal from the photodetector and the function generator always has to be properly chosen. As we are working in the regime where the sidebands are completely reflected off the cavity we can simplify

$$R(\omega)R^*(\omega + \Omega) - R^*(\omega)R(\omega - \Omega) \approx -i 2 \cdot \text{Im} \{ R(\omega) \}. \quad (4.27)$$

In this limit, we can neglect the real part of (4.24) and we finally arrive at an expression for the error-signal

$$\epsilon_{PDH} = -2\sqrt{P_c P_{\pm}} \cdot \text{Im} \{ R(\omega)R^*(\omega + \Omega) - R^*(\omega)R(\omega - \Omega) \}. \quad (4.28)$$

As can be seen from figure 4.4, the error-signal has a maximal slope and also crosses zero when the laser is on resonance. For a rigorous derivation of the Pound-Drever-Hall error-signal, including the case  $\kappa > \Omega$ , see [111].

For most of our experiments we have used a broadband EOM (New Focus 4004), driven by a function generator (Agilent 33220A). The function generator (FG) has a maximum output voltage of 10 V<sub>pp</sub>, which only corresponds to a very small  $\beta$ . We therefore built a RLC circuit, where the output of the function generator is the resistance (50  $\Omega$ ), the EOM itself is the capacitor (18 nF) and a self wound coil the inductance of 4.3  $\mu\text{H}$ . This circuit had a resonance frequency of approximately 18 MHz (which easily fulfills  $\kappa \ll \Omega$ , as  $\kappa$  typically is  $\lesssim 2\pi \times 1$  MHz), and a  $Q$ -factor of almost 10. By splitting off a small fraction of the function generators' output (Minicircuits ZDC-10-1) we ensured  $\Omega = \Omega'$ . The mixing of the output signal from the photodetector and the coupled output of the function generator was performed on a Minicircuits ZAD-1-1. The signal was subsequently low-pass filtered (Minicircuits BLP-10.7) to remove higher-order terms from the signal. For locking, this error-signal was amplified with a home-built amplifier and a variable  $\pm 100$  mV signal was added for fine tuning of the setpoint of the lock. In order to decrease the optical power needed to generate the error-signal we replaced the original EOM with a resonant New Focus 4003 (resonance frequency 20 MHz), for which the half-wave voltage (the voltage needed to make a  $\pi$  phase-shift) is approx. 16 V<sub>pp</sub>. Instead of using one FG, we now use two that are frequency locked, which allows us to adjust the phase between the EOM driving and the demodulation signal arbitrarily.

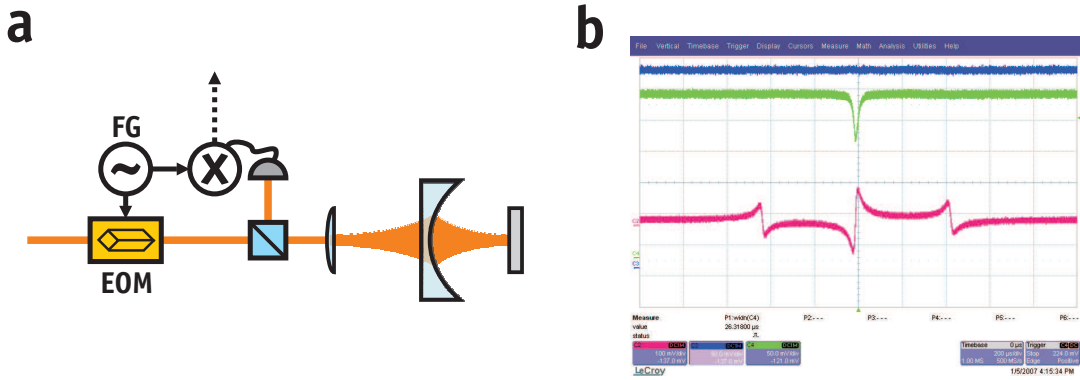


Figure 4.4: A schematic drawing for the Pound-Drever-Hall (PDH) locking technique is shown in **a**. A laser is phase-modulated using an electro-optical modulator (EOM), which is driven by a function generator (FG) at a frequency  $\Omega$ . After being reflected off a cavity, the laser with its modulated frequency sidebands is detected on a photodiode. The interference signal of the sidebands with the carrier contains information on the length of the cavity, which is accessible after being mixed with the FG signal. For details see the text. The magenta trace in **b** shows a typical experimental PDH error-signal, while the green signal is the cavity resonance obtained from scanning the cavity length. The cavity finesse for this particular case was approx. 7,000, with a length of 25 mm. The cavity amplitude decay rate was hence  $\kappa = 2\pi \times 430$  kHz, while  $\Omega \approx 18$  MHz.

### 4.3.2 Tilt Locking

A technique for generating a modulation-free error-signal is the so called tilt lock. It purely relies on the interference of different spatial modes. Any optical field can be decomposed in an orthonormal basis, such as the Hermite-Gauss modes, which are also a solution of the paraxial Helmholtz equation. They are of particular importance, as they have paraboloidal wavefronts and hence match the curvature of spherical mirrors. Hermite-Gauss modes are a natural choice for decomposing the field of an optical cavity. Their amplitude is given by [106]

$$U_{l,m}(x, y, z) = A_{l,m} \left[ \frac{W_0}{W(z)} \right] G_l \left[ \frac{\sqrt{2}x}{W(z)} \right] G_m \left[ \frac{\sqrt{2}y}{W(z)} \right] \times \exp \left[ -ikz - ik \frac{x^2 + y^2}{2R(z)} + i(l + m + 1)\zeta(z) \right], \quad (4.29)$$

where  $W(z)$  is the beam width,  $W_0$  the waist radius,  $k$  the wavenumber,  $R(z)$  the wavefront curvature and  $\zeta(z)$  the Gouy phase.  $G_l(u) = H_l(u) \exp\left(\frac{-u^2}{2}\right)$  is the so-called Hermite-Gaussian function,  $H_l(u)$  are the Hermite polynomials and  $A_{l,m}$  is a constant (for more details see [106]). The Hermite-Gauss mode with  $l = m = 0$  is simply the Gaussian mode (c.f. figure 4.5). In the reflected signal of a cavity which length is scanned over a full free spectral range, one can see a number of higher order modes, with different amplitude. If the laser output would be perfectly Gaussian and

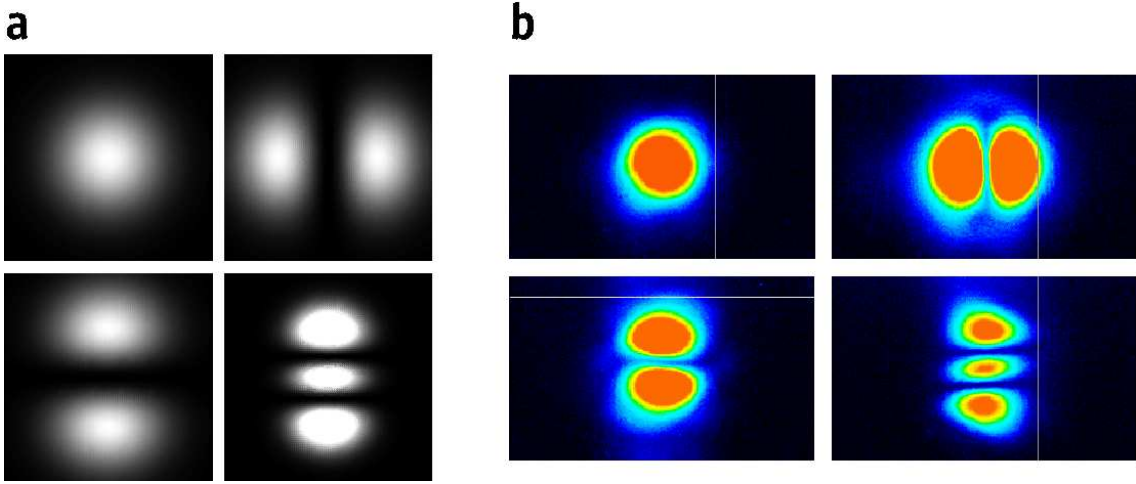


Figure 4.5: **a** shows the theoretical intensity profiles  $|U_{l,m}|^2$  for several Hermite-Gaussian (HG) modes defined by (4.29), that are supported by an optical cavity. From top-left to lower-left (in clockwise direction) the modes are  $(l = m = 0)$ ,  $(l = 1, m = 0)$ ,  $(l = 0, m = 1)$ , and  $(l = 0, m = 2)$ , respectively. In **b** the same modes are recorded experimentally using a CCD camera placed at the output port of a ring-cavity. In order to obtain the images, the cavity length was scanned and the cavity itself was slightly misaligned. Higher order HG modes were also observed, as well as Laguerre-Gaussian and more exotic modes, which are however not shown here.

the cavity perfectly aligned all modes but the  $U_{0,0}$  would vanish. As this is never the case in a real cavity, it is possible to use the different spatial properties of the modes to generate an error-signal. More precisely, distinct modes have different Guoy phase shifts and therefore have different resonance frequencies in the cavity. The phase of a mode with indices  $l, m$  on the beam axis is given by  $\varphi = kz - (l + m + 1)\zeta(z)$  and for a beam to be resonant to a cavity its phase has to change by multiples of  $2\pi$  over a full roundtrip (cf. section 4.2.1). Therefore, modes where  $l + m$  differs, have different resonant frequencies. It is hence possible to use a higher order Hermite-Gauss mode as a phase reference for the fundamental Gaussian mode, e.g. the  $U_{1,0}$  mode. The signal on a photodetector of the two reflected modes is

$$S_{0,0+1,0} = \int_{-\infty}^{+\infty} \int_{-\infty}^{+\infty} |U_{0,0}(x, y) + U_{1,0}(x, y)|^2 dx dy = \text{const.}, \quad (4.30)$$

for constant signal amplitudes. This is intuitively clear, as the interference term of the two fields is proportional to

$$I_{0,0+1,0} = \left| \int_{-\infty}^{+\infty} \int_{-\infty}^{+\infty} U_{0,0}^*(x, y) U_{1,0}(x, y) dx dy \right|, \quad (4.31)$$

which is always equal to zero as the Hermite-Gaussian modes form an orthonormal basis and hence their overlap integral per definition is zero. In order to obtain a

usable error-signal, one cannot detect the whole signal on a photodetector but rather has to use the unique spatial properties of the  $U_{1,0}$  mode: by using a photodiode that is split into two halves and subtracting their photocurrents, it is possible to obtain the constructively and destructively interfering parts of the fields separately [112]:

$$\epsilon_{Tilt} = \int_{-\infty}^{+\infty} \int_{-\infty}^0 |U_{0,0}(x, y) + U_{1,0}(x, y)|^2 dx dy - \int_{-\infty}^{+\infty} \int_0^{+\infty} |U_{0,0}(x, y) + U_{1,0}(x, y)|^2 dx dy. \quad (4.32)$$

For the case where  $U_{0,0}$  is on resonance with the cavity, the two terms cancel each other out. However, when the fundamental mode slightly shifts out of resonance it acquires a phase shift (the phase change for an on-resonance mode is very steep, while the phase acquired by an off-resonant mode is almost zero), which leads to different signals on the two photodiode halves and produces a non-zero error-signal (c.f. figure 4.6). The 1, 0 mode acts as a stable phase-reference for the fundamental mode. In our experiments this locking technique is used for the stabilization of the ring filter cavities, as well as for one Fabry-Pérot filter cavity. For more details on the cavities and the split photodiode detectors see [105]. Note, that the original design of the detectors included a small error, which is however easy to fix: the numbering of the pins was clockwise but in fact should be counterclockwise. This can be corrected by short-circuiting pins 2 and 8.

### 4.3.3 Experimental Locking

Once an error-signal is generated it is electronically processed and an appropriate signal is fed back either to the laser or to a piezo actuator in order to stabilize the cavity. Our error-signals are typically amplified with home-built wide-band amplifiers and then fed into a proportional-integral-derivative controller (PID controller). The PID controller we use for almost all lock-loops is the Toptica PID 110. It has a low-voltage bandwidth of up to 1.5 MHz (a jumper can be set to operate it in a low-voltage mode of  $\pm 10$  V output), although we mostly operate it in the high-voltage mode ( $-30$  to  $+150$  V, bandwidth  $> 10$  kHz), which gives us a larger dynamic range, while sacrificing some of the bandwidth.

- In our early experiments (see section 6.1) we actively stabilized the length of the optomechanical Fabry-Pérot cavity. The input coupler was mounted on a ring piezo (Piezomechanik HPSt 150/14-10/12), which was part of the cavity. Besides the glue (Master Bond EP21TDC-2), which attached the holder for the input mirror to the piezo stack, slowly decomposing the piezo (figure 4.7a), there was an additional major drawback to the design: while working well at room temperature, the design did not allow any stable lock of a cryogenic cavity. Below 100 K it was only possible to find a stable lock during the first few minutes, until the piezo thermalized. We measured the piezo capacitance to quantify the amount of extra driving that would be necessary for stabilizing the cavity, and saw that it decreased from an initial  $2.8 \mu\text{F}$  at room temperature to  $800 \text{ nF}$  at 17 K (cf. figure 4.7b). Driving the piezo at even higher voltages (an increase of a factor of approximately 4 would have been necessary) was not possible as the output of the PID controller was limited to



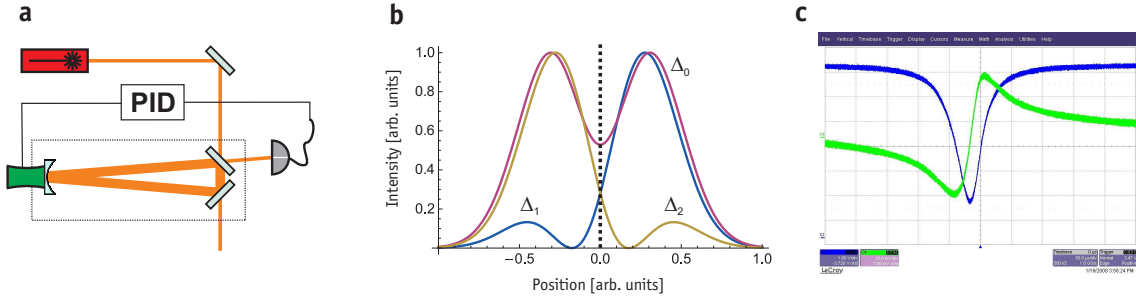


Figure 4.6: **a** shows a simplified sketch of a cavity which is stabilized with the tilt locking scheme. The reflected port of the resonator is detected on a split-photodiode, and the difference signal of the two halves of the diode is used as an error-signal for the stabilization. **b** The intensity of the photo-current on the split-diode is shown as a function of the position on the detector. The purple curve is the signal when the fundamental cavity mode is on resonance, i.e. has a detuning  $\Delta_0$  – as the two halves have equal signals their difference is zero. When the fundamental mode is off-resonance it acquires a phase shift with respect to the  $U_{1,0}$  mode and their interference results in an unbalanced signal on the diode which can be used as an error-signal. The blue curve, detuning  $\Delta_1$ , comes from a negative phase shift, while the dark yellow curve ( $\Delta_2$ ) corresponds to a positive phase shift. The dotted line indicates the two halves of the photodetector which are subtracted. **c** The difference signal of the detector halves (green trace) exhibits the characteristic tilt lock error-signal when the cavity length is scanned. The blue trace is the cavity response obtained from adding the signal of the detector halves.

150 V and with an additional amplifier we would have not only reduced our locking bandwidth (due to the finite output current of the amplifier) but we would have also created an even higher heat load on the cryostat, which would have increased the minimum bath temperature. The solution we devised was to mount the piezo stack with the input coupler on the outer shield of the cryostat (however still in vacuum), effectively keeping it at room temperature throughout the experiments (see section 6.1 for a detailed sketch of the mounting). This approach had two main limitations: first, the cavity was split into two halves, making it more unstable and second, the heat load created from blackbody radiation of a 300 K object in close proximity (a few millimeters) to the sample, increased the mechanical mode temperature by almost a factor of 2. The optical resonator finesse used in the locking tests was between 5,000 and 8,000.

- Our lasers, see section 4.4, have a fast piezo input for tuning the laser frequency, which can take an input voltage of up to  $\pm 100$  V, while the corresponding range is approximately 1 MHz/V at a bandwidth of 100 kHz. We use a voltage divider (a simple high-voltage potentiometer) to reduce the maximum output voltage of the PID box to the appropriate input voltage of the laser and in most experiments used a BNC T-adaptor to combine the PID signal with

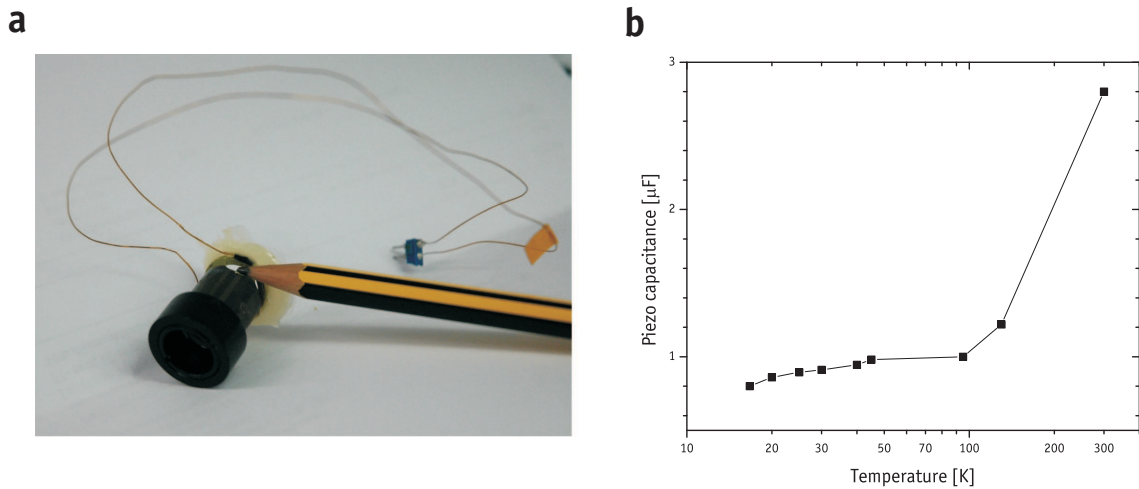


Figure 4.7: **a** Shown is the ring-piezo used for locking the Fabry-Pérot cavity in section 6.1 after approximately half a year being glued to a Teflon stage. The part that is covered in glue peeled off the remaining piezo ceramics over time. **b** The capacitance of the piezo stack as a function of temperature. The capacitance clearly decreases and makes it impossible to lock the cavity at low temperature.

the calibration signal from the function generator (see 4.9 for details). The combined signal then feeds back to the laser frequency, such that it always stays resonant with the cavity. The laser frequency lock is exclusively used for locking the Fabry-Pérot cavity using a PDH error-signal in section 6.2 and chapters 7 & 8.

- The filtering cavities are locked using the tilt locking technique. The output of the PID controller is directly applied to a piezo holding the back mirror of the cavity. In the early designs these mirrors (1" diameter, 2 m radius of curvature, see [105] for details) were mounted on Piezomechanik PSt 150/7/20 VS 12 piezo actuators, that had an unloaded resonance frequency of 30 kHz. The mirror, with a mass of 6.9 g reduced the resonance frequency of the piezo according to  $f'_0 = f_0 \sqrt{\frac{m_{\text{piezo}}}{m_{\text{piezo}} + m_{\text{mirror}}}} \approx 20$  kHz. Given that one can typically only use the bandwidth of up to a third or one half of the piezo's resonance frequency without starting to excite it (as they normally have small  $Q$  factors), this is rather low. A stable lock of the filtering cavities with an input beam of the high-finesse (which is typically around 4,000) polarization therefore proved to be rather difficult. In order to improve the lock we tried to reduce the mass of the mirror and increase the resonance frequency of the piezo itself. The latter one was easily achieved by replacing the piezo elements with Piezomechanik PSt 150/7x7/2, that have an intrinsic resonance frequency of  $>500$  kHz. The reduction of the mass of the mirrors was somewhat more difficult as no ultra-thin mirrors with a proper radius of curvature were readily available. We therefore decided to cut out a small piece of the mirrors by using a diamond mill. The diameter was reduced from 1" to approximately 1/4",

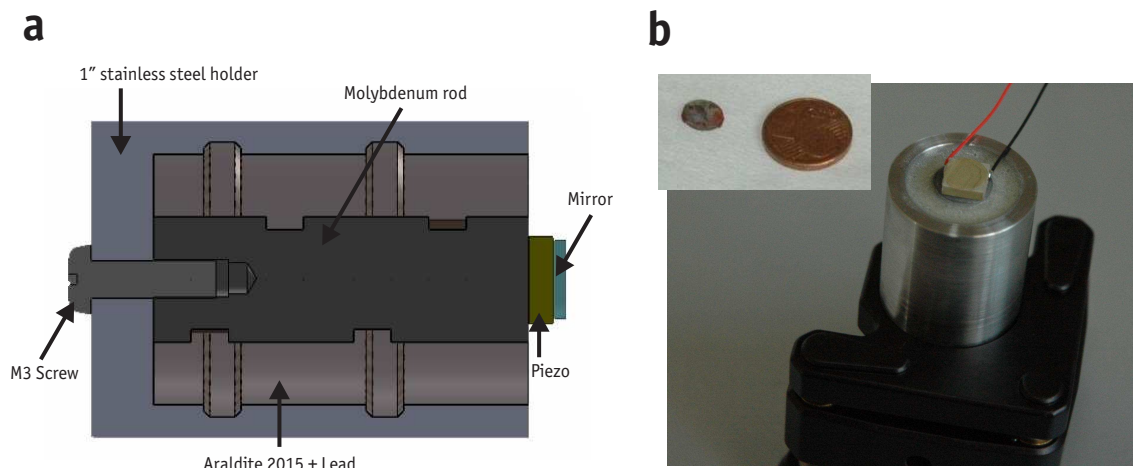


Figure 4.8: **a** Model for a high-bandwidth mirror mount. The holder is made of stainless steel, with a rod of molybdenum mounted inside. On top of the rod is a high-frequency piezo (we typically use a Piezomechanik PSt 150/7x7/2), which holds a small mirror. The gap between the holder is filled with glue (Araldite 2015) and lead-cuttings in order to damp vibrational modes from the steel holder. The gaps in both the holder and the rod are for increasing the surface for better damping. The holder is used for the filtering cavities, as well as for locking the phase of the homodyne detectors. The mount was designed by Stefan Gößler. **b** Picture of an actual mirror-mount. The piezo and the mirror are clearly visible. The inset shows an image of a filter cavity mirror with 2 m radius of curvature, that was cut out of the original 1" mirror to significantly reduce the mass and hence increase the lock bandwidth. The diameter of the mirror is approx. 6.5 mm, while it is less than 1 mm thick. A 1 Cent coin is shown for comparison. The mirror in the picture is still covered with a protective layer of photoresist.

while the thickness was cut down to less than 1 mm, greatly reducing the mass to approximately 0.35 g. In order to protect the high-reflectivity coating of the mirror, we coated it with a thick layer of photoresist, which we removed after the process with acetone (see figure 4.8b). The resonance frequency with the attached mirror was estimated to be  $f'_0 \approx 450$  kHz. In addition to maximizing the resonance frequency it is also vital to reduce all other mechanical resonances in the system, i.e. damp out any mechanical modes of the mirror and piezo holder. To achieve this, we built a special mount that was designed by Stefan Gößler [113]. The idea is to use a molybdenum rod and embed it in a holder filled with glue and lead-cuttings. Figure 4.8a shows a sketch of the holder design. This design was finally used in both filtering cavities, allowing us to stably lock the cavities either at high finesse or lock all 3 (2 filter + FP cavity) at once, which is a major challenge but necessary for shot-noise limited operation of the setup (see section 4.4 for details).

- Recently, we have also started to use a modified tilt locking technique for

Fabry-Pérot cavities. In order to have access to the spatial properties of the light field we introduce a polarizing beamsplitter and a quarter-wave plate in front of the cavity and look at the interference of the Gaussian mode with higher order modes in the reflected signal on a split photodiode, just as in the conventional tilt locking scheme.

- Several different PID controllers were tested throughout this thesis. An idea was to incorporate the locking into a computer based program and automatize (re-) locking of the cavities, which is a very useful feature for a cascaded lock (see section 4.4). Initial tests were done with a field-programmable gate array (FPGA) based input-output card (National Instruments PCI-7833R), which is programmable in LabView. The main problem with this approach was the limited analog-to-digital conversion (ADC) rate of the card (200 kS/s), which was too slow for the digitization of even a medium-finesse error-signal. We therefore tested a commercial product, namely the Toptica DigiLock 110, which seemed to work sufficiently well, even came with an auto-lock feature but had no interfaces with LabView or any other lab software. It was essentially a digital standalone version of the PID 110. We therefore decided to build a proper FPGA based PID controller that featured all our requirements. We worked with Thomas Lehner from [dotfast-consulting](#) to develop a system that incorporated the following envisioned features: input voltage range  $\pm 1$  V, 12 bit ADC, variable output range with a variable offset point – maximum of  $\pm 5$  V, bandwidth for input and output 10 MHz, triangular output for scanning and finding the resonance, interface for computer control and LabView integration. The PID boxes were built by Thomas Lehner and first tests show promising results, meeting the specifications. Further tests are currently underway and if successful the controllers should replace the Toptica PID 110, allowing us to use new features such as auto-lock or re-locking a cascaded cavity system.

## 4.4 Experimental setup

The experimental setup has evolved significantly over the course of this thesis and was also adapted to meet the different requirements for the measurements presented in chapters 6 - 8. While it is beyond the scope of this work to discuss the “historical” development of the setup, we would like to discuss the most important features and present the latest setup. Most of the more relevant parts are discussed in great detail throughout this chapter.

### 4.4.1 Two-color setup

The original setup used in [38], as well as in the experiment described in section 6.1, comprised a single laser beam for read-out and radiation-pressure cooling of the mechanical oscillator. This had the consequence that the read-out sensitivity was a function of detuning and laser power. In addition, the locking of the Fabry-Pérot cavity became rather complicated – for close to resonance operation the Pound-Drever-Hall error-signal was used, while locking at or beyond the detuning by the mechanical frequency required to use the cavity reflection signal as an error-signal.

This resulted in more unstable locks, as the error-signal did not have a perfectly linear dependence for all setpoints. We therefore decided to replace the single-laser with a two-color scheme. The idea was to have a faint read-out beam that was always kept on resonance with the FP cavity and a detuned cooling beam that was variable in power. The two beams were to have similar frequency, however with a variable detuning of the cooling beam with respect to the cavity resonance. Therefore, the laser was simply split on a polarizing beam splitter (PBS) and both beams sent through a double-pass acousto-optic modulator (AOM) beam line (see section 4.5 for details). The reason why we had to use an AOM for each beam, was that AOMs always have a fixed offset frequency of 80 MHz or more, around which the frequency can be detuned. In this scheme, the beams are recombined just before entering the FP cavity on a PBS. This allows us to use the beams in the same spatial mode, making sure that they couple to the same cavity mode, but always keep them separate as they have orthogonal polarizations. For separating the beams reflected off the cavity from the input beams we had to introduce a non-reciprocal polarizing element – a Faraday rotator. In combination with a half-wave plate and a PBS it allows to distinguish two counter-propagating beams with equal polarizations. The Faraday rotators we use (Leysop FOI-1064) have an aperture of 5 mm, a transmission of  $\sim 99\%$ , a polarization rotation of  $45 \pm 0.5^\circ$  and a temperature stability of  $0.1^\circ \text{ K}^{-1}$ . The cooling beam also has two steering mirrors, with which the spatial overlap with the locking beam can be adjusted. The main challenge in this scheme is the polarization separation – the cooling beam is typically more than 3 orders of magnitude stronger than the locking beam and a beat signal between the two will appear in the locking beam spectrum, which is close to the mechanical peak and will add significant noise to the spectrum. The situation is not as dramatic as it would be if the FP cavity were polarization independent, however due to a small birefringence the cavity resonances for the two beams are approximately 800 kHz apart (the birefringence of the AlGaAs samples can be much higher, resulting in two distinct resonance peaks when scanning the cavity length). Nonetheless, the polarization separation is crucial, as any extra noise from the beating signal or other noise from the cooling beam will make it extremely hard to perform a shot-noise limited read-out. While a PBS typically has an extinction ratio of  $10^{-3}$  for the reflected port, the transmission port has only  $\sim 10^{-2}$ . We therefore chose the cooling beam to be vertically polarized when impinging on the combining PBS. The polarization of the two beams before entering the FP cavity is matched to the cavity polarization axis by a half- and a quarter-wave plate. This is crucial, as this also sets the polarization incident on the PBS upon reflection from the cavity. In addition, the cooling beam is adjusted with a half-wave plate just in front of the PBS. This scheme worked satisfactory for most experiments, however when using large cooling powers, the leakage of the cooling beam into the locking beam became significant, raising the noise-floor and making the temperature calibration less accurate. We therefore replaced the PBS with a Wollaston polarizer (FOCtek WSP7010) that has an extinction ratio of  $< 5 \times 10^{-6}$ . The improvement was not as good as expected and the high transmission loss ( $> 10\%$ ) precluded the use of the Wollaston polarizer in any experiment. However, replacing the wave plates with yttrium vanadate ( $\text{YVO}_4$ , 0.3 mm thick) crystals (one before the PBS in the cooling beam and one behind the PBS) improved the separation significantly. The crystals are birefringent and one

can rotate the polarization by tilting and rotating the crystal with respect to the laser beam.

Only recently however, we have completely eliminated the problem of beating between the locking and the cooling beam – we replaced the AOM in the locking arm with a fiber based high-bandwidth electro-optic modulator (EOM) (EOSpace PM-5K5-20-PFA-PFA-106-LV-UL). Using a high-frequency signal generator (Rohde & Schwarz SMF100A) we generate frequency sidebands (as explained in section 4.3.1) that are 3 times the free spectral range of the cavity away from the cooling beam. In order to obtain a laser field solely oscillating at this sideband frequency we pass the laser through a volume holographic filter (Ondax, 90 pm or 24 GHz bandwidth) and are left with the sideband plus a few percent of residual higher order sidebands. We perform additional filtering with a very short ( $L = 2$  mm) low-finesse ( $F = 350$ ) FP cavity, which suppresses any higher order sidebands and hence leaves us with a clean single-mode laser beam at the modulated sideband frequency. This signal is used to lock the cavity and the beating of the cooling and the locking beam is now completely negligible as it occurs at approximately 18 GHz for our standard FP cavity of 25 mm length.

#### 4.4.2 Laser systems

For most experiments we used a Nd:YAG laser (Innolight Mephisto) with a nominal output power of approximately 1.1 W at 1064 nm wavelength. The natural linewidth of the laser is specified to be  $<1$  kHz. The laser has a fast frequency tuning port (100 kHz bandwidth,  $\pm 100$  V maximum input voltage,  $>1$  MHz/V tuning, 2 M $\Omega$  input impedance, and 2 nF capacitance), with which a piezo acting on the laser cavity is tuned and which we use for locking the laser frequency to the Fabry-Pérot cavity resonance. It also has a slow frequency tuning port (1 Hz bandwidth,  $\pm 10$  V input voltage, -3 GHz/K tuning, and a tuning range of 30 GHz), with which the temperature of the laser crystal is controlled – we use this port to find the cavity resonance and for compensating for long-term cavity drifts. The laser has an intensity noise peak at around 700 kHz that is due to relaxation oscillations from changes of the pump power in the gain medium. Most of this noise peak is suppressed by a noise-eater (suppression of around 40 dB), however it adds to the overall intensity noise of the laser – if the laser is not additionally filtered it exhibits noise that is above its shot-noise up to 5 MHz. Due to the need for slightly more laser power we recently replaced the Mephisto laser with a Prometheus (also Innolight) laser, that has an output power of 1.32 W, while almost all the other specifications remain the same. Only the relaxation peak is now centered around 1 MHz and the laser only starts to be shot-noise limited at frequencies higher than 12 MHz. An additional feature of the Prometheus is that it also has a 70 mW output at the frequency doubled wavelength (532 nm). This second laser is completely coherent with the 1064 nm output and we envision to potentially use it as a read-out beam for the mechanical motion. The advantages would be that we could have two cavities with different finesse that are truly distinct in frequency. One possible application would be to build a high-finesse cavity for 1064 nm for the cooling beam, while the cavity mirrors only have low reflectivity for 532 nm, which would allow the read-out field to follow the mechanical oscillations adiabatically (i.e. with no time delay due to

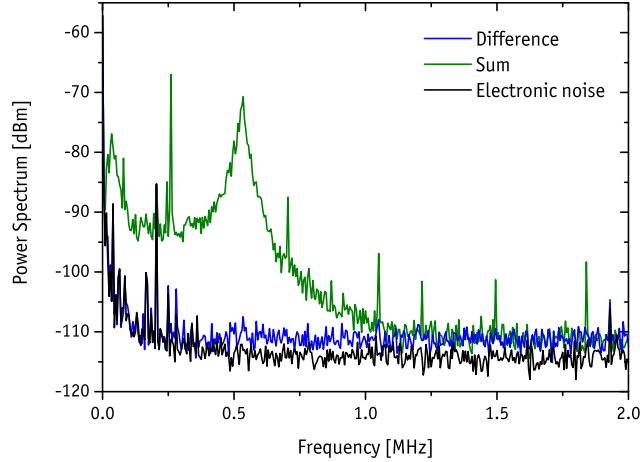


Figure 4.9: Shot-noise measurement of the laser. The difference- (blue curve) and sum-signal (green) of two photodetectors are measured and their power spectra plotted. Just around 1.1 MHz the two curves start to coincide, which is the frequency above which the laser is shot-noise limited, i.e. free of classical noise. The traces were taken after filtering the laser with a ring cavity (finesse 4,000 and  $L \approx 0.7$  m). The detector noise is shown for comparison (black).

the cavity linewidth  $\kappa$ ). We did initial tests for such a scheme, however with non-optimized mirrors, which made it very hard to see any mechanical displacement in the power spectrum of the 532 nm beam.

### 4.4.3 Cavities

Immediately after the laser there is a Faraday isolator (Linos FI-1060-5SI) preventing any reflected light from entering and possibly destabilizing the laser. Before the beam is split into the locking and the cooling fields we have an optional filter cavity – it can either serve as a spatial filter (with a finesse of 400) or additionally as an intensity noise filter. For the latter implementation, the input polarization is chosen such that the mirrors are highly reflective (dielectric  $45^\circ$  mirrors always show some dependence of their reflectivity on polarization), which gives us a finesse of 4,000 - 7,000, depending on the cleanliness of the mirrors. This, with a length of  $L \approx 0.7$  m gives a cavity linewidth of  $\kappa = 270$  kHz for the low- and of  $\kappa = 27 - 15$  kHz for the high-finesse cavity. This allows us to obtain a shot-noise limited pump beam for frequencies greater than 1 MHz (see figure 4.9). The cavity itself is made of a solid Invar body in order to reduce thermal variations from affecting the cavity stability (see Hannes Böhm’s thesis for details [105]). The error-signal for the cavity is generated using the tilt lock technique. The curved back mirror was substantially reduced in mass and the piezo bandwidth increased in order to be able to lock the cavity simultaneously with the Fabry-Pérot cavity (see section 4.3). The difficulty

here is that if the frequency change required for locking the FP cavity is large and fast, the bandwidth of the filter cavity lock must be even larger as it always has to follow the laser in addition to its own lock. Also, if the filter cavity loses lock, the FP cavity loses lock too and starts to oscillate as it looks for a lock point but no laser light is hitting the detector, making it impossible for the filter cavity to re-lock. The purpose of a cascaded lock with digital lock boxes would be to “know” when the filtering cavity loses the lock and therefore automatically stop the lock of the FP cavity and restart one lock after the other.

We use a second filter cavity in the arm of the cooling beam for a reduction of the laser power on the photo detectors. The idea is to lock the cavity on its low-finesse polarization and while the laser in the first pass goes through the cavity unhindered, on the way back from the Fabry-Pérot cavity only the original pump frequency gets transmitted. The mechanical sidebands created inside the FP-cavity are not resonant with the filter cavity and are therefore reflected (the effective reflectivity for the sidebands with frequency  $\omega_{sb}$  is given by  $R_{eff} = 1 - \frac{\kappa^2}{\kappa^2 + \omega_{sb}^2}$ ). Due to the cavity’s ring-design, the non-resonant part of the laser is reflected under an angle of approximately  $45^\circ$ . This makes it easy to pick it off and it is the actual information we would like to detect. Even if the cooling beam is very strong, the sidebands that are detected are very weak (they are only created with a rate given by equation (3.72)) and therefore we do not run into the problem that the detectors saturate, even though we have to use a local oscillator that is up to 50 times stronger than the signal.

As already mentioned in section 4.2.1, the finesse of a cavity is easily determined by scanning its length and measure the free spectral range and the width of the cavity resonance, with the ratio of the two being the finesse. This method is quick and simple and gives a good estimate, however it is limited by the linearity of the piezo used for scanning and by the speed of the photodetector. For high finesse cavities (>a few thousand) the detector has to have a bandwidth of around  $10^6$  Hz, which is in principle easily possible with the diodes we use (rise times <10 ns) but requires small modifications of the circuits we use. The reason is that the photodetectors are built such that they have a DC and an AC output with a cut-off frequency at around 30 kHz. By removing the capacitance providing the high-pass for the AC part (C7) and shorting another capacitance (C9) all the signal is DC coupled (see [114] for details) and the full bandwidth of the circuit ( $\sim 10$  MHz) can be used in one port to reliably measure the finesse. Such a modified detector is placed in the second output port of the PBS that combines the local oscillator and the signal in the locking beam and is used for finesse measurements, as well as initial alignment of the cavity. A more precise method of measuring the finesse is to lock the cavity on resonance and scan the cooling beam in frequency with very little power and in small steps over the resonance – fitting this peak gives direct access to the cavity decay rate  $\kappa$  and hence its optical quality. This scheme is normally used once the cavity is properly aligned as it is much more involved than the scanning measurement. We have also tested a third method, that is useful for very high-finesse cavities but also requires fast detectors. It is described in detail in [115].



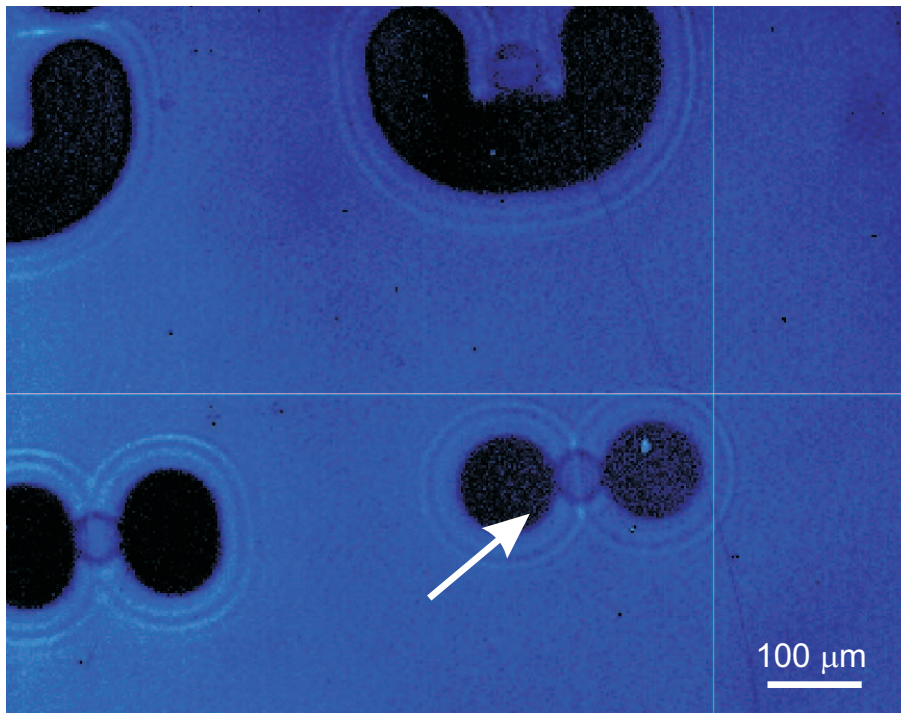


Figure 4.10: An image of a group of mechanical resonators inside the  $^4\text{He}$  cryostat taken with a CCD camera, which is used for alignment of the mechanical system to the cavity mode. The arrow indicates the oscillator used in experiments 6.2, 7 and 8.

#### 4.4.4 Imaging & miscellaneous

In order to see which of the mechanical resonators we are addressing with our laser, we require some kind of imaging system. As dielectric high-reflectivity mirrors (and optics in general) for 1064 nm are almost completely transparent for white light, the imaging can be build independent of the setup. We placed a charge-coupled device (CCD) camera such that we could look straight into the cryostat and used the mode-matching lens in combination with a second lens as a microscope. A typical image of a group of cantilevers is shown in figure 4.10. Thanks to the non-zero sensitivity of the silicon CCD at 1064 nm, the laser spot can easily be seen and the position of the mechanical resonators can be adjusted accordingly. In the setup with the  $^4\text{He}$  cryostat, the illumination was realized by shining a white light source through the second onto the first alignment mirror and the few percent (typically around 4%) that are reflected off the uncoated (for white light) mirror surface were directed into the cryostat onto the chip. The situation is somewhat more complicated for the dilution refrigerator, as the arms are rather long (for details see section 4.11). However, the imaging itself works exactly the same as for the small cryostat and only the illumination is more tedious. We swapped the position of the CCD with the illumination, so now the illumination goes straight into the cryostat and the imaging is done via a 50/50 beamsplitter. The image quality is worse than before due to the sub-optimal illumination, but still good enough to get a rough idea of where the laser is hitting the chip.

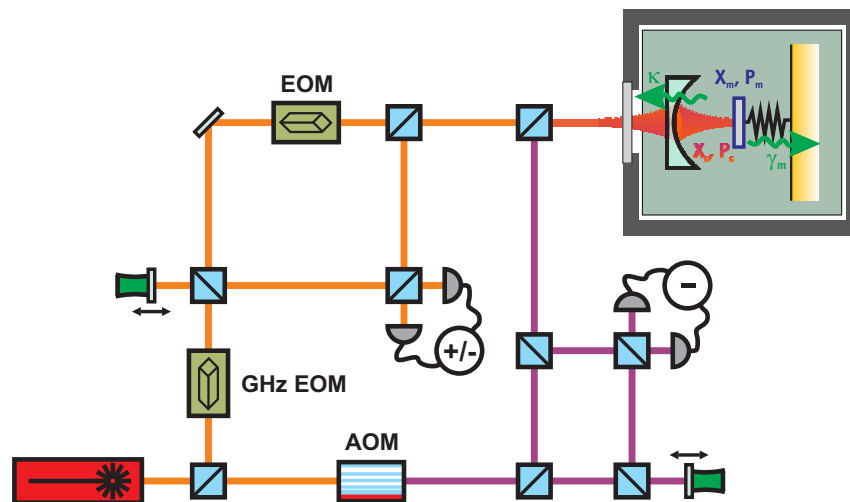


Figure 4.11: Functional sketch of the experimental setup. A Nd:YAG laser is split into a faint locking beam and a strong cooling or driving beam. The locking beam is shifted in frequency by several free spectral ranges of the Fabry-Pérot (FP) cavity using a high-bandwidth (GHz) electro-optical modulator (EOM) and subsequent filtering, which is not shown here. The beam is then split into a local oscillator and a signal field, which passes another EOM for Pound-Drever-Hall locking. The beam is sent into the FP cavity (which is mounted inside a cryostat) and measured in reflection in a homodyne detector. The strong field in turn is shifted in frequency by an acousto-optic modulator (AOM), split into a local oscillator and a signal field and then recombined with the locking signal beam on a polarizing beamsplitter. Also the reflected strong field can be measured in a homodyne detector. For a complete sketch of the setup see figure 4.12.

As electronic noise can be a major problem for the detection of the small signals we typically want to observe, we typically want to observe, we power all the sensitive equipment (detectors, signal combiners, amplifiers, etc.) with car-batteries, as they provide a perfectly quiet source with enough power for our requirements. Before introducing the batteries we had a lot of problems with noise from the power line (50 Hz), which could then be eliminated.

A sketch of the complete experimental setup can be found in figure 4.12, while a simplified sketch is shown in figure 4.11.

## 4.5 Acousto-optic modulator

An integral part of the setup are the acousto-optic modulators (AOM). They allow us to change the frequency of the cooling beam with respect to the locking beam. The basic working principle of an AOM is a crystal (typically made of  $\text{SiO}_2$  or  $\text{TeO}_2$ ) in which sound waves are produced by a piezo transducer forming a grating. An incoming light beam is diffracted off that grating, acquiring a Doppler-shift that is

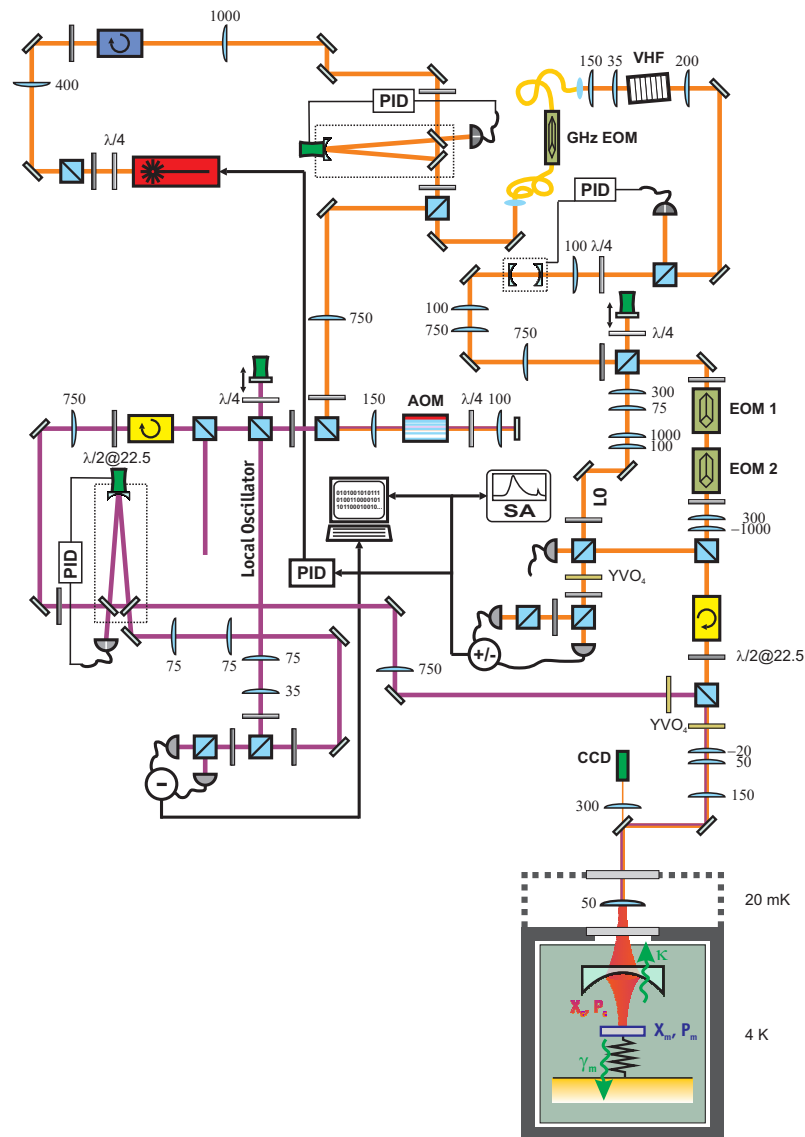


Figure 4.12: The picture shows a complete overview of the current experimental setup. A less detailed, functional sketch can be found in figure 4.11. The red box with the laser symbol in the top-left corner is a Nd:YAG laser. The unlabeled plates are half-wave plates, while the quarter-wave plates are marked as  $\lambda/4$ . All beamsplitters in the figure are polarizing beamsplitters. Proportional-integral-derivative controllers (PID) are used for stabilizing several cavities and also the phase between the signal and local oscillator beams for the homodyne detectors (those PID loops are omitted for reasons of simplicity). The blue box represents a Faraday isolator, while the yellow boxes are Faraday rotators. Electro-optical modulators are labeled EOM, while AOM stands for the acousto-optic modulator. The volume holographic filter (VHF) is used, in combination with a low-finesse cavity, for filtering unwanted modes left after modulation with the high-bandwidth EOM. The Fabry-Pérot cavity comprising the mechanical oscillator is either inside a  $^4\text{He}$  cryostat (4 K) or a dilution refrigerator (20 mK). For detailed discussions of the experimental parts see the various sections throughout this chapter.

proportional to the driving frequency and the diffraction order. Typical diffraction efficiencies into the first order are around 80%, however they can vary significantly with the spot size of the laser beam. We use our AOMs in a double-pass configuration, i.e. after the first pass the laser is reflected right back into the AOM giving it double the frequency shift. The advantage of this scheme is that the beam is always superimposed with the original incoming beam (independent of the AOM frequency), while in single-pass the beam direction changes with the applied frequency shift. The outgoing field can be separated from the incoming beam using a quarter-wave plate and a PBS. In our double-pass configuration we typically achieve a total efficiency of shifting the input laser by the desired frequency of  $\sim 50\%$ .

We chose our AOMs to be as high frequency as possible while still providing us with a reasonable efficiency – the higher the frequency, the higher the bandwidth of the AOM, which is important in order for the laser beam not to experience any drop in intensity while changing its frequency. The central frequency of our AOMs (AA Opto-Electronic MT200-B100A0.5-1064) is 200 MHz and their bandwidth is 50 MHz, more than sufficient for our mechanical frequencies of around 1 MHz, with a single-pass diffraction efficiency of 80% into the first order.

In the beginning we used direct digital synthesizer drivers (AA Opto-Electronics DDSA-B431b-0-M01 with AMPA-B-33 amplifiers) to produce the sound waves inside the AOM crystal. The advantage of such drivers is that they are very stable in frequency ( $\sim 200$  Hz/K), can easily be computer controlled and their frequencies can be almost perfectly matched. However, they exhibit spurious emission of around 55 dBc, which produced regularly spaced noise peaks in our homodyne power spectrum, which we had to remove from the spectrum in order to obtain good fits of our mechanical peaks. We therefore replaced the digital drivers with analog drivers (EQ Photonics AODR 1205FM-2), which are essentially voltage controlled oscillators (VCO) with a high-frequency amplifier. These drivers are much quieter, however at the cost of frequency stability and also the integration into LabView requires analog output voltages from the computer, with a frequency calibration that depends strongly on the temperature of the drivers.

## 4.6 Homodyne detection

In our experiments the quantity we are normally interested in is the motion of the mechanical resonator. When probing the optomechanical cavity with a resonant laser beam, the displacement couples directly to the phase of the beam, as the mechanical oscillation corresponds to a length change of the cavity, which translates into a phase change of the optical field. A phase measurement of a light field always requires some form of reference, which is normally another laser and the measurement is typically performed interferometrically. In our setup we already have such a reference which is generated for the Pound-Drever-Hall lock: the sidebands that are reflected off the cavity. The same way we can produce the error-signal, we can also extract the mechanical motion by just splitting off a small part of the signal and spectrally analyze it – as the mechanical frequency in our case is much larger than the locking bandwidth, the locking and the analysis can be seen as two completely separate parts of the setup. In the early experiments ([38] and section 6.1) this was

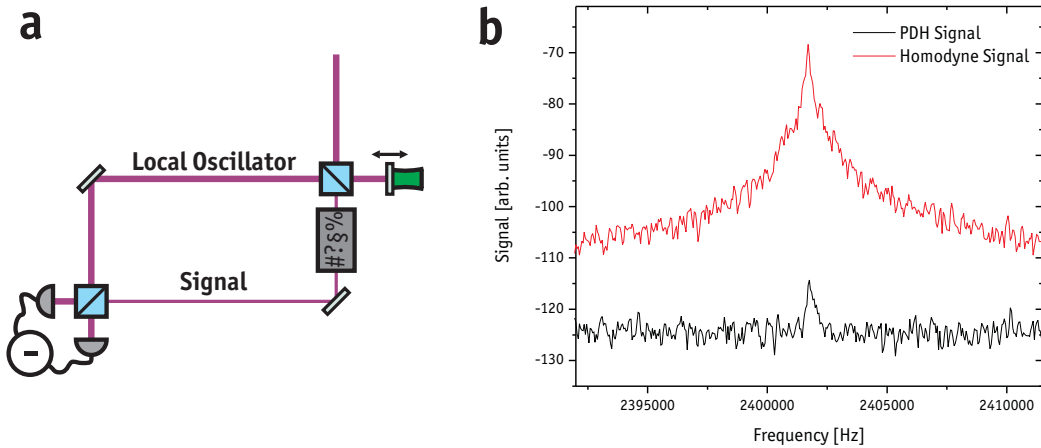


Figure 4.13: Generic scheme of a homodyne detector. A laser is split into a strong local oscillator and a weak signal beam. The signal passes a blackbox which represents any phase- and/or amplitude-modification which is the actual information to be measured. The phase of the local oscillator can be controlled by, for example, a piezo actuator. The two beams are interfered on a beamsplitter and the two output signals are detected. The difference signal of the detector is the homodyne signal, containing information on the amplitude- and phase quadratures of the signal field, depending on the relative phase between the two optical beams. **b** Mechanical noise power-spectrum measured using the Pound-Drever-Hall (PDH) error-signal (black curve) and using the homodyne detection scheme (red). The signal-to-noise ratio is at least 30 dB better for the latter case, probably owing to the non-ideal modulation depth of the phase modulation in this measurement.

also the way we measured the mechanical displacement. However, we quickly ran into a signal-to-noise problem, as the modulation depth of the sidebands was rather low (we still used the broadband EOM). In addition, the power in the locking arm and therefore the detector noise became problematic. The noise equivalent power (NEP) of our self-made detectors is approximately  $400 \mu\text{W}$  at 15 MHz and  $100 \mu\text{W}$  at 1 MHz. Also, using the PDH signal for the read-out allows to only measure the phase and not the amplitude fluctuations of the field.

We therefore decided to implement a homodyne read-out for our mechanical system. Homodyne detection is a common technique in quantum optics used to measure amplitude and phase fluctuations of laser fields and can be a quantum limited read-out technique, i.e. not be susceptible to classical noise (the improvement in signal-to-noise from the PDH read-out to the homodyne detection can be seen in figure 4.13b). The basic scheme for a homodyne detector is sketched in figure 4.13a. A signal with a steady-state amplitude  $\alpha_s$  and amplitude and phase quadratures

$\delta X_s(t)$  and  $\delta Y_s(t)$  can be written as

$$\alpha_s(t) = \alpha_s + \delta X_s(t) + i\delta Y_s(t), \quad (4.33)$$

where  $\alpha_s$ ,  $\delta X_s(t)$  and  $\delta Y_s(t) \in \mathbb{R}$ . The quadratures are the amplitude and phase fluctuations around a steady-state value  $\alpha$ . The signal is mixed with a strong field, typically called the local oscillator (LO), on a 50/50 beam-splitter and subsequently detected in two detectors. In order for the two beams to interfere on the beamsplitter, they of course not only have to be in the same spatial mode but also have to have the same polarization. The local oscillator signal can be written as

$$\alpha_{lo}(t) = [\alpha_{lo} + \delta X_{lo}(t) + i\delta Y_{lo}(t)] e^{i\varphi}, \quad (4.34)$$

where  $\varphi$  is an arbitrary phase between the signal and local oscillator beam. Normally, the two beams are derived from the same laser, which makes their frequencies match exactly. If they have different frequencies, the detection is called heterodyning, but here we will concentrate on the homodyning only. Following the derivation of [8], the field on the detectors  $D1$  and  $D2$  can be written as

$$\begin{aligned} \alpha_{D1}(t) &= \sqrt{\frac{1}{2}}\alpha_{lo}(t) + \sqrt{\frac{1}{2}}\alpha_s(t), \\ \alpha_{D2}(t) &= \sqrt{\frac{1}{2}}\alpha_{lo}(t) - \sqrt{\frac{1}{2}}\alpha_s(t), \end{aligned} \quad (4.35)$$

where one of the fields experiences a  $\pi$ -phase shift upon reflection off the beamsplitter. As the detectors only measure intensities, the photocurrents are

$$\begin{aligned} i_{D1}(t) &= |\alpha_{D1}(t)|^2 = \frac{1}{2} (|\alpha_{lo}(t)|^2 + \alpha_{lo}(t)\alpha_s^*(t) + \alpha_{lo}^*(t)\alpha_s(t) + |\alpha_s(t)|^2), \\ i_{D2}(t) &= |\alpha_{D2}(t)|^2 = \frac{1}{2} (|\alpha_{lo}(t)|^2 - \alpha_{lo}(t)\alpha_s^*(t) - \alpha_{lo}^*(t)\alpha_s(t) + |\alpha_s(t)|^2). \end{aligned} \quad (4.36)$$

If we substitute equations (4.33) and (4.34) into (4.36) and use the fact that  $|\alpha_{lo}|^2 \gg |\alpha_s|^2$ , i.e. we can neglect terms of the form  $\alpha_s\delta X^*$  and similar, as well as all terms containing two quadrature components, we can approximate

$$\begin{aligned} i_{D1}(t) &\approx \frac{1}{2}\alpha_{lo}^2 + \alpha_{lo}\delta X_{lo}(t) + \cos\varphi \cdot \alpha_{lo}\alpha_s + \cos\varphi \cdot \alpha_{lo}\delta X_s(t) + \sin\varphi \cdot \alpha_{lo}\delta Y_s(t), \\ i_{D2}(t) &\approx \frac{1}{2}\alpha_{lo}^2 + \alpha_{lo}\delta X_{lo}(t) - \cos\varphi \cdot \alpha_{lo}\alpha_s - \cos\varphi \cdot \alpha_{lo}\delta X_s(t) - \sin\varphi \cdot \alpha_{lo}\delta Y_s(t). \end{aligned} \quad (4.37)$$

The final step to obtain the homodyne signal now is to subtract the two photocurrents and we find

$$i_-(t) = i_{D1}(t) - i_{D2}(t) \approx 2\cos\varphi \cdot \alpha_{lo}\alpha_s + 2\alpha_{lo} [\cos\varphi \cdot \delta X_s(t) + \sin\varphi \cdot \delta Y_s(t)]. \quad (4.38)$$

This result is very interesting insofar as the difference signal, besides a DC term that is proportional to  $\alpha_{lo} \cdot \alpha_s$ , only depends on the amplitude of the local oscillator and

on the relative phase  $\varphi$  between the signal and the local oscillator – by changing  $\varphi$  we can measure either one of the signal’s quadrature or a combination of both.

Experimentally this means that the local oscillator power needs to be at least a factor of 10 higher than the signal power. As a true 50/50 splitter is very hard to find (normally they are more closer to 45/55), we realize our splitting with a polarizing beam splitter. For this purpose the beams are first combined on a PBS, where they remain orthogonally polarized but are already in the same spatial mode. The adjustable splitting is then realized with a half-wave plate, with which the polarizations are rotated into the  $45^\circ$  basis and subsequently mixed on another PBS. As the PBS are however far from perfect (the extinction ration between horizontal and vertical polarization is only around  $10^{-2}$  in the transmitted beam), we insert another wave plate and a PBS into the reflected port of the second PBS to filter out any remaining horizontally polarized light (cf. figure 4.12).

In our experiment the relative phase  $\varphi$  between the local oscillator and the signal can be controlled in two different ways: for both schemes the local oscillator is reflected off a mirror that is mounted on a piezo actuator. This allows us to actively change the phase, which we then lock to the setpoint that corresponds to the desired quadrature. The error-signal is simply the DC output of one of the two homodyne detectors, which contains the interference signal of the two laser beams. However, this approach does not allow us to lock to any arbitrary phase, as the interference signal is a  $\sin^2$  and it is not possible to lock on the maxima and minima of the signal. This can be circumvented however, by taking the interference signal on the PBS where the signal and the local oscillator beams are combined as the error-signal for locking the phase (cf. figure 4.12). The phase is then changed by introducing an additional YVO<sub>4</sub> crystal in between the two PBS where the beams are already in the same spatial mode but still have orthogonal polarizations. The setpoint can be chosen such that the lock is on the maximum slope of the error-signal – by tilting the birefringent crystal, the relative phase can now be arbitrarily changed over  $2\pi$ . This scheme relies on the phase being stable in between the two PBS, which for all practical purposes is the case in our experiment.

The interference signals between the local oscillator and the signal beam are  $\pi/2$  out of phase on the two homodyne detectors and therefore when taking the sum cancel each other out. The signal beam also contains sidebands, that are created for the PDH lock, that oscillate at relatively high frequency, typically 18 MHz in our experiments. These terms are not canceled in the sum signal and hence can be used to derive the Pound-Drever-Hall error-signal. In a real experiment it is very hard to make the interference terms perfectly cancel and if we don’t take great care, the level of the PDH signal oscillates with the interference. When locking the relative phase of the signal and the local oscillator however, this problem is eliminated. Another way of avoiding that problem is to use an additional detector before combining the signal with the LO and use this to generate the PDH error-signal. This approach can be very handy as it is completely independent of the relative phase – we have simply connected a JDSU ETX-500 diode to an ultra-low noise transimpedance amplifier (Femto DHPA-S). In the future it might also be interesting to replace the home-built photodetector circuits in the homodyning with such a configuration, as the amplification is adjustable, allowing detection of even very low power levels and the noise figure of  $1.5 \text{ pA}/\sqrt{\text{Hz}}$  at  $10^5$  gain, with a bandwidth of 14 MHz and

a measured NEP of  $15 \mu\text{W}$  at 1 MHz is very hard to match.

Homodyne detection is a very sensitive way of measuring the amplitude and the phase quadrature of the light field and is therefore used in quantum optics to reconstruct the full quantum state of a system. For our system the situation is slightly different as we do not probe the mechanical oscillator directly but rather measure the light field that has interacted with it. Therefore, we are currently limited to measuring the displacement quadrature  $x$  of the mechanical resonator only and cannot directly measure the energy of the system, known as a  $x^2$ -measurement. Thus, we have to rely on the fact that the system we are looking at behaves like a harmonic oscillator and that the equipartition theorem is valid. However there are ideas and implementations on how to measure the energy of the oscillator directly [77].

In our experiments, the reconstruction of the phase-space distribution of the mechanical motion, such as the Wigner function (3.50), can be done by measuring the phase quadrature of the resonant locking beam. This is a direct measure of the mechanical displacement, however oscillating at the mechanical frequency  $\omega_m$ . The extraction of the mechanical quadratures from the raw, digitized detector data is done by post-processing the data in LabView and MatLab, which makes it highly adjustable and the experiment itself remains very simple. The same technique, however with no post-processing was used in [35]. We multiply the digitized signal with  $\sin(\omega_m t + \phi)$  and also with  $\cos(\omega_m t + \phi)$ , where  $\omega_m$  is determined from fitting the spectra and  $\phi$  is an arbitrary phase typically set to zero. The two signals we obtain are the quadratures of the mechanical oscillator, after we remove higher order terms by low-pass filtering the data. The quadratures can be plotted in a phase-space diagram or histograms of the data can be generated and displayed in a 3-dimensional distribution plot. Such plots are shown for various cooling beam detunings for a mechanical resonator at low bath temperatures in figure 4.14.

In order to reconstruct quantum states with homodyne detection it is essential to avoid losses in the detection – any loss means that the quantum state of the light, which is used to measure the quantum state of the mechanical oscillator, is mixed with an equivalent amount of the vacuum state, reducing the fidelity of the quantum state. Losses in an experiment are manifold, where four main contributions can be identified in our setup:

- Diffraction and absorption losses on optical components. While this is currently the biggest contribution to our loss budget it is also one that can be managed relatively easily – we are upgrading most of the lenses that are in the path of our read-out beam from standard Thorlabs components to high-quality, specifically anti-reflection (AR) coated optics from Layertec. At the moment we have losses on the order of 15% solely due to non-ideal optics, which should be reduced to a few percent with the upgrade.
- Another loss contribution is that the optomechanical cavity is not perfectly single-sided. Light that leaves the cavity through the transmitted port is lost and therefore reduces the read-out fidelity. The ratio of the reflectivities of the input coupler with the mechanical oscillator is a measure of how much of the light created inside the cavity, i.e. the sidebands on the light field, can be detected in the reflected port. Typically this ratio is 1:10 but can be almost



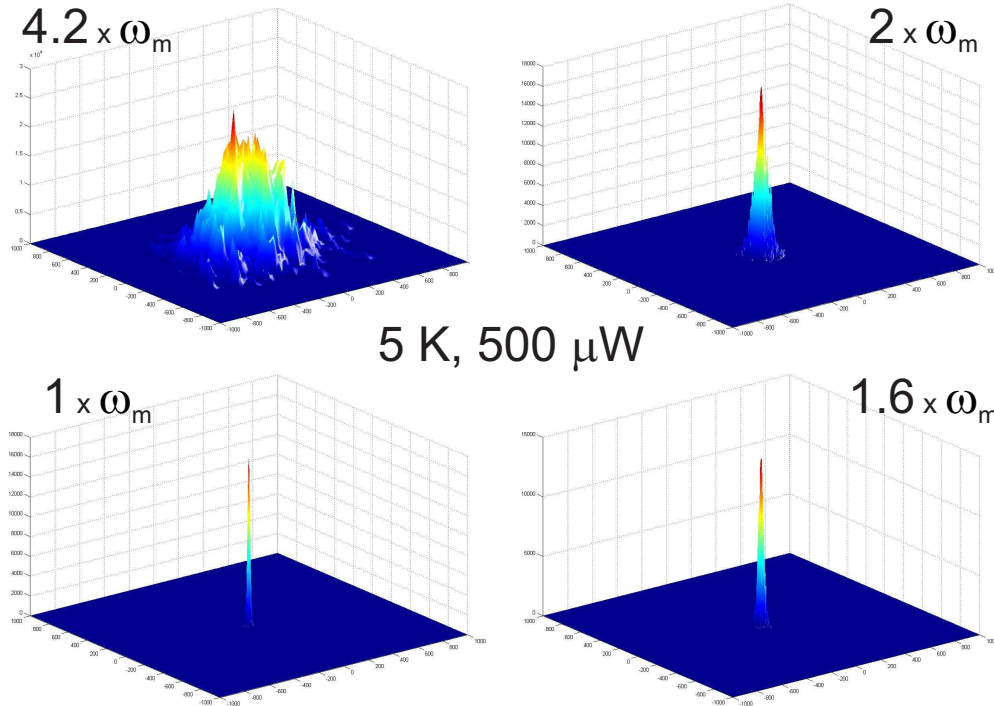


Figure 4.14: Shown are the thermal phase-space distributions of a mechanical resonator ( $\omega_m = 2\pi \times 944.7$  kHz) at 5 K and with an optical power in the cooling beam of  $500 \mu\text{W}$ . The detunings are shown in units of  $\omega_m$ , and the corresponding effective temperatures of the mechanical mode are (from top-left to bottom-left in clockwise direction) 3.5, 0.28, 0.08 and 0.04 K, respectively. The axes are in arbitrary units.

arbitrarily adjusted at the cost of the cavity finesse or by using micromirrors with better coatings.

- The spatial mode matching of the local oscillator with the signal beam is another loss mechanism – we typically achieve interference visibilities of greater than 90%, which could be further improved if needed by spatially filtering the local oscillator in a cavity.
- The finite quantum efficiency (QE)  $\eta$  of the photo-detectors also introduces losses and therefore it is desirable to have photodiodes with an as high QE as possible. While in the past it was possible to buy diodes from JDSU with  $\eta > 99\%$ , the diodes they manufacture now have much lower efficiencies. Apparently, the QE depends on which part of the InGaAs wafer the diode comes from – they used to measure the QE of their diodes and it was possible to cherry-pick the best devices. However, as they changed their manufacturing process they do not measure the QE anymore. We therefore ordered a large set of photodiodes and measured their quantum efficiencies ourselves, picking the best and also making pairs of diodes that had the best match in efficiency.

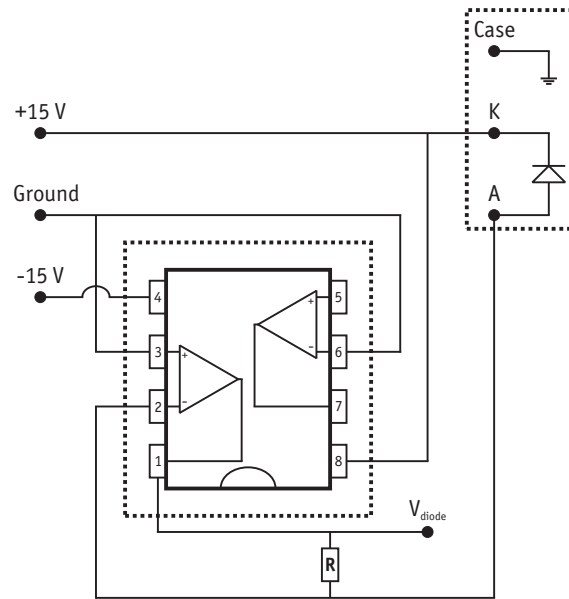


Figure 4.15: Circuit for measuring the quantum efficiency of a photodiode. The left box is an operational amplifier, for example a SGS Thomson low noise J-FET TL072, while the upper right box represents the photodiode to be measured. Here  $K$  stands for the cathode and  $A$  for the anode of the diode. The output voltage  $V_{diode}$  is measured across a resistor  $R$  for several optical input powers, which gives the quantum efficiency according to (4.39).

The QE of a diode is defined as

$$\eta = \frac{I_{diode} \cdot \hbar \cdot \omega}{P_{opt} \cdot e}, \quad (4.39)$$

where  $\omega$  is the optical frequency,  $P_{opt}$  the optical power on the diode and  $e = 1.602 \text{ C}$  the elementary charge. We obtain  $I_{diode}$  from fitting  $V_{diode}/R$  plotted against  $P_{opt}$  for several  $P_{opt}$ .  $V_{diode}$  is measured with the help of the circuit shown in figure 4.15, where  $R = 1 \text{ k}\Omega$  and  $P_{opt}$  is determined with a power meter. A comparison of the first batch of diodes can be seen in table 4.1 (all diodes are from JDSU).

## 4.7 Data Acquisition

The data we need to acquire changed with the advance of the experiment. While in the first experiments ([38] and 6.1) it was sufficient to just save the trace from the spectrum analyzer (plus the bandpowers of the mechanical and the calibration peak), when we started doing homodyning it became favorable to record the time trace of the difference signal. With this data it is possible to calculate spectra with different amount of averaging and to obtain correlation functions of two homodyne detectors, as is needed for the experiment presented in chapter 8. However the demand on the performance on the acquisition system is greatly increased, as now the acquisition

Type	# of diode	Slope	$\eta$ [%]	Box #
ETX500	1	0.86209	84.271	6
ETX500	2	0.86227	84.288	7
ETX500	3	0.85591	83.666	11
ETX500	4	0.84718	82.813	12
ETX500	5	0.85923	83.991	-
ETX500	6	0.85427	83.506	-
ETX500	7	0.857	83.773	10
ETX500	8	0.85641	83.715	-
ETX500	9	0.86341	84.4	-
ETX500	10	0.85827	83.897	-
ETX1000	1	0.94005	91.891	1
ETX1000	2	0.94068	91.953	5

Table 4.1: Typical quantum efficiencies for a batch of photodiodes. They are measured by determining the current produced in the diode  $I_{diode}$  for several optical input powers  $P_{opt}$  and using equation (4.39). More precisely, the potential difference  $V_{diode}$  across a resistor  $R$  (here 1.1922 k $\Omega$ ) is measured in a circuit similar to that shown in figure 4.15 and the slope of  $V_{diode}/R$  over  $P_{opt}$  is fitted to obtain  $I_{diode}$ . The errors of the QEs are less than 1% and the number of the box corresponds to the detector it is used in the experimental setup. While the ETX500 diodes have rather poor  $\eta$ , the ETX1000 show close to unity QEs, given that all diodes were measured with a protective window that typically reduces  $\eta$  by around 4%. The colors emphasize matching diodes. The values shown here were actually measured in Copenhagen by Alexander Huck.

rate must be larger than the mechanical oscillation frequency to at least be equal to the Nyquist rate [116]. In addition, the amount of data taken directly influences the resolution one can achieve in the power spectrum, which is crucial especially for high-Q mechanical resonances. Some of the early tests we made were done with a National Instruments PCI-5640R card, which featured a maximum sampling rate of 100 MS/s at 14 bit. The main limitation, besides the pure AC coupling, was that the data was acquired via the FPGA chip of the card, allowing for fast rates but quickly overflowing the FIFO (first-in first-out) buffer. The PCI-5640R card was not intended to be an actual fast data acquisition card acquiring broadband signals and we therefore replaced it with a proper data acquisition (DAQ) system. We purchased a National Instruments PXIe-1062Q chassis, which is a configurable and expandable controller that uses the PCI Express standard for data transfers between different acquisition cards and the host computer. The DAQ card we use is a NI PXIe-5122 digitizer, with a maximum sampling rate of 100 MS/s at 14 bit. If not run at maximum speed and in combination with a hard disk array (NI HDD-8264) this system is capable of streaming two channels continuously onto the hard disk without dropping a single bit. In addition, one can expand the DAQ with a second PXIe-5122 and run 4 channels at a rate of 10 MS/s each, limited only by the

hard disk array that can take up to 600 MB/s. In combination with the fast channels we also use an acquisition card (NI PXI-6251) for slow signals, like the ramp for the phase scan in chapter 8.

## 4.8 Data Analysis

In all recent experiments we digitize the homodyne current and perform different post-processing procedures to obtain the desired measurement values. Most programs for the data analysis are written in LabView, where some routines are realized using MatLab. For example, the mechanical spectra are calculated using a LabView routine, which turned out to be more efficient than the corresponding MatLab code. Post-processing the data offers great flexibility and can be automated to a very large extent, which makes it very convenient.

## 4.9 Calibration

The spectrum of the mechanical oscillation contains the information on the (effective) frequency and linewidth of the mechanical motion, as well as its displacement as the area under the mechanical peak is directly proportional to  $\langle \Delta x^2 \rangle$ . Without knowing the exact values of the laser power, the quantum efficiency of the detectors, the amplification gain, etc. the mechanical power spectrum however only gives a signal that is proportional to the displacement, with unknown prefactors. Our signal is therefore calibrated, which is done by applying a known frequency (or phase) modulation to the laser that is close to the mechanical motion in frequency and use this as a reference to get absolute numbers for the displacement. In most experiments this was done by directly applying a modulation signal to the lasers fast frequency modulation port – the same that is used for stabilizing the Fabry-Pérot cavity. The signal for locking the cavity is simply combined with the output of a function generator on a BNC T-piece (typical modulations were 1.05 MHz for a mechanical resonance of 950 kHz and a voltage of 10 mV<sub>pp</sub>), while the output of the function generator is protected by a DC-block (e.g. a capacitor or the Minicircuits BLK-222) from the high-voltage signal of the PID controller. This has the drawback, besides the obvious one of combining a high- and low-voltage signal, that all laser fields have the same modulation, while it is only needed for the read-out beam. We therefore recently introduced a second, broad-band phase modulator (New Focus 4004) in the locking beam, which allows us to phase modulate only the signal arm of the locking beam. The actual calibration remains the same.

We apply an oscillating voltage of amplitude  $A_{FM}$  at frequency  $\Omega$  either to the piezo giving optical feedback to the laser diode or the EOM, frequency modulating the laser according to:

$$E(t) = A_{FM} \cos(2\pi\nu_L t + \beta \sin(2\pi\Omega t)), \quad (4.40)$$

where  $\nu_L$  is the laser frequency,  $\beta = \Delta\nu/\Omega$  is the modulation index and  $\Delta\nu$  is the peak frequency-deviation. In the frequency domain, applying the modulation creates sidebands of frequency  $n\cdot\Omega$  from the carrier frequency, where  $n = \pm 1$  for small modulations. The presence of these sidebands gives rise to an optical beating

in the amplitude  $E$ , which in principle can be detected directly and the modulation index could be determined from the beat amplitude, however this requires strong amplification as the signal is very small.

A different way to observe the small frequency modulation, is to lock a cavity at half its maximum and detect its transmission. The frequency modulation is translated into an appreciable amplitude modulation, proportional to the gradient of the cavity's frequency response  $\partial U/\partial\nu$ , where  $U(\nu)$  is the Lorentzian cavity spectrum (neglecting any offset in central frequency and DC output level):

$$U(\nu) = \frac{\Gamma^2 U_p}{4\nu^2 + \Gamma^2}, \quad (4.41)$$

with  $\Gamma$  being the full width at half maximum (FWHM) of the cavity resonance and  $U_p$  the peak voltage generated by the photodiode at cavity resonance. Its spectral derivative is

$$\frac{\partial U}{\partial\nu} = \frac{-8\Gamma^2 U_p \nu}{(4\nu^2 + \Gamma^2)^2}. \quad (4.42)$$

For  $\nu = \kappa = \Gamma/2$  the slope of the cavity response is

$$\frac{\partial U(\kappa)}{\partial\nu} = \frac{-U_p}{2\kappa} = \frac{-U_{1/2}}{\kappa}, \quad (4.43)$$

with  $U_p = 2 \cdot U_{1/2}$  and  $\kappa$  is the cavity linewidth (HWHM). The free spectral range of a ring cavity (used in our setup) is  $FSR_o = c/L$ , where  $L$  is the cavity length and the finesse is  $F = FSR_o/(2\kappa_o)$ , thus giving

$$\kappa_o = \frac{c}{2LF}. \quad (4.44)$$

The amplitude modulation is converted into a frequency modulation according to

$$\Delta\nu = \frac{A_{AM}}{\partial U(\kappa_o)/\partial\nu}, \quad (4.45)$$

where  $A_{AM}$  is the amplitude of the oscillation in root mean square (rms) voltage and hence  $\Delta\nu$  is in rms units. As an aside,

$$\beta = \frac{k_\nu A_{FM}}{\Omega} = \frac{\Delta\nu}{\Omega}, \quad (4.46)$$

where  $k_\nu$  is the frequency deviation constant of the laser and  $A_{FM}$  is the amplitude of the modulating signal. Thus, the laser frequency will deviate for a given voltage according to  $k_\nu = \Delta\nu/A_{FM}$ .

Now, in order to determine the calibrated displacement of the mechanical motion, we apply a modulation to the laser with  $\Delta\nu_{cal}$ , calibrated as outlined above. We can use

$$\frac{\Delta\nu_{cal}}{\nu_L} = \frac{\Delta x_{cal}}{L_{FP}}, \quad (4.47)$$

where  $\Delta x_{cal}$  is the equivalent cavity displacement and  $L_{FP}$  the Fabry-Pérot cavity length. The rms micromirror displacement is then given by

$$\Delta x_m = \frac{\Delta\nu_{cal} L_{FP}}{\nu_L} \frac{V_m}{V_{cal}}, \quad (4.48)$$

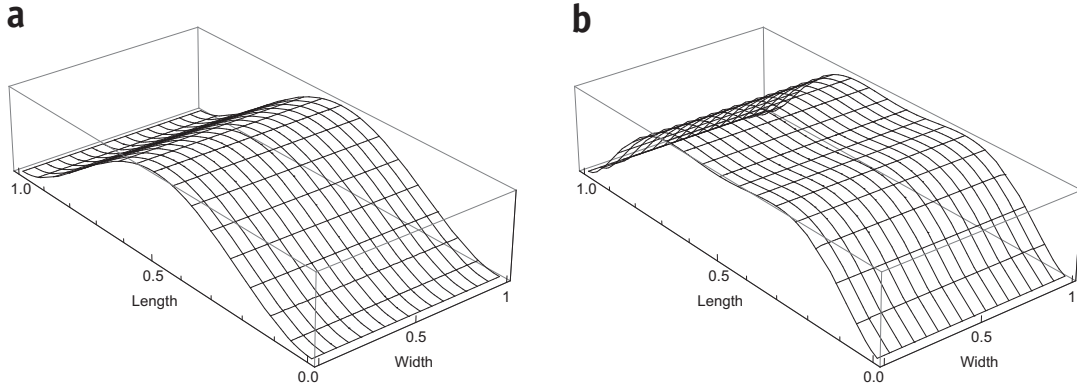


Figure 4.16: **a** mode shape of a doubly clamped resonator. **b** in contrast shows the polynomial approximation (4.55) to a doubly clamped, flat top mode shape, which is closer to the actual mode shape of the resonator used in the experiments in section 6.2 and chapters 7 & 8. This mode was used for calculating the effective mass of the resonator.

where  $V_m$  and  $V_{cal}$  are the band powers converted to volts rms of the mechanical and the calibration peak, respectively. These band powers can be directly measured on a spectrum analyzer. To convert a power  $P_{dBm}$  measured across a resistor  $R$  to volts rms use:

$$V_{rms} = \sqrt{\frac{R}{1000}} 10^{P_{dBm}/20}. \quad (4.49)$$

It is now possible to measure a fully calibrated noise power spectrum and hence, for example, determine the effective mass  $m_{eff}$  using (4.48)

$$m_{eff} = \frac{k_B T_{eff}}{\omega_m^2 \langle \Delta x_m^2 \rangle}, \quad (4.50)$$

or similarly the effective mode temperature  $T_{eff}$ .

## 4.10 Effective mass

While the effective mass of a particular mode of the mechanical resonator can be experimentally determined according to section 4.9 it is also possible to calculate the effective mass one expects as a function of the optical beam size, the position of the laser on the mechanical oscillator and the mode of the oscillator itself. The idea is to take the mode of a doubly clamped beam (in the Euler-Bernoulli approximation) [117]

$$M_{FF}(x, y) = \left[ \cosh\left(\frac{\xi x}{L}\right) - \cos\left(\frac{\xi x}{L}\right) - \frac{\cosh \xi - \cos \xi}{\sinh \xi + \sin \xi} \left[ \sinh\left(\frac{\xi x}{L}\right) - \sin\left(\frac{\xi x}{L}\right) \right] \right] M(y), \quad (4.51)$$

where  $L$  is the length of the beam,  $M(y) = 1$  the mode shape of the beam in the  $y$ -direction, and  $\xi$  is 4.73, 7.85, and 11 for the 0<sup>th</sup>, 1<sup>st</sup>, and 2<sup>nd</sup> order mode, respectively (see [117–119] for details). The effective mass of a mechanical resonator

is the overlap of its mode mass (the mass actually contributing to the motion of the mode) with the optical mode probing the motion. The fundamental mode mass is

$$m_{mode} = m_{extra} + \rho \cdot t \int_0^L \int_0^w M_{FF}^2(x, y) dx dy, \quad (4.52)$$

where  $m_{extra}$  is any additional mass on the resonator that is not directly contributing to its motion (such as a mirror pad),  $\rho$  is the density of the material,  $t$  the thickness of the beam and  $w$  its width. Here the fact that only  $\sim 74\%$  of the total mass of a doubly clamped resonator contribute to the mechanical motion is taken into account [62]. The overlap of the spot where the laser field is probing the mechanical motion with  $M_{FF}$  is

$$A_{Laser} = \text{Re} \left\{ \int_0^L \int_0^w M_{FF}(x, y) M_{Beam}^2(x, y) dx dy \right\}, \quad (4.53)$$

with  $M_{Beam}$  being the mode shape of the laser beam, which typically is a two-dimensional Gaussian. The effective mass is then given by [62]

$$m_{eff} = \frac{m_{mode}}{A_{Laser}^2}. \quad (4.54)$$

For our doubly-clamped resonator used in section 6.2 and chapters 7 & 8 this calculation underestimates the effective mass by a factor of  $\sim 2$ . The reason for that is that the real mode shape of the doubly clamped beam loaded with a mirror pad of comparable size is somewhat different. We did the same calculation only replacing  $M_{FF}$  with a polynomial fit to the mode shape of the FEM simulation of the mechanical resonator (see figure 4.16 for a graphical comparison of the two)

$$\begin{aligned} M'_{FF}(x, y) = & (-0.03 + 19654.35x + 5.3 \cdot 10^9 x^2 - 3.11 \cdot 10^{14} x^3 + 6.81 \cdot 10^{18} x^4 - \\ & - 6.6 \cdot 10^{22} x^5 + 2.35 \cdot 10^{26} x^6 - 955291.46x^7 - 110.43x^8 - 0.01x^9)M(y). \end{aligned} \quad (4.55)$$

This adjusted calculation gave us a more accurate result to within 10% of the actually measured value of the effective mass.

A third way of determining the effective mass is to use finite element method (FEM) simulation. This is briefly described in the supplementary information of [43].

## 4.11 Cryogenic operation of an optical cavity

According to  $T_{eff} = T \frac{\gamma_m}{\gamma_{eff}}$  (cf. section 3.3), if we would like to reduce the effective mode temperature of the mechanical resonator we have to minimize the coupling to its environment. There are two ways of achieving that: first by increasing the mechanical quality factor  $Q$ , i.e. reducing the damping of the mechanical mode  $\gamma_m$ , where several approaches are discussed in chapter 5, or secondly by decreasing the bath temperature  $T$  to which the mechanics is coupled to. This can be done by putting the chip with the oscillator inside a cryostat. In the simplest case this is a  $^4\text{He}$  cryostat, which can in principle reach temperatures of 4.2 K – or even as low as around 1 K if the pressure of the helium is decreased by pumping on it.

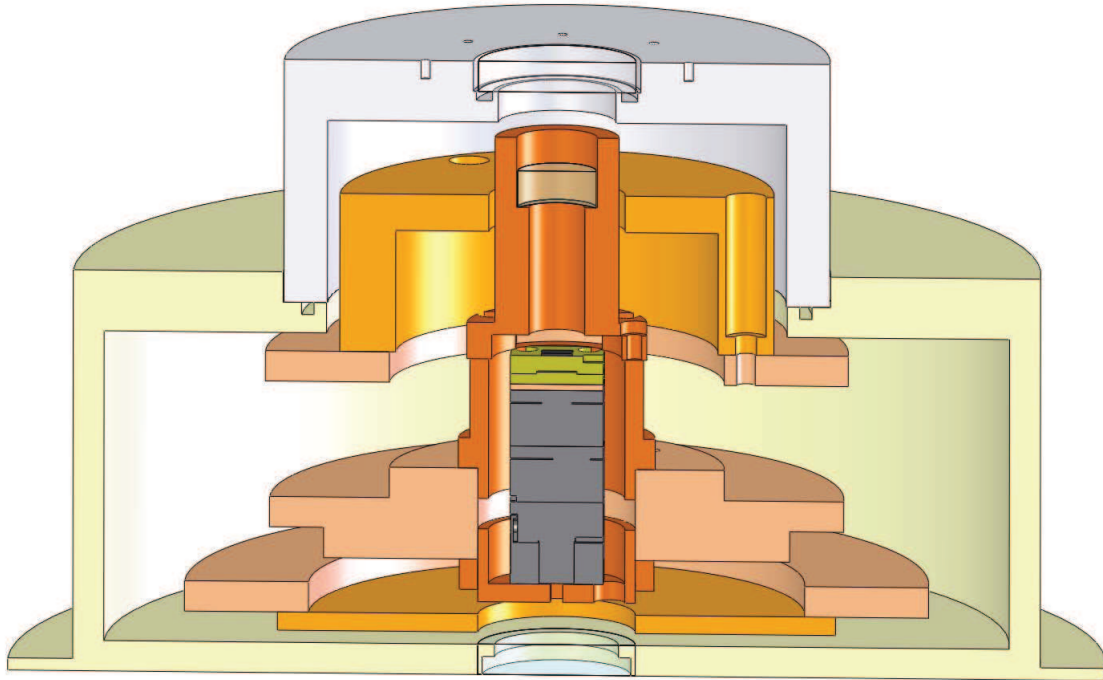


Figure 4.17: Shown is a SolidWorks drawing of the Janis ST-500 continuous-flow  $^4\text{He}$  cryostat in the configuration used for the experiments described in section 6.2 and chapter 7. The input mirror is mounted in a solid piece of copper (the reddish components are the copper mounts we designed for the cavity), while the chip with the micromechanical oscillator (black) sits on top of xyz-positioning piezo actuators (gray) and a thermalization copper-block (gold). The radiation shields (orange) keep 300 K blackbody radiation from heating up the experiment.

#### 4.11.1 Continuous-flow $^4\text{He}$ cryostat

Our 4 K experiments were performed using a Janis ST-500 microscopy cryostat. This cryostat is a continuous-flow cryostat, where liquid helium is taken from a dewar with a transfer line and run through a spiral to cool the cold-finger inside the cryostat. The sample chamber is evacuated to a pressure of around  $10^{-6}$  mbar at room temperature and  $10^{-7}$  mbar when cooled down, as additional cryo-pumping helps to freeze out residual gas inside the cryostat. The vacuum prevents freezing of water and nitrogen inside the cryostat and for our experiments it is required to avoid damping of the mechanical mode from residual gas, which can severely limit the mechanical  $Q$  at pressures above  $10^{-3}$  mbar. For optimizing the coupling of the laser light to the mechanical resonator one needs to be able to position the mechanics to within a precision of around a  $\mu\text{m}$ . This is achieved by mounting the chip on a three-axis piezo positioning system (2x Attocube ANPx51 + 1x Attocube ANPz51), which has a resolution of  $\sim 10$  nm at low temperature. In between the Attocubes and the chip is a thin ( $\sim 5$  mm) copper piece with copper braids (they are cold-pressed into the copper), which can be clamped to the cold-finger and are used for thermalizing the chip. The chip is attached to the copper block by applying



a thin layer of Apiezon N grease for better thermal contact and the chip is typically also clamped down with two small copper slabs. The thermalization block also has a small clearance for a Si-diode (DT-670A1-SD) for measuring the temperature as close to the chip as possible. The rest of the cavity, i.e. the input coupler, was also mounted inside the cavity throughout all our experiments.

In the first low-temperature experiment (see section 6.1) the cavity was still locked with the help of a ring-piezo which could not be thermalized and therefore had to be attached to the cryostat cap to remain at room temperature. In the subsequent experiment (section 6.2), this was replaced with a solid copper block directly attached to the cold-finger. The input coupler was therefore also thermalized at the base temperature of the cryostat. This approach helped greatly in reducing the cryostat temperature as well as the mode temperature of the mechanical oscillator. However, only the use of radiation shielding, which minimizes the effect of 300 K blackbody radiation heating up the experiment, and proper thermalization of all wiring inside the cryostat allowed us to reach a base temperature of approximately 5 K. Prior to that, temperatures in excess of 10 - 15 K were the lower limit. We attached the wires connecting the Attocubes to the cold-finger by tying them down at several different points using dental floss and Teflon tape. The laser was coupled to the cavity through a 1" anti-reflection coated window. The cross section of the cryostat in a rigid 25 mm configuration (i.e. the cavity is 25 mm long and the input coupler is mounted on a solid copper piece) can be seen in figure 4.17. While we mostly operated the cryostat with a 25 mm long cavity, we also tested 50 mm long cavities and any arbitrary length should in principle be feasible. For a typical cool-down it took us around 1 hour to reach 5 K and we used a little more than 10 liters of liquid helium, while during operation at low temperature we used around 2 liters/hour. We could not observe any significant ( $>$  a few hundred mK) heating of the sample stage from laser absorption, not even at high input powers of  $>20$  mW and a locked Fabry-Pérot cavity, even though all the transmitted laser power was dumped into the thermalization copper block. This is due to the large cooling power of the cryostat of approximately 1 W at 5 K. Also, we did not experience any problems with stabilizing the cavity during cryogenic operation even for high-finesse configurations (the specified vibration level of the cryostat is 25 nm at the cold finger) once we removed the vibrations generated in the liquid helium dewar due to evaporating and boiling helium (this was achieved by putting the transfer line all the way into the liquid helium). The copper we used to build the sample and input coupler holder was mostly oxygen-free (OFHC) copper, which in retrospect however, is probably not necessary for a 4 K cryostat. The mode matching to the cavity was performed with a lens (50 mm focal length) outside of the cryostat.

### 4.11.2 Closed-cycle $^4\text{He}$ cryostat

In the continuous-flow  $^4\text{He}$  cryostat helium is vented directly into the atmosphere and therefore lost. Even though it can also be collected and recycled, running a  $^4\text{He}$  cryostat can be rather expensive. We therefore started looking into closed-cycle systems, in which the helium is directly reused and the operation of such a cryostat only requires electrical power and cooling water. The test system we had was a Vericold VT4-500 pulse tube cooler, which delivered a cooling power of 500 mW at

$\sim 2.8$  K. The cryostat worked using the Joule-Thomson effect, where a gas (helium in this case) is forced through a valve and if well isolated cools during expansion (as no heat exchange is performed). The helium is then compressed again and reused for cooling (see [120] for a detailed introduction into pulse-tube cooling). The main disadvantage of this cooling approach is that large vibrations are generated when the gas passes the valve, typically on the  $\mu\text{m}$  scale. For our experimental trials this was a major limitation, as the cavity was directly attached to the cold-finger in which the vibrations are generated and our cavity started to move with a big enough amplitude, that the beam reflected off it was visibly steering around, making any alignment very hard and locking of the cavity impossible. We could therefore only perform tests at low temperature when we switched the cooling off, which resulted in a quick heat up of the cold-finger and the sample. We tried to increase the time it needed to warm up by adding additional mass to the cold finger (a solid lead block, as lead has one of the highest specific heat capacitance at low temperatures of all materials) but even though, within 15 mins the temperature increased from 4.6 K to 9 K.

### 4.11.3 Dilution refrigerator

As our experiments in the  $^4\text{He}$  cryostat already allowed us to cool to thermal occupations of the mechanical resonators of around 30 (see section 6.2) we decided to go to even lower bath temperatures by using a closed-cycle dilution refrigerator (see for example [121] for a detailed introduction) that can operate with a 3 order of magnitude lower base temperature (typically around 10 mK) compared to a  $^4\text{He}$  cryostat. In such a cryostat the mK regime is reached by having a cold mixture of  $^3\text{He}/^4\text{He}$ , which below a certain temperature (the triple point) separates into two phases – a  $^3\text{He}$  and a  $^4\text{He}$  rich phase. The  $^3\text{He}$  poor phase saturates at a level of approximately 6%  $^3\text{He}$  and when pumping on this part of the mixture,  $^3\text{He}$  is removed (it evaporates at a much higher rate than  $^4\text{He}$ ) and is refilled with  $^3\text{He}$  from the other phase in order to restore an equilibrium state. However, the  $^3\text{He}$  needs energy to cross the boundary of the two phases and therefore provides cooling, as this energy is taken from the surrounding of the mixing chamber. The pumped  $^3\text{He}$  is circulated back into the  $^3\text{He}$  rich phase.

Vericold had come up with a completely new design that would allow them to meet all of our requirements: optical access with large windows, low vibrations ( $<1$  nm at the sample stage), 200  $\mu\text{W}$  cooling power at 100 mK and a base temperature of 20 mK. The idea for the design was to mechanically decouple the experimental stage from the rest of the cryostat and only thermally connect it. This was realized with two glass-fiber reinforced plastic tubes, that are connected to the sample stage on one of their ends and can be bolted down to the optical table on the other side. In this configuration the experiment is floating inside the cryostat and only rigidly connected to the optical table. In order to reach a base temperature of 20 mK the tubes have to have a length of approximately 1 m each and are thermally linked to each of the different temperature stages (except for the mixing chamber) of the cryostat (approximately 55 K, 4 K, 1 K, and 200 mK, with cooling powers of 200 mW, 20 mW, 2 mW and 20  $\mu\text{W}$ , respectively) with copper braids. After a few tests those braids turned out to be too stiff at low temperatures, hence transmitting excess

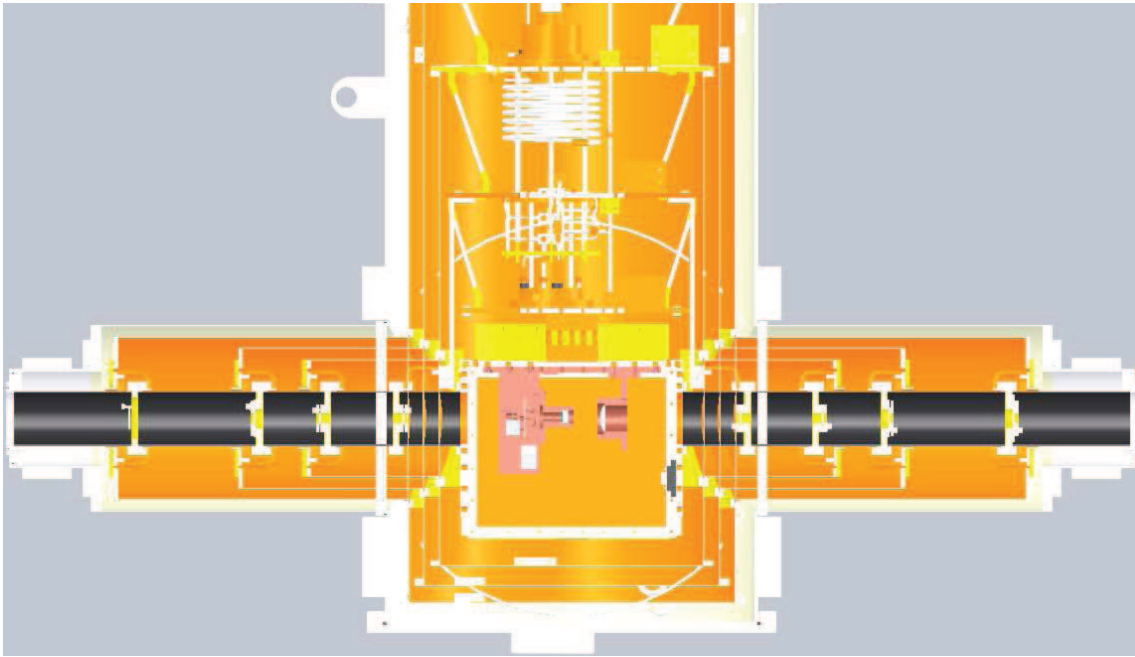


Figure 4.18: Cross section of the lower part of our Vericold dilution refrigerator. The black pipe is the glass fiber reinforced plastic tube, which allows us to directly mount the 20 mK experiment (copper colored assembly in the center – cf. figure 4.19) on the optical table. The experiment is only thermally connected to the cryostat through copper wires. This design reduces the mechanical vibrations coupled from the refrigerator to our cold optical setup.

vibrations of the cryostat onto the experiment, and were replaced with unbraided copper wires. The experimental stage itself is also connected to the cryostat with copper wires, specifically to the mixing chamber. A cross section of the design is shown in figure 4.18. Optical access to the cold experiment is provided through several special windows (Suprasil WF with AR coating for 1064 nm) that are inside the tubes at the different temperatures in order to reduce the heat load generated by blackbody radiation. Great care has to be taken to prevent radiation leaks in general, while the tubes still have to be able to move with respect to the cryostat in order to avoid coupling of mechanical vibrations to the experiment as well as to allow for thermal contraction upon cool-down, which can be up to a few mm. While the base temperature at the mixing chamber actually reaches 20 mK, the temperature of the experiment is slightly higher, at or around 30 mK. Even though the base temperature is very low, the actual working temperature we expect is around 150 mK or more, as diffraction of the laser on the lenses and absorption of the transmitted cavity light heat up the cryostat. The latter issue can be eliminated by designing the cavity such that the transmitted light can be collected with a lens and guided out through the other arm of the cryostat. We have included this feature in all new designs, however the samples also need to have the back-side of the wafer removed, which is not a trivial task for all resonator designs. A full cool-down from room temperature to 20 mK takes approximately 2.5 days, while there is in principle

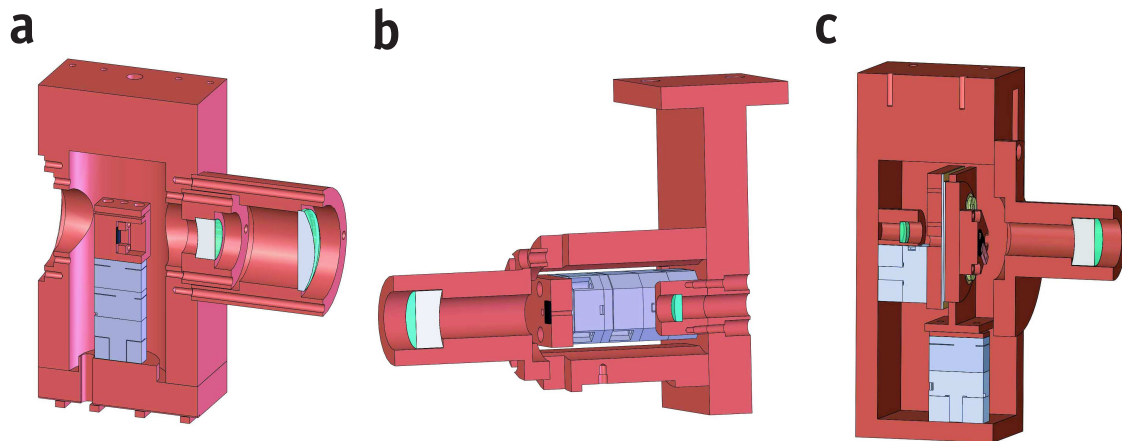


Figure 4.19: Dilution refrigerator cavity designs. **a** was the very first design, where the Attocube positioners were aligned vertically, which was too unstable for operation inside the refrigerator. **b** This configuration was essentially the same as in the ST-500 cryostat, improving the stability over **a** significantly, however the design was still not stable enough for high-finesse cavities. The latest design is shown in **c**, where the cavity only features one positioner, while alignment in the x-y plane is done from the side. This configuration relies on the low friction of Teflon on Teflon and shows promising first results at low temperatures.

no limit on how long the fridge can stay cold.

Due to the closed-cycle operation of the cryostat only electrical power, cooling water and liquid nitrogen for an external cold trap for the  $^3\text{He}/^4\text{He}$  mixture are necessary, greatly reducing the complexity of operating a dilution refrigerator compared to the standard design. Everything is computer controlled and in principle the cryostat can be switched on and only needs further attention after it is cold. In practice however, the cavity needs to be regularly realigned as the copper contracts upon cooling and the cavity therefore becomes misaligned. Despite the design and great attention in reducing the vibration level at the sample stage there is still significant mechanical movement of the cryostat coupling onto the experiment. For our laser-lock performance the maximum allowed relative movement of the cavity mirrors can be estimated to be on the order of a few picometers or less (see section 4.3). In practice, at optical finesses of smaller than 3,500 the cavity can be continuously locked, however the lock gets noisy with increasing optical quality and starts to regularly unlock. The vibrations couple to the stack of Attocubes that are quite compliant and therefore are susceptible to mechanical noise, making a stable lock difficult. We have reduced a few of the noise sources and coupling mechanisms, e.g. as mentioned already the braided copper wires have been replaced with unbraided ones and the line connecting the roughing pump to the turbo pumping on the helium mixture is running through a tub filled with concrete, which removed all the vibrations of the roughing pump on the cryostat. In addition, we have designed several different cavity holders trying to make the cavity as rigid as possible:

- Our first design was a block of copper with a cylindrical hole at the bottom

in which the Attocube stack could be mounted. It was built such that the stack was standing up, which we initially thought would make the design more stable. However, it turned out to be the contrary – the direction of least stability in this configuration was the cavity axis and the Attocube stack was free to wobble, making it impossible to lock the cavity while the dilution refrigerator was running. We also tried to replace the piezo positioners with the bigger, supposedly more stable version, the ANPx101 (ANPz101). The difference in stability was however marginal. In addition, the copper piece holding the chip was relatively heavy and therefore made the stack even more unstable. Thermalization of the mechanical chip was achieved using copper braids that connected the chip holder to the copper block.

- In our second approach we therefore returned to the original design from our  $^4\text{He}$  cryostat – here the Attocubes were aligned horizontally and any shaking of the stack would to first order only result in a misalignment of the mechanical resonator with respect to the optical cavity mode. In this degree of freedom we are only susceptible to  $\mu\text{m}$  vibrations, which is orders of magnitude larger than the expected vibration level at the sample stage. In fact, the stability of our cavity was significantly improved, now allowing continuous locks of cavities with a finesse  $< 3,500$ . While this is a great improvement, the lock becomes quite noisy when working at large finesse and the cavity starts to frequently unlock when the finesse is increased above 3,500.
- We therefore decided to remove as many of the Attocubes as possible, which are the most unstable part in our cavity. While the z-axis is indispensable, as we require very precise control of the cavity length, the x- and y-axis do not necessarily have to be part of the cavity itself. All that is required is control of the chip position to within a few hundred nanometers over a few tens of  $\mu\text{m}$  at low temperatures. In our newest design we hence only left the ANPz51 directly attached to the chip and positioned the ANPx51 and an additional ANPz51 such that they can push and pull the sample holder on which the chip is attached to. A cross-section of the design is shown in figure 4.19c. The main challenge here is that one copper piece has to glide on top of another with as little friction as possible, while a force from the top has to keep it in place. We try to minimize the friction by attaching a thin Teflon sheet on each copper piece and the chip holder is kept in place by springs. While the details are currently still subject to testing, the main purpose of the new design was already shown to work: we built a test cavity with only one ANPz51 as part of the cavity and it showed a very stable lock even at low temperatures and with additional noise (like hitting the optical table with a hammer). We are therefore confident that, if the movements in the x-y-plane work, we can stably lock any finesse in the fully operating dilution refrigerator.

All designs have in common the fact that the mode-matching lens is inside the cryostat and therefore is also thermalized at the base temperature. The copper pieces that are cooled to temperatures of a few hundred mK and lower are tempered, i.e. they are baked in vacuum at  $700\text{ }^\circ\text{C}$  for 10 hours. This has the effect that magnetic inclusions of iron or similar metals in the copper get oxidized, increasing the thermal

conductivity of the copper significantly. The standard copper that can typically be purchased has a residual resistivity ratio (RRR) of 50 to 100. The RRR is a measure of the purity and the thermal conductivity at low temperatures of a material. By annealing the copper, the RRR can be increased to around 1,000. It is important to not use OFHC copper for this purpose as this lacks the oxygen for the oxidation process [122] (for details see for example [123]).

Recently, we have also included a fiber feedthrough into the dilution refrigerator. 10 fibers (6x SMF-28 and 4x SM980-5.8-125) are running through a single KF-25 flange, where each of the fibers has a separate feedthrough. The design for a single fiber feedthrough can be found in [124]. The vacuum level we achieve in the dilution fridge, typically around  $5 \cdot 10^{-7}$  mbar at low temperatures, has not changed since the fibers were put in. Each fiber is thermalized at every temperature stage and tests show that no significant increase in base temperature can be observed due to the fibers running into the cryostat. This newly added feature will allow us to not only do free-space but also perform fiber based experiments.

## 5 High-reflectivity, high-Q mechanical resonators

In order to perform quantum optical experiments with macroscopic mechanical oscillators the mechanical systems have to fulfill a number of criterions:

- the optical quality must be outstanding for several reasons: the finesse of the cavity influences the optomechanical coupling strength  $g$  (3.67), as well as the sensitivity of the read-out of the mechanical motion. No absorption of laser light in the mirror should be present, as this results in heating of the mechanical mode, limiting the achievable radiation-pressure cooling. Note that the required optical quality sets a lower bound on the size of the mechanical resonator: the lateral dimensions have to be around  $40 \mu\text{m}$  or bigger, otherwise diffraction losses become dominant as we can only achieve a finite optical mode size (see figure 4.3). Also, the reflectivity sets a limit on the thickness of the mechanical structures – typically a distributed Bragg reflector (DBR) has to be thicker than  $5 \mu\text{m}$  to allow for reflectivities of 99.99% or more. Those constraints are hard to circumvent and currently limit our possible geometries.
- the mechanical quality factor  $Q$  of the resonator determines its thermal coupling rate  $\Gamma_m = k_B T / \hbar Q$  to the environment, which sets a bound for the achievable radiation-pressure cooling and the lifetime of a mechanical quantum state. It is therefore highly favorable to fabricate as high-Q resonators as possible.
- the mechanical frequency  $\omega_m = 2\pi \cdot f_m$  plays a manifold role in what kind of experiments can be realized: the most obvious one is that it sets the ground state temperature for a mechanical oscillator, favoring higher frequencies to make quantum experiments more easy to realize. In addition, high frequencies are also a big technical advantage as there tends to be more noise at low frequencies, e.g. lasers are typically shot-noise limited (i.e. no excess classical amplitude noise is present) around 10 MHz. However, excessively high frequencies are also technically challenging, namely GHz electronics typically comes at the price of more losses and optical detectors sacrifice responsivity, which is crucial for continuous variable quantum optics experiments. Also, low frequency mechanics has a large ground state extension, which is important for tests of macroscopic realism [125–127]. Therefore it is crucial to optimize the mechanical frequency to the desired range, which for our experiments is typically around a few MHz.
- the effective mass  $m_{eff}$  of the mechanical system is a measure of how well the optical cavity and the mechanical mode spatially overlap. It can be minimized,

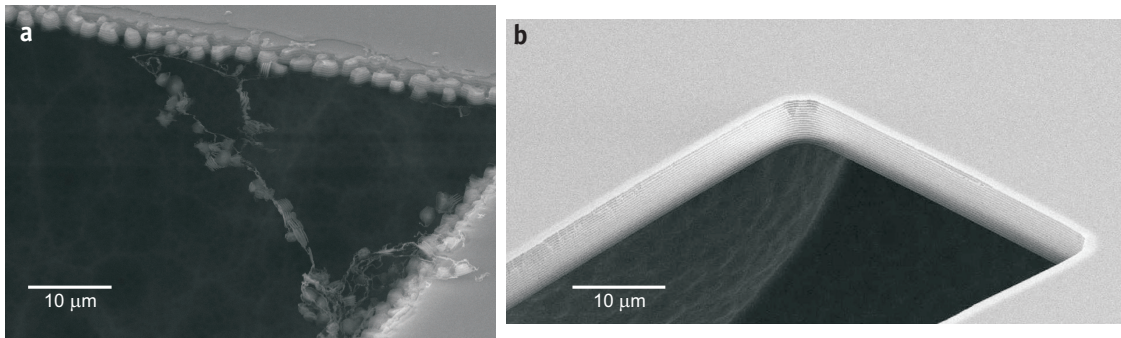


Figure 5.1: Image **a** shows a close-up of a scanning electron microscope (SEM) image of a micro-resonator made of  $\text{TiO}_2/\text{SiO}_2$ . The beam-forming was done using laser ablation in which the material is partially molten, which resulted in very rough, non-uniformly cut edges. In comparison, image **b** is a mechanical oscillator made of  $\text{Ta}_2\text{O}_5/\text{SiO}_2$ , which was processed using a reactive ion etch.

and hence the optomechanical coupling maximized, by optimizing the waist size of the optical mode in the cavity and by aligning the maximum deflection of the mechanical mode to the cavity axis. The minimum achievable effective mass is approx. 74% of the total mass of the mechanical system, for the fundamental mode of a doubly clamped resonator (see for example section 4.10, [128] or any other standard literature on elasticity theory). Hence, it is important to reduce the mass of the mechanical oscillator to the minimum that is compatible with the desired frequency and cavity finesse.

The first proof-of-principle experiment of radiation-pressure cavity cooling of a micromechanical oscillator was performed in Vienna [38] and featured a mechanical oscillator with a frequency  $f_m = 278.3$  kHz, a mechanical quality factor  $Q$  of  $\sim 10,000$ , an effective mass of 400 ng, and a reflectivity  $R$  of 99.6%. It became clear that the utilized mechanical resonator had to be significantly improved in reflectivity for more refined experiments. It was suspected that the net-cooling effect in this work was only about half due to actual radiation-pressure interaction, while the remaining cooling could be attributed to bolometric (photothermal) effects, similar to [129]. The mechanical system was made of a DBR of alternating layers of  $\text{TiO}_2$  and  $\text{SiO}_2$  [114]. Further attempts to improve the mechanical system were not successful and different materials systems such as  $\text{Ta}_2\text{O}_5/\text{SiO}_2$  had to be investigated. The various approaches to high reflectivity and high mechanical quality resonators will be discussed in the following sections.

## 5.1 $\text{Ta}_2\text{O}_5/\text{SiO}_2$ Distributed Bragg reflector resonators

In the spirit of the early approaches we fabricated devices that were made entirely of DBR material, combining the optical and mechanical system into one device. For



mechanical material	clamping type	dimensions	$\omega_m/2\pi$	FEM $\omega_m/2\pi$	$Q$ @ RT	$Q$ @ 5 K	$f_m \cdot Q$	$m_{eff}$
TiO <sub>2</sub> /SiO <sub>2</sub>	doubly	$520 \times 120 \times 2.4 \mu\text{m}^3$	278 kHz	-	10,000	-	$2.8 \times 10^9$	400 ng
TaO <sub>5</sub> /SiO <sub>2</sub>	singly	$50 \times 50 \times 5.98 \mu\text{m}^3$	557 kHz	663 kHz	1,400	1,400	$7.8 \times 10^8$	40 ng
Si <sub>3</sub> N <sub>4</sub>	doubly	$80 \times 50 \times 1.2 \mu\text{m}^3$	359 kHz	422 kHz	-	63,000	$2.3 \times 10^{10}$	-
Si <sub>3</sub> N <sub>4</sub>	doubly	$100 \times 50 \times 1.2 \mu\text{m}^3$	297 kHz	326 kHz	-	82,000	$2.4 \times 10^{10}$	-
Si <sub>3</sub> N <sub>4</sub>	doubly	$120 \times 50 \times 1.2 \mu\text{m}^3$	256 kHz	259 kHz	-	128,000	$3.3 \times 10^{10}$	-
Si <sub>3</sub> N <sub>4</sub>	doubly	$140 \times 50 \times 1.2 \mu\text{m}^3$	229 kHz	210 kHz	-	120,000	$2.8 \times 10^{10}$	-
Si <sub>3</sub> N <sub>4</sub>	doubly	$200 \times 50 \times 1.2 \mu\text{m}^3$	180 kHz	125 kHz	-	153,000	$2.8 \times 10^{10}$	-
Si <sub>3</sub> N <sub>4</sub>	doubly	$150 \times 50 \times 1 \mu\text{m}^3$	945 kHz	950 kHz	6,700	30,000	$2.8 \times 10^{10}$	50 ng
Si	free-free	$150 \times 75 \times 4.5 \mu\text{m}^3$	2.58 MHz	2.68 MHz	-	12,500	$3.2 \times 10^{10}$	-
Si	free-free	$100 \times 50 \times 4.5 \mu\text{m}^3$	6.04 MHz	5.82 MHz	-	48,000	$2.9 \times 10^{11}$	-
Al <sub>x</sub> Ga <sub>1-x</sub> As	doubly	$150 \times 50 \times 5.5 \mu\text{m}^3$	700 kHz	-	2,200	12,000	$8.4 \times 10^9$	-
Al <sub>x</sub> Ga <sub>1-x</sub> As	free-free	$130 \times 40 \times 6.8 \mu\text{m}^3$	2.44 MHz	2.32 MHz	5,000	94,000	$2.3 \times 10^{11}$	-
Al <sub>x</sub> Ga <sub>1-x</sub> As	free-free	$100 \times 50 \times 6.8 \mu\text{m}^3$	3.84 MHz	3.92 MHz	7,000	86,000	$3.3 \times 10^{11}$	-

Table 5.1: List of different mechanical resonators and their mechanical properties. The values in column “FEM  $\omega_m/2\pi$ ” are the mechanical frequencies obtained from finite element simulation. It is interesting to note, that all Si<sub>3</sub>N<sub>4</sub> resonators exhibit almost the same  $f_m \cdot Q$  product, despite very different frequencies. The displayed effective masses are measured values, which were only determined for those used in an actual experiment.

our laser wavelength of 1064 nm the natural choice was to use  $\text{Ta}_2\text{O}_5$  and  $\text{SiO}_2$  as high- and low-index materials for the mirror, as those are widely used in high-finesse cavity applications such as gravitational wave antennae (such as LIGO, VIRGO and GEO) or cavity QED and show reflectivities in excess of 99.999% and absorptions coefficients below  $10^{-6}$  [130, 131]. For the fabrication we used standard silicon wafers that were coated with the DBR by Advanced Thin Films (ATFilms), growing 40 alternating layers of  $\text{Ta}_2\text{O}_5$  and  $\text{SiO}_2$  on the wafer by ion beam sputtering. The design reflectivity was  $> 99.99\%$ , with an overall thickness of the DBR of  $5.98 \mu\text{m}$ . The successive fabrication itself was done by Jared Hertzberg, back then a graduate student of Keith Schwab at Maryland, MD, based on a recipe developed by him, Sylvain Gigan and Hannes R. Böhm. In contrast to the laser ablated samples from references [38, 114], they used a reactive ion etch to form the resonators and underetched them in a  $\text{XeF}_2$  atmosphere (see section 5.2 for details). The process itself overcame a lot of the drawbacks of the laser ablation, namely the rough edges and the relatively large device size (for a comparison see figure 5.1). The devices, a variety of singly- and doubly-clamped beams, had a range of mechanical frequencies  $f_m$  between a few tens of a kHz up to a few hundred kHz. We measured the reflectivity by building a Fabry-Pérot cavity, where the mechanical resonator was one of the end mirrors (see sections 3.3 and 4.2.1 for more details) and the optical finesse gave us a measure of the losses inside the cavity. For several input mirrors with different, yet known reflectivities, we determined the finesse and could not find any degradation in the micromirror reflectivity due to processing with respect to the design reflectivity. We measured the mechanical properties of the individual devices by using the fiber interferometer (see section 4.1) and for consistency also confirmed the numbers in the actual experiment with the Fabry-Pérot cavity. The frequencies of the resonators were close to the values we expected from simple beam theory [117]. However, the mechanical quality factors did not exceed 2,000 for all the devices, and did not change (or got even worse) upon cooling to a few Kelvin. At first it was unclear what caused the uniform low-Q values and we tested several possible explanations including (micro-) cracking or an excessive undercut of the structures. After ruling them out, we found that our data is consistent with the effect being due to thermal noise in the coating, which is a well studied loss mechanism in gravitational wave antennae. More precisely, internal friction in the tantala layer causes mechanical losses, which limits the mechanical quality to a few thousand [132, 133]. We however did not perform additional measurements to confirm this hypothesis. The low  $Q$  posed a serious limit to our cooling efforts. Nevertheless, we used the devices for radiation-pressure cooling to perform a proof-of-principle experiment without any bolometric effects but rather pure radiation-pressure coupling at cryogenic temperatures (see section 6.1).

## 5.2 $\text{Si}_3\text{N}_4 + \text{Ta}_2\text{O}_5/\text{SiO}_2$ resonators

Given the high reflectivity we achieved with the micro-fabricated  $\text{Ta}_2\text{O}_5/\text{SiO}_2$  resonators that overcame all the possible absorption problems from the early  $\text{TiO}_2/\text{SiO}_2$  samples, we decided to stick to the same mirror material but decouple the mechanical from the optical system. In the first new devices we experimented with, the

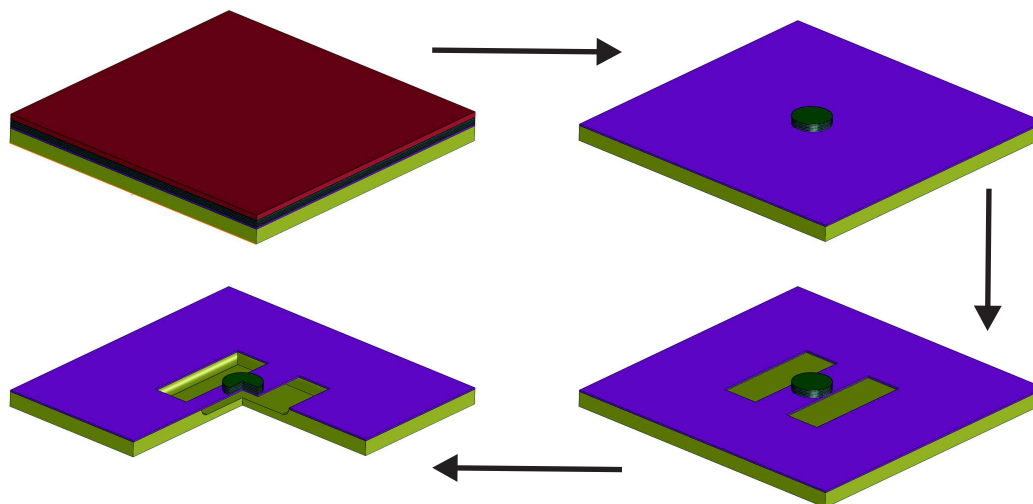


Figure 5.2: Microfabrication of  $\text{Si}_3\text{N}_4 + \text{Ta}_2\text{O}_5/\text{SiO}_2$  resonators. For the fabrication process we start with a Si wafer (yellow), with a layer of  $\text{Si}_3\text{N}_4$  which is coated with a dielectric mirror made of  $\text{Ta}_2\text{O}_5/\text{SiO}_2$ . The red layer symbolizes the photoresist which is omitted in the subsequent images. In a first step (top right) the mirror is etched and only small pads (with a typical diameter of  $50 \mu\text{m}$ ) are left. In the next fabrication step the mechanical resonator is formed by plasma etching through the  $\text{Si}_3\text{N}_4$ . Finally, the mechanical resonator is released in a  $\text{XeF}_2$  atmosphere. The lower left picture shows the final free-standing resonator, where a quarter of the chip is removed for clarity. A detailed description of the etching process can be found in table 5.2 and pictures of actual resonators in figures 5.3 and 4.1.

mechanical part was made of a  $1 \mu\text{m}$  thick layer of  $\text{SiO}_2$  (which we had already coated previously with mirror). However, those were mostly intended to work out a fabrication process and exhibited poor mechanical quality. The actual material we wanted to work with was silicon nitride ( $\text{SiN}$ ), as  $\text{SiN}$ , despite being an amorphous material, has shown excellent mechanical properties in previous experiments [134–136]. Also its similarity to  $\text{SiO}_2$  in terms of fabrication made it a perfect choice as we had wafers with silica and a mirror coating ready for testing. For the processing we first grew  $2 \mu\text{m}$  of low stress ( $\sim 200 \text{ MPa}$ )  $\text{Si}_3\text{N}_4$  in a furnace at  $700 \text{ }^\circ\text{C}$  for 11 hours. After the deposition we measured the surface roughness, which was around  $7 \text{ \AA}$  rms. We also attempted to grow even thicker silicon nitride but at a thickness larger than  $2.2 \mu\text{m}$  the nitride showed stress induced cracking, which would have significantly degraded any optical coating. The wafers were sent to ATFilms and a 36 layers  $\text{Ta}_2\text{O}_5/\text{SiO}_2$  mirror was deposited, with a design reflectivity of 99.991%. The actual device fabrication (as well as the growing of the nitride film) was done in collaboration with Keith Schwab and Jared Hertzberg at Cornell University, NY. The process is sketched in figure 5.2 and described in detail in table 5.2.

As expected from the first experiments with tantala/silica mirrors the reflectivity

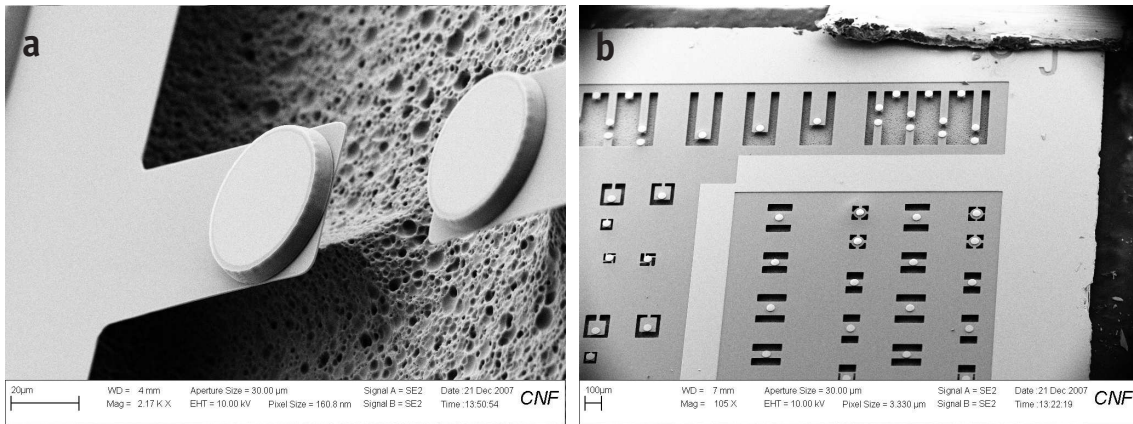


Figure 5.3: **a** Scanning electron microscope (SEM) image of a pair of cantilevers made of  $\text{Si}_3\text{N}_4$  with a distributed Bragg reflector pad (DBR). The silicon etched in the  $\text{XeF}_2$  atmosphere is very rough, making it easy to distinguish the undercut areas. **b** Part of a chip with mechanical resonators of different shapes and sizes.

was not degraded in the processing. The mechanical properties were again measured in the fiber interferometer and most of the devices showed a much lower frequency than expected from our simulations. The main reason for that was a thinning of the SiN in the mirror etch, as well as in the freeing of the beams in the  $\text{XeF}_2$  atmosphere. The selectivity of Si to  $\text{Si}_3\text{N}_4$  in  $\text{XeF}_2$  is approximately 100:1, where the exact selectivity can vary with the silicon content in the SiN. However, a few of the mechanical resonators had frequencies close to one MHz, which was the regime we were aiming for. A list of  $Q$  values and frequencies can be found in table 5.1. The gain in mechanical quality with respect to the previous devices was small at room temperature but a significant improvement could be observed at low temperature. The devices are most likely limited by thermo-elastic damping at room temperature (see section 5.4 for details). It is interesting to note that the product between the mechanical frequency and the mechanical quality factor  $f_m \cdot Q$  seems to be constant at low temperatures at around  $2.7 \times 10^{10}$  throughout the measured set of devices. It is likely that the dominant loss mechanism here is an inherent material property. One possible explanation would be losses either in the SiN itself or the pads made of dielectric multilayer coatings as these materials systems exhibit particularly large losses as a consequence of their intrinsic amorphous structure [133, 137, 138].

One of the resonators was used in the experiments described in section 6.2 and chapters 7 & 8 and such SiN oscillators will most likely be used in a number of future experiments due to their relatively easy fabrication process and their high  $f_m \cdot Q$  product.

---

---

 **$\text{Si}_3\text{N}_4 + \text{Ta}_2\text{O}_5/\text{SiO}_2$**  **$\text{Si} + \text{Ta}_2\text{O}_5/\text{SiO}_2$** 

---

---

The wafers are first cleaned in a hot resist stripping bath and then dried. Shipley SPR220-7 resist is spun on the wafers at 3,000 RPM for 30 s, with a ramp of 1,000 RPM/s, which results in a 8 - 9 micron thick resist layer. The wafers are then baked for 90 s at 115 °C. Exposure of the resist with the desired mirror pattern is done in an ABM contact aligner for 18 s and subsequently exposed with an edge-bead removal mask for 50 s. Before post-exposure baking the resist for 90 s at 115 °C the wafers have to sit for around 2.5 hours. They are finally developed by hand in MIF 300 for approximately 120 s and can also be dry spinned. In order to avoid cracking and wrinkling of the resist during the etch the wafers are hard baked in a convection oven at 90 °C for several hours (>3).

Etching of the mirror is done in an Oxford PlasmaLab 100 RIE system. The process we use is a  $\text{CHF}_3/\text{O}_2$  etch, where we use 52 cm<sup>3</sup> of  $\text{CHF}_3$  and 2 cm<sup>3</sup> of  $\text{O}_2$ . The other parameters of the etch are ICP: 2500 W, RF power: 25 W, pressure: 5 mTorr, He backing: 10 Torr and a table temperature of 10 °C. The etch is done in short steps, typically interrupted by an oxygen clean of the plasma chamber with a dummy wafer of 5 - 10 mins. Normally we start with two 15 min etches and subsequently use shorter steps of a few minutes and check the etch depth and the remaining resist in a profilometer until the mirror is completely removed. This process can take up to 50 minutes of total etch time. The remaining resist is then stripped in a hot resist stripping bath.

The back-side of the SOI wafers needs to have a thick silicon oxide layer that can be later used as a mask for the back-side etch. If it is not already there, it should be grown latest at this stage, possibly already before doing the first etch. The front-side of the wafer is covered with a protective layer of resist and a  $\sim 1.6 \mu\text{m}$  layer of  $\text{SiO}_2$  is grown in the IPE 1000 plasma enhanced chemical vapor deposition (PECVD) system at 100 °C in around 40 minutes. After the deposition the resist is stripped again.

---

For the device pattern, a new layer of resist is spun on top of the etched mirror pads, following the same steps as above. It is important to pre-bake the wafer, let it cool down, then apply P20 primer and wait for 10 s before covering the wafer in resist for the silicon devices as otherwise the resist does not adhere properly to the substrate. If after developing there is still resist left in the openings, an oxygen plasma clean can be used to remove the resist, which typically takes a few minutes in an Oxford PlasmaLab 80+ RIE System. It is important to check by how much the wanted resist is thinned during this etch in a profilometer, especially on top of the mirror pads.

---

The devices are etched in an Oxford PlasmaLab 80+ RIE System using a  $\text{CHF}_3/\text{O}_2$  nitride etch (50 cm<sup>3</sup>  $\text{CHF}_3$ , 5 cm<sup>3</sup>  $\text{O}_2$ , 150 W RF power, and 55 mTorr pressure). Typical etch times are around 30 minutes total – it is good to over-etch the silicon nitride in order to make sure that it is completely removed throughout the wafer. After etching, the resist is removed in a hot resist stripping bath.

The silicon device layer is etched in a Bosch etcher, for example the Unaxis 770, where it only takes a few cycles (12 with the 0TRENCH program for a 4  $\mu\text{m}$  device layer) to etch through the silicon. It is important not to strip the resist as this is used as protection in the final release of the devices.

---

A protective layer of resist is spun on the wafer and it is diced into 5.5 × 5.5 mm square pieces in a K&S 7100 dicing saw using the S1235 blade. There is very few debris generated in this process.

Now resist is spun the usual way on the back-side of the wafer. This can be done using a special non-vacuum chuck, however with the risk of the wafer falling off and shattering into pieces. The back-side alignment is done in the EV620 contact aligner and exposed for 15 s. The development can also be done in the HMP 900.

---

After stripping the resist (e.g. in acetone), the beams are freed in XeF<sub>2</sub>. The etch recipe is 4 Torr XeF<sub>2</sub> for 60 s and a 0 Torr pumpout. Normally around 7 such cycles are needed to completely free the beam.

The mask is transferred into the SiO<sub>2</sub> by etching it for a total time of approximately 1 hour in an Oxford PlasmaLab 80+ RIE System using a CHF<sub>3</sub>/O<sub>2</sub> oxide etch (50 cm<sup>3</sup> CHF<sub>3</sub>, 2 cm<sup>3</sup> O<sub>2</sub>, 200 W RF power, and 50 mTorr pressure). The back-side etch is performed in a Bosch etcher such as the Unaxis 770. There the program is called 0TRENCH and etches at a rate of ~500 nm per cycle, where one cycle takes around 15 s. That allows to perform the full etch in approximately 3.5 hours, where the progress can be measured using a standard light microscope. After the etch the wafer is diced into 5.5 × 5.5 mm square pieces.

Final release of the device from the buried oxide is done in 38% HF. While BOE takes so long that the mirror is slowly attacked, the HF only requires an etch of 2 minutes for a 500 nm BOX layer and leaves the mirror completely intact. When etch times approach 3 mins however, the resist starts to peel. The remaining resist can be removed with acetone or 1165.

Some general remarks on the processing:

- Never bake resist at >115 °C, not even for a few seconds, as it is very difficult to get off again. However, if this ever happens, hot piranha slowly removes the resist and does not attack the mirror at all.
- The back-side mask needs large openings around the alignment marks and the marks should be in the same row.
- The mask must be mirrored if used as a back-side mask.

Table 5.2: Fabrication recipes for silicon nitride and silicon resonators with TaO<sub>5</sub>/SiO<sub>2</sub> mirror pads. The recipes were worked out together with Jared Hertzberg and Tchefor Ndikum at the Cornell NanoScale Science & Technology Facility (CNF), with significant help from Meredith Metzler, Rob Ilic and Mike Skvarla.

### 5.3 Si + Ta<sub>2</sub>O<sub>5</sub>/SiO<sub>2</sub> resonators

In order to reach even higher frequencies than are possible with the SiN + Ta<sub>2</sub>O<sub>5</sub>/SiO<sub>2</sub> resonators due to the limited thickness of SiN we used silicon as the mechanical part of the hybrid approach. We had SOI (silicon on insulator) wafers coated with the same mirror as the SiN resonators, where the device layer of the SOI varied in thickness between 2 and 7  $\mu\text{m}$ . The buried oxide layer (BOX) was between 0.5 and 1  $\mu\text{m}$  thick. The processing was slightly more elaborate than for the SiN, as the beams could not be freed in a XeF<sub>2</sub> atmosphere and therefore we had to perform a back-side etch, which was done using a deep reactive ion etch (RIE), specifically the Bosch process – details on the processing can be found in table 5.2. In a first processing run in December 2008 we used a 4.5  $\mu\text{m}$  device layer SOI wafer and fabricated only free-free resonators. The idea behind this design is to minimize clamping losses by not attaching the mechanical resonators on their short end at all (hence the name “free-free”) but only have four very thin support beams that hold the resonators in their zero-displacement points (for the fundamental mode). This way the clamping losses in such a device should in principle be negligible – for a detailed discussion see [104, 139, 140]. The fundamental free-free mode had frequencies between 2 and 6 MHz, depending on the geometry of the beam, and the best mechanical quality factors we observed at low temperatures were around 40,000 for the lower end of the frequency spectrum. A summary of a selection of resonators can be found in table 5.1.

In a second fabrication run in July 2010 we experimented with normal doubly-clamped designs, as well as membranes with mirror pads in the center. We processed two wafers – one with a 2 and the other with a 4  $\mu\text{m}$  device layer. While the thicker one was destroyed in the processing (during resist spinning on a non-vacuum chuck), the 2  $\mu\text{m}$  wafer was completed, however had a very small yield of working resonators. The reason for that was that the back-side etch was done in a new RIE deep-etcher, in which the back-side mask did not hold up very well and the edge of the wafer slowly disintegrated, not allowing us to etch through the whole wafer everywhere. See table 5.1 for a list of their mechanical properties. A very likely reason for the limit in mechanical quality is the finite contribution of the Ta<sub>2</sub>O<sub>5</sub>/SiO<sub>2</sub> mirror pad to the mechanical motion, which probably introduces dissipation and hence limits the  $Q$ .

### 5.4 Al<sub>x</sub>Ga<sub>1-x</sub>As resonators

Another approach we took was to use a completely different materials system: III-V semiconductors, i.e. semiconductors made of elements of the groups III and V of the periodic table like Al, Ga and As. In collaboration with Prof. Arthur Gossard’s group at UCSB we manufactured GaAs wafers with epitaxially grown DBRs made of 32 alternating layers Al<sub>0.12</sub>Ga<sub>0.88</sub>As and Al<sub>0.92</sub>Ga<sub>0.08</sub>As, with a measured surface roughness of 1.5  $\text{\AA}$  and with a reflectivity of  $\gtrsim 99.98\%$  at 1064 nm at low temperatures. Such a materials system is ideally suited for micromechanical structures as it is single-crystalline, which removes the problem of intrinsic losses such as the dangling bonds in Ta<sub>2</sub>O<sub>5</sub> completely. With the AlGaAs resonators, thermo elastic damping (TED) is found to be the limiting loss mechanism at room temperature [141–143].



This mechanism is a coupled thermo-mechanical process involving the scattering of thermal phonons with the acoustic phonons responsible for the vibrations of the resonator. It is important to note that the TED limited quality factor has an inverse temperature dependence and thus TED can be minimized through cryogenic operation of the optomechanical system. The mechanical resonators we fabricated indeed showed a small improvement in  $Q$  upon cooling, however much lower than we had anticipated. The most likely reason for that are additional loss mechanisms, such as processed-induced damages as well as clamping losses into the supporting structures. The optical absorption in the first device set [144] was less than 10 ppm (possibly only a few ppm), while newer samples [104] showed absorptions of up to 70 ppm. This is probably due to different growing techniques – molecular beam epitaxy (MBE) vs. metalorganic vapour phase epitaxy (MOVPE, also known as MOCVD). The source of the excess absorption in the MOVPE-grown mirrors is currently unknown, but probably originates from impurities incorporated in the structure during the growth process, with the most likely constituents being carbon and oxygen. In MOVPE, carbon is incorporated as a decomposition product of the metalorganic reactants. MBE typically exhibit lower unintentional dopant concentrations as the process operates at ultra-high vacuum (total pressure  $< 10^{-10}$  mbar) and with elemental sources [145].

The clamping losses have been further reduced in new designs like the free-free devices [104, 139, 140] and tests of different growing techniques are underway, as well as the use of different compounds [146].

## Monocrystalline $\text{Al}_x\text{Ga}_{1-x}\text{As}$ heterostructures for high-reflectivity high- $Q$ micromechanical resonators in the megahertz regime

Garrett D. Cole,<sup>1,a)</sup> Simon Gröblacher,<sup>2</sup> Katharina Gugler,<sup>2</sup> Sylvain Gigan,<sup>2,b)</sup> and Markus Aspelmeyer<sup>2</sup>

<sup>1</sup>Center for Micro- and Nanotechnologies, Lawrence Livermore National Laboratory, 7000 East Avenue, Livermore, California 94550, USA

<sup>2</sup>Institute for Quantum Optics and Quantum Information (IQOQI), Austrian Academy of Sciences, Boltzmannngasse 3, A-1090 Vienna, Austria

(Received 4 February 2008; accepted 6 June 2008; published online 1 July 2008)

We present high-performance megahertz micromechanical oscillators based on freestanding epitaxial  $\text{Al}_x\text{Ga}_{1-x}\text{As}$  distributed Bragg reflectors. Compared with dielectric reflectors, the low mechanical loss of the monocrystalline heterostructure gives rise to significant improvements in the achievable mechanical quality factor  $Q$  while simultaneously exhibiting near unity reflectivity. Experimental characterization yields an optical reflectivity exceeding 99.98% and mechanical quality factors up to 20 000 at 4 K. This materials system is not only an interesting candidate for optical coatings with ultralow thermal noise, but also provides a promising path toward quantum optical control of massive micromechanical mirrors. © 2008 American Institute of Physics. [DOI: 10.1063/1.2952512]

High-quality Bragg mirrors with small mechanical dissipation have generated recent interest due to their versatile use in both fundamental and applied sciences. Specifically, mechanical dissipation in optical coatings is known to limit the performance of high-finesse cavity applications, in particular gravitational wave interferometry<sup>1</sup> and laser frequency stabilization for optical clocks<sup>2</sup> because of residual phase noise, also referred to as coating thermal noise.<sup>3</sup> On the other hand, microstructures of high mechanical and optical quality have become a leading candidate to achieve quantum optical control of mechanical systems. One specific goal in this emerging field of quantum optomechanics is to combine the concepts of cavity quantum optics with radiation-pressure coupling to generate and detect quantum states of massive mechanical systems such as the quantum ground state<sup>4–6</sup> or even entangled quantum states.<sup>7–9</sup> The recent demonstrations of cavity-assisted laser cooling of mechanical modes<sup>10–13</sup> can be considered an important milestone in this direction.

Most of these schemes rely crucially on mechanical structures that combine both high optical reflectivity  $R$  and low mechanical dissipation, i.e., a high quality factor  $Q$  of the mechanical mode of interest. In addition, entering the quantum regime will require operation in the so-called sideband-limited regime,<sup>4–6</sup> in which the cavity bandwidth of the optomechanical device is much smaller than the mechanical resonance frequency. While toroidal microcavities have recently shown such performance,<sup>14</sup> high-quality distributed Bragg reflectors (DBRs) in combination with Fabry–Pérot cavities have not yet reached this regime.<sup>11,12,15,16</sup> For example, whereas DBRs based on  $\text{SiO}_2/\text{Ta}_2\text{O}_5$  can achieve  $R$  values in excess of 99.99%,<sup>17</sup> the mechanical quality factor of freestanding DBRs is limited to below 3000 due to internal losses in the  $\text{Ta}_2\text{O}_5$  layers.<sup>18</sup> It is interesting to note that

the low  $Q$ -value obtained with these devices is consistent with the coating loss angles observed in the LIGO studies of gravitational wave detector coatings of the same material.<sup>1,3</sup> On the other hand, the use of  $\text{SiO}_2/\text{TiO}_2$ -based DBRs has led to the demonstration of mechanical quality factors approaching 10 000 at room temperature;<sup>11</sup> there, however, optical absorption in  $\text{TiO}_2$  at 1064 nm both limits the reflectivity and results in residual photothermal effects.

The concept outlined here seeks to improve upon these previous works by fabricating the oscillator directly from a *single-crystal* Bragg reflector. In particular, the use of compound semiconductor materials such as GaAs and related alloys allows for the generation of arbitrary stacks of high-index-contrast materials that maintain nearly perfect crystalline order, resulting in significant improvements in the achievable mechanical quality factor. Given the alleviation of the dangling bonds typically found in amorphous dielectric materials such as  $\text{Ta}_2\text{O}_5$ ,<sup>3</sup> the use of a single-crystal mirror stack should allow for a significant reduction in the dissipation, while maintaining excellent reflectivity. Neglecting support loss or modal coupling, mechanical dissipation in a single-crystal is ultimately limited by intrinsic processes such as thermoelastic damping, as well as phonon-phonon and phonon-electron interactions. Our devices do not approach this fundamental value but are most likely limited by extrinsic effects including process-induced damage (e.g., ion bombardment and surface roughness created during microfabrication) as well as acoustic loss to the surrounding support structure. For example, if thermoelastic damping were the lower limit to the mechanical dissipation of the device, we would expect a room temperature  $Q$  value of approximately  $4 \times 10^8$  for a GaAs resonator.<sup>19</sup>

Although a somewhat uncommon materials system for the development of micromechanical structures, GaAs and its alloys exhibit a number of advantageous properties.<sup>20</sup> The direct bandgap optical transition in GaAs allows for the integration of optoelectronic functionality with micromechanical elements.<sup>21</sup> Furthermore, the noncentrosymmetric nature of the zinc-blende crystal structure gives rise to an appre-

<sup>a)</sup>Electronic mail: cole35@llnl.gov.

<sup>b)</sup>Present address: Laboratoire Photon et Matière, Ecole Supérieure de Physique et de Chimie Industrielle, CNRS-UPR A0005, 10 rue Vauquelin, 75005 Paris, France.

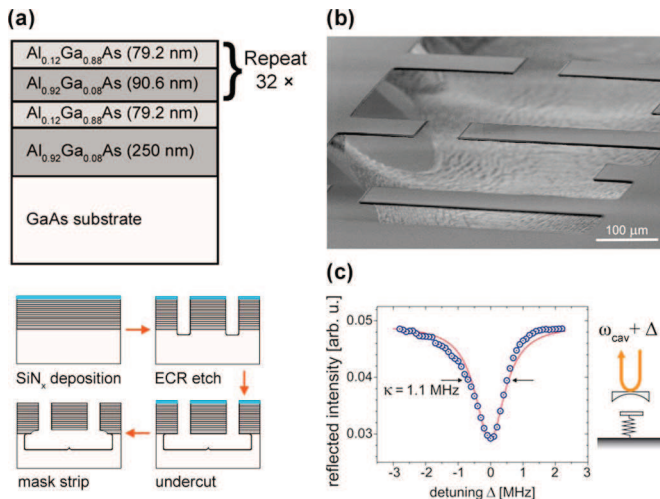


FIG. 1. (Color online) (a) Sketch of the initial layers constituting the Bragg mirror and illustration of the etch process used to fabricate freestanding structures. (b) Micrograph of a group of cantilevers. The beams shown have a width of  $50\ \mu\text{m}$  and vary in length between  $50$  and  $200\ \mu\text{m}$ . (c) The finesse of the cavity is obtained by measuring the reflected intensity as a function of laser detuning  $\Delta$ . The observed linewidth  $\kappa$  of  $1.1\ \text{MHz}$  corresponds to an optical finesse of  $5500$ .

cial piezoelectric coefficient, allowing for efficient actuation or transduction in these materials. For our purposes, we take advantage of the ability to produce high-quality single-crystal Bragg stacks through the use of lattice-matched ternary alloys based on  $\text{Al}_x\text{Ga}_{1-x}\text{As}$ . These materials may be epitaxially grown as monocrystalline heterostructures via deposition methods such as molecular beam epitaxy (MBE) and metal-organic chemical vapor deposition. The ability to control the lattice matching condition through alloying gives one the ability to “strain engineer” films in order to create built-in tensile or compressive stresses. In addition, variations in the aluminum composition allow for a wide range of selective etch chemistries over GaAs. Generally, these films display extremely high etch selectivities—in fact HF etching of the lattice-matched binary material AlAs versus GaAs exhibits a selectivity approaching  $10^7:1$ .<sup>22</sup>  $\text{Al}_x\text{Ga}_{1-x}\text{As}$  heterostructures may thus be processed using standard micromachining techniques to yield atomically flat optical surfaces that are ideal for optomechanical structures, as previously demonstrated in micromechanically tunable surface-normal photonic devices.<sup>23–25</sup>

As shown in Fig. 1, the epitaxial materials structure for the monocrystalline oscillators consists of  $32.5$  periods of alternating  $\text{Al}_{0.12}\text{Ga}_{0.88}\text{As}$  (high index) and  $\text{Al}_{0.92}\text{Ga}_{0.08}\text{As}$  (low index), followed by a  $250\text{-nm}$ -thick high-aluminum-content etch-protection layer, grown on a  $3\ \text{in.}$  semi-insulating GaAs substrate via MBE. In this design, the thick high-aluminum-content layer below the Bragg stack is included to protect the bottom of the mirror structure in subsequent processing steps. The peak reflectivity of the DBR is designed to be at  $1078\ \text{nm}$  at room temperature; in this case, the wavelength of maximum reflectivity is redshifted to allow for thermo-optic effects upon cooling. The refractive index of the ternary compounds at cryogenic temperatures is estimated using the modified Afromowitz model developed in Ref. 26. Assuming no absorption and atomically smooth interfaces, the maximum reflectivity (after stripping the protective  $\text{Al}_{0.92}\text{Ga}_{0.08}\text{As}$  layer and with air cladding top and

bottom) is calculated to be  $99.991\%$  at  $1064\ \text{nm}$  for temperatures below  $20\ \text{K}$  and  $99.976\%$  at  $300\ \text{K}$ .

Fabrication of the resonators begins with the deposition of a  $\text{SiN}_x$  hard mask via plasma enhanced chemical vapor deposition. Next, the device geometry is patterned lithographically using a standard positive photoresist. This pattern is then transferred into the  $\text{SiN}_x$  via plasma etching with  $\text{CF}_4/\text{O}_2$ . Definition of the resonator geometry in the  $\text{Al}_x\text{Ga}_{1-x}\text{As}$  epilayers relies on electron cyclotron resonance etching through the mirror stack using  $\text{Cl}_2/\text{Ar}$ , with masking provided by the resist/ $\text{SiN}_x$ . To undercut the cantilevers, a buffered citric acid solution is utilized.<sup>27</sup> This selective wet etch allows for the removal of the binary GaAs, in this case the substrate, over the low-aluminum content ternary  $\text{Al}_{0.12}\text{Ga}_{0.88}\text{As}$  layers with excellent selectivity.<sup>25</sup> During the undercutting process, the  $\text{SiN}_x$  coating protects the top of the mirror surface, while the thick  $\text{Al}_{0.92}\text{Ga}_{0.08}\text{As}$  layer protects the bottom, ensuring minimal surface roughness and maximum reflectivity. To complete the fabrication sequence, the protective  $\text{SiN}_x$  and  $\text{Al}_{0.92}\text{Ga}_{0.08}\text{As}$  layers are removed in a dilute HF solution and the beams are allowed to air dry after soaking in methanol. The resonators characterized here consist of both fixed-fixed (doubly clamped) and cantilever (singly clamped) beams with a thickness of  $5.5\ \mu\text{m}$ , a nominal width of  $50$  or  $100\ \mu\text{m}$ , and nominal lengths between  $50$  and  $400\ \mu\text{m}$ . A scanning electron micrograph highlighting a completed set of cantilevers is shown in Fig. 1.

We have characterized the mechanical properties of the resonators optically via interferometric measurements of their displacement. Room-temperature measurements were performed in a standard fiber interferometer<sup>28</sup> while temperature-dependent measurements were carried out using a cryogenic Fabry–Pérot cavity, in which the micromirror formed one of the cavity’s end mirrors (this setup is described in detail in Refs. 15 and 18). In the case of the fiber interferometer, the displacement power spectrum is directly obtained from the interferometer output, while in the case of the cryogenic Fabry–Pérot cavity, the noise spectrum of the Pound–Drever–Hall error signal of the cavity is used.<sup>18</sup> At room temperature we obtain mechanical quality factors of up to  $7000$  for singly clamped and  $5000$  for doubly clamped beams. We observe fundamental resonance frequencies of the beams up to  $1\ \text{MHz}$  in accordance with theoretical estimates based on standard beam theory (see for example, Ref. 29). In particular, we identified a doubly clamped resonator ( $150 \times 50\ \mu\text{m}$ ) with a fundamental frequency of  $730\ \text{kHz}$  and higher order resonance at  $1.99\ \text{MHz}$ . At low temperatures, i.e., operating inside a  $4\ \text{K}$  helium cryostat, we measure a quality factor of the high frequency mode of  $20\ 000$ , compared to a  $Q$  value of  $5000$  at room temperature. We observe a similar increase of  $Q$  for the fundamental mode of the micromirror, namely from  $2200$  at room temperature to  $12\ 000$  at  $4\ \text{K}$  (see Fig. 2). As expected, the frequency of the resonator modes does not change significantly upon cooling. Cryogenic  $Q$  values of a similar range ( $10\ 000 < Q < 30\ 000$ ) have previously been reported for micromechanical resonators fabricated in this materials system;<sup>30,31</sup> however, these examples exhibited insufficient reflectivity for our application. Although our devices are not optimized for force detection, we have estimated the thermal force noise of the resonators, which provides an upper bound for the achievable resolution.<sup>32</sup> For the vibration mode near  $700\ \text{kHz}$  ( $2\ \text{MHz}$ ), we calculate an approximate force sensitivity of

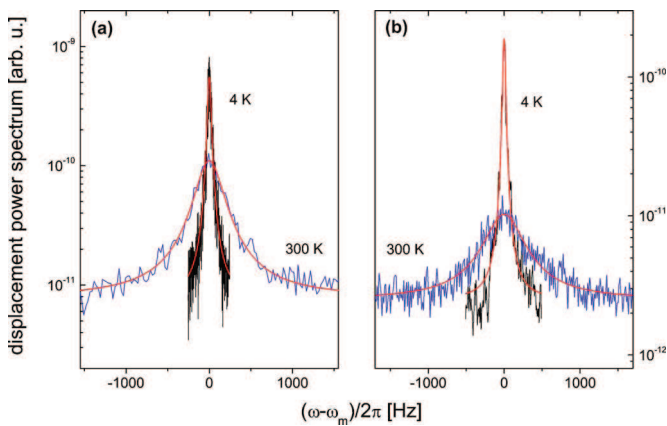


FIG. 2. (Color online) (a) Fundamental mechanical mode of a 150  $\mu\text{m}$  long doubly clamped resonator at 300 and 4 K. Central frequencies are 731 and 697 kHz, respectively. The corresponding  $Q$  factors are 2200 and 12 000. (b) Second order mode of the same resonator showing  $Q$ s of 5000 and 20 000 for frequencies of 1.997 and 1.971 MHz at 300 and 4 K, respectively.

220  $\text{fN}/\sqrt{\text{Hz}}$  (24  $\text{fN}/\sqrt{\text{Hz}}$ ) at 300 K, decreasing to roughly 20  $\text{fN}/\sqrt{\text{Hz}}$  (3  $\text{fN}/\sqrt{\text{Hz}}$ ) at cryogenic temperatures. These values are on par with previous examples of GaAs-based nanomechanical resonators as presented in Ref. 33.

In order to obtain the micromirror reflectivity, we measure the finesse of the Fabry–Pérot cavity (see above), which provides a measure of the overall intensity losses in the cavity. Knowing the independently determined reflectivity of the macroscopic input mirror ( $R_{\text{in}}=99.91\%$ ) one hence obtains a lower limit on the reflectivity  $R_{\text{micro}}$  of the micromirror. The observed finesse of greater than 5500 [Fig. 1(c)] yields a reflectivity  $R_{\text{micro}} \geq 99.98\%$ , in good agreement with the expected values from theory. The reflectivity of our  $\text{Al}_x\text{Ga}_{1-x}\text{As}$  Bragg mirrors is comparable to that measured in high-finesse semiconductor microcavities.<sup>34</sup>

We have demonstrated high-performance micromechanical megahertz oscillators based on freestanding monocrystalline  $\text{Al}_x\text{Ga}_{1-x}\text{As}$  DBRs. We observe optical reflectivities exceeding 99.98% combined with mechanical quality factors up to 20 000 at 4 K for mechanical modes as high as 2 MHz. Given the alleviation of mechanical dissipation compared to previous high reflectivity dielectric stacks, this materials system is an interesting candidate for low-noise optical coatings as needed for example for gravitational-wave detection or for high-precision frequency stabilization of lasers as used for optical frequency standards. The reported performance can readily achieve an optical finesse of up to 30 000, assuming a matched input coupler reflectivity of  $R_{\text{micro}}$ , allowing these micromechanical devices to operate in a regime of mechanical-sideband limited performance as is required to achieve ground state cavity-cooling of mechanical systems. As the microfabrication process does not deteriorate the reflectivity of the coating, higher finesse values should be achievable by further improving the initial DBR quality.

This work was performed under the auspices of the U.S. Department of Energy by LLNL under Contract No. DE-AC52-07NA27344. We acknowledge financial support by the FWF (Projects P19539-N20 and L426-N20) and by the Foundational Questions Institute fqxi.org (Grant RFP1-06-

14). We thank A. Jackson of UCSB for the growth of the Bragg mirror. S.G. is a recipient of a DOC-fellowship of the Austrian Academy of Sciences and also acknowledges support from the FWF doctoral program Complex Quantum Systems (W1210).

<sup>1</sup>G. M. Harry, H. Armandula, E. Black, D. R. M. Crooks, G. Cagnoli, J. Hough, P. Murray, S. Reid, S. Rowan, P. Sneddon, M. M. Fejer, R. Route, and S. D. Penn, *Appl. Opt.* **45**, 1569 (2006).

<sup>2</sup>K. Numata, A. Kemery, and J. Camp, *Phys. Rev. Lett.* **93**, 250602 (2004).

<sup>3</sup>G. M. Harry, A. M. Gretarsson, P. R. Saulson, S. E. Kittelberger, S. D. Penn, W. J. Startin, S. Rowan, M. M. Fejer, D. R. M. Crooks, G. Cagnoli, J. Hough, and N. Nakagawa, *Class. Quantum Grav.* **19**, 897 (2002).

<sup>4</sup>I. Wilson-Rae, N. Nooshi, W. Zwerger, and T. J. Kippenberg, *Phys. Rev. Lett.* **99**, 093901 (2007).

<sup>5</sup>F. Marquardt, J. P. Chen, A. A. Clerk, and S. M. Girvin, *Phys. Rev. Lett.* **99**, 093902 (2007).

<sup>6</sup>C. Genes, D. Vitali, P. Tombesi, S. Gigan, and M. Aspelmeyer, *Phys. Rev. A* **77**, 033804 (2007).

<sup>7</sup>S. Bose, K. Jacobs, and P. L. Knight, *Phys. Rev. A* **56**, 4175 (1997).

<sup>8</sup>J. Zhang, K. Peng, and S. L. Braunstein, *Phys. Rev. A* **68**, 013808 (2003).

<sup>9</sup>D. Vitali, S. Gigan, A. Ferreira, H. R. Böhm, P. Tombesi, A. Guerreiro, V. Vedral, A. Zeilinger, and M. Aspelmeyer, *Phys. Rev. Lett.* **98**, 030405 (2007).

<sup>10</sup>C. H. Metzger and K. Karrai, *Nature (London)* **432**, 1002 (2004).

<sup>11</sup>S. Gigan, H. R. Böhm, M. Paternostro, F. Blaser, G. Langer, J. B. Hertzberg, K. C. Schwab, D. Bäuerle, M. Aspelmeyer, and A. Zeilinger, *Nature (London)* **444**, 67 (2006).

<sup>12</sup>O. Arcizet, P. F. Cohadon, T. Briant, M. Pinard, and A. Heidmann, *Nature (London)* **444**, 71 (2006).

<sup>13</sup>T. J. Kippenberg and K. J. Vahala, *Opt. Express* **15**, 17172 (2007).

<sup>14</sup>A. Schliesser, R. Rivière, G. Anetsberger, O. Arcizet, and T. J. Kippenberg, *Nat. Phys.* **4**, 415 (2008).

<sup>15</sup>H. R. Böhm, S. Gigan, G. Langer, J. B. Hertzberg, F. Blaser, D. Bäuerle, K. C. Schwab, A. Zeilinger, and M. Aspelmeyer, *Appl. Phys. Lett.* **89**, 223101 (2006).

<sup>16</sup>D. Kleckner and D. Bouwmeester, *Nature (London)* **444**, 75 (2006).

<sup>17</sup>G. Rempe, R. J. Thompson, H. J. Kimble, and R. Lalezari, *Opt. Lett.* **17**, 363 (1992).

<sup>18</sup>S. Gröblacher, S. Gigan, H. R. Böhm, A. Zeilinger, and M. Aspelmeyer, *Europhys. Lett.* **81**, 54003 (2008).

<sup>19</sup>V. B. Braginsky, V. P. Mitrofanov, and V. I. Panov, *Systems with Small Dissipation* (University of Chicago Press, Chicago, 1985).

<sup>20</sup>K. Hjort, Ph.D. thesis, Uppsala University, Uppsala, Sweden, 1993.

<sup>21</sup>H. Ukita, Y. Uenishi, and H. Tanaka, *Science* **260**, 786 (1993).

<sup>22</sup>E. Yablonovitch, T. Gmitter, J. P. Harbison, and R. Bhat, *Appl. Phys. Lett.* **51**, 2222 (1987).

<sup>23</sup>G. D. Cole, E. S. Bjorlin, C. S. Wang, N. C. MacDonald, and J. E. Bowers, *IEEE Photonics Technol. Lett.* **17**, 2526 (2005).

<sup>24</sup>M. Maute, B. Kögel, G. Böhm, P. Meissner, and M.-C. Amann, *IEEE Photonics Technol. Lett.* **18**, 688 (2006).

<sup>25</sup>M. C. Huang, Y. Zhou, and C. J. Chang-Hasnain, *Nat. Photon.* **1**, 119 (2007).

<sup>26</sup>Y. A. Akulova, Ph.D. thesis, University of California, Santa Barbara, USA, 1998.

<sup>27</sup>T. Kitano, S. Izumi, H. Minami, T. Ishikawa, K. Sato, T. Sonoda, and M. Otsubo, *J. Vac. Sci. Technol. B* **15**, 167 (1997).

<sup>28</sup>D. Rugar, H. J. Mamin, and P. Guethner, *Appl. Phys. Lett.* **55**, 2588 (1989).

<sup>29</sup>S. S. Rao, *Mechanical Vibrations* (Addison-Wesley, Reading, MA, 1990).

<sup>30</sup>J. G. E. Harris, D. D. Awschalom, K. D. Maranowski, and A. C. Gossard, *J. Appl. Phys.* **87**, 5102 (2000).

<sup>31</sup>P. Mohanty, D. A. Harrington, K. L. Ekinci, Y. T. Yang, M. J. Murphy, and M. L. Roukes, *Phys. Rev. B* **66**, 085416 (2002).

<sup>32</sup>T. D. Stowe, K. Yasumura, T. W. Kenny, D. Botkin, K. Wago, and D. Rugar, *Appl. Phys. Lett.* **71**, 288 (1997).

<sup>33</sup>H. X. Tang, X. M. H. Huang, M. L. Roukes, M. Bichler, and W. Wegscheider, *Appl. Phys. Lett.* **81**, 3879 (2002).

<sup>34</sup>N. G. Stoltz, M. Rakher, S. Strauf, A. Badolato, D. D. Lofgreen, P. M. Petroff, L. A. Coldren, and D. Bouwmeester, *Appl. Phys. Lett.* **87**, 031105 (2005).

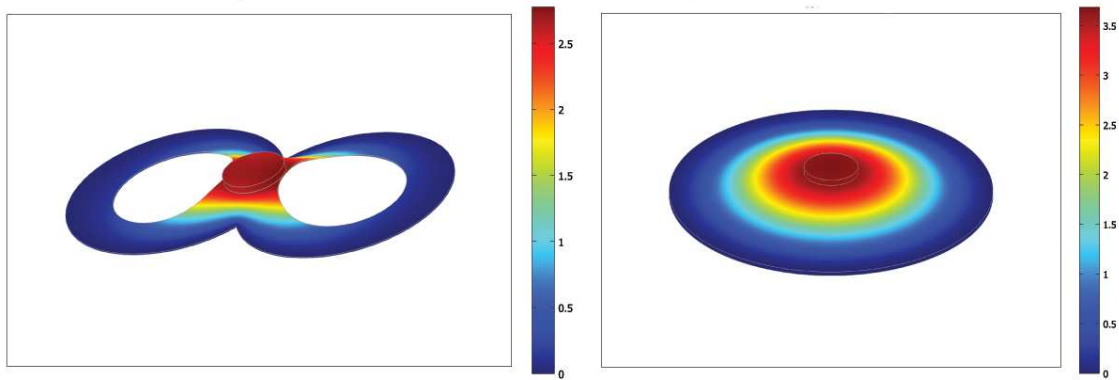


Figure 5.4: On the left is a finite element method (FEM) simulation of the fundamental mode of the doubly-clamped resonator used in section 6.2 and chapter 7. The color coding shows different displacement amplitudes, where the scale is in arbitrary units. The right image is a simulation of a membrane with a diameter of  $300 \mu\text{m}$  made of  $4 \mu\text{m}$  thick silicon and with a central DBR mirror pad. Its fundamental frequency is approx. 800 kHz. Both figures show the free standing part of the resonators only.

## 5.5 FEM simulations

In order to simulate the mechanical devices before we actually fabricate them we use finite element (FEM) simulation software (Comsol Multiphysics) and extract the expected frequency and effective mass for different geometries. We also analyze the higher order modes, as the spacing between them and the fundamental mode (which is the one we typically work with) should be large enough such that they do not overlap upon radiation-pressure cooling. FEM simulation is especially useful for the SiN and Si devices with the mirror pads, as it can simulate arbitrary shapes and sizes. The design is simply drawn in SolidWorks and then imported into the FEM software, where parameters such as length, width and thickness can be automatically varied and a plot of, for example, the resonance frequency vs. the length can be generated (see table 5.1 for a comparison of frequencies obtained from FEM simulation with measured values). In addition, for the free-free devices Garrett Cole and Ignacio Wilson-Rae have developed a routine in which they can calculate the limit on the mechanical  $Q$  from clamping losses [140].



## 6 Mechanical laser cooling in cryogenic cavities

In order to control mechanical systems in the quantum regime it is necessary to prepare the resonator in or close to its quantum ground state. This can be achieved by cooling it cryogenically if the mechanical frequency is high enough (for a dilution refrigerator around 1 GHz) [147], by using active feedback cooling [29, 72, 148–150] or by using the radiation-pressure interaction presented in this thesis to passively cool the mechanical motion. A combination of cryogenic precooling and radiation-pressure cooling relaxes the requirements in quality and frequency on the mechanical systems and should make ground state cooling experimentally accessible even for low frequencies. The two experiments in this chapter aim at demonstrating that this is in principle possible and show the current limitations of our experiment.

### 6.1 Radiation-pressure self-cooling of a micromirror in a cryogenic environment

While a first experiment in our group [38] demonstrated that radiation-pressure cooling worked in principle, it operated at room temperature and suffered from a high effective mass, relatively low  $Q$  and probably some absorption of the laser in the mirror. We subsequently replaced the mechanical oscillator with a different DBR material (see chapter 5 for details) to make sure we were not limited by the latter and also reduced the mechanical resonators significantly in size. In addition, we lowered the starting temperature to that of liquid helium by mounting the cavity inside a continuous flow  $^4\text{He}$  cryostat and demonstrated pure radiation-pressure cooling of the mechanical resonance to 290 mK, corresponding to a mean thermal occupation  $\bar{n}$  of  $10^4$  phonons. This was the first experiment ever to demonstrate radiation-pressure self-cooling in a cryogenic environment. The performance was limited by the piezo stabilizing the cavity, which had to be mounted at room temperature in order to function properly and therefore raised the base temperature of the cryostat to  $\sim 35$  K due to blackbody radiation heating the micromirror. Also the low mechanical  $Q$  of the devices of approximately 1,000 did not allow us to cool any further.



## Radiation-pressure self-cooling of a micromirror in a cryogenic environment

S. GRÖBLACHER<sup>1</sup>, S. GIGAN<sup>1(a)</sup>, H. R. BÖHM<sup>1,2</sup>, A. ZEILINGER<sup>1,2</sup> and M. ASPELMEYER<sup>1</sup>

<sup>1</sup>*Institute for Quantum Optics and Quantum Information (IQOQI), Austrian Academy of Sciences Boltzmannngasse 3, A-1090 Vienna, Austria*

<sup>2</sup>*Faculty of Physics, University of Vienna - Boltzmannngasse 5, A-1090 Vienna, Austria*

received 16 November 2007; accepted in final form 10 January 2008

published online 12 February 2008

PACS 42.50.-p – Quantum optics

PACS 07.10.Cm – Micromechanical devices and systems

PACS 42.50.Wk – Mechanical effects of light on material media, microstructures and particles

**Abstract** – We demonstrate radiation-pressure cavity-cooling of a mechanical mode of a micromirror starting from cryogenic temperatures. To achieve that, a high-finesse Fabry-Pérot cavity ( $F \approx 2200$ ) was actively stabilized inside a continuous-flow <sup>4</sup>He cryostat. We observed optical cooling of the fundamental mode of a  $50 \mu\text{m} \times 50 \mu\text{m} \times 5.4 \mu\text{m}$  singly clamped micromirror at  $\omega_m = 3.5 \text{ MHz}$  from 35 K to approximately 290 mK. This corresponds to a thermal occupation factor of  $\langle n \rangle \approx 1 \times 10^4$ . The cooling performance is only limited by the mechanical quality and by the optical finesse of the system. Heating effects, *e.g.* due to absorption of photons in the micromirror, could not be observed. These results represent a next step towards cavity-cooling a mechanical oscillator into its quantum ground state.

Copyright © EPLA, 2008

Optomechanical interactions in high-finesse cavities offer a new promising route for the ongoing experimental efforts to achieve the quantum regime of massive mechanical systems [1,2]. They allow to cool mechanical degrees of freedom of movable mirrors via radiation-pressure backaction [3], in principle even into their quantum ground state [4–6]. The working principle of this cooling method has been demonstrated in a series of recent experiments [7–10]. Ground-state cooling will eventually require to realize the scheme in a cryogenic environment. Optomechanical feedback cooling [11–15], another quantum limited strategy [6,16,17], has recently taken this step by demonstrating cooling of a 3.8 kHz resonator mode from a starting temperature of 2 K to an effective noise temperature of 2.9 mK (or  $\langle n \rangle \approx 2.1 \times 10^4$ ) [15]. To achieve and surpass such a performance for radiation-pressure backaction schemes requires stable operation of a high-finesse cavity inside a cryostat [18] and sufficiently strong optomechanical coupling [7–10]. Here we report the combination of these requirements in a single experiment using a high-reflectivity micromechanical resonator. We observe radiation-pressure backaction

cooling of the fundamental mode of the micromirror at  $\omega_m/2\pi = 557 \text{ kHz}$  from 35 K to 290 mK (or  $\langle n \rangle \approx 1 \times 10^4$ ), limited only by the optical finesse of the cavity and by the mechanical quality of the micromirror.

How does radiation-pressure cooling work? The basic setup comprises an optical cavity of frequency  $\omega_c$ , pumped by a laser at frequency  $\omega_l$ , that is bounded by a mechanical oscillator of resonance frequency  $\omega_m$ . By reflecting photons off the mechanical resonator, in our case a movable micromirror, the intracavity field exerts a radiation-pressure force on the mechanical system. Detuning of the optical cavity ( $\Delta = \omega_c - \omega_l \neq 0$ ) can result in a net positive ( $\Delta < 0$ ) or negative ( $\Delta > 0$ ) energy transfer from the radiation field to the mechanical oscillator, corresponding to either heating or cooling of the mechanical mode. There are different views to understand the cooling effect. Considering the full dynamics of the system, radiation-pressure forces in a detuned cavity behave as a viscous force that modifies the mechanical susceptibility [3,19,20]. Cooling occurs as a consequence of the delayed (retarded) force response to thermal fluctuations of the mechanical resonator, which is caused by the finite cavity decay rate  $\kappa$ . It is worth noting that retardation-based optomechanical cooling is not restricted to radiation pressure and its principle was in fact for the first

<sup>(a)</sup>Permanent address: Laboratoire Photon et Matière, Ecole Supérieure de Physique et de Chimie Industrielles, CNRS-UPR A0005 - 10 rue Vauquelin, 75005 Paris, France.



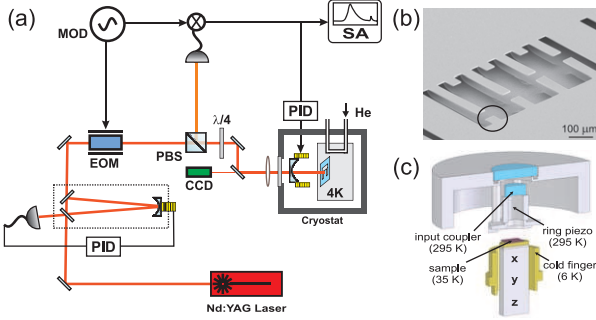
S. Gröblacher *et al.*

Fig. 1: (Color online) Experimental scheme. (a) The pump beam is spatially and spectrally filtered in a ring cavity locked to the laser frequency. After phase modulation using an electro-optic modulator (EOM), for Pound-Drever-Hall (PDH) locking, the pump is injected into the micromirror Fabry-Pérot (FP) cavity, which is mounted inside a  $^4\text{He}$  cryostat. The beam reflected from the FP cavity is detected behind a polarizing beam splitter (PBS). The PDH signal is obtained by demodulating the detected signal by the EOM driving frequency and is used for actively stabilizing the cavity length and for monitoring the dynamics of the mechanical mode. Alignment is done via a CCD camera. (b) SEM picture of a group of micromirrors. (c) Cavity mounting inside the cryostat (see text).

time demonstrated using photothermal forces [19]. Going beyond (semi-)classical descriptions, a full quantum treatment [4,5,21,22] can provide an interesting interpretation of the cooling effect as quantum state transfer between two oscillators, *i.e.* the cavity field and the mechanical mode [23]. This is related to the thermodynamic analogy, by which an entropy flow occurs from the thermally excited mechanical mode to the low-entropy laser field. Finally, the comparison of the photon-phonon interaction with three-wave mixing leads to the intuitive picture of sideband-cooling [4,5], as is well known from laser-cooling of atoms and ions<sup>1</sup>.

Our mechanical objects are oscillating micromirrors of high reflectivity that consist solely of a dielectric Bragg-mirror coating [24]. Compared to our previous work [7] we have used a different coating material to achieve both higher reflectivity and lower inherent absorption. This allowed us to increase the radiation-pressure coupling and to avoid residual photothermal effects. For the fabrication process we start from a high-reflectivity coating ( $R > 0.9999$ ) made out of 40 alternating layers of  $\text{Ta}_2\text{O}_5$  and  $\text{SiO}_2$  deposited on silicon. We used reactive ion etching to define the resonator shape and selective dry etching of the substrate to free the structures. All mechanical resonators form singly clamped cantilevers with a thickness of  $5.4 \mu\text{m}$ , a width of  $50 \mu\text{m}$  and a length between  $50 \mu\text{m}$  and  $300 \mu\text{m}$  (fig. 1b). We found mechanical quality factors  $Q \approx 1000\text{--}3000$  and reflectivities of  $R > 0.9999$ .

<sup>1</sup>Note that in our case radiation pressure originates from the reflection of photons off the mirror surface and not from absorption and re-emission as is the case in conventional laser cooling. Still, the cooling mechanism of both schemes is completely analogous.

The full experimental setup is sketched in fig. 1a. We use the micromirror as an end mirror in a high-finesse Fabry-Pérot (FP) cavity, which is pumped by an ultra-stable Nd:YAG laser operating in continuous-wave mode at a wavelength of 1064 nm. The input coupler of the FP cavity is a concave massive mirror (radius of curvature: 25 mm; reflectivity at 1064 nm: 0.9993) that is attached to a ring piezo (PZT) in order to actively modify the cavity length. We chose the length  $L$  of the cavity slightly shorter than for the semi-concentric case ( $L = 25 \text{ mm}$ ) in order to have a stable cavity and a small cavity-mode waist  $w_0$  on the micromirror ( $w_0 \approx 10 \mu\text{m}$ ). The cavity is mounted inside a continuous-flow  $^4\text{He}$  cryostat (fig. 1c). The input coupler is attached to the outer shield of the cryostat and therefore always maintains at room temperature. The silicon wafer that holds the micromirrors is glued on a sample holder that is in thermal contact with the cryostat cold finger. A 3-axis translation stage allows precise positioning of the micromirror on the chip with respect to the footprint of the cavity beam. We monitor both position and size of the cavity mode via an external imaging system. In operation, the cryostat is first evacuated to  $10^{-6}$  mbar. Cryogenic cooling is achieved by a continuous flow of helium in direct contact with the cold finger. The additional cryogenic freeze-out reduces the pressure to below  $3 \times 10^{-7}$  mbar. On cooling the cryostat from room temperature to approximately 6 K (measured temperature at the cold finger), the thermal contraction of the cavity (1–2 mm in total) can be compensated by the 3-axis translation stage. The temperature of the sample holder is monitored via an additional sensor directly attached to it. For a measured cold-finger temperature of 6 K we observe a sample holder temperature of approximately 20 K and an actual sample temperature of 35 K, which we infer from the calibrated power spectrum of the micromirror motion as mode temperature at zero optical detuning (see below). We attribute the temperature gradient to heating of the sample by blackbody radiation from the input coupler, which is kept at 295 K only a few millimeters away from the sample, in combination with finite thermal conductivity between sample, sample holder and cold finger. Both at room temperature and at cryogenic temperatures we observe stable locking of the cavity for a finesse of up to 8000. We achieve typical mode matching efficiencies into the cavity of 80%.

To observe the desired backaction cooling we monitor the dynamics of the different eigenmodes of the micromirror vibration by measuring its displacement power spectrum  $S_x(\omega)$  [21]. This is done by analyzing the Pound-Drever-Hall (PDH) signal in the light backreflected from the FP cavity [7,14,18], a method which is based on the interference of phase-modulated side bands of the pump laser [7,8]. The main idea is that the PDH error signal of a locked cavity is proportional to the cavity length. While we use the low-frequency part of the PDH signal as an error signal to actively stabilize the cavity length to the wanted detuning  $\Delta$ , the high-frequency part is directly

proportional to the displacement power spectrum  $S_x$  of the micromirror [21]<sup>2</sup>. One can evaluate the effective mode temperature via the area of the measured power spectrum as  $T_{eff} = \frac{m\omega_0^2}{k_B} \langle x^2 \rangle$  ( $m$ : effective mass at the probing point,  $\omega_0$ : mode frequency,  $k_B$ : Boltzmann's constant,  $\langle x^2 \rangle = \int_{-\infty}^{+\infty} d\omega S_x(\omega)$ ).

Backaction cooling is accompanied by a modified dynamics of the mechanical mode, specifically by a shift both in resonance frequency  $\omega_{eff}$  and in damping  $\gamma_{eff}$ . This can be used to identify the nature of the backaction force: for a known effective mass and optical pump power, radiation-pressure forces are uniquely determined by the time dependence of the cavity decay and can therefore be distinguished from forces of dissipative nature such as photothermal forces [4]. We obtain these effective values directly via the power spectrum  $S_x$ , which, for a classical harmonic oscillator, is given by

$$S_x(\omega) = \frac{4k_B T \gamma_0}{\pi m} \frac{1}{(\omega_{eff}^2 - \omega^2)^2 + 4\gamma_{eff}^2 \omega^2}, \quad (1)$$

where  $\gamma_0$  is the mechanical damping of the unperturbed mechanical oscillator, *i.e.* the damping at zero detuning. To minimize radiation-pressure effects we used very low input power ( $\approx 30 \mu\text{W}$ ) and probed the mode at a point of high effective mass, *i.e.* close to a nod of vibration. The values for  $\gamma_{eff}$  and  $\omega_{eff}$  were obtained from fits to the measured power spectra using eq. (1).

We first confirmed that our optomechanical system is dominated by radiation-pressure backaction. For that purpose, we monitor the modified dynamics of the mechanical mode of a micromirror and compare it with the theoretical predictions for radiation-pressure effects. The results for various cavity detunings are shown in fig. 2. The solid lines are fits to the data using the semi-classical approach described in [20]. We obtain a fitted cavity finesse  $F = 2300$  and a fitted effective mass of  $m = 125 \text{ ng}$ . These values are consistent with our independent estimate of  $F = 2800 \pm 600$  and  $m = (110 \pm 30) \text{ ng}$  (obtained from  $S_{ref}$ )<sup>3</sup>. Note that the finesse is measured by slowly scanning the cavity length. The corresponding measurement uncertainty arises from mechanical vibrations of the setup. We also performed a measurement on the mirror at 35 K (fig. 2), however with a reduced detuning range (for technical reasons the full detuning range was not available at low temperature). Again, the fit values of  $F = 2200$  and  $m = 40 \text{ ng}$  are consistent with our estimates of  $F = 2800 \pm 800$  and  $m = (30 \pm 10) \text{ ng}$  and therefore

<sup>2</sup>The ratio between PDH power spectrum and displacement power spectrum  $S_x$  depends on the cavity detuning  $\Delta$ . We can eliminate the unwanted detuning dependence by normalizing  $S_x$  via a reference signal of a known constant displacement power spectrum  $S_{ref}$  that is generated by frequency modulation of the pump laser. In addition,  $S_{ref}$  is an absolute calibration of the effective mass of the mechanical oscillator, as is outlined in detail, *e.g.*, in [7].

<sup>3</sup>The reduction in finesse compared to the value of 8000 is due to our choice of the optimal working point on the cantilever close to the tip of the micromirror, where edge diffraction increased the losses in the cavity.

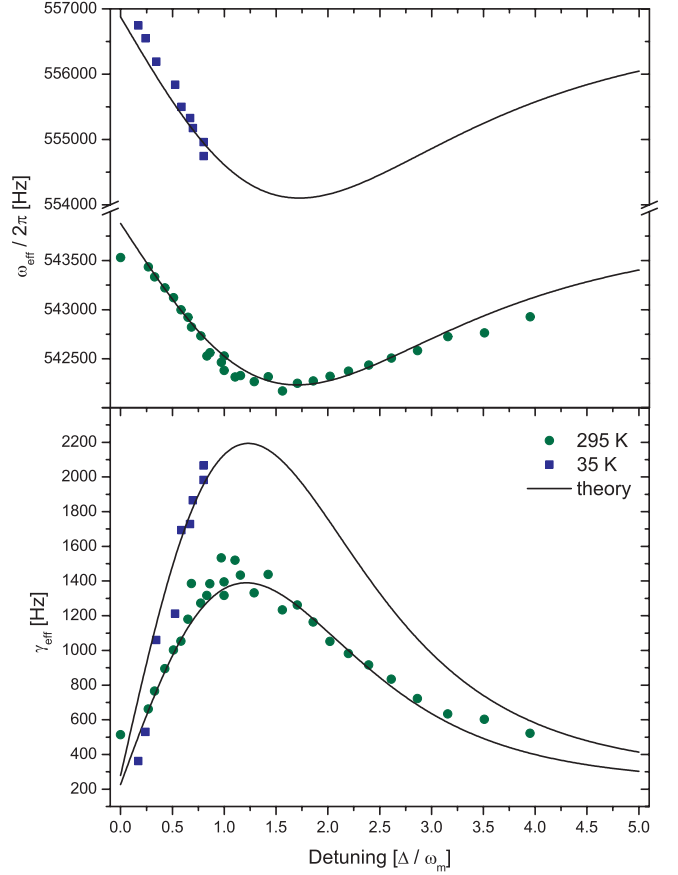


Fig. 2: (Color online) Modified micromirror dynamics due to cavity detuning. Shown is the micromirror's effective frequency  $\omega_{eff}/2\pi$  and effective damping  $\gamma_{eff}$  both at room temperature and at 35 K for various detuning values at a laser power of 1 mW. Maximal cooling is obtained approximately at a detuning of  $\omega_m$ , where the net phonon transfer to the optical field is maximized. The solid lines are fits to the data based on the semi-classical model for radiation-pressure backaction (see text).

confirm the radiation-pressure nature of the interaction. In contrast to radiation-pressure forces, photothermal forces are always subject to an exponential retardation due to the dissipative nature of the force and therefore produce a different dynamics on detuning [4]. We have used the same parameters to simulate the expected behavior resulting from such a force (fig. 3), which can clearly not serve as an explanation for our data.

Finally, we demonstrate radiation-pressure backaction cooling in a cryogenic cavity. Figure 4 shows measurements performed on the fundamental mechanical mode at  $\omega_m = 2\pi \times 557 \text{ kHz}$  of the micromirror. For each detuning and optical power level we obtained  $\langle x^2 \rangle$ ,  $\omega_{eff}$  and  $\gamma_{eff}$  directly from the fits to the measured displacement power spectrum  $S_x$ . The effective mass  $m_{eff}$  is obtained as described in the previous paragraph by fitting the data sets of same optical power (at a given cryostat temperature) using a semi-classical approach to radiation-pressure backaction. The effective temperature is obtained by plotting

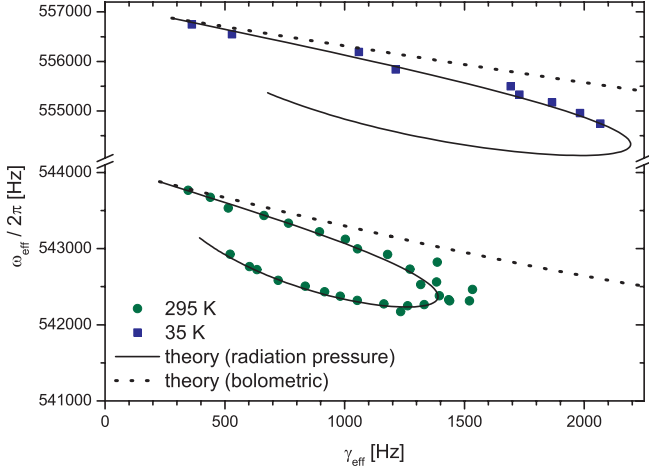
S. Gröblacher *et al.*

Fig. 3: (Color online) Radiation-pressure backaction. The data follow the curve from the top left to the bottom left. The solid lines are fits to the data based on the semi-classical model for pure radiation-pressure backaction (see text). The dotted lines show the expected behavior for bolometric (photothermal) forces when using the same parameters. Even at low temperature a clear deviation from photo-thermal behavior is observed and the data is well described by radiation-pressure effects.

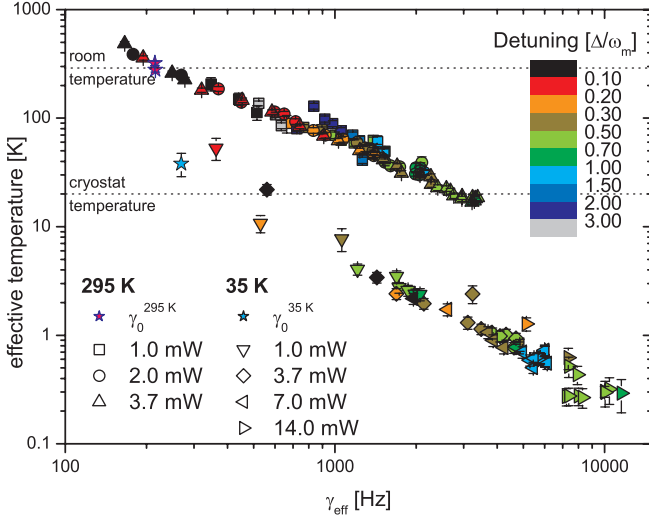


Fig. 4: (Color online) Radiation-pressure cooling in a cryogenic high-finesse cavity. Shown are the effective temperature  $T_{eff}$  and the effective damping  $\gamma_{eff}$  in a detuned cavity for various laser powers. Different laser powers correspond to different symbols. Values of detuning (in units of  $\omega_m$ ) are encoded in color. Starting from cryogenic temperatures (the given cryostat temperature is the measured sample holder temperature) we observe backaction cooling down to 290 mK (or  $\langle n \rangle \approx 1 \times 10^4$ ). The cooling performance is not limited by heating but by optical finesse and mechanical quality factor of the optomechanical system.

$m_{eff} \cdot \omega_{eff}^2 \cdot \langle x^2 \rangle$  normalized to the value obtained at zero detuning at room temperature (295 K). When cooling the cavity down to a sample holder temperature of 20 K we find a measured mode temperature at zero detuning

(corresponding to  $\gamma_0^{35\text{K}} = 2\pi \times 269\text{ Hz}$ ) of approximately 35 K. On detuning, the mode temperature decreases as expected for both starting temperatures. For a given laser power the effective mode temperature decreases with increasing detuning until  $\Delta \approx \omega_m$ , where the cooling is optimal. The effective temperature increases again on further increasing the detuning. When starting from room temperature we observe a minimum temperature of approximately 17 K at an input laser power of 3.7 mW. Starting with a cryogenic cavity we observe a minimum mode temperature of approximately 290 mK for 14 mW laser power. This corresponds to a thermal occupation factor of  $\langle n \rangle \approx 1 \times 10^4$ .

The cooling performance is not limited by residual heating effects. In the ideal (semi-)classical case  $T_{eff} \approx T_0 \frac{\gamma_0}{\gamma_{eff}}$  (for  $\omega_{eff} \ll \gamma_{eff}$  and  $T_0$ : environment temperature), as one can see from integrating eq. (1) and by using the equipartition theorem. We observe this behavior as linear dependence on the double-logarithmic scale of fig. 4. In case of heating, *e.g.* by absorption of photons, one would expect a dependence of the mode temperature on the laser power even for the same effective damping  $\gamma_{eff}$ . In other words, data points taken at different laser powers would not fall on the same line. The fact that we observe no deviation from the linear dependence for increasing laser power indicates that no significant heating of the mode occurs. We should also note that our experimental parameters ( $F = 2200$ ,  $\omega_m = 3.5 \times 10^6$ ) fulfill the threshold condition for ground-state cooling, because  $\omega_m/\kappa = 0.2 > 1/\sqrt{32}$  [5]. Our present cooling performance is only limited by the initial temperature  $T_0$  of the environment, *i.e.* the performance of the cryostat, and by the achieved damping ratio  $\frac{\gamma_0}{\gamma_{eff}}$ . Future improvements will have to include a further reduction of  $T_0$ , *e.g.* by including a radiation shield to protect the sample from blackbody radiation, a decrease in  $\gamma_0$ , *i.e.* a larger mechanical  $Q$ , and an increase of optical intracavity power, in particular via an increase of finesse.

We have demonstrated radiation-pressure backaction cooling of a micromirror in a high-finesse cavity at cryogenic temperatures. Starting from a sample temperature of approximately 35 K we achieve an effective mode temperature of 290 mK ( $\langle n \rangle \approx 1 \times 10^4$ ), limited only by the micromirror's mechanical quality factor and by its optical reflectivity. We consider this a next step towards exploiting the rich structure promised by optomechanical systems when entering the mechanical quantum regime [22,25–27]. We believe that the combination of cryogenic cooling with (active or passive) feedback techniques [15,28,29] will be an essential step to achieve this goal.

\*\*\*

We are grateful to J. B. HERTZBERG and K. SCHWAB for valuable support in sample preparation, and to K. GUGLER, T. PATEREK, M. PATERNOSTRO and D. VITALI for discussion. We acknowledge financial support by the FWF (Projects P19539-N20 and L426-N20), by the IST

funded Integrated Project QAP (Contract 015846) of the European Commission, by the City of Vienna and by the Foundational Questions Institute [fqxi.org](http://fqxi.org) (Grant RFP1-06-14). S. GRÖBLACHER is recipient of a DOC-fellowship of the Austrian Academy of Sciences.

## REFERENCES

- [1] LAHAYE M. D., BUU O., CAMAROTA B. and SCHWAB K. C., *Science*, **304** (2004) 74.
- [2] SCHWAB K. C. and ROUKES M. L., *Phys. Today*, **58** issue No. 7 (2005) 36.
- [3] BRAGINSKY V. and VYATCHANIN S. P., *Phys. Lett. A*, **293** (2002) 228.
- [4] MARQUARDT F., CHEN J. P., CLERK A. A. and GIRVIN S. M., *Phys. Rev. Lett.*, **99** (2007) 093902.
- [5] WILSON-RAE I., NOOSHI N., ZWERGER W. and KIPPENBERG T. J., *Phys. Rev. Lett.*, **99** (2007) 093901.
- [6] GENES C., VITALI D., TOMBESI P., GIGAN S. and ASPELMEYER M., arXiv:0705.1728 (2007).
- [7] GIGAN S., BÖHM H. R., PATERNOSTRO M., BLASER F., LANGER G., HERTZBERG J. B., SCHWAB K. C., BÄUERLE D., ASPELMEYER M. and ZEILINGER A., *Nature*, **444** (2006) 67.
- [8] ARCIZET O., COHADON P. F., BRIANT T., PINARD M. and HEIDMANN A., *Nature*, **444** (2006) 71.
- [9] SCHLIESSER A., DEL'HAYE P., NOOSHI N., VAHALA K. J. and KIPPENBERG T. J., *Phys. Rev. Lett.*, **97** (2006) 243905.
- [10] CORBITT T., CHEN Y., INNERHOFER E., MÜLLER-EBHARDT H., OTTAWAY D., REHBEIN H., SIGG D., WHITCOMB S., WIPF C. and MAVALVALA N., *Phys. Rev. Lett.*, **98** (2007) 150802.
- [11] MANCINI S., VITALI D. and TOMBESI P., *Phys. Rev. Lett.*, **80** (1998) 688.
- [12] COHADON P., HEIDMANN A. and PINARD M., *Phys. Rev. Lett.*, **83** (1999) 3174.
- [13] KLECKNER D. and BOUWMEESTER D., *Nature*, **444** (2006) 75.
- [14] ARCIZET O., COHADON P.-F., BRIANT T., PINARD M., HEIDMANN A., MACKOWSKI J.-M., MICHEL C., PINARD L., FRANÇAIS O. and ROUSSEAU L., *Phys. Rev. Lett.*, **97** (2006) 133601.
- [15] POGGIO M., DEGEN C. L., MAMIN H. J. and RUGAR D., *Phys. Rev. Lett.*, **99** (2007) 017201.
- [16] COURTY J.-M., HEIDMANN A. and PINARD M., *Eur. Phys. J. D*, **17** (2001) 399.
- [17] VITALI D., MANCINI S., RIBICHINI L. and TOMBESI P., *Phys. Rev. A*, **65** (2002) 063803.
- [18] TITTONEN I., BREITENBACH G., KALKBRENNER T., MÜLLER T., CONRADT R., SCHILLER S., STEINSLAND E., BLANC N. and DE ROOIJ N. F., *Phys. Rev. A*, **59** (1999) 1038.
- [19] METZGER C. H. and KARRAI K., *Nature*, **432** (2004) 1002.
- [20] ARCIZET O., BRIANT T., HEIDMANN A. and PINARD M., *Phys. Rev. A*, **73** (2006) 033819.
- [21] PATERNOSTRO M., GIGAN S., KIM M. S., BLASER F., BÖHM H. R. and ASPELMEYER M., *New J. Phys.*, **8** (2006) 107.
- [22] VITALI D., GIGAN S., FERREIRA A., BÖHM H. R., TOMBESI P., GUERREIRO A., VEDRAL V., ZEILINGER A. and ASPELMEYER M., *Phys. Rev. Lett.*, **98** (2007) 030405.
- [23] ZHANG J., PENG K. and BRAUNSTEIN S. L., *Phys. Rev. A*, **68** (2003) 013808.
- [24] BÖHM H. R., GIGAN S., BLASER F., ZEILINGER A., ASPELMEYER M., LANGER G., BÄUERLE D., HERTZBERG J. B. and SCHWAB K. C., *Appl. Phys. Lett.*, **89** (2006) 223101.
- [25] BOSE S., JACOBS K. and KNIGHT P. L., *Phys. Rev. A*, **56** (1997) 4175.
- [26] PINARD M., DANTAN A., VITALI D., ARCIZET O., BRIANT T. and HEIDMANN A., *Europhys. Lett.*, **72** (2005) 747.
- [27] PIRANDOLA S., VITALI D., TOMBESI P. and LLOYD S., *Phys. Rev. Lett.*, **97** (2006) 150403.
- [28] NAIK A., BUU O., LAHAYE M. D., ARMOUR A. D., CLERK A. A., BLENCOWE M. P. and SCHWAB K. C., *Nature*, **443** (2006) 193.
- [29] THOMPSON J. D., ZWICKL B. M., JAYICH A. M., MARQUARDT F., GIRVIN S. M. and HARRIS J. G. E., arXiv:0707.1724 (2007).

## 6.2 Demonstration of an ultracold micro-optomechanical oscillator in a cryogenic cavity

Our first demonstration of self-cooling of a cryogenically precooled mechanical resonator left a lot of room for experimental improvements. First of all, we developed new, hybrid mechanical structures combining excellent reflectivities with relatively high mechanical quality factors – see section 5.2. The optical setup was modified to include a locking / read-out beam and a separate cooling beam (the details are explained in section 4.4). The single photodetector read-out was replaced with a homodyne detection scheme (section 4.6), which improved our signal-to-noise ratio by several orders of magnitude (cf. figure 4.13). In addition, acting back on the laser frequency for cavity stabilization, instead of the piezo-lock that was used in the early experiments ([38] and section 6.1), enabled stable operation of the full cavity at cryogenic temperatures. The cavity was now a rigid design, where both the micromirror and the input coupler were cryogenically cooled, allowing us to routinely reach temperatures as low as 5 K. All these improvements finally allowed us to use the radiation-pressure force to cool the mechanical motion by a factor of more than 4,000 to a thermal occupation of 30 quanta. The cooling performance was limited only by the coupling of the mechanical device to its environment. It is also worth noting that the measurement precision in this experiment was better than the standard quantum limit of the mechanical oscillator [3].

# Demonstration of an ultracold micro-optomechanical oscillator in a cryogenic cavity

Simon Gröblacher<sup>1,2</sup>, Jared B. Hertzberg<sup>3,4</sup>, Michael R. Vanner<sup>1,2</sup>, Garrett D. Cole<sup>1,5</sup>, Sylvain Gigan<sup>6</sup>, K. C. Schwab<sup>3\*</sup> and Markus Aspelmeyer<sup>1†</sup>

**Preparing and manipulating quantum states of mechanical resonators is a highly interdisciplinary undertaking that now receives enormous interest for its far-reaching potential in fundamental and applied science<sup>1,2</sup>. Up to now, only nanoscale mechanical devices achieved operation close to the quantum regime<sup>3,4</sup>. We report a new micro-optomechanical resonator that is laser cooled to a level of 30 thermal quanta. This is equivalent to the best nanomechanical devices, however, with a mass more than four orders of magnitude larger (43 ng versus 1 pg) and at more than two orders of magnitude higher environment temperature (5 K versus 30 mK). Despite the large laser-added cooling factor of 4,000 and the cryogenic environment, our cooling performance is not limited by residual absorption effects. These results pave the way for the preparation of 100- $\mu\text{m}$  scale objects in the quantum regime. Possible applications range from quantum-limited optomechanical sensing devices to macroscopic tests of quantum physics<sup>5,6</sup>.**

Recently, the combination of high-finesse optical cavities with mechanical resonators has opened up new possibilities for preparing and detecting mechanical systems close to—and even in—the quantum regime by using well-established methods of quantum optics. Most prominently, the mechanism of efficient laser cooling has been demonstrated<sup>7–13</sup> and has been shown to be capable, in principle, of reaching the quantum ground state<sup>14–16</sup>. A particularly intriguing feature of this approach is that it can be applied to mechanical objects of almost arbitrary size, from the nanoscale in microwave strip-line cavities<sup>13</sup> up to the centimetre scale in gravitational-wave interferometers<sup>11</sup>. In addition, whereas quantum-limited readout is still a challenging development step for non-optical schemes<sup>3,17,18</sup>, optical readout techniques at the quantum limit are readily available<sup>19</sup>.

Approaching and eventually entering the quantum regime of mechanical resonators through optomechanical interactions essentially requires the following three conditions to be fulfilled: (1) sideband-resolved operation; that is, the cavity amplitude decay rate  $\kappa$  has to be small with respect to the mechanical frequency  $\omega_m$ ; (2) both ultralow noise and low absorption of the optical cavity field (phase noise at the mechanical frequency can act as a finite-temperature thermal reservoir and absorption can increase the mode temperature and even diminish the cavity performance in the case of superconducting cavities); and (3) sufficiently small coupling of the mechanical resonator to the thermal environment; that

is, low environment temperature  $T$  and large mechanical quality factor  $Q$  (the thermal coupling rate is given by  $k_B T / \hbar Q$ , where  $k_B$  is the Boltzmann constant and  $\hbar$  is the reduced Planck constant). So far, no experiment has demonstrated all three requirements simultaneously. Criterion (1) has been achieved<sup>10,13,20</sup>; however, the performance was limited in one case by laser phase noise<sup>10</sup> and in the other cases by absorption in the cavity<sup>13,20</sup>. Other, independent, experiments have implemented only criterion (2)<sup>11,12,19,21</sup>. Finally, criterion (3) has been realized in several cryogenic experiments<sup>4,13,21,22</sup>, however not in combination with both (1) and (2).

We have designed a novel micro-optomechanical device that enables us to meet all requirements at the same time. Specifically, we have fabricated a  $\text{Si}_3\text{N}_4$  micromechanical resonator that carries a high-reflectivity, ultralow-loss Bragg mirror (Fig. 1a), which serves as the end mirror of a Fabry–Pérot cavity. We designed the system to exhibit a fundamental mechanical mode at relatively high frequency (of the order of 1 MHz; Fig. 1b) such that sideband-resolved operation (criterion (1)) can be achieved already with a medium-finesse cavity. Criterion (2) can first be fulfilled because our solid-state pump laser used for optical cooling exhibits low phase noise (laser linewidth below 1 kHz). Second, absorption in the Bragg mirror is sufficiently low to prevent residual heating in the mechanical structure. Absorption levels as low as  $10^{-6}$  have been reported for similar Bragg mirrors<sup>23</sup> and recent measurements suggest even lower values of  $4 \times 10^{-7}$  for the specific coatings used in this experiment (R. Lalezari, private communication). In addition, although absorption in  $\text{Si}_3\text{N}_4$  is comparable to silicon, the transmission mismatch of the two cavity mirrors ( $\sim 10:1$ ) and the resulting low transmission through the Bragg mirror prevents residual heating of the resonator as has been observed for cryogenically cooled silicon cantilevers<sup>24</sup>. Finally, criterion (3) requires low temperature and high mechanical quality. The mechanical properties of our design are dominated by the  $\text{Si}_3\text{N}_4$ , which is known to exhibit superior performance in particular at low temperatures, where  $Q$ -factors beyond  $10^6$  have been observed at millikelvin temperatures<sup>25</sup>.

We operate our device, a  $100 \mu\text{m} \times 50 \mu\text{m} \times 1 \mu\text{m}$  microresonator, in a cryogenic  $^4\text{He}$  environment at  $10^{-7}$  mbar and in direct contact with the cryostat cold finger. To measure the mechanical displacement, the frequency of a  $7 \mu\text{W}$  continuous-wave Nd:YAG laser is locked close to resonance of the cryogenic Fabry–Pérot cavity (length  $L \approx 25$  mm), which consists of a fixed macroscopic mirror and the moving micromechanical mirror. The optical

<sup>1</sup>Institute for Quantum Optics and Quantum Information (IQOQI), Austrian Academy of Sciences, Boltzmannngasse 3, A-1090 Vienna, Austria, <sup>2</sup>Faculty of Physics, University of Vienna, Boltzmannngasse 5, A-1090 Vienna, Austria, <sup>3</sup>Department of Physics, Cornell University, Ithaca, New York 14853, USA, <sup>4</sup>Department of Physics, University of Maryland, College Park, Maryland 20742, USA, <sup>5</sup>The Center for Micro- and Nanostructures (ZMNS), Vienna University of Technology, Floragasse 7, A-1040 Vienna, Austria, <sup>6</sup>Laboratoire Photon et Matière, Ecole Supérieure de Physique et de Chimie Industrielles, CNRS-UPRA0005, 10 rue Vauquelin, 75005 Paris, France. \*Permanent address: Department of Applied Physics, Caltech, Pasadena, California 91125, USA. <sup>†</sup>e-mail: markus.aspelmeyer@quantum.at.

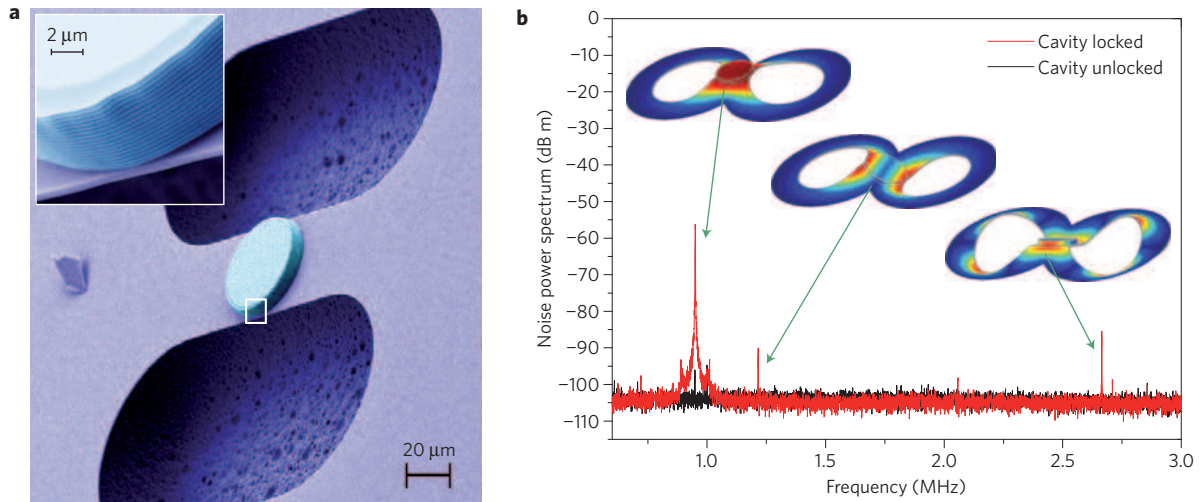


**Figure 1 | High-quality micro-optomechanical resonator.** **a**, Scanning electron micrograph of the basic mechanical system, which is formed by a doubly clamped  $\text{Si}_3\text{N}_4$  beam. A circular, high-reflectivity Bragg mirror is used as the end mirror of a Fabry–Pérot cavity. The Bragg mirror is made of low-absorption, alternating dielectric stacks of  $\text{Ta}_2\text{O}_5/\text{SiO}_2$ . The magnified section in the inset shows the stacking sequence. **b**, Micromechanical displacement spectra shown as noise power spectra of the readout-beam phase quadrature for a locked and an unlocked cavity. The fundamental mode at  $\omega_m = 2\pi \times 945$  kHz and all higher mechanical modes are identified by finite element simulation. For the cases that involve large Bragg mirror displacements, we provide the simulated mode profile.

cavity of finesse  $F \approx 3,900$  achieves moderate sideband resolution ( $\kappa \approx 0.8\omega_m$ ), which in principle would allow cooling to a final occupation number  $\langle n \rangle_{\min} = (\kappa^2/4\omega_m^2) \approx 0.16$ , that is, well into the quantum ground state<sup>14,15</sup>. The experimentally achievable temperature is obtained as the equilibrium state of two competing processes, namely the laser cooling rate and the coupling rate to the thermal (cryogenic) environment. In essence, laser cooling is driven (in the ideal resolved-sideband limit and at detuning  $\Delta = \omega_m$ ) at a rate  $\Gamma \approx G^2/(2\kappa)$  ( $G$  is the effective optomechanical coupling rate, as defined in ref. 16), whereas mechanical relaxation to the thermal environment at temperature  $T$  takes place at a rate  $(k_B T/\hbar Q)$ . The final achievable mechanical occupation number is therefore, to first order, given by  $n_f \approx (1/\Gamma) \times (k_B T/\hbar Q)$ . A more accurate derivation taking into account effects of non-ideal sideband resolution can be found, for example, in refs 14–16, 26. Our experimental parameters limit the minimum achievable mode temperature to approximately 1 mK ( $n_f \approx 30$ ). The fact that we can observe this value in the experiment (see below) shows that other residual heating effects are negligible. The micromechanical flexural motion modulates the cavity-field phase quadrature, which is measured by optical homodyning. For  $Q \gg 1$  its noise power spectrum (NPS) is a direct measure of the mechanical position spectrum  $S_q(\omega)$ , as described in ref. 16. We observe a minimum noise floor of  $2.6 \times 10^{-17}$  m  $\text{Hz}^{-0.5}$ , which is a factor of 4 above the achievable quantum (shot-noise) limit, when taking into account the finite cavity linewidth, the cavity losses and the non-perfect mode-matching, and due to the residual amplitude noise of the pump laser at the sideband frequency of our mechanical mode. We observe the fundamental mechanical mode at  $\omega_m = 2\pi \times 945$  kHz with an effective mass  $m_{\text{eff}} = 43 \pm 2$  ng and a quality factor  $Q \approx 30,000$  at 5.3 K ( $Q \approx 5,000$  at 300 K). These values are consistent with independent estimates based on finite-element method simulations yielding  $\omega_m = 2\pi \times 945$  kHz and  $m_{\text{eff}} = 53 \pm 5$  ng (see Supplementary Information).

Optomechanical laser cooling requires driving of the cavity with a red-detuned (that is, off-resonant), optical field<sup>6–13</sup>. We achieve this by coupling a second laser beam—detuned by  $\Delta$  in frequency but orthogonal in polarization—into the same spatial cavity mode (Fig. 2a). Birefringence of the cavity material leads to both an optical path length difference for the two cavity modes (resulting in an 800 kHz frequency difference of the cavity peak

positions) and a polarization rotation of the outgoing fields. We compensate both effects by an offset in  $\Delta$  and by extra linear optical phase retarders, respectively. A change in detuning  $\Delta$  modifies the mechanical rigidity and results in both an optical spring effect ( $\omega_{\text{eff}}(\Delta)$ ) and damping ( $\gamma_{\text{eff}}(\Delta)$ ), which is directly extracted by fitting the NPS using the expressions from ref. 16. Figure 2b shows the predicted behaviour for several powers of the red-detuned beam. The low-power curve at 140  $\mu\text{W}$  is used to determine both the effective mass of the mechanical mode,  $m_{\text{eff}}$ , and the cavity finesse,  $F$ . For higher powers and detunings closer to cavity resonance, the onset of cavity instability prevents a stable lock (see, for example, ref. 16). All experimental data are in agreement with theory and hence in accordance with pure radiation-pressure effects<sup>15</sup>.

The effective mode temperature is obtained through the equipartition theorem. For our experimental parameter regime,  $Q \gg 1$  and  $\langle n \rangle \gg 0.5$ , the integrated NPS is also a direct measure of the mean mechanical mode energy and hence, through the equipartition theorem, of its effective temperature through  $T_{\text{eff}} = (m_{\text{eff}} \omega_{\text{eff}}^2/k_B) \int_{-\infty}^{+\infty} \text{NPS}(\omega) d\omega$ . Note that, for the case of strong optomechanical coupling, normal-mode splitting can occur and has to be taken into account when evaluating the mode temperature<sup>27</sup>. In our present case, this effect is negligible because of the large cavity decay rate  $\kappa$ . The amplitude of the NPS is calibrated by comparing the mechanical NPS with the NPS of a known frequency modulation applied to the laser (see, for example, ref. 28). For a cold-finger temperature of 5.3 K, we obtain a mode temperature  $T = 2.3$  K, which is consistent with an expected moderate cooling due to slightly off-resonant locking of the Fabry–Pérot cavity (by less than 3% of the cavity intensity linewidth). The locking point is deliberately chosen to be on the cooling side to avoid unwanted parametric mechanical instabilities. The mean thermal occupancy was calculated according to  $\langle n \rangle = k_B T_{\text{eff}}/\hbar\omega_{\text{eff}}$ . We note, however, that Bose–Einstein statistics will have a dominant role as one approaches the quantum ground state.

Figure 3a shows mechanical noise power spectra with the cooling beam switched off and with maximum cooling beam pump power at 7 mW. For a detuning  $\Delta \approx \omega_m$ , we demonstrate laser cooling to a mean thermal occupancy of  $32 \pm 4$  quanta, which is more than 2 orders of magnitude lower than previously reported values for optomechanical devices<sup>10</sup> and is comparable to the lowest

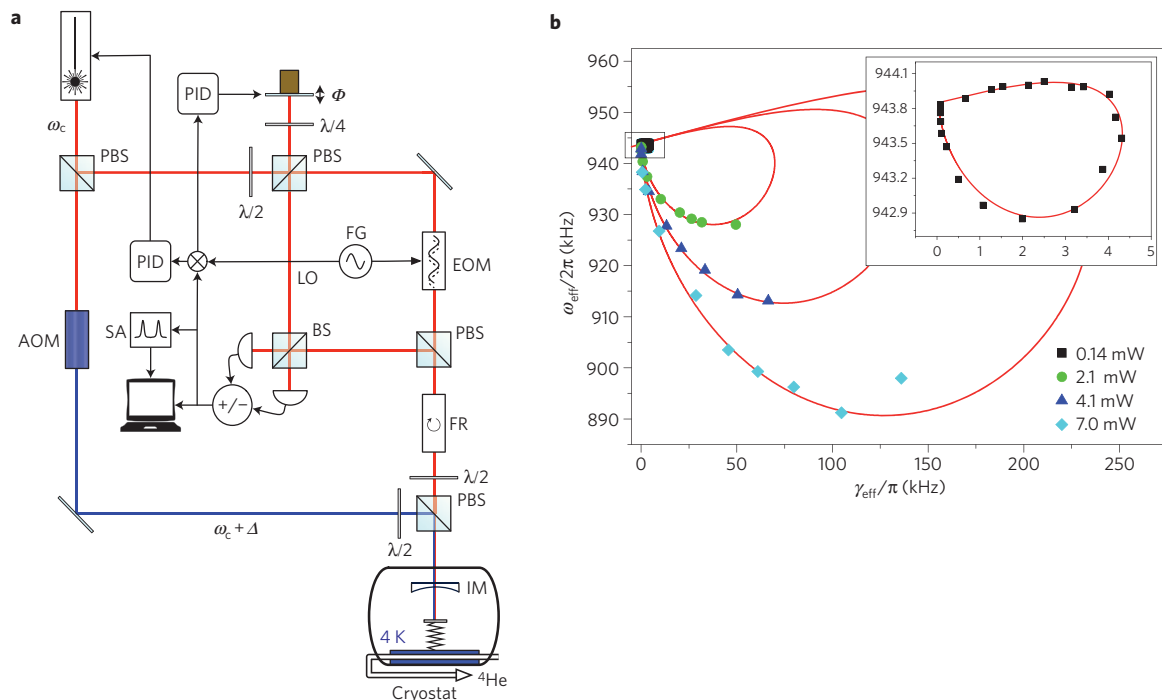


**Figure 2 | Experimental set-up and characterization of optomechanical radiation-pressure interaction. a**, The laser is split at a polarizing beamsplitter (PBS) into a weak locking field (red) tuned near cavity resonance  $\omega_c$  and the cooling field (blue) tuned off-resonant with an acousto-optical modulator (AOM) to  $\omega_c + \Delta \approx \omega_c - \omega_m$ . An electro-optical modulator (EOM) in the weak field is used to generate a Pound-Drever-Hall error signal for cavity locking. The beams are recombined on a PBS into the same spatial mode at orthogonal polarization before they enter the cavity comprising an input mirror (IM) and the micro-mechanical mirror. The phase quadrature of the locking beam is measured in a homodyne detection scheme (BS: beamsplitter; LO: local oscillator;  $\Phi$ : local oscillator phase; SA: spectrum analyser).  $\Phi$  is stabilized in a separate proportional-integral-derivative controller (PID). A combination of a Faraday rotator (FR) and a half-wave plate ( $\lambda/2$ ) separates the reflected from the original signal. **b**, The effective frequency  $\omega_{\text{eff}}$  and damping  $\gamma_{\text{eff}}$  of the micro-mechanical motion for different detuning and power settings. All power levels follow the theoretical predictions for pure radiation-pressure interaction. The symbols are experimental data, and the solid lines are simulations based on ref. 16. The inset shows the data set taken at 140  $\mu$ W optical power.

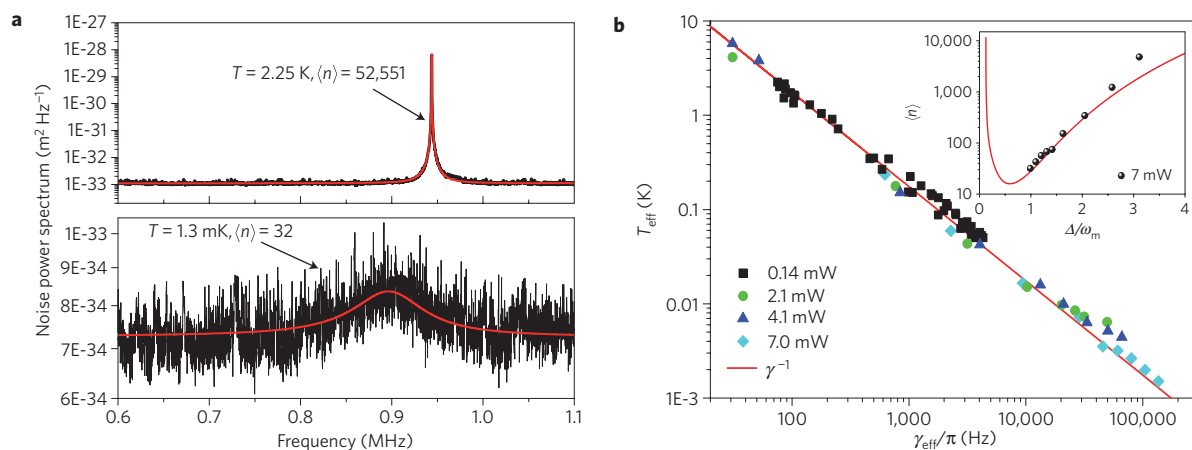


**Figure 3 | Optomechanical laser cooling inside a cryogenic cavity. a**, Calibrated noise power spectra for the fundamental mechanical mode at 5.3 K environmental temperature with small cavity cooling (top) and at maximum cooling (bottom). The thermal energy is reduced from  $\approx 53,000$  quanta at 7  $\mu$ W laser power to  $32 \pm 4$  quanta at 7 mW. The vertical axes in both plots are logarithmic. The change in the technical noise floor is due to different locking levels of the local oscillator phase  $\Phi$  in the homodyne detection. **b**, Plot of the calibrated effective temperature  $T_{\text{eff}}$  versus the observed damping  $\gamma_{\text{eff}}$  for various power and detuning values of the cooling beam. No deviations from the theoretically expected power-law dependence (red solid line) can be observed. The inset shows the mean thermal occupation  $\langle n \rangle$  as a function of detuning for maximal laser power. Cavity instability prevents detunings arbitrarily close to resonance. The red solid curve is a simulation based on ref. 16 that uses only experimentally obtained parameters.

reported temperature of 25 quanta for nano-electromechanical systems<sup>4</sup> (NEMS). In contrast to previous experiments<sup>10,13</sup>, the achieved cooling performance is not limited by optical absorption or residual phase noise, but follows exactly the theoretically predicted behaviour (Fig. 3b). This agrees with the expected device

performance: a fraction of approximately  $10^{-6}$  of the intra-cavity power is absorbed by the Bragg mirror ( $\sim 13 \mu\text{W}$  at maximum cooling) and a maximum of 1% of the transmitted power is absorbed by the  $\text{Si}_3\text{N}_4$  beam<sup>29</sup> ( $\sim 14 \mu\text{W}$  at maximum cooling and taking into account the impedance mismatch of the cavity mirrors).



The cryogenic cooling power of the cryostat used is orders of magnitude larger than the maximum heat load expected on the micromechanical structures. The absence of absorption can also be seen from the inferred mode temperature  $T_{\text{eff}}$ , which decreases with the mechanical damping rate  $\gamma_{\text{eff}}$  in strict accordance with the power law  $T_{\text{eff}} \propto \gamma_{\text{eff}}^{-1}$ . This relation follows immediately from the simple expression for the mechanical occupation  $n_f$  given above ( $n_f \propto \Gamma^{-1}$ ) and from the fact that the laser cooling rate  $\Gamma$  is to first approximation equivalent to the effective mechanical damping  $\gamma_{\text{eff}}$ , at least for all data points of our experiment. Both heating and the onset of normal-mode splitting for strong coupling<sup>27</sup> would result in a deviation of this behaviour.

The remaining obstacle that prohibits us from reaching the quantum ground state is the intrinsic phonon coupling to the thermal environment at rate  $k_B T / \hbar Q \approx 1.4 \times 10^7$  Hz. By reducing the reservoir temperature to that of NEMS experiments (20 mK), this coupling will significantly reduce, not only owing to the lower bath temperature but also because  $\text{Si}_3\text{N}_4$  resonators markedly improve in mechanical  $Q$  with decreasing temperature. For example, thermal heating rates as low as  $3 \times 10^3$  Hz have been observed for  $\text{Si}_3\text{N}_4$  at 300 mK (ref. 25), which would place our effective mode temperature already well into the quantum ground state using otherwise unchanged parameters.

In summary, we have demonstrated optical cooling of the fundamental mode of a 100  $\mu\text{m}$  scale mechanical resonator in a cryogenic cavity to a thermal occupation of only  $32 \pm 4$  quanta. This is comparable to the performance of state-of-the-art NEMS devices. In contrast to previous approaches, the large laser cooling rates attained are no longer limited by residual absorption or phase-noise effects. This is achieved by a new micro-optomechanical resonator design with exceptionally low intrinsic optical absorption and both high optical and mechanical quality. This leaves the reduction of the thermal coupling, for example, by further decreasing the environment temperature to those available in conventional  $^3\text{He}$  cryostats, as the only remaining hurdle to prepare the mechanical quantum ground state. Our approach hence establishes a feasible route towards the quantum regime of massive micromechanical systems.

## Methods

**Micro-mirror fabrication.** Our micro-mechanical oscillator is made of 1- $\mu\text{m}$ -thick low-stress  $\text{Si}_3\text{N}_4$  deposited on a Si substrate and coated through ion beam sputtering with a high-reflectivity Bragg mirror. Standard photolithography and plasma etching is used for forming, in subsequent steps, the mirror pad and the micro-mechanical resonator, which is finally released from the Si substrate in a  $\text{XeF}_2$  atmosphere. The mirror stack, designed and deposited by ATFilms, comprises 36 alternating layers of  $\text{Ta}_2\text{O}_5$  and  $\text{SiO}_2$  with an overall nominal reflectivity of 99.991% at 1,064 nm. The measured finesse of 3,900 is consistent with an input coupler reflectivity of 99.91% and with extra diffraction losses due to a finite size of the cavity beam waist.

Received 5 March 2009; accepted 1 May 2009;  
published online 7 June 2009

## References

- Schwab, K. C. & Roukes, M. L. Putting mechanics into quantum mechanics. *Phys. Today* **58**, 36–42 (2005).
- Aspelmeyer, M. & Schwab, K. C. (eds) Mechanical systems at the quantum limit. *New J. Phys.* **10**, 095001 (2008).
- LaHaye, M., Buu, O., Camarota, B. & Schwab, K. C. Approaching the quantum limit of a nanomechanical resonator. *Science* **304**, 74–77 (2004).
- Naik, A. *et al.* Cooling a nanomechanical resonator with quantum backaction. *Nature* **443**, 193–196 (2006).
- Marshall, W., Simon, C., Penrose, R. & Bouwmeester, D. Towards quantum superpositions of a mirror. *Phys. Rev. Lett.* **91**, 130401 (2003).
- Vitali, D. *et al.* Optomechanical entanglement between a movable mirror and a cavity field. *Phys. Rev. Lett.* **98**, 030405 (2007).
- Metzger, C. H. & Karrai, K. Cavity cooling of a microlever. *Nature* **432**, 1002–1005 (2004).
- Gigan, S. *et al.* Self-cooling of a micromirror by radiation pressure. *Nature* **444**, 67–71 (2006).
- Arcizet, O., Cohadon, P.-F., Briant, T., Pinard, M. & Heidmann, A. Radiation-pressure cooling and micromechanical instability of a micromirror. *Nature* **444**, 71–75 (2006).
- Schliesser, A., Rivière, R., Anetsberger, G., Arcizet, O. & Kippenberg, T. J. Resolved-sideband cooling of a micromechanical oscillator. *Nature Phys.* **4**, 415–419 (2007).
- Corbitt, T. *et al.* An all-optical trap for a gram-scale mirror. *Phys. Rev. Lett.* **98**, 150802 (2007).
- Thompson, J. D. *et al.* Strong dispersive coupling of a high-finesse cavity to a micromechanical membrane. *Nature* **452**, 72–75 (2008).
- Teufel, J. D., Harlow, J. W., Regal, C. A. & Lehnert, K. W. Dynamical backaction of microwave fields on a nanomechanical oscillator. *Phys. Rev. Lett.* **101**, 197203 (2008).
- Wilson-Rae, I., Nooshi, N., Zwerger, W. & Kippenberg, T. J. Theory of ground state cooling of a mechanical oscillator using dynamical backaction. *Phys. Rev. Lett.* **99**, 093901 (2007).
- Marquardt, F., Chen, J. P., Clerk, A. A. & Girvin, S. M. Quantum theory of cavity-assisted sideband cooling of mechanical motion. *Phys. Rev. Lett.* **99**, 093902 (2007).
- Genes, C., Vitali, D., Tombesi, P., Gigan, S. & Aspelmeyer, M. Ground-state cooling of a micromechanical oscillator: Comparing cold damping and cavity-assisted cooling schemes. *Phys. Rev. A* **77**, 033804 (2008).
- Regal, C. A., Teufel, J. D. & Lehnert, K. W. Measuring nanomechanical motion with a microwave cavity interferometer. *Nature Phys.* **4**, 555–560 (2008).
- Poggio, M. *et al.* An off-board quantum point contact as a sensitive detector of cantilever motion. *Nature Phys.* **4**, 635–638 (2008).
- Arcizet, O. *et al.* High-sensitivity optical monitoring of a micromechanical resonator with a quantum-limited optomechanical sensor. *Phys. Rev. Lett.* **97**, 133601 (2006).
- Cole, G. D., Gröblacher, S., Gugler, K., Gigan, S. & Aspelmeyer, M. Monocrystalline AlGaAs heterostructures for high-reflectivity high-Q micromechanical resonators in the MHz regime. *Appl. Phys. Lett.* **92**, 261108 (2008).
- Gröblacher, S., Gigan, S., Böhm, H. R., Zeilinger, A. & Aspelmeyer, M. Radiation-pressure self-cooling of a micromirror in a cryogenic environment. *Eur. Phys. Lett.* **81**, 54003 (2008).
- Poggio, M., Degen, C. L., Mamin, H. J. & Rugar, D. Feedback cooling of a cantilever's fundamental mode below 5 mK. *Phys. Rev. Lett.* **99**, 017201 (2007).
- Rempe, G., Thompson, R. J., Kimble, H. J. & Lalezari, R. Measurement of ultralow losses in an optical interferometer. *Opt. Lett.* **17**, 363–365 (1996).
- Bleszynski-Jayich, A. C., Shanks, W. E. & Harris, J. G. E. Noise thermometry and electron thermometry of a sample-on-cantilever system below 1 K. *Appl. Phys. Lett.* **92**, 013123 (2008).
- Zwickl, B. M. *et al.* High quality mechanical and optical properties of commercial silicon nitride membranes. *Appl. Phys. Lett.* **92**, 103125 (2008).
- Wilson Rae, I., Nooshi, N., Dobrindt, J., Kippenberg, T. J. & Zwerger, W. Cavity-assisted backaction cooling of mechanical resonators. *New J. Phys.* **10**, 095007 (2008).
- Dobrindt, J. M., Wilson-Rae, I. & Kippenberg, T. J. Optomechanical normal-mode splitting. *Phys. Rev. Lett.* **101**, 263602 (2008).
- Pinard, M., Hadjar, Y. & Heidmann, A. Effective mass in quantum effects of radiation pressure. *Eur. Phys. J. D* **7**, 107–116 (1997).
- Edward, D., Palik, E. D. & Ghosh, G. (eds) *Handbook of Optical Constants of Solids* (Academic, 1998).

## Acknowledgements

We thank R. Lalezari (ATFilms) and M. Metzler, R. Ilic and M. Skvarla (CNF) and F. Blaser, T. Corbitt and W. Lang for discussion and support. We acknowledge support by the Austrian Science Fund FWF (Projects P19539, L426, START), by the European Commission (Projects MINOS, IQOS) and by the Foundational Questions Institute fqxi.org (Grants RFP2-08-03, RFP2-08-27). Part of this work was carried out at the Cornell NanoScale Facility, a member of the National Nanotechnology Infrastructure Network, which is supported by the National Science Foundation (Grant ECS-0335765). S.Gr. is a recipient of a DOC-fellowship of the Austrian Academy of Sciences and G.D.C. of a Marie Curie Fellowship of the European Commission. S.Gr. and M.R.V. are members of the FWF doctoral program Complex Quantum Systems (W1210).

## Author contributions

All authors have made a significant contribution to the concept, design, execution or interpretation of the presented work.

## Additional information

Supplementary information accompanies this paper on [www.nature.com/naturephysics](http://www.nature.com/naturephysics). Reprints and permissions information is available online at <http://npq.nature.com/reprintsandpermissions>. Correspondence and requests for materials should be addressed to M.A.

**Demonstration of an ultracold micro-optomechanical oscillator in a cryogenic cavity**

Simon Gröblacher<sup>1,2</sup>, Jared B. Hertzberg<sup>3,4</sup>, Michael R. Vanner<sup>1,2</sup>, Garrett D. Cole<sup>1</sup>, Sylvain Gigan<sup>5</sup>, K. C. Schwab<sup>3</sup> & Markus Aspelmeyer<sup>1</sup>

## SUPPLEMENTARY INFORMATION

**Effective Mass**

We have estimated the effective mass of the fundamental mode of our micromechanical structure using both analytic models and FEM analysis. The experimentally observed value of  $43 \pm 2$  ng agrees to within 10% with the estimated value of  $53 \pm 5$  ng.

The total mass of the dielectric Bragg mirror (radius  $R \approx 24.5 \pm 0.5$   $\mu\text{m}$ ) made of 36 alternating layers of  $\text{Ta}_2\text{O}_5$  ( $\rho \approx 8200$   $\text{kg/m}^3$ ,  $t = 126.4$  nm) and  $\text{SiO}_2$  ( $\rho = 2200$   $\text{kg/m}^3$ ,  $t = 179.6$  nm) is  $45 \pm 5$  ng, not taking into account the lateral etch and tapering of the mirror pad. The large error stems from the uncertainty in the exact value of the  $\text{Ta}_2\text{O}_5$  density, which can vary between 6800 and 8300  $\text{kg/m}^3$ . The mass of the  $\text{Si}_3\text{N}_4$  resonator ( $\rho = 3000$   $\text{kg/m}^3$ , approximate dimensions of  $100 \times 50 \times 1$   $\mu\text{m}^3$ ) is approx. 11 ng, resulting in a maximum total mass of  $56 \pm 5$  ng for the full optomechanical device.

The mode mass, i.e. the actual mass contributing to the motion of the  $\text{Si}_3\text{N}_4$  resonator fundamental mode, is approx. 74% of the total mass of the  $\text{Si}_3\text{N}_4$  resonator (see any standard literature on elasticity theory, for example [S1]). This would result in a total mode mass of the optomechanical resonator ( $\text{Si}_3\text{N}_4$  beam plus micromirror) of approx.  $53 \pm 5$  ng. However, because of the flat-top mode shape of our actual device (see the FEM simulation shown in

---

<sup>1</sup> Institute for Quantum Optics and Quantum Information (IQOQI), Austrian Academy of Sciences, Boltzmannngasse 3, A-1090 Vienna, Austria

<sup>2</sup> Faculty of Physics, University of Vienna, Boltzmannngasse 5, A-1090 Vienna, Austria

<sup>3</sup> Department of Physics, Cornell University, Ithaca, NY 14853, USA

<sup>4</sup> Department of Physics, University of Maryland, College Park, MD 20742, USA

<sup>5</sup> Laboratoire Photon et Matière, Ecole Supérieure de Physique et de Chimie Industrielles, CNRS-UPRA0005, 10 rue Vauquelin, 75005 Paris, France

## SUPPLEMENTARY INFORMATION

DOI: 10.1038/NPHYS1301

Figure S1), this value is only a conservative lower bound. A more realistic value that takes into account the actual mode shape can be obtained directly from FEM simulation and is approx.  $56 \pm 5$  ng (see below).

Finally, to calculate the effective mass one has to take into account the mode overlap between the mechanical resonator mode and the mode of the optical probe beam (for a detailed analysis on the calculation of the effective mass see for example [S2]). Based on the experimentally obtained optical finesse, which is limited by intensity losses due to a finite mirror size, we can provide an upper bound on the cavity beam waist at the micromirror position of  $8 \pm 2$   $\mu\text{m}$ . If we assume a mechanical mode shape of an ideal doubly-clamped beam of dimensions  $100 \times 50 \times 1$   $\mu\text{m}^3$  we would calculate an effective mass (see e.g. [S2,S3]) of  $50 \pm 5$  ng. Again, the actual flat-top mode shape of our device results in a decreased mean square displacement (by approx. 6%) compared to the ideal doubly-clamped beam. Taking this into account yields a final effective mass of  $53 \pm 5$  ng, which agrees to within 10% with the experimentally observed value of  $43 \pm 2$  ng.

The abovementioned FEM simulations make use of the exact geometry and material data for our resonator. The main idea is to impose a force on the structure and have the FEM simulation calculate the deflection. Using Hooke's law one can then extract the spring constant  $k$  of the device. The mode mass can be extracted by using  $\omega_m = \sqrt{k/m_{\text{mode}}}$ . For our specific device the FEM solver provides us with a spring constant of 2196 N/m and a fundamental mode at  $\omega_m = 2\pi \times 945$  kHz, which results in  $m_{\text{mode}} = 57 \pm 5$  ng.

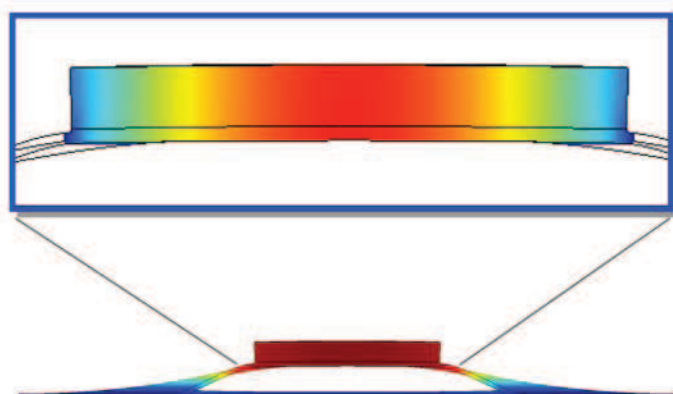


**Figure S1:** FEM simulation of our optomechanical device. Shown is the side-view of the fundamental resonance mode at its maximum displacement (below). The cylindrical mirror pad on top of the  $\text{Si}_3\text{N}_4$  beam induces a flat-top mode shape (inset).

### Error Analysis

The error associated with the noise power spectra peak areas, which provide the mechanical mean square displacement, can be estimated as follows: Assuming that the NPS comprises a sequence of  $N$  independent data points  $(x_i, y_i)$  (with  $i = 1 \dots N$ ) with measurement uncertainty  $(\delta x_i, \delta y_i)$  one can calculate the area underneath the NPS by Riemann integration

as  $A = \sum_{i=1}^{N-1} (x_{i+1} - x_i) y_i$  with an uncertainty  $\delta A = \sqrt{\sum_{i=1}^{N-1} (x_{i+1} - x_i)^2 (\delta y_i)^2}$ , which is obtained by

Gaussian error propagation and neglecting the uncertainty in  $x$ . The strongly cooled NPS shown in Figure 3a is given by a data set of  $N = 5000$  points with  $x_{i+1} - x_i = 100$  Hz and with  $\delta y_i \approx 1 \times 10^{-34} \text{ m}^2 \text{ Hz}^{-1}$  for all  $i$ . We obtain  $A = 3.780 \times 10^{-28} \text{ m}^2$  (by numerically integrating the data set),  $\delta A \approx \sqrt{N} \times 100 \text{ Hz} \times 1 \times 10^{-34} \text{ m}^2 \text{ Hz}^{-1} = 7.1 \times 10^{-31} \text{ m}^2$  and an integrated noise floor of  $N \times 100 \text{ Hz} \times 7.3 \times 10^{-34} \text{ m}^2 \text{ Hz}^{-1} = 3.65 \times 10^{-28} \text{ m}^2$ . This results in an integrated “real thermal noise” of  $(3.78 - 3.65) \times 10^{-28} \text{ m}^2 = 1.3 \times 10^{-29} \text{ m}^2$  with an overall error of approx.  $\sqrt{2} \times 7.3 \times 10^{-31} \text{ m}^2 \approx 1 \times 10^{-30} \text{ m}^2$ , i.e. with an error of approx. 8%. The SNR of our measurement is therefore sufficient to support our result of  $\langle n \rangle = 32$  and accounts for an uncertainty of  $\delta \langle n \rangle = \pm 1.5$ .

Other possible sources of experimental uncertainty are: an uncertainty related to the absolute displacement amplitude calibration (amounting to approx. 12% relative uncertainty), an uncertainty related to determining the mechanical resonance frequency (known up to an error of approx. 5%) and an uncertainty related to the absolute power calibration of the intracavity optical pump field (known up to an error of approx. 10%). These additional experimental uncertainties add up to an overall error of approx. 25%. All errors are conservatively estimated and finally result in  $\langle n \rangle = 32 \pm 4$ .

### Shot-Noise

The noise floor of our measurement is limited by optical shot-noise. The corresponding displacement noise can be calculated according to [S4] as

$$\delta x_{Shot} = \frac{\lambda}{16F} \sqrt{\frac{P\lambda}{hc}} \cdot \sqrt{1 + \left(\frac{\omega_m}{\kappa}\right)^2} \cdot \sqrt{\frac{T+l}{T}} \cdot \sqrt{\frac{P}{P_{MM}}}.$$

Our experimental parameters (finesse  $F = 3900$ , input power  $P = 14 \mu\text{W}$ ,  $\lambda = 1064 \text{ nm}$ ,  $\omega_m = 2\pi \times 945 \text{ kHz}$ ,  $\kappa = 2\pi \times 770 \text{ kHz}$ , input coupler transmission  $T = 900 \text{ ppm}$ , overall intra-cavity losses  $l = 620 \text{ ppm}$ , optical input power (corrected for imperfect mode-matching)  $P_{MM} = 7 \mu\text{W}$ ) result in a minimal noise-floor of  $\delta x_{Shot} = 6 \times 10^{-18} \text{ m Hz}^{-0.5}$ .

[S1] D. A. Harrington and M. L. Roukes, Caltech Technical Rep. No. CMP-106 (1994).

[S2] M. Pinard, M. Y. Hadjar, and A. Heidmann, Effective mass in quantum effects of radiation pressure, *Eur. Phys. J. D* **7**, 107-116 (1999).

[S3] S. Gigan et al., Self-cooling of a micromirror by radiation pressure, *Nature* **444**, 67-71 (2006).

[S4] T. Briant, Caractérisation du couplage optomécanique entre la lumière et un miroir: bruit thermique et effets quantiques, PhD thesis, l'Université Paris VI (2003).



## 7 Opto-mechanics in the strong coupling regime

Full coherent quantum control over optomechanical systems is one of the main outstanding goals in the young research field of cavity opto-mechanics. While the progress towards low-entropy states was tremendous in recent years (including the cooling experiments presented in chapter 6), the second necessary condition for most quantum protocols [31, 32, 81, 151] has received far less attention: the system needs to be in the so-called strong coupling regime. In this regime, the optomechanical coupling rate  $g$  must be larger than the individual coupling rates of the subsystems to their environments, namely  $\kappa$  for the cavity and  $\gamma_m$  for the mechanical resonator and therefore allowing for coherent energy exchange between the systems, i.e.  $g \geq \kappa, \gamma_m$ . In most experiments  $\gamma_m$  is negligibly small but the cavity amplitude decay rate  $\kappa$  poses a major challenge. According to equation (3.61), in order to increase the bare single photon coupling rate  $g_0$  either the cavity length  $L$  can be decreased or the zero point motion  $x_{zp}$  of the mechanics increased (by decreasing the effective mass and/or the frequency of the oscillator). Table 7.1 shows a comparison of  $g_0$  for a selection of publications. In most experiments the coupling rate is several orders of magnitude lower than the cavity decay rate. Nonetheless, linearizing the interaction allows to reach the strong coupling regime by increasing the intra-cavity field  $\alpha_s$  (cf. equation (3.67)). In this chapter we present the first experiment that was able to enter this strong coupling regime. We gradually increased  $g$  by increasing the laser input power to approx. 11 mW, which corresponded to a coupling rate  $g = 325$  kHz, while  $\kappa = 215$  kHz and  $\gamma_m = 140$  Hz. We observed normal mode splitting as unambiguous evidence for entering the strong coupling regime (see sections 3.1.1 & 3.3.5 and [76, 86]).

Besides simultaneous ground state cooling and strong coupling, it would be highly interesting to also reach the single photon strong coupling regime, where the full non-linear character of the Hamiltonian (3.60) could be exploited for quantum experiments with macroscopic mechanical resonators.

	$\omega_m/2\pi$ [Hz]	$g_0/2\pi$ [Hz]	$g_0/\kappa$
Gigan et al., Nature (2006) [38]	$278 \times 10^3$	3.09	$4.1 \times 10^{-7}$
Arcizet et al., Nature (2006) [39]	$817 \times 10^3$	0.86	$8.3 \times 10^{-7}$
Schliesser et al., Phys. Rev. Lett. (2006) [40]	$57.8 \times 10^6$	161	$6.5 \times 10^{-6}$
Corbitt et al., Phys. Rev. Lett. (2007) [72]	$1 \times 10^3$	$8.2 \times 10^{-3}$	$8.6 \times 10^{-8}$
Thompson et al., Nature (2008) [77]	$134 \times 10^3$	4.7	$2.9 \times 10^{-5}$
Schliesser et al., Nature Phys. (2008) [152]	$62 \times 10^6$	380	$4.0 \times 10^{-5}$
Anetsberger et al., Nature Phys. (2009) [153]	$10.7 \times 10^6$	589	$1.2 \times 10^{-4}$
Gröblacher et al., Nature Phys. (2009) [43]	$945 \times 10^3$	5.1	$6.6 \times 10^{-6}$
Eichenfield et al., Nature (2009) [154]	$8.2 \times 10^6$	$6.0 \times 10^5$	$6.0 \times 10^{-4}$
Gröblacher et al., Nature (2009) [46]	$945 \times 10^3$	2.8	$1.3 \times 10^{-5}$
Eichenfield et al., Nature (2009) [155]	$2.3 \times 10^9$	$2.3 \times 10^5$	$4.3 \times 10^{-5}$
Wilson et al., Phys. Rev. Lett. (2009) [156]	$4.82 \times 10^6$	6.1	$4.9 \times 10^{-7}$
Li et al., Phys. Rev. Lett. (2009) [157]	$25.5 \times 10^6$	37.8	$4.7 \times 10^{-8}$
Safavi-Naeini et al., Appl. Phys. Lett. (2010) [158]	$150 \times 10^6$	$8.0 \times 10^5$	$1.0 \times 10^{-2}$
Ding et al., arXiv (2010) [159]	$383.5 \times 10^6$	$1.7 \times 10^5$	$1.0 \times 10^{-4}$

Table 7.1: Comparison of the single photon coupling strength  $g_0$  for several opto-mechanics experiments. In order to reach the single photon strong coupling regime  $g_0$  must be greater than  $\kappa$ , which for most current experiments seems to be out of reach.



## LETTERS

# Observation of strong coupling between a micromechanical resonator and an optical cavity field

Simon Gröblacher<sup>1,2</sup>, Klemens Hammerer<sup>3,4</sup>, Michael R. Vanner<sup>1,2</sup> & Markus Aspelmeyer<sup>1</sup>

Achieving coherent quantum control over massive mechanical resonators is a current research goal. Nano- and micromechanical devices can be coupled to a variety of systems, for example to single electrons by electrostatic<sup>1,2</sup> or magnetic coupling<sup>3,4</sup>, and to photons by radiation pressure<sup>5–9</sup> or optical dipole forces<sup>10,11</sup>. So far, all such experiments have operated in a regime of weak coupling, in which reversible energy exchange between the mechanical device and its coupled partner is suppressed by fast decoherence of the individual systems to their local environments. Controlled quantum experiments are in principle not possible in such a regime, but instead require strong coupling. So far, this has been demonstrated only between microscopic quantum systems, such as atoms and photons (in the context of cavity quantum electrodynamics<sup>12</sup>) or solid state qubits and photons<sup>13,14</sup>. Strong coupling is an essential requirement for the preparation of mechanical quantum states, such as squeezed or entangled states<sup>15–18</sup>, and also for using mechanical resonators in the context of quantum information processing, for example, as quantum transducers. Here we report the observation of optomechanical normal mode splitting<sup>19,20</sup>, which provides unambiguous evidence for strong coupling of cavity photons to a mechanical resonator. This paves the way towards full quantum optical control of nano- and micromechanical devices.

A common feature of all coupled quantum systems is that their dynamics are dominated by the competition between the joint coupling rate and the rates at which the coupled systems decohere into their local environments. Only for sufficiently strong coupling can the effects of decoherence be overcome. This so-called ‘strong coupling regime’ is, in all cases, indispensable for the experimental investigation of a manifold of quantum phenomena. Nano- and micro-optomechanical oscillators are currently emerging as a new ‘textbook’ example for coupled quantum systems. In this case, a single electromagnetic field mode is coupled to a (nano- or micrometre sized) mechanical oscillator. In analogy to cavity quantum electrodynamics (cQED), one can identify strong coupling as the regime where the coupling rate  $g$  exceeds both the cavity amplitude decay rate  $\kappa$  and the mechanical damping rate  $\gamma_m$ —as required, for example, in refs 15–17. Another class of proposals requires the weaker condition of ‘large cooperativity’, that is,  $g > \sqrt{\kappa\gamma_m}$  (refs 18, 21). Strong coupling, ideally in combination with the preparation of zero entropy initial states (for example, by ground-state cooling of the mechanical resonator), is essential to obtain (quantum) control over this new domain of quantum physics. Whereas ground state preparation is a goal of continuing research (in which much progress has been made, in particular by using optical laser cooling techniques<sup>22</sup>), here we demonstrate strong optomechanical coupling using state-of-the-art micromechanical resonators.

Consider the canonical situation in which a mechanical resonator is coupled to the electromagnetic field of a high-finesse cavity via

momentum transfer of the cavity photons (Fig. 1). The system naturally comprises two coupled oscillators: the electromagnetic field at cavity frequency  $\omega_c$  (typically of the order of  $10^{15}$  Hz) and the mechanical resonator at frequency  $\omega_m$  ( $\sim 10^7$  Hz). At first sight, the large discrepancy in the oscillator frequencies seems to inhibit any coupling; it is, however, alleviated by the fact that the cavity is driven by a laser field at frequency  $\omega_L$ , which effectively creates an optical oscillator at frequency  $A = \omega_c - \omega_L - \delta_{rp}$  (in a reference frame rotating at  $\omega_L$ ;  $\delta_{rp}$  is the mean shift of the cavity frequency due to radiation pressure). Each of the two oscillators decoheres into its local environment: the optical field at the cavity amplitude decay rate  $\kappa$  and the mechanics at the damping rate  $\gamma_m$ . Entering the desired strong coupling regime requires a coupling rate  $g \gtrsim \kappa, \gamma_m$ .

The fundamental optomechanical radiation-pressure interaction  $H_{\text{int}} = -\hbar g_0 n_c X_m$  couples the cavity photon number  $n_c$  to the position  $X_m$  of the mechanics ( $\hbar$  is  $h/2\pi$ , where  $h$  is Planck’s constant). On the single-photon level, this interaction provides an intrinsically nonlinear coupling, where the coupling rate  $g_0 = \frac{\omega_c}{L} \sqrt{\frac{\hbar}{m\omega_m}}$  ( $L$ , cavity length;  $m$ , effective mass) describes the effect of a single photon on the optomechanical cavity. In all currently available optomechanical systems, however,  $g_0$  is well below 100 Hz. Because the corresponding cavity decay rates are typically much larger than 10 kHz, the effect is too small to exploit the strong coupling regime on the single-photon level. For our experiment  $g_0 = 2\pi \times 2.7$  Hz, which is smaller than both  $\kappa$  ( $2\pi \times 215$  kHz) and  $\gamma_m$  ( $2\pi \times 140$  Hz). To circumvent this limitation, we use a strong optical driving field ( $\lambda = 1,064$  nm), which shifts the optomechanical steady state by means of radiation pressure from vacuum to a mean cavity amplitude  $\alpha$  (mean cavity photon number  $\langle n_c \rangle = \alpha^2$ ) and from zero displacement to a mean mechanical displacement  $\beta$ . The resulting effective interaction is obtained by standard mean-field expansion, and resembles two harmonic oscillators that are coupled linearly in their optical and mechanical position quadratures  $X_c = (a_c + a_c^\dagger)$  and  $X_m = (a_m + a_m^\dagger)$ , respectively. This strongly driven optomechanical system is then described by equation (1) (see Supplementary Information):

$$H = \frac{\hbar A}{2} (X_c^2 + P_c^2) + \frac{\hbar \omega_m}{2} (X_m^2 + P_m^2) - \hbar g X_c X_m \quad (1)$$

The effective coupling strength  $g = g_0 \alpha$  is now enhanced by a factor of  $\alpha = \sqrt{\langle n_c \rangle}$ . Note that this enhancement comes at the cost of losing the nonlinear character of the interaction. Although there exist proposals that do require strong nonlinear coupling at the single-photon level<sup>16</sup>, the majority of schemes for quantum optomechanical state manipulation work well within the regime of linear albeit strong coupling. They rely on the fact that linear interactions allow for protocols such as quantum state transfer and readout<sup>23</sup>, generation of entanglement<sup>15,17</sup>, conditional preparation of states via projective measurements on

<sup>1</sup>Institute for Quantum Optics and Quantum Information (IQOQI), Austrian Academy of Sciences, Boltzmanngasse 3, A-1090 Vienna, Austria. <sup>2</sup>Faculty of Physics, University of Vienna, Strudlhofgasse 4, A-1090 Vienna, Austria. <sup>3</sup>Institute for Quantum Optics and Quantum Information (IQOQI), Austrian Academy of Sciences, Technikerstraße 21a, A-6020 Innsbruck, Austria. <sup>4</sup>Institute for Theoretical Physics, University of Innsbruck, Technikerstrasse 25, A-6020 Innsbruck, Austria.

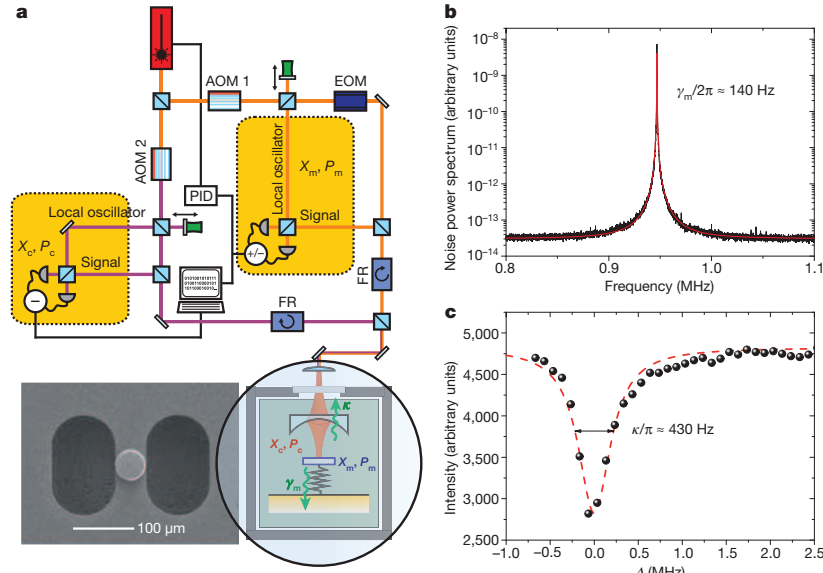


**Figure 1 | Experimental set-up and characterization of the uncoupled mechanical and optical oscillator.** **a**, Our micromechanical resonator with a high-reflectivity mirror pad ( $R > 0.99991$ ) that forms the end-face of a 25-mm-long Fabry–Pérot cavity (magnified view circled, bottom right). A strong continuous-wave Nd:YAG laser is used to drive the optomechanical system (purple beam). By splitting off a faint part (15  $\mu$ W) of the drive laser, the laser frequency is actively locked to the Fabry–Pérot cavity frequency (orange beam). Locking is achieved by phase-modulation (electro-optical modulator, EOM) and by obtaining a Pound–Drever–Hall error signal required for feedback with a proportional–integral–derivative controller (PID). Acousto-optical modulators (AOM) control the relative frequency detuning  $\Delta$  and thus allow for off-resonant driving of the cavity. Data presented here have been taken by varying the detuning  $\Delta$  and the power of the drive beam. Both beams are coupled to the Fabry–Pérot cavity via the same spatial mode but orthogonal in polarization. The measured cavity linewidth (full-width at half-maximum, FWHM)  $2\kappa \approx 2\pi \times 430$  kHz corresponds to an optical finesse  $F \approx 14,000$ . The fundamental mechanical

mode of the microresonator at  $\omega_m = 2\pi \times 947$  kHz has a natural linewidth (FWHM) of  $\gamma_m \approx 2\pi \times 140$  Hz (mechanical quality factor  $Q \approx 6,700$ ) at room temperature. With  $\kappa/\omega_m \approx 0.2$ , these parameters place us well into the resolved sideband regime  $\kappa/\omega_m \ll 1$ . The effective mass of 145 ng was obtained by direct fitting of the optomechanical response at low driving powers. After interaction with the optomechanical system, both (drive and lock) beams are separated by a polarizing beamsplitter and Faraday rotators (FR) and are each independently measured by optical homodyne (Supplementary Information). Each homodyne phase can be either scanned or locked to a fixed value by actuating a piezo-driven mirror. **b**, Mechanical noise power spectrum obtained by homodyne detection of the lock beam. Red line, fit to the data assuming an ideal harmonic oscillator in thermal equilibrium. **c**, Intensity of the drive beam that is reflected off the Fabry–Pérot cavity when scanning its detuning  $\Delta$ , which provides direct access to the cavity transfer function. Dashed red line, Lorentzian fit to the data.

light<sup>18,21</sup>, and so on, a fact which is well established in the fields of quantum optics and quantum information. In our experiment, by using external optical pump powers of up to 11 mW, we are able to achieve an increase in coupling by more than five orders of magnitude, sufficient to reach the desired strong coupling regime.

An unambiguous signature of strongly coupled systems is the occurrence of normal mode splitting, a phenomenon known to both classical and quantum physics. In the simplest case, two independent harmonic oscillators coupled via an additional joint spring will behave as a pair of uncoupled oscillators—so-called normal modes—with shifted resonance frequencies compared to the individual resonators. For the particular case of resonators with equal bare frequencies, a sufficiently strong coupling will introduce a spectral splitting of the two normal modes that is of the order of the coupling strength  $g$ . Normal mode splitting has been observed in a number of realizations of cQED, where it is also known as Rabi-splitting, with photons coupled either to atoms<sup>24,25,26</sup>, to excitons in semiconductor structures<sup>27,28,29</sup> or to Cooper pair box qubits in circuit QED<sup>14</sup>. In case of the strongly driven optomechanical system described by equation (1), the normal modes occur at frequencies  $\omega_{\pm}^2 = \frac{1}{2}(\Delta^2 + \omega_m^2 \pm \sqrt{(\Delta^2 - \omega_m^2)^2 + 4g^2\omega_m\Delta})$  and exhibit a splitting of  $\omega_+ - \omega_- \approx g$ . In the given simple expression for normal mode frequencies, cavity decay and mechanical damping are neglected. A more careful analysis is carried out in the Supplementary Information, and shows that normal mode splitting occurs only above a threshold  $g \gtrsim \kappa$  (refs 19, 20) for our damped optomechanical system. The

Hamiltonian can be re-written in terms of the normal modes and one obtains:

$$H = \frac{\hbar\omega_+}{2}(X_+^2 + P_+^2) + \frac{\hbar\omega_-}{2}(X_-^2 + P_-^2) \quad (2)$$

For the resonant case  $\Delta = \omega_m$ , equation (2) describes two uncoupled oscillators with position and momentum quadratures  $X_{\pm} = \sqrt{\frac{\omega_m \pm g}{2\omega_m}}(X_c \pm X_m)$  and  $P_{\pm} = \sqrt{\frac{\omega_m}{2(\omega_m \pm g)}}(P_c \pm P_m)$ . These new dynamical variables cannot be ascribed to either the cavity field or the mechanical resonator, but are true hybrid optomechanical degrees of freedom. The overall system energy spectrum  $E_{m,n}$  is therefore given by the sum of the energies of the two normal modes, that is,  $E_{m,n} = \hbar(m\omega_+ + n\omega_-)$ . The degeneracy of the uncoupled energy levels is lifted, and normal mode splitting of adjacent levels occurs with a separation that is equivalent to the coupling strength  $g$ . In the presence of decoherence, the spectral lines are broadened to a width of  $(\kappa + \gamma_m)$  and the splitting can therefore only be resolved for  $g \gtrsim \kappa, \gamma_m$ , that is, for strong coupling.

We observe normal mode splitting via direct spectroscopy of the optical field emitted by the cavity. Emission of a cavity photon can in general be understood as a transition between dressed states of the optomechanical system, that is, between mechanical states that are dressed by the cavity radiation field. The structure of the optomechanical interaction only allows for transitions that lower or raise the total number of normal mode excitations by one (see Supplementary Information). Photons emitted from the cavity therefore

have to lie at sidebands equal to the dressed state frequencies  $\omega_{\pm}$  relative to the incoming laser photons of frequency  $\omega_L$ , that is, they have to be emitted at sideband frequencies  $\omega_L \pm \omega_{\pm}$  or  $\omega_L \pm \omega_{-}$ . Homodyne detection provides us with direct access to the optical sideband spectrum, which is presented in Fig. 2a for the resonant case  $\Delta \approx \omega_m$ . For small optical pump power, that is, in the regime of weak coupling, the splitting cannot be resolved and one obtains the well-known situation of resolved sideband laser cooling, in which Stokes and anti-Stokes photons are emitted at one specific sideband frequency. The splitting becomes clearly visible at larger pump powers, which is unambiguous evidence for entering the strong coupling regime. Indeed, at a maximum optical driving power of  $\sim 11$  mW, we obtain a coupling strength  $g = 2\pi \times 325$  kHz, which is larger than both  $\kappa = 2\pi \times 215$  kHz and  $\gamma_m = 2\pi \times 140$  Hz and which corresponds to the magnitude of the level crossing shown in Fig. 2b. As is expected, for detunings  $\Delta$  off resonance, the normal mode frequencies approach the values of the uncoupled system.

These characteristics of our strongly driven optomechanical system are reminiscent of a strongly driven two-level atom, and indeed a strong and instructive analogy exists. If an atom is pumped by a strong laser field, optical transitions can only occur between dressed atomic states, that is, atomic states ‘dressed’ by the interaction with the laser field. For strong driving, any Rabi splitting that is induced by strong coupling is effectively of order  $G_0 \sqrt{\langle n_L \rangle}$  ( $n_L$ , mean number of laser photons;  $G_0$ , electric dipole coupling) and one therefore obtains an equally spaced level splitting, fully analogous to the coupled optomechanical spectrum. From this point of view, the optomechanical modes can be interpreted in a dressed state approach as excitations of mechanical states that are dressed by the cavity radiation field. The origin of the sideband doublet as observed in the output field of the strongly driven optomechanical cavity corresponds to the resonance fluorescence spectrum of a strongly driven atom, in which strong

coupling gives rise to the two side-peaks in the so-called Mollow triplet. It is interesting to note that the analogy even holds for the single-photon regime, in which both systems are close to their quantum ground state. For both cases (that is, the atom–cavity system and the cavity–optomechanical system), a sufficiently strong single-photon interaction  $g_0$  would allow one to obtain the well-known vacuum Rabi splitting as well as state-dependent level spacing, which is due to intrinsic nonlinearities in the coupling.

We should stress that normal mode splitting alone does not establish a proof for coherent dynamics, that is, for quantum interference effects. With the present experimental parameters, such effects are washed out by thermal decoherence and normal mode splitting has a classical explanation in the framework of linear dispersion theory<sup>30</sup>. Still, the demonstration of normal mode splitting is a necessary condition for future quantum experiments.

We finally comment on the prospects for mechanical quantum state manipulation in the regime of strong coupling. One important additional requirement in most proposed schemes is the initialization of the mechanical device close to its quantum ground state. Recent theoretical results show that both ground state laser cooling and strong coupling can be achieved simultaneously, provided that the conditions  $\frac{\hbar\kappa T}{\hbar Q} \ll \kappa \ll \omega_m$  are fulfilled<sup>20,22</sup>. Thus, in addition to operating in the resolved sideband regime, a thermal decoherence rate that is small compared to the cavity decay rate is required. Cryogenic experiments have demonstrated thermal decoherence rates as low as 20 kHz for nanomechanical resonators for a 20 mK environment temperature<sup>9</sup>. For our experiment, temperatures below 300 mK would be sufficient to combine strong coupling with ground state cooling.

We have demonstrated strong coupling of a micromechanical resonator to an optical cavity field. This regime is a necessary precondition to obtaining quantum control of mechanical systems.

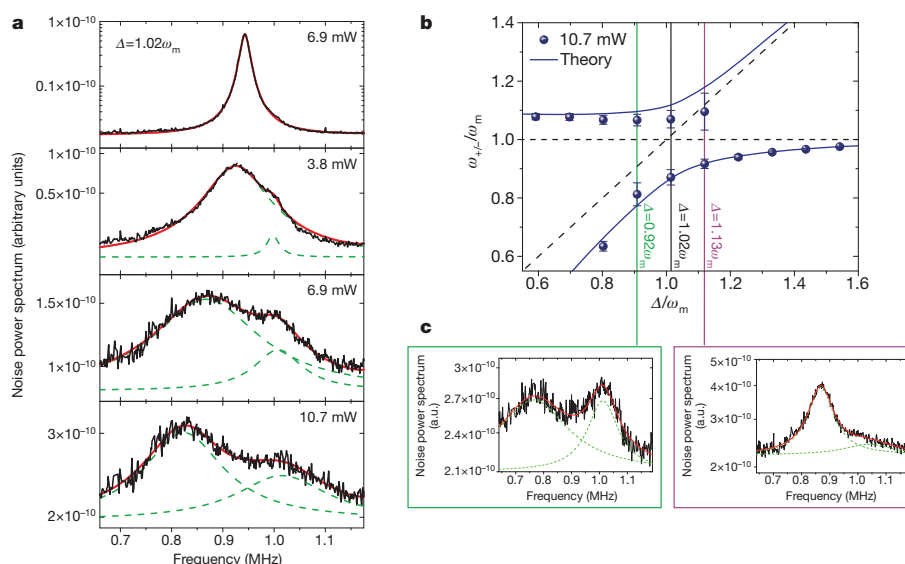


**Figure 2 | Optomechanical normal mode splitting and avoided crossing in the normal-mode frequency spectrum.** **a**, Emission spectra of the driven optomechanical cavity, obtained from sideband homodyne detection on the strong driving field after its interaction with the optomechanical system (see Supplementary Information). The power levels from top to bottom (0.6, 3.8, 6.9, 10.7 mW) correspond to an increasing coupling strength of  $g = 78, 192, 260$  and  $325$  kHz ( $g = 0.4, 0.9, 1.2, 1.5 \kappa$ ). All measurements are performed close to resonance ( $\Delta = 1.02 \omega_m$ ). For strong driving powers a splitting of the cavity emission occurs, corresponding to the normal mode frequencies of true hybrid optomechanical degrees of freedom. This normal mode splitting is an unambiguous signature of the strong coupling regime. All plots are shown on a logarithmic scale. Green dashed lines are fits to the data

assuming two independent Lorentzian curves, red solid lines are the sum signal of these two fits. **b**, Normal mode frequencies obtained from the fits to the spectra as a function of detuning  $\Delta$ . For far off-resonant driving, the normal modes approach the limiting case of two uncoupled systems. Dashed lines indicate the frequencies of the uncoupled optical (diagonal) and mechanical (horizontal) resonator, respectively. At resonance, normal mode splitting prevents a frequency degeneracy, which results in the shown avoided level crossing. Error bars, s.d. Solid lines are simulations (see Supplementary Information). For larger detuning values, the second normal mode peak could no longer be fitted owing to a nearby torsional mechanical mode. **c**, Normal mode spectra measured off resonance.

Together with the availability of high-quality mechanical resonators operated at low temperatures, which minimizes thermal decoherence of the mechanics, strong optomechanical coupling provides the basis for full photonic quantum control of massive mechanical resonators. We suggest that future developments will eventually also allow strong coupling to be achieved in the nonlinear regime, that is, at the single-photon level<sup>11,16</sup>, to exploit optomechanical vacuum Rabi splitting.

Received 4 February; accepted 26 May 2009.

- Naik, A. *et al.* Cooling a nanomechanical resonator with quantum back-action. *Nature* **443**, 193–196 (2006).
- Cleland, A. N., Aldridge, J. S., Driscoll, D. C. & Gossard, A. C. Nanomechanical displacement sensing using a quantum point contact. *Appl. Phys. Lett.* **81**, 1699–1701 (2002).
- Rugar, D., Budakian, R., Mamin, H. J. & Chui, B. W. Single spin detection by magnetic resonance force microscopy. *Nature* **430**, 329–332 (2004).
- Rabl, P. *et al.* Strong magnetic coupling between an electronic spin qubit and a mechanical resonator. *Phys. Rev. B* **79**, 041302(R) (2009).
- Kippenberg, T. J., Rokhsari, H., Carmon, T., Scherer, A. & Vahala, K. J. Analysis of radiation-pressure induced mechanical oscillation of an optical microcavity. *Phys. Rev. Lett.* **95**, 033901 (2005).
- Gigan, S. *et al.* Self-cooling of a micromirror by radiation pressure. *Nature* **444**, 67–71 (2006).
- Arcizet, O., Cohadon, P.-F., Briant, T., Pinard, M. & Heidmann, A. Radiation-pressure cooling and micromechanical instability of a micromirror. *Nature* **444**, 71–75 (2006).
- Thompson, J. D. *et al.* Strong dispersive coupling of a high-finesse cavity to a micromechanical membrane. *Nature* **452**, 72–75 (2008).
- Regal, C. A., Teufel, J. D. & Lehnert, K. W. Measuring nanomechanical motion with a microwave cavity interferometer. *Nature Phys.* **4**, 555–560 (2008).
- Eichenfield, M., Michael, C. P., Perahia, R. & Painter, O. Actuation of micro-optomechanical systems via cavity-enhanced optical dipole forces. *Nature Photon.* **1**, 416–422 (2007).
- Li, M. *et al.* Harnessing optical forces in integrated photonic circuits. *Nature* **456**, 480–484 (2008).
- Walther, H., Varcoe, B. T. H., Englert, B.-G. & Becker, T. Cavity quantum electrodynamics. *Rep. Prog. Phys.* **69**, 1325–1382 (2006).
- Khitrova, G., Gibbs, H. M., Kira, M., Koch, S. W. & Scherer, A. Vacuum Rabi splitting in semiconductors. *Nature Phys.* **2**, 81–90 (2006).
- Wallraff, A. *et al.* Strong coupling of a single photon to a superconducting qubit using circuit quantum electrodynamics. *Nature* **431**, 162–167 (2004).
- Bose, S., Jacobs, K. & Knight, P. L. Preparation of nonclassical states in cavities with a moving mirror. *Phys. Rev. A* **56**, 4175–4186 (1997).
- Marshall, W., Simon, C., Penrose, R. & Bouwmeester, D. Towards quantum superpositions of a mirror. *Phys. Rev. Lett.* **91**, 130401 (2003).
- Vitali, D. *et al.* Optomechanical entanglement between a movable mirror and a cavity field. *Phys. Rev. Lett.* **98**, 030405 (2007).
- Clerk, A. A., Marquardt, F. & Jacobs, K. Back-action evasion and squeezing of a mechanical resonator using a cavity detector. *N. J. Phys.* **10**, 095010 (2008).
- Marquardt, F., Chen, J. P., Clerk, A. A. & Girvin, S. M. Quantum theory of cavity-assisted sideband cooling of mechanical motion. *Phys. Rev. Lett.* **99**, 093902 (2007).
- Dobrindt, J. M., Wilson-Rae, I. & Kippenberg, T. J. Parametric normal-mode splitting in cavity optomechanics. *Phys. Rev. Lett.* **101**, 263602 (2008).
- Hammerer, K., Aspelmeyer, M., Polzik, E. & Zoller, P. Establishing Einstein-Podolsky-Rosen channels between nanomechanics and atomic ensembles. *Phys. Rev. Lett.* **102**, 020501 (2009).
- Wilson Rae, I., Nooshi, N., Dobrindt, J., Kippenberg, T. J. & Zwerger, W. Cavity-assisted backaction cooling of mechanical resonators. *N. J. Phys.* **10**, 095007 (2008).
- Zhang, J., Peng, K. & Braunstein, S. L. Quantum-state transfer from light to macroscopic oscillators. *Phys. Rev. A* **68**, 013808 (2003).
- Thompson, R. J., Rempe, G. & Kimble, H. J. Observation of normal-mode splitting for an atom in an optical cavity. *Phys. Rev. Lett.* **68**, 1132–1135 (1992).
- Colombe, Y. *et al.* Strong atom–field coupling for Bose–Einstein condensates in an optical cavity on a chip. *Nature* **450**, 272–276 (2007).
- Aoki, T. *et al.* Observation of strong coupling between one atom and a monolithic microresonator. *Nature* **443**, 671–674 (2006).
- Reithmaier, J. P. *et al.* Strong coupling in a single quantum dot–semiconductor microcavity system. *Nature* **432**, 197–200 (2004).
- Weisbuch, C., Nishioka, M., Ishikawa, A. & Arakawa, Y. Observation of the coupled exciton-photon mode splitting in a semiconductor quantum microcavity. *Phys. Rev. Lett.* **69**, 3314–3317 (1992).
- Yoshie, T. *et al.* Vacuum Rabi splitting with a single quantum dot in a photonic crystal nanocavity. *Nature* **432**, 200–203 (2004).
- Zhu, Y. *et al.* Vacuum Rabi splitting as a feature of linear-dispersion theory: analysis and experimental observations. *Phys. Rev. Lett.* **64**, 2499–2502 (1990).

Supplementary Information is linked to the online version of the paper at [www.nature.com/nature](http://www.nature.com/nature).

**Acknowledgements** We are grateful to T. Corbitt, C. Genes, S. Gofßler, P. K. Lam, G. Milburn, P. Rabl and P. Zoller for discussions. We also thank M. Metzler, R. Ilic and M. Skvarla (CNF), and K. C. Schwab and J. Hertzberg, for microfabrication support, and R. Blach for technical support. We acknowledge financial support from the Austrian Science Fund FWF, the European Commission and the Foundational Questions Institute. S.G. is a recipient of a DOC fellowship of the Austrian Academy of Sciences; S.G. and M.R.V. are members of the FWF doctoral programme Complex Quantum Systems (CoQuS).

**Author Contributions** All authors have made a significant contribution to the concept, design, execution or interpretation of the presented work.

**Author Information** Reprints and permissions information is available at [www.nature.com/reprints](http://www.nature.com/reprints). Correspondence and requests for materials should be addressed to M.A. ([markus.aspelmeyer@quantum.at](mailto:markus.aspelmeyer@quantum.at)).

## SUPPLEMENTARY INFORMATION

## I. NORMAL MODE FREQUENCIES AND DAMPING RATES

As shown in [1–3] the linearized Hamiltonian for a driven cavity mode coupled via radiation pressure to a harmonically bound mirror is

$$H = \frac{\hbar\Delta}{2}(X_c^2 + P_c^2) + \frac{\hbar\omega_m}{2}(X_m^2 + P_m^2) - \hbar g X_c X_m \quad (\text{S1})$$

with an opto-mechanical coupling rate  $g = g_0\alpha = \frac{2}{L}\sqrt{\frac{P\kappa\omega_c}{m\omega_m(\kappa^2 + \Delta^2)}}$  (following [3]) for an input power  $P$  of the driving laser ( $L$ ,  $\omega_c$  and  $\kappa$  are cavity length, resonance and amplitude decay rate respectively,  $m$  the effective mass of the mechanical oscillator). For a two-sided cavity with decay rate  $\kappa$  through the input-coupler and  $\bar{\kappa}$  through the oscillating mirror, this formula generalizes to  $g = \frac{2}{L}\sqrt{\frac{P\kappa\omega_c}{m\omega_m((\kappa + \bar{\kappa})^2 + \Delta^2)}}$ .

It is convenient to define  $\vec{R}^T = (X_c, P_c, X_m, P_m)$  and express the Hamiltonian as  $H = \frac{\hbar}{2}\vec{R}^T M \vec{R}$  where

$$M = \begin{pmatrix} \Delta & 0 & g & 0 \\ 0 & \Delta & 0 & 0 \\ g & 0 & \omega_m & 0 \\ 0 & 0 & 0 & \omega_m \end{pmatrix}.$$

The transformation to normal modes  $\vec{R}^{\text{NM}} = (X_+, P_+, X_-, P_-)$  is achieved with a linear transformation  $\vec{R}^{\text{NM}} = S\vec{R}$ , where  $S$  fulfills  $M = S^T \text{diag}(\omega_+, \omega_+, \omega_-, \omega_-)S$  and is symplectic, i.e. it obeys  $J = SJS^T$  where

$$J = \begin{pmatrix} 0 & 1 & 0 & 0 \\ -1 & 0 & 0 & 0 \\ 0 & 0 & 0 & 1 \\ 0 & 0 & -1 & 0 \end{pmatrix}.$$

The latter property guarantees that canonical commutation relations are conserved, i.e.  $[\vec{R}_i, \vec{R}_j] = [\vec{R}_i^{\text{NM}}, \vec{R}_j^{\text{NM}}] = iJ_{ij}$ . The explicit form of  $S$  can in principle be determined, but is quite involved and does not give much insight. As will become clear in a moment, the normal mode frequencies  $\omega_{\pm}$  can be easily calculated without constructing  $S$  and are given by

$$\omega_{\pm}^2 = \frac{1}{2} \left( \Delta^2 + \omega_m^2 \pm \sqrt{(\Delta^2 - \omega_m^2)^2 + 4g^2\omega_m\Delta} \right). \quad (\text{S2})$$

The canonical operators evolve according to

$$\begin{aligned} \dot{\vec{R}}(t) &= i[H, \vec{R}(t)] - D\vec{R}(t) - \sqrt{2D}\vec{R}_{\text{in}}(t) \\ &= (JM - D)\vec{R}(t) - \sqrt{2D}\vec{R}_{\text{in}}(t), \end{aligned} \quad (\text{S3})$$

where we included damping of the cavity field and the mechanical resonator with  $D = \text{diag}(\kappa, \kappa, \gamma_m^0, \gamma_m^0)$  and Langevin forces  $\vec{R}_{\text{in}}(t) = (x_{\text{in}}, p_{\text{in}}, f_{X_m}, f_{P_m})$ . For white vacuum noise input to the cavity and a thermal white noise bath coupling to the mechanical system, all first moments vanish  $\langle \vec{R}(t) \rangle \equiv 0$  and the only non-zero two time correlation functions are

$$\begin{aligned} \langle x_{\text{in}}(t)x_{\text{in}}(t') \rangle &= \langle p_{\text{in}}(t)p_{\text{in}}(t') \rangle = \frac{1}{2}\delta(t - t'), \\ \langle f_{X_m}(t)f_{X_m}(t') \rangle &= \langle f_{P_m}(t)f_{P_m}(t') \rangle = \left( \bar{n} + \frac{1}{2} \right) \delta(t - t'), \end{aligned} \quad (\text{S4})$$

where  $\bar{n} \simeq \frac{kT}{\hbar\omega_m}$ .

From Eq. (S3) it is clear that eigenfrequencies and effective damping rates of the system are given by, respectively, the imaginary and real parts of the eigenvalues of  $i(JM - D)$ . The eigenvalues occur in complex conjugate pairs and the imaginary parts of the ones in the upper half plane determine eigenfrequencies. For the undamped system,  $D = 0$ , the eigenvalues are purely complex and one arrives at expression (S2) for the normal mode frequencies. For the damped system,  $D \neq 0$ , the eigenvalues of  $i(JM - D)$  will in general be complex and thus determine normal mode frequencies  $\omega_{\pm}$  and effective damping rates  $\gamma_{\pm}$  of normal modes, as exemplified in Fig. S1. The theoretical values of the normal mode frequencies  $\omega_{\pm}$  in Fig. 2a of the main text were as well determined in this way. While normal mode splitting (NMS) occurs for any non-zero coupling  $g$  in an undamped system, a threshold of  $g \gtrsim \kappa$  has to be surpassed to observe NMS [2, 4]. Effective damping rates behave complementary and merge above the same threshold. Comparison of the normal mode damping rates  $\gamma_{\pm}$  to the effective mechanical damping rate  $\gamma_m = \gamma_m^0 + \frac{2g^2\kappa\Delta\omega_m}{[\kappa^2 + (\Delta - \omega_m)^2][\kappa^2 + (\Delta + \omega_m)^2]}$ , as derived in the theory for cavity-assisted cooling [1, 3], shows that the condition for resolving the normal mode peaks is  $g \gg \kappa, \gamma_m$ .

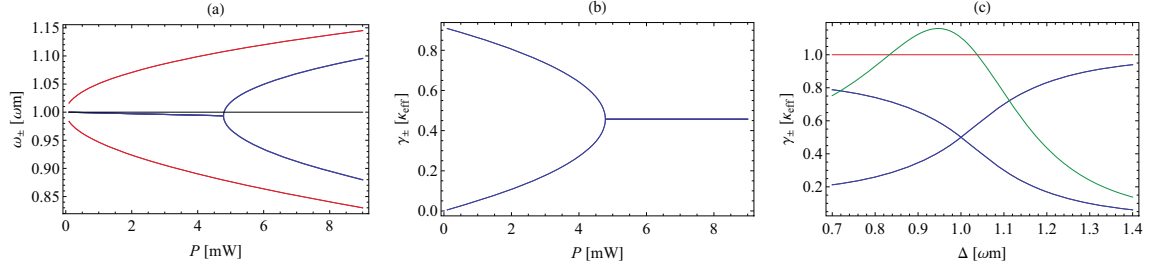


FIG. S1: (a) Normal mode frequencies  $\omega_{\pm}$  for undamped system (red) and damped system (blue) for varying power of driving laser. (b) Same for effective normal mode damping  $\gamma_{\pm}$ . (c) Effective damping rates of normal modes (blue), cavity amplitude decay rate  $\kappa$  (red) and effective mechanical decay rate  $\gamma_m$  (green) for varying detuning. Not shown is the natural mechanical damping rate as  $\gamma_m^0/\kappa \simeq 10^{-3}$ . Parameters are as in the main text,  $\omega_m = 2\pi \times 947$  kHz,  $\gamma_m^0 = 2\pi \times 140$  Hz,  $m = 145$  ng,  $L = 2.5$  cm,  $\omega_c = 1.77 \times 10^{15}$  Hz,  $\kappa = 2\pi \times 172$  kHz and  $\bar{\kappa} = 2\pi \times 43$  kHz. In (a) and (b)  $\Delta = \omega_m$  and in (c)  $P = 10.7$  mW.

## II. CAVITY EMISSION SPECTRUM

### A. Dressed States and Exact Diagonalization

In terms of normal mode operators the linearized Hamiltonian (S1) is given by  $H = \frac{\hbar\omega_{\pm}}{2}(X_{\pm}^2 + P_{\pm}^2) + \frac{\hbar\omega_{\mp}}{2}(X_{\mp}^2 + P_{\mp}^2)$ . It can be expressed also in terms of creation and annihilation operators  $a_{\pm} = (X_{\pm} + iP_{\pm})/\sqrt{2}$  as  $H = \hbar\omega_{+}(a_{+}^{\dagger}a_{+} + \frac{1}{2}) + \hbar\omega_{-}(a_{-}^{\dagger}a_{-} + \frac{1}{2})$ . The Eigenstates and -energies are thus  $H|n, m\rangle = E_{n, m}|n, m\rangle$ , where

$$|n, m\rangle = \frac{1}{\sqrt{n!m!}}(a_{+}^{\dagger})^n(a_{-}^{\dagger})^m|0, 0\rangle,$$

$$E_{n, m} = \hbar\omega_{+}(n + \frac{1}{2}) + \hbar\omega_{-}(m + \frac{1}{2}).$$

Emission of a cavity photon is in general accompanied by a transition of the opto-mechanical system from one eigenstate to another by changing a single excitation,  $|n, m\rangle \leftrightarrow |n-1, m\rangle$  and  $|n, m\rangle \leftrightarrow |n, m-1\rangle$ . The energy splitting between these states is  $E_{n, m} - E_{n-1, m} = \hbar\omega_{+}$  and  $E_{n, m} - E_{n, m-1} = \hbar\omega_{-}$  respectively. Photons emitted from the cavity have to carry away this energy excess/deficiency relative to the incoming laser photons of frequency  $\omega_L$ , i.e. they have to have frequencies  $\omega_L \pm \omega_{+}$  or  $\omega_L \pm \omega_{-}$ . Transitions between the dressed opto-mechanical states and the associated emission doublet is illustrated in Fig. S2.

In order to compare the low-energy part of the opto-mechanical spectrum to the one of the Jaynes Cummings system, as shown in Fig. 2 of the main text, we give here the exact eigenstates and -values of the non-linear radiation pressure Hamiltonian

$$H = \hbar\omega_m a_m^{\dagger} a_m + \hbar\Delta a_c^{\dagger} a_c - \hbar g_0 a_m^{\dagger} a_m (a_c + a_c^{\dagger}).$$

It is straight forward to check that  $H|\psi_{k, n}\rangle = E_{k, n}|\psi_{k, n}\rangle$

with

$$|\psi_{k, n}\rangle = \exp\left[\frac{g_0 n}{\omega_m}(a_m - a_m^{\dagger})\right]|k\rangle_m|n\rangle_c,$$

$$E_{k, n} = \hbar\left(\omega_m k + \Delta n + \frac{g_0^2}{\omega_m} n^2\right).$$

That is, the eigenstates are shifted Fock states of the uncoupled system and the energy spectrum is anharmonic with a *quadratic* dependence in the photon number. The "opto-mechanical Rabi splitting" is thus  $\frac{g_0^2}{\omega_m}$ , see also Fig. S2.

### B. Emission Power Spectrum

The power spectral density of light emitted by the cavity is explicitly determined as follows: In frequency space  $[\vec{R}(\omega) = \int d\omega \vec{R}(t) \exp(i\omega t)/\sqrt{2\pi}]$  the steady state solutions to the equations of motion (S3) are

$$\vec{R}(\omega) = \frac{1}{i\omega + JM - D} \sqrt{2D} \vec{R}_{\text{in}}(\omega). \quad (\text{S5})$$

With the quantum optical cavity input-output relations it follows that

$$\begin{aligned} \vec{R}_{\text{out}}(\omega) &= \sqrt{2D} \vec{R}(\omega) + \vec{R}_{\text{in}}(\omega) \\ &= \left( \sqrt{2D} \frac{1}{i\omega + JM - D} \sqrt{2D} + 1 \right) \vec{R}_{\text{in}}(\omega), \end{aligned}$$

where  $\vec{R}_{\text{out}}(\omega) = (x_{\text{out}}, p_{\text{out}}, f_{X_m, \text{out}}, f_{P_m, \text{out}})$ .  $(x_{\text{out}}, p_{\text{out}})$  are quadratures for the cavity output field which are subject to homodyne detection. In order to calculate their stationary properties we formally introduce also "phononic output fields"  $f_{X_m, \text{out}}, f_{P_m, \text{out}}$ . The spectral correlation functions can be collected in a Hermitean spectral  $4 \times 4$  correlation matrix  $\gamma_{ij}^{\text{out}}(\omega, \omega') = \langle (\vec{R}_{\text{out}}(\omega'))_i (\vec{R}_{\text{out}}(\omega))_j \rangle$ . Straight forward

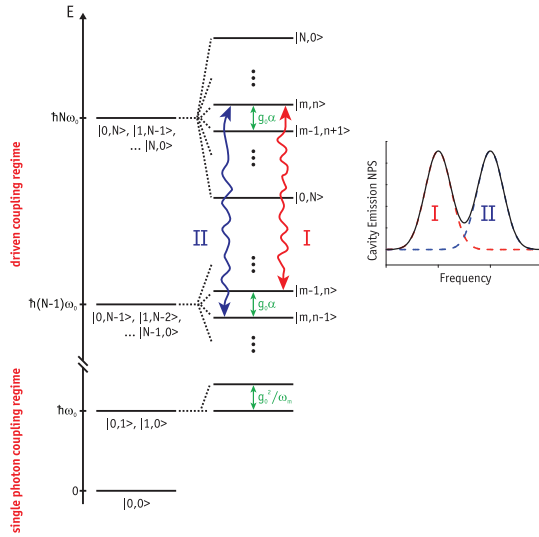


FIG. S2: Energy spectrum of a driven opto-mechanical cavity. For a degenerate, uncoupled system (left),  $\omega_m = \Delta$ ,  $g_0 = 0$ , the spectrum consists of equidistant multiplets of energy  $\hbar N\omega_m$  and degeneracy  $N$  ( $\hbar$ : Planck's constant;  $N$ : number of excitations;  $\omega_m$ : mechanical resonance frequency). For a coupled system (right),  $g_0 \neq 0$ , the degeneracy is broken. In the strongly driven regime, where the cavity is in a coherent state with mean number of photons  $\langle n_c \rangle$ , the levels in each  $N$ -multiplet split up by  $g = g_0\sqrt{\langle n_c \rangle}$  into dressed states  $|m, n\rangle$  with  $m + n = N$ . Emission of a cavity photon is accompanied only by transitions  $|m, n\rangle \leftrightarrow |m-1, n\rangle$  or  $|m, n\rangle \leftrightarrow |m, n-1\rangle$  between dressed states. Accordingly, emitted photons have to lie at sideband-frequencies  $\omega_L \pm \omega_{\pm}$ . This gives rise to a doublet structure in the sideband spectrum (bottom) with a splitting  $\omega_+ - \omega_- \approx g$ . The observed normal-mode splitting is shown in Figure 2 of the main text. In the single photon coupling regime, the fundamentally anharmonic nature of the spectrum becomes important, with a splitting between dressed states scaling like  $\frac{g_0^2 n_c^2}{\omega_m^3}$  (shown is the "opto-mechanical vacuum Rabi-splitting" for  $n_c = 1$ ). In the present experiment we cannot access this nonlinear regime, which would require a large single photon coupling  $g_0 \gg \kappa, \gamma_m$ .

calculation yields  $\gamma^{\text{out}}(\omega, \omega') = \delta(\omega + \omega')\Gamma(\omega)$  where

$$\Gamma(\omega) = \left( \sqrt{2\bar{D}} \frac{1}{i\omega + JM - D - \bar{D}} \sqrt{2\bar{D} + 1} \right) N \times \left( \sqrt{2\bar{D}} \frac{1}{-i\omega + JM - D - \bar{D}} \sqrt{2\bar{D} + 1} \right)^T$$

and  $N = \text{diag}(\frac{1}{2}, \frac{1}{2}, \bar{n} + \frac{1}{2}, \bar{n} + \frac{1}{2})$ . If losses through the second mirror with amplitude decay rate  $\bar{\kappa}$  are taken into

account, the last expression generalizes to

$$\Gamma(\omega) = \left( \sqrt{2\bar{D}} \frac{1}{i\omega + JM - D - \bar{D}} \sqrt{2\bar{D} + 1} \right) N \times \left( \sqrt{2\bar{D}} \frac{1}{-i\omega + JM - D - \bar{D}} \sqrt{2\bar{D} + 1} \right)^T + \left( \sqrt{2\bar{D}} \frac{1}{i\omega + JM - D - \bar{D}} \sqrt{2\bar{D}} \right) \bar{N} \times \left( \sqrt{2\bar{D}} \frac{1}{-i\omega + JM - D - \bar{D}} \sqrt{2\bar{D}} \right)^T, \quad (\text{S6})$$

where  $\bar{D} = \text{diag}(\bar{\kappa}, \bar{\kappa}, 0, 0)$  and  $\bar{N} = \text{diag}(\frac{1}{2}, \frac{1}{2}, 0, 0)$ .

Finally, the spectral density  $S(\omega)$  is defined as  $S(\omega)\delta(\omega + \omega') = \langle a_{\text{out}}^\dagger(\omega')a_{\text{out}}(\omega) \rangle$  where the amplitude operator for the cavity output field is  $a_{\text{out}}(\omega) = (x_{\text{out}}(\omega) + ip_{\text{out}}(\omega))\sqrt{2}$ . It follows from the definition of the spectral correlation matrix given above that

$$S(\omega) = \frac{1}{2} [\Gamma_{11}(\omega) + \Gamma_{22}(\omega) + i(\Gamma_{12}(\omega) - \Gamma_{21}(\omega))].$$

This expression gives the spectral density of sideband modes at a frequency  $\omega_L + \omega$ . In homodyne detection of sideband modes we do not distinguish sideband frequencies  $\omega_L \pm \omega$  and extract only the overall noise power spectrum at a sideband frequency  $|\omega|$ , which is given by  $S_{NPS}(\omega) = \sqrt{S(\omega)^2 + S(-\omega)^2}$  and shown in Fig. S3. The simple consideration in terms of dressed state transitions as given above shows good agreement with the exact calculated positions of spectral peaks, which are in turn in excellent agreement with measured data presented already in Fig. 2b of the main text.

### III. HOMODYNE DETECTION OF OPTICAL AND MECHANICAL QUADRATURES

We obtain the generalized optical and mechanical quadratures  $X_c$  and  $X_m$  via two independent, simultaneous optical homodyne measurements. Homodyne detection requires the mixing of a strong local oscillator field with the signal beam at a symmetric beamsplitter and a balanced photodetection at the beamsplitter output ports. The difference photocurrent then provides a direct measure of the generalized quadrature  $X(\phi, t) = a(t)e^{i\phi} + a^\dagger(t)e^{-i\phi}$  of an optical beam ( $\phi$ : local oscillator phase), where  $X(\phi = 0, t)$  and  $X(\phi = \frac{\pi}{2}, t)$  are the well-known amplitude and phase quadratures, respectively. To measure  $X_c$ , homodyning was performed on the driving beam after its interaction with the cavity. The second homodyning measures the locking beam after its resonant interaction with the cavity. Because of the weak interaction (we choose the power of the lock beam such that  $g \ll \kappa$ ) the cavity field phase quadrature adiabatically follows the evolution of the mechanics and hence provides direct access to  $X_m$ . The local oscillator phase in the homodyne measurement of the locking

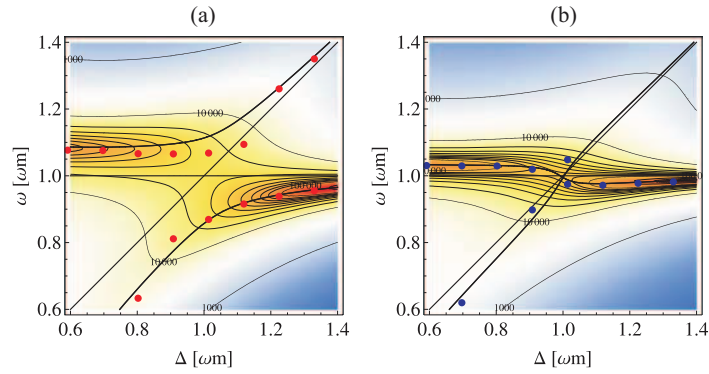


FIG. S3: (a) Emission spectrum  $S_{NPS}(\omega)$  of opto-mechanical system for varying detuning (colors refer to a logarithmic scale of arbitrary units). Peak positions are well described by the normal mode eigenfrequencies  $\omega_{\pm}$  (black lines). For comparison we reproduce also the measured data of presented in Fig. 3b of the main text. Parameters are as in S1, the input input power was  $P = 10.7$  mW. Expression (S6) was used to evaluate the spectrum with a cavity decay rate through the input-coupler  $\kappa = 2\pi \times 172$  kHz and at rate  $\bar{\kappa} = 2\pi \times 43$  kHz through the oscillating mirror. (b) Same for a power value  $P = 3.8$  mW just below threshold for normal mode splitting, cf. Fig. S1a.

field was always actively stabilized to detect the locking beam phase quadrature. Each of the two difference photocurrents was recorded independently by a high-speed analogue-to-digital converter (14 bit, 10 MSample  $\text{sec}^{-1}$ ).

The mechanical and optical noise power spectra from Figures 1b and 2a, respectively, were directly inferred from these recorded time traces. In that case, the local oscillator phase of the drive field was locked to a fixed value.

- 
- [1] I. Wilson-Rae, N. Nooshi, W. Zwerger, T. J. Kippenberg, Phys. Rev. Lett. **99**, 093901 (2007)
  - [2] F. Marquardt, J. P. Chen, A. A. Clerk, S. M. Girvin, Phys. Rev. Lett. **99**, 093902 (2007)
  - [3] C. Genes, D. Vitali, P. Tombesi, S. Gigan, M. Aspelmeyer, Phys. Rev. A **77**, 033804 (2008)
  - [4] J. M. Dobrindt, I. Wilson-Rae, T. J. Kippenberg, Phys. Rev. Lett. **101**, 263602 (2008)
  - [5] *Gradshteyn and Ryzhik's Table of Integrals, Series, and Products*, Alan Jeffrey and Daniel Zwillinger (eds.), Seventh edition, Academic Press (2007)
  - [6] V. Giovannetti, D. Vitali, Phys. Rev. A **63**, 023812 (2001)
  - [7] C.W. Gardiner, P. Zoller, *Quantum Noise*, Springer Series in Synergetics (2004)



## 8 Optomechanical down-conversion

To demonstrate optomechanical down-conversion we follow the scheme described in section 3.3.6. We set the detuning  $\Delta \approx \omega_m$  for the pump beam and increase the pump power until breaking the rotating wave approximation. For our parameters the limit for  $g \gtrsim \omega_m$  is at a power level of  $P \gtrsim 15$  mW (this takes into account a typical coupling efficiency of  $\sim 75\%$  of the pump beam to the cavity mode). Our optomechanical cavity comprises a micromechanical resonator, made of a  $150 \times 50 \times 1 \mu\text{m}^3$  SiN beam with a high reflectivity ( $> 99.991\%$ ) dielectric mirror pad in its center (diameter  $50 \mu\text{m}$ ) as one of the end mirrors of a Fabry-Pérot cavity of length  $L = 25$  mm and linewidth  $\kappa = 464$  kHz. Its mechanical resonance frequency is  $\omega_m/2\pi \approx 950$  kHz, its mechanical quality factor  $Q \approx 6,700$  and the effective mass  $m_{eff} = 55$  ng (see section 4.10). Due to the lower reflectivity of the second cavity mirror (99.91%) we obtain a good approximation of a single-sided cavity of finesse  $F \approx 6,300$ . We use a Nd:YAG laser at  $\lambda = 1,064$  nm both for pumping the optomechanical cavity and for read-out of the mechanics. For this we split the laser beam into a faint ( $\approx 15 \mu\text{W}$ ) read-out and a strong (up to 4 mW) driving beam on a polarizing beam splitter (PBS), as is shown in figure 8.1 and described in detail in section 4.4. In addition, the faint beam is phase modulated by an electro-optical modulator (EOM) to achieve Pound-Drever-Hall stabilization (cf. section 4.3.1) of the pump laser frequency with respect to the optomechanical cavity by acting back on the laser. Frequency detuning of the driving beam with respect to the cavity frequency is achieved by acousto-optic modulation (AOM). Both beams are then recombined into the same spatial mode of the optomechanical cavity. Note, however that they always remain distinguishable due to their orthogonal polarization. The experiment is performed at room temperature in vacuum ( $\sim 10^{-6}$  mbar).

We confirm the specific nature of the optomechanical interaction via direct phase-sensitive correlation measurements. The generalized optical and mechanical quadratures  $X_c$  and  $X_m$  are obtained via two independent, simultaneous optical homodyne measurements, which are performed on the reflected parts of the driving and the locking field, respectively. For the homodyne detection the signal beam is mixed with a strong local oscillator on a 50 : 50 beamsplitter and each output port is measured on balanced photodetectors. The two photocurrents are subtracted, which gives direct access to the generalized quadrature  $X(\phi, t) = a(t)e^{i\phi} + a^\dagger(t)e^{-i\phi}$  of the signal beam. Here  $\phi$  is the phase between the local oscillator and the signal field, with  $X(\phi = 0, t)$  and  $X(\phi = \frac{\pi}{2}, t)$  being the amplitude and phase quadratures, respectively. In order to measure  $X_c(\phi)$ , the off-resonant driving beam is homodyned after its interaction with the cavity, while in the second homodyne detector the locking beam is measured after its resonant interaction with the cavity (cf. Figure 8.1). The lock beam is chosen to be very faint  $g \ll \kappa$  and hence its cavity fields phase

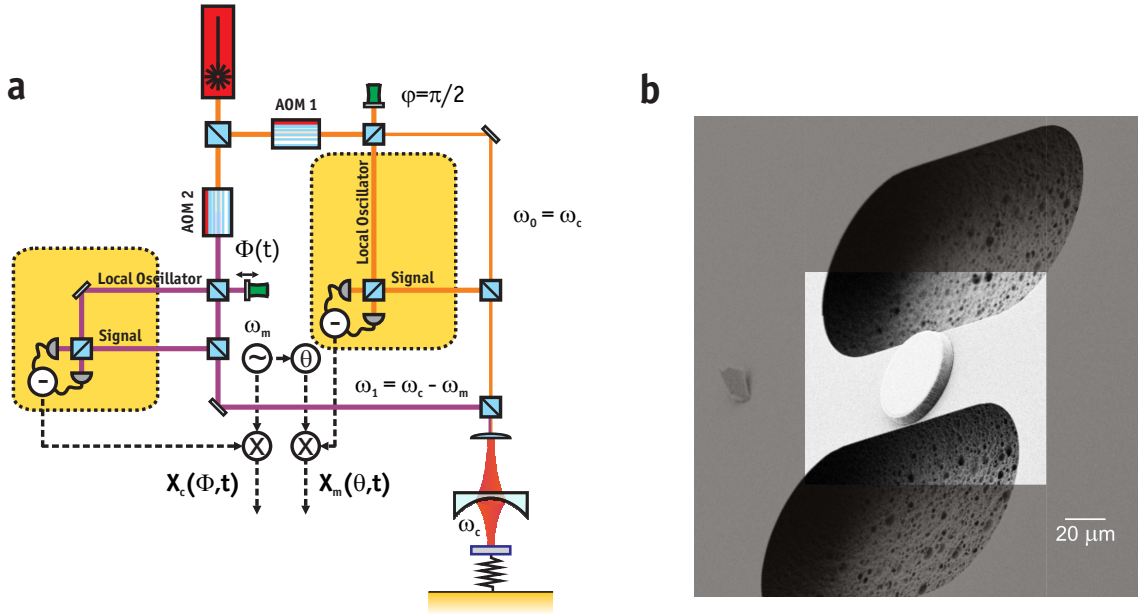


Figure 8.1: **a** Experimental setup. The generalized optical and mechanical quadratures  $X_c(\phi, t)$  and  $X_m(\theta, t)$  are obtained from two independent, time-synchronized homodyne measurements of the driving and the locking beam, respectively. Electronic demodulation of the homodyne currents at the mechanical frequency  $\omega_m$  provides access to this slowly varying sideband components of the optical fields. The phase angles  $\phi$  and  $\theta$  are varied by scanning both the optical local oscillator phase of the driving beam homodyne and the electronic phase of the lock beam demodulation. We only consider the regime of resonant coupling, i.e.  $\Delta = \omega_m$ . **b** Scanning electron microscope (SEM) picture of the micromechanical resonator, with the high-reflectivity dielectric mirror pad in its center.

quadrature adiabatically follows the evolution of the mechanical resonator, providing direct access to  $X_m$ . In addition, the phase between the local oscillator and the lock beam signal is actively stabilized in order to only detect the fields phase quadrature. We finally have to consider that the generalized quadratures  $X_c$  and  $X_m$  are defined relative to a frame rotating at their respective eigenmode frequencies  $\Delta$  and  $\omega_m$ . Since we only consider the resonant case, multiplication of each real time data set by  $\sin(\omega_m t + \theta_{c,m})$  and application of a low-pass filter to suppress higher order harmonics of the demodulation results in the wanted quadratures [35].

For our measurements the local oscillator phase  $\phi$  of the drive beam homodyne measurement was scanned at a rate of 0.1 Hz while independently storing the real time data for both homodyne detectors with a high-speed analogue-to-digital converter (14 bit, 10 MSample  $\text{sec}^{-1}$ ). Each  $2\pi$  interval of the traces is divided into 36 equidistant time bins, in which  $\phi$  is assumed to be constant. After electronic demodulation, in which the phase  $\theta$  is only varied for the mechanical quadrature, i.e. the data of the resonant field, we therefore obtain data pairs  $\{X_c(\phi, t), X_m(\theta, t)\}$ . The correlation function  $\langle X_c(\phi)X_m(\theta) \rangle$  is obtained by calculating the normalized

co-variances

$$C(\theta, \phi) = \frac{\langle (A - \langle A \rangle) \cdot (B - \langle B \rangle) \rangle}{\sqrt{\langle (A - \langle A \rangle)^2 \rangle \cdot \langle (B - \langle B \rangle)^2 \rangle}} \quad (8.1)$$

for data sets measured within the same time window. Here  $A$  ( $B$ ) is the demodulated and low-pass filtered signal for the weak (strong) field and  $\langle \cdot \rangle$  denotes the mean for data pairs measured at different times  $t$  at a fixed electronic and optical phase  $\theta$  and  $\phi$ , respectively. By changing both phases over  $2\pi$  the density plots (Fig. 8.2b) of the correlation function  $C(\theta, \phi)$  were obtained.

In the regime where the rotating wave approximation is valid, and where the interaction between the optical and the mechanical mode is effectively given by a “beam splitter” Hamiltonian  $H_{bs} = g(a_c a_m^\dagger + a_c^\dagger a_m)$ , the observed correlations obey the specific symmetry  $C(\phi, \phi) = \text{const.}$ , independent of  $\phi$ . This implies in particular  $\langle X_c X_m \rangle = \langle P_c P_m \rangle$ . This symmetry is actually required by the interaction Hamiltonian  $H_{bs}$  itself, which is invariant under a change of phases  $a_m \rightarrow a_m e^{i\phi}$  and  $a_c \rightarrow a_c e^{i\phi}$ , imposing this symmetry also for the steady state of the system, and therefore also on the observed correlations. In the regime beyond the rotating wave approximation, where counter-rotating terms contribute, the steady state will be determined by the full Hamiltonian in Eq. (3.84). The said symmetry is broken in this Hamiltonian, and by the same reasoning, also in the observed correlations  $C(\phi, \phi) \neq C(\phi', \phi')$ . This symmetry breaking can be attributed to the contribution of down-conversion dynamics in the optomechanical interaction.

Moreover, if the observed correlations were solely due to a down-conversion interaction, we would expect an oscillation between positive and negative values of  $C$ , corresponding to correlations in the  $X$ -quadratures  $-C(\phi, \phi) = \langle X_c X_m \rangle$  – and anti-correlations in the  $P$ -quadratures  $C(\phi + \frac{\pi}{2}, \phi + \frac{\pi}{2}) = \langle P_c P_m \rangle$ . For the present system we accordingly observe increasing oscillations in  $C$  for larger optomechanical coupling  $g$ , however no negative values as the maximum coupling rate achieved was  $g \approx \omega_m/2 < \omega_m$ . In a more refined experiment we expect to be able to overcome the technical difficulties currently limiting  $g$  and be able to show anti-correlations, which would demonstrate important characteristics of EPR correlations.

In order to witness entanglement, it is in fact enough to measure correlations  $C$  which are strong on a scale set essentially by the zero point fluctuations of the system. The data presented here was taken at room temperature, such that no quantum entanglement can occur. However, our measurements do show striking evidence of optomechanical down-conversion dynamics and accordingly strong correlations between a micromechanical resonator and an optical cavity field.

At this stage the presented data is unpublished but as soon as more refined measurements are performed will be made public.

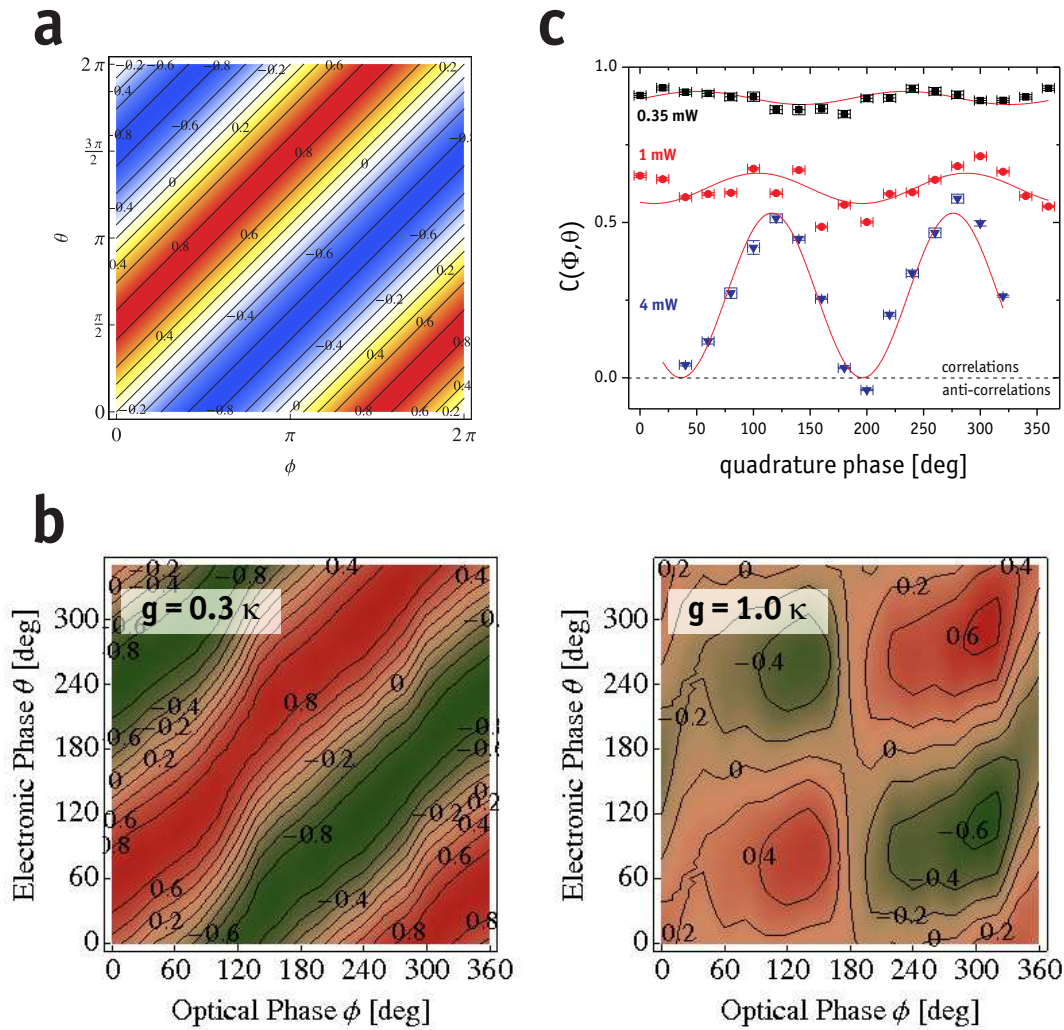


Figure 8.2: Optomechanical correlations. **a** Theoretical plot of the correlation function (8.1) for  $g \ll \omega_m$  and various values of  $\theta$  and  $\phi$ . **b** The correlation measurements were performed close to resonant coupling ( $\Delta = 1.03 \omega_m$ ). To achieve the mechanical read-out with minimum disturbance we use  $\kappa = 2\pi \times 475$  kHz and hence fulfill strong adiabaticity in the coupling of the lock beam ( $g_{lock} \leq 30$  kHz  $\ll \kappa, \omega_m$ ). For weak driving power ( $P = 0.35$  mW,  $g \approx 2\pi \times 135$  kHz) the symmetry is still present, indicating the validity of the rotating wave approximation (RWA) to a high degree. When approaching the strong coupling regime ( $P = 4$  mW,  $g \approx 2\pi \times 464$  kHz  $\approx \kappa$ ) the symmetry is clearly broken, which can be directly attributed to the counter-rotating interaction terms and a corresponding breakdown of the RWA. **c** Although the contribution of the counter-rotating terms for  $g_{4mW} \approx \omega_m/2 < \omega_m$  is already visible, they are not sufficiently strong to produce detectable 2-mode squeezing, which is the reason why the correlations remain fully positive. The crossing between correlations and anti-correlations is determined by the noise floor – if it is dominated by classical (quantum) noise, anti-correlations correspond to optomechanical squashing (squeezing). The quadrature phase denotes the phase difference between  $\theta$  and  $\phi$ .

## 9 Conclusions & Outlook

In this work we have shown how light can be used to modify the dynamics of a mechanical oscillator via the radiation-pressure force. By utilizing the toolbox of quantum optics, the interaction can in principle be used to demonstrate mechanical quantum behavior of a truly macroscopic system. We have demonstrated the necessary experimental requirements for entering this regime, including a high-finesse Fabry-Pérot cavity, a mechanical resonator with high optical reflectivity and very good mechanical quality, homodyne detection, cryogenic precooling of the mechanical system, a classical-noise free laser system and stable locking loops, among others. In our experiments we have demonstrated all the ingredients needed for showing macroscopic quantum phenomena. We have passively cooled the mechanical motion close to its quantum ground state in a cryogenic cavity, as well as shown that the optical and mechanical system in our experiment can be strongly coupled, which is necessary for achieving coherent energy exchange between the two. In addition, we have performed an experiment where we have measured the correlations of the optical and the mechanical system, a prerequisite for demonstrating optomechanical entanglement. While we were not able to actually show any quantum effect yet, we are very confident that this is within very close reach.

Future experimental improvements might include a digital locking system for cascaded cavity locks, allowing stable operation of multiple high-finesse cavities.

Further advances in the quality of our mechanical systems are vital as a higher quality factor  $Q$  allows for larger cooling factors in our self-cooling scheme. Also, the stable operation of a cavity inside the dilution refrigerator at mK temperatures will most likely be achieved soon, finally allowing us to cool the mechanical oscillation into its ground state.

More ambitious future goals include the realization of an optomechanical system that can be strongly coupled to a single photon. This would open up the possibility to directly exploit the single photon non-linearities, with consequences for both the classical and quantum domain. For example, experiments such as the observation of optomechanical vacuum Rabi splitting would become feasible, which is the basis for several quantum information schemes [160].

The field of cavity opto-mechanics has evolved very rapidly over the past years and is on the verge of becoming the field of cavity quantum-optomechanics. A lot of work has already been done but the most exciting and revolutionary experiments are yet to come.



## 10 Bibliography

- [1] L. Bergmann and C. Schaefer, *Lehrbuch der Experimentalphysik: Band 1 - Mechanik, Relativität, Wärme* (de Gruyter, 1998). [11](#), [12](#)
- [2] L. D. Landau and E. M. Lifshitz, *Mechanics*, 3<sup>rd</sup> edn. (Butterworth-Heinemann, 1976). [13](#)
- [3] A. A. Clerk, M. H. Devoret, S. M. Girvin, F. Marquardt, and R. J. Schoelkopf, Introduction to quantum noise, measurement, and amplification, *Rev. Mod. Phys.* **82**, 1155 (2010). [14](#), [19](#), [23](#), [29](#), [101](#)
- [4] G. Breitenbach, *Quantum state reconstruction of classical and nonclassical light and a cryogenic opto-mechanical sensor for high-precision interferometry*, Ph.D. thesis, Universität Konstanz (1998). [14](#), [20](#)
- [5] R. Givens, O. F. de Alcantara Bonfim, and R. B. Ormond, Direct observation of normal modes in coupled oscillators, *Am. J. Phys.* **71**, 87 (2003). [15](#)
- [6] E. Schrödinger, Der stetige Übergang von der Mikro- zur Makromechanik, *Naturwissenschaften* **14**, 664 (1926). [18](#)
- [7] R. J. Glauber, Coherent and Incoherent States of the Radiation Field, *Phys. Rev.* **131**, 2766 (1963). [18](#)
- [8] H.-A. Bachor and T. C. Ralph, *A Guide to Experiments in Quantum Optics*, 2<sup>nd</sup> edn. (Wiley-VCH, 2004). [19](#), [62](#)
- [9] E. Wigner, On the Quantum Correction for Thermodynamic Equilibrium, *Phys. Rev.* **40**, 749 (1932). [19](#)
- [10] R. W. Spekkens, Negativity and Contextuality are Equivalent Notions of Non-classicality, *Phys. Rev. Lett.* **101**, 020401 (2009). [20](#)
- [11] M. Hillery, R. F. O’Connell, M. O. Scully, and E. P. Wigner, Distribution functions in physics: Fundamentals, *Phys. Rep.* **106**, 121 (1984). [20](#)
- [12] J. Kepler, Letter to Galileo Galilei (1610). [20](#)
- [13] J. Kepler, *De Cometis Libelli Tres* (Augsburg, 1619). [20](#)
- [14] P. Lebedev, Untersuchungen über die Druckkräfte des Lichtes, *Ann. Phys.* **6**, 433 (1901). [21](#)
- [15] E. F. Nichols and G. F. Hull, About Radiation pressure, *Ann. Phys.* **12**, 225 (1903). [21](#)

- 
- [16] J. C. Maxwell, *A treatise on electricity and magnetism*, vol. 2 (Clarendon Press, Oxford, 1873). 21
- [17] A. G. Bartoli, *Sopra i movimenti prodotti dalla luce e dal calore e sopra il radiometro di Crookes* (Le Monnier, Florence, 1876). 21
- [18] V. B. Braginsky, *Eksp. Teor. Fiz.* **53**, 1434 (1967). 21
- [19] V. B. Braginsky and Y. I. Vorontsov, Quantum-mechanical limitations in macroscopic experiments and modern experimental technique, *Sov. Phys. Usp.* **17**, 644 (1975). 21
- [20] V. Braginsky and A. Manukin, *Measurement of weak forces in Physics experiments* (Univ. of Chicago Press, 1977). 21
- [21] C. M. Caves, Quantum-Mechanical Radiation-Pressure Fluctuations in an Interferometer, *Phys. Rev. Lett.* **45**, 75 (1980). 21
- [22] P. Meystre, E. M. Wright, J. D. McCullen, and E. Vignes, Theory of radiation-pressure-driven interferometers, *J. Opt. Soc. Am. B* **2**, 1830 (1985). 21
- [23] A. Dorsel, J. McCullen, P. Meystre, E. Vignes, and H. Walther, Optical Bistability and Mirror Confinement Induced by Radiation Pressure, *Phys. Rev. Lett.* **51**, 1550 (1983). 21
- [24] C. Fabre, M. Pinard, S. Bourzeix, A. Heidmann, E. Giacobino, and S. Reynaud, Quantum-noise reduction using a cavity with a movable mirror, *Phys. Rev. A* **49**, 1337 (1994). 21
- [25] S. Mancini and P. Tombesi, Quantum noise reduction by radiation pressure, *Phys. Rev. A* **49**, 4055 (1994). 21
- [26] K. Jacobs, P. Tombesi, M. J. Collett, and D. F. Walls, Quantum-nondemolition measurement of photon number using radiation pressure, *Phys. Rev. A* **49**, 1961 (1994). 21, 27
- [27] M. Pinard, C. Fabre, and A. Heidmann, Quantum-nondemolition measurement of light by a piezoelectric crystal, *Phys. Rev. A* **51**, 2443 (1995). 21, 27
- [28] S. Mancini, D. Vitali, and P. Tombesi, Optomechanical Cooling of a Macroscopic Oscillator by Homodyne Feedback, *Phys. Rev. Lett.* **80**, 688 (1998). 21
- [29] P.-F. Cohadon, A. Heidmann, and M. Pinard, Cooling of a Mirror by Radiation Pressure, *Phys. Rev. Lett.* **83**, 3174 (1999). 21, 95
- [30] S. Mancini, V. I. Man'ko, and P. Tombesi, Ponderomotive control of quantum macroscopic coherence, *Phys. Rev. A* **55**, 3042 (1997). 21
- [31] S. Bose, K. Jacobs, and P. L. Knight, Preparation of nonclassical states in cavities with a moving mirror, *Phys. Rev. A* **56**, 4175 (1997). 32, 111



- 
- [32] W. Marshall, C. Simon, R. Penrose, and D. Bouwmeester, Towards Quantum Superpositions of a Mirror, *Phys. Rev. Lett.* **91**, 130401 (2003). [21](#), [111](#)
- [33] J. Zhang, K. Peng, and S. L. Braunstein, Quantum-state transfer from light to macroscopic oscillators, *Phys. Rev. A* **68**, 013808 (2003). [21](#)
- [34] I. Tittoen, G. Breitenbach, T. Kalkbrenner, T. Müller, R. Conradt, S. Schiller, E. Steinsland, N. Blanc, and N. F. de Rooij, Interferometric measurements of the position of a macroscopic body: Towards observation of quantum limits, *Phys. Rev. A* **59**, 1038 (1999). [21](#)
- [35] T. Briant, P. Cohadon, M. Pinard, and A. Heidmann, Optical phase-space reconstruction of mirror motion at the attometer level, *Eur. Phys. J. D* **22**, 131 (2003). [64](#), [122](#)
- [36] O. Arcizet, P.-F. Cohadon, T. Briant, M. Pinard, A. Heidmann, J.-M. Mackowski, C. Michel, L. Pinard, O. François, and L. Rousseau, High-sensitivity optical monitoring of a micro-mechanical resonator with a quantum-limited optomechanical sensor, *Phys. Rev. Lett.* **97**, 133601 (2006). [21](#)
- [37] T. Kippenberg, H. Rokhsari, T. Carmon, A. Scherer, and K. Vahala, Analysis of Radiation-Pressure Induced Mechanical Oscillation of an Optical Microcavity, *Phys. Rev. Lett.* **95**, 033901 (2005). [21](#), [26](#)
- [38] S. Gigan, H. R. Böhm, M. Paternostro, F. Blaser, G. Langer, J. B. Hertzberg, K. C. Schwab, D. Bäuerle, M. Aspelmeyer, and A. Zeilinger, Self-cooling of a micromirror by radiation pressure, *Nature* **444**, 67 (2006). [21](#), [27](#), [34](#), [52](#), [60](#), [66](#), [80](#), [82](#), [95](#), [101](#), [112](#)
- [39] O. Arcizet, P.-F. Cohadon, T. Briant, M. Pinard, and A. Heidmann, Radiation-pressure cooling and optomechanical instability of a micromirror, *Nature* **444**, 71 (2006). [23](#), [112](#)
- [40] A. Schliesser, P. Del’Haye, N. Nooshi, K. J. Vahala, and T. J. Kippenberg, Radiation Pressure Cooling of a Micromechanical Oscillator Using Dynamical Backaction, *Phys. Rev. Lett.* **97**, 243905 (2006). [34](#), [112](#)
- [41] T. Corbitt, Y. Chen, E. Innerhofer, H. Müller-Ebhardt, D. Ottaway, H. Rehbein, D. Sigg, S. Whitcomb, C. Wipf, and N. Mavalvala, An All-Optical Trap for a Gram-Scale Mirror, *Phys. Rev. Lett.* **98**, 150802 (2007). [21](#), [27](#)
- [42] S. Gröblacher, S. Gigan, H. R. Böhm, A. Zeilinger, and M. Aspelmeyer, Radiation-pressure self-cooling of a micromirror in a cryogenic environment, *Europhys. Lett.* **81**, 54003 (2008). [21](#)
- [43] S. Gröblacher, J. B. Hertzberg, M. R. Vanner, S. Gigan, K. C. Schwab, and M. Aspelmeyer, Demonstration of an ultracold micro-optomechanical oscillator in a cryogenic cavity, *Nature Phys.* **5**, 485 (2009). [71](#), [112](#)
- [44] Y.-S. Park and H. Wang, Resolved-sideband and cryogenic cooling of an optomechanical resonator, *Nature Phys.* **5**, 489 (2009).

- 
- [45] A. Schliesser, O. Arcizet, R. Rivière, G. Anetsberger, and T. J. Kippenberg, Resolved-sideband cooling and position measurement of a micromechanical oscillator close to the Heisenberg uncertainty limit, *Nature Phys.* **5**, 509 (2009). [21](#)
- [46] S. Gröblacher, K. Hammerer, M. R. Vanner, and M. Aspelmeyer, Observation of strong coupling between a micromechanical resonator and an optical cavity field, *Nature* **460**, 724 (2009). [21](#), [29](#), [32](#), [112](#)
- [47] E. F. Nichols and G. F. Hull, The Pressure Due to Radiation, *Proc. Am. Acad. Arts Sci.* **38**, 559 (1903). [21](#)
- [48] T. J. Kippenberg and K. J. Vahala, Cavity Opto-Mechanics, *Opt. Express* **15**, 17172 (2007). [21](#)
- [49] M. Aspelmeyer and K. C. Schwab, Mechanical Systems at the Quantum Limit, *New J. Phys.* **10**, 095001 (2008).
- [50] I. Favero and K. Karrai, Optomechanics of deformable optical cavities, *Nature Photon.* **3**, 201 (2009).
- [51] F. Marquardt and S. M. Girvin, Optomechanics, *Physics* **2**, 40 (2009).
- [52] C. Genes, A. Mari, D. Vitali, and P. Tombesi, Quantum effects in optomechanical systems, *Adv. At. Mol. Opt. Phys.* **57**, 33 (2009).
- [53] M. Aspelmeyer, S. Gröblacher, K. Hammerer, and N. Kiesel, Quantum optomechanics—throwing a glance, *J. Opt. Soc. Am. B* **27**, A189 (2010). [21](#)
- [54] A. Naik, O. Buu, M. D. LaHaye, A. D. Armour, A. A. Clerk, M. P. Blencowe, and K. C. Schwab, Cooling a nanomechanical resonator with quantum back-action, *Nature* **443**, 193 (2006). [21](#), [27](#)
- [55] C. A. Regal, J. D. Teufel, and K. W. Lehnert, Measuring nanomechanical motion with a microwave cavity interferometer, *Nature Phys.* **4**, 555 (2008).
- [56] J. D. Teufel, J. W. Harlow, C. A. Regal, and K. W. Lehnert, Dynamical Backaction of Microwave Fields on a Nanomechanical Oscillator, *Phys. Rev. Lett.* **101**, 197203 (2008). [27](#)
- [57] T. Rocheleau, T. Ndukum, C. Macklin, J. B. Hertzberg, A. A. Clerk, and K. C. Schwab, Preparation and detection of a mechanical resonator near the ground state of motion, *Nature* **463**, 72 (2010). [21](#), [27](#)
- [58] J. D. Jost, J. P. Home, J. M. Amini, D. Hanneke, R. Ozeri, C. Langer, J. J. Bollinger, D. Leibfried, and D. J. Wineland, Entangled mechanical oscillators, *Nature* **459**, 683 (2009). [21](#)
- [59] J. Kerr, On a New Relation between Electricity and Light: Dielectric Media Birefringent, *Phil. Mag.* **1**, 337 (1875). [21](#)

- 
- [60] D. J. Wineland and W. M. Itano, Laser cooling of atoms, *Phys. Rev. A* **20**, 1521 (1979). [22](#)
- [61] H. B. Callen and T. A. Welton, Irreversibility and Generalized Noise, *Phys. Rev.* **83**, 34 (1951). [23](#)
- [62] M. Pinard, Y. Hadjar, and A. Heidmann, Effective mass in quantum effects of radiation pressure, *Eur. Phys. J. D* **7**, 107 (1999). [24](#), [71](#)
- [63] M. Paternostro, S. Gigan, M. S. Kim, F. Blaser, H. R. Böhm, and M. Aspelmeyer, Reconstructing the dynamics of a movable mirror in a detuned optical cavity, *New J. Phys.* **8**, 107 (2006). [24](#), [26](#)
- [64] C. Genes, D. Vitali, P. Tombesi, S. Gigan, and M. Aspelmeyer, Ground-state cooling of a micromechanical oscillator: comparing cold damping and cavity-assisted cooling schemes, *Phys. Rev. A* **77**, 033804 (2008). [24](#), [26](#), [27](#)
- [65] C. K. Law, Effective Hamiltonian for the radiation in a cavity with a moving mirror and a time-varying dielectric medium, *Phys. Rev. A* **49**, 433 (1994). [24](#)
- [66] P. Langevin, Sur la théorie du mouvement brownien, *C. R. Acad. Sci.* **146**, 530 (1908). [24](#)
- [67] W. T. Coffey, Y. P. Kalmykov, and J. T. Waldron, *The Langevin Equation*, 2<sup>nd</sup> edn. (World Scientific Publishing, 2004). [25](#)
- [68] M. Vogel, C. Mooser, K. Karrai, and R. Wartburton, Optically tunable mechanics of microlevers, *Applied Physics Letters* **83**, 1337 (2003). [26](#)
- [69] B. Sheard, M. Gray, C. Mow-Lowry, and D. McClelland, Observation and characterization of an optical spring, *Phys. Rev. A* **69**, 051801 (2004). [26](#)
- [70] T. Corbitt, D. Ottaway, E. Innerhofer, J. Pelc, and N. Mavalvala, Measurement of radiation-pressure-induced optomechanical dynamics in a suspended Fabry-Perot cavity, *Phys. Rev. A* **74**, 021802 (2006).
- [71] A. D. Virgilio, L. Barsotti, S. Braccini, C. Bradaschia, G. Cella, C. Corda, V. Dattilo, I. Ferrante, F. Fidecaro, I. Fiori, F. Frasconi, A. Gennai, A. Giazotto, P. L. Penna, G. Losurdo, E. Majorana, M. Mantovani, A. Pasqualetti, D. Passuello, F. Piergiovanni, A. Porzio, P. Puppo, P. Rapagnani, F. Ricci, S. Solimeno, G. Vajente, and F. Vetrano, Experimental evidence for an optical spring, *Phys. Rev. A* **74**, 013813 (2006). [26](#)
- [72] T. Corbitt, C. Wipf, T. Bodiya, D. Ottaway, D. Sigg, N. Smith, S. Whitcomb, and N. Mavalvala, Optical Dilution and Feedback Cooling of a Gram-Scale Oscillator to 6.9 mK, *Phys. Rev. Lett.* **99**, 160801 (2007). [26](#), [95](#), [112](#)
- [73] L. Diósi, Laser linewidth hazard in optomechanical cooling, *Phys. Rev. A* **78**, 021801(R) (2008). [26](#)

- 
- [74] P. Rabl, C. Genes, K. Hammerer, and M. Aspelmeyer, Phase-noise induced limitations on cooling and coherent evolution in optomechanical systems, *Phys. Rev. A* **80**, 063819 (2009). [26](#)
- [75] I. Wilson-Rae, N. Nooshi, W. Zwerger, and T. J. Kippenberg, Theory of ground state cooling of a mechanical oscillator using dynamical back-action, *Phys. Rev. Lett.* **99**, 093901 (2007). [27](#)
- [76] F. Marquardt, J. P. Chen, A. A. Clerk, and S. M. Girvin, Quantum Theory of Cavity-Assisted Sideband Cooling of Mechanical Motion, *Phys. Rev. Lett.* **99**, 093902 (2007). [27](#), [31](#), [111](#)
- [77] J. D. Thompson, B. M. Zwickl, A. M. Jayich, F. Marquardt, S. M. Girvin, and J. G. E. Harris, Strong dispersive coupling of a high-finesse cavity to a micromechanical membrane, *Nature* **452**, 72 (2008). [27](#), [64](#), [112](#)
- [78] C. M. Caves, K. S. Thorne, R. W. P. Drever, V. D. Sandberg, and M. Zimmermann, On the measurement of a weak classical force coupled to a quantum-mechanical oscillator. I. Issues of principle, *Rev. Mod. Phys.* **52**, 341 (1980). [29](#)
- [79] V. Braginsky and F. Khalili, *Quantum Measurements* (Cambridge University Press, 1995). [29](#)
- [80] V. B. Braginsky, Y. I. Vorontsov, and K. S. Thorne, Quantum Nondemolition Measurements, *Science* **209**, 547 (1980). [29](#)
- [81] A. A. Clerk, F. Marquardt, and K. Jacobs, Back-action evasion and squeezing of a mechanical resonator using a cavity detector, *New J. Phys.* **10**, 095010 (2008). [111](#)
- [82] J. B. Hertzberg, T. Rocheleau, T. Ndukum, M. Savva, A. A. Clerk, and K. C. Schwab, Back-action-evading measurements of nanomechanical motion, *Nature Phys.* **6**, 213 (2009). [29](#)
- [83] H. Walther, B. T. H. Varcoe, B.-G. Englert, and T. Becker, Cavity quantum electrodynamics, *Rep. Prog. Phys.* **69**, 1325 (2006). [29](#)
- [84] A. Wallraff, D. I. Schuster, A. Blais, L. Frunzio, R.-S. Huang, J. Majer, S. Kumar, S. M. Girvin, and R. J. Schoelkopf, Strong coupling of a single photon to a superconducting qubit using circuit quantum electrodynamics, *Nature* **431**, 162 (2004). [29](#)
- [85] G. Khitrova, H. M. Gibbs, M. Kira, S. W. Koch, and A. Scherer, Vacuum Rabi splitting in semiconductors, *Nature Phys.* **2**, 81 (2006). [29](#)
- [86] J. M. Dobrindt, I. Wilson-Rae, and T. J. Kippenberg, Parametric Normal-Mode Splitting in Cavity Optomechanics, *Phys. Rev. Lett.* **101**, 263602 (2008). [31](#), [111](#)

- 
- [87] M. J. Collett and C. W. Gardiner, Squeezing of intracavity and traveling-wave light fields produced in parametric amplification, *Phys. Rev. A* **30**, 1386 (1984). [32](#)
- [88] C. W. Gardiner and M. J. Collett, Input and output in damped quantum systems: Quantum stochastic differential equations and the master equation, *Phys. Rev. A* **31**, 3761 (1985). [32](#)
- [89] E. Schrödinger, Die gegenwärtige Situation in der Quantenmechanik, *Die Naturwissenschaften* **48**, 808 (1935). [32](#)
- [90] C. H. Bennett, G. Brassard, C. Crépeau, R. Jozsa, A. Peres, and W. K. Wootters, Teleporting an unknown quantum state via dual classical and Einstein-Podolsky-Rosen channels, *Phys. Rev. Lett.* **70**, 1895 (1993). [33](#)
- [91] D. Bouwmeester, J.-W. Pan, K. Mattle, M. Eibl, H. Weinfurter, and A. Zeilinger, Experimental quantum teleportation, *Nature* **390**, 575 (1997). [33](#)
- [92] Z. Y. Ou, S. F. Pereira, H. J. Kimble, and K. C. Peng, Realization of the Einstein-Podolsky-Rosen paradox for continuous variables, *Phys. Rev. Lett.* **68**, 3663 (1992). [33](#), [34](#)
- [93] P. G. Kwiat, K. Mattle, H. Weinfurter, A. Zeilinger, A. V. Sergienko, and Y. Shih, New High-Intensity Source of Polarization-Entangled Photon Pairs, *Phys. Rev. Lett.* **75**, 4337 (1995). [33](#)
- [94] A. Einstein, B. Podolsky, and N. Rosen, Can Quantum-Mechanical Description of Physical Reality Be Considered Complete?, *Phys. Rev.* **47**, 777 (1935). [33](#), [34](#)
- [95] S. L. Braunstein and P. van Loock, Quantum information with continuous variables, *Rev. Mod. Phys.* **77**, 513 (2005). [34](#)
- [96] C. Simon and D. Bouwmeester, Theory of an Entanglement Laser, *Phys. Rev. Lett.* **91**, 053601 (2003). [34](#)
- [97] A. Furusawa, J. L. Sørensen, S. L. Braunstein, C. A. Fuchs, H. J. Kimble, and E. S. Polzik, Unconditional Quantum Teleportation, *Science* **282**, 706 (1998). [34](#)
- [98] M. B. Plenio, Logarithmic Negativity: A Full Entanglement Monotone That is not Convex, *Phys. Rev. Lett.* **95**, 090503 (2005). [35](#)
- [99] V. Braginsky and S. P. Vyatchanin, Low quantum noise tranquilizer for Fabry-Perot interferometer, *Phys. Lett. A* **293**, 228 (2002). [34](#)
- [100] P. Meystre and M. Sargent, *Elements of Quantum Optics* (Springer, Heidelberg, 1990). [34](#)

- [101] S. Hofferberth, B. Fischer, T. Schumm, J. Schmiedmayer, and I. Lesanovsky, Ultracold atoms in radio-frequency dressed potentials beyond the rotating-wave approximation, *Phys. Rev. A* **76**, 013401 (2007). 35
- [102] D. Rugar, H. J. Mamin, R. Erlandsson, J. E. Stern, and B. D. Terris, Force microscope using a fiber-optic displacement sensor, *Rev. Mod. Instrum.* **59**, 2337 (1988). 37
- [103] K. Gugler, *Aufbau und Charakterisierung eines Faser-Interferometers für Quantenexperimente an mikromechanischen Spiegeln*, Master's thesis, Universität Wien (2008). 37
- [104] G. D. Cole, I. Wilson-Rae, M. R. Vanner, S. Gröblacher, J. Pohl, M. Zorn, M. Weyers, A. Peters, and M. Aspelmeyer, Megahertz monocrystalline optomechanical resonators with minimal dissipation, in *23rd IEEE International Conference on Microelectromechanical Systems, Hong Kong SAR, China, 24-28 January 2010, TP133*. (2010). 37, 88, 89
- [105] H. R. Böhm, *Radiation-Pressure Cooling of a Mechanical Oscillator*, Ph.D. thesis, Universität Wien (2008). 37, 43, 48, 50, 55
- [106] B. E. A. Saleh and M. C. Teich, *Fundamentals of Photonics* (John Wiley & Sons, Inc., 1991). 39, 40, 41, 46
- [107] R. Paschotta, *Encyclopedia of Laser Physics and Technology* (Wiley-VCH, 2008). 39
- [108] A. E. Siegman, *Lasers* (University Science Books, 1986). 39
- [109] R. W. P. Drever, J. L. Hall, F. V. Kowalski, J. Hough, G. M. Ford, A. J. Munley, and H. Ward, Laser phase and frequency stabilization using an optical resonator, *Appl. Phys. B* **31**, 97 (1983). 43
- [110] R. V. Pound, Electronic Frequency Stabilization of Microwave Oscillators, *Rev. Sci. Instrum.* **17**, 490 (1946). 43
- [111] E. D. Black, An introduction to Pound-Drever-Hall laser frequency stabilization, *Amer. Jour. of Phys.* **69**, 79 (2001). 44, 45
- [112] D. A. Shaddock, M. B. Gray, and D. E. McClelland, Frequency locking a laser to an optical cavity by use of spatial mode interference, *Opt. Lett.* **24**, 1499 (1999). 48
- [113] S. Goßler, Private communication. 51
- [114] H. R. Böhm, S. Gigan, G. Langer, J. B. Hertzberg, F. Blaser, D. Bäuerle, K. C. Schwab, A. Zeilinger, and M. Aspelmeyer, High reflectivity high-Q micromechanical Bragg mirror, *Appl. Phys. Lett.* **89**, 223101 (2006). 56, 80, 82
- [115] J. Poirson, F. Bretenaker, M. Vallet, and A. L. Floch, Analytical and experimental study of ringing effects in a Fabry–Perot cavity. Application to the measurement of high finesses, *J. Opt. Soc. Am. B* **14**, 2811 (1997). 56

- 
- [116] H. S. Black, *Modulation Theory* (Van Nostrand, 1953). 67
- [117] R. D. Blevins, *Formulas for Natural Frequency and Mode Shape* (Krieger Publishing Company, 1984). 70, 82
- [118] L. D. Landau, L. P. Pitaevskii, E. M. Lifshitz, and A. M. Kosevich, *Theory of Elasticity*, 3<sup>rd</sup> edn. (Butterworth-Heinemann, 1986).
- [119] F. Blaser, *Mechanical FEM Analysis and Optical Properties of micromirrors for radiation-pressure experiments*, Master's thesis, Université de Neuchâtel (2008). 70
- [120] I. Tanaeva, *Low-temperature cryocooling*, Ph.D. thesis, Technische Universiteit Eindhoven (2004). 74
- [121] K. Uhlig, <sup>3</sup>He/<sup>4</sup>He dilution refrigerator with pulse-tube refrigerator precooling, *Cryogenics* **42**, 73 (2002). 74
- [122] D. Wernicke, Private communication. 78
- [123] F. Pobell, *Matter and Methods at Low Temperatures*, 3<sup>rd</sup> edn. (Springer, 2007). 78
- [124] E. R. I. Abraham and E. A. Cornell, Teflon feedthrough for coupling optical fibers into ultrahigh vacuum systems, *Appl. Optics* **37**, 1762 (1998). 78
- [125] A. J. Leggett, Testing the limits of quantum mechanics: motivation, state of play, prospects, *J. Phys.: Condens. Matter* **14**, R415 (2002). 79
- [126] M. Arndt, M. Aspelmeyer, and A. Zeilinger, How to extend quantum experiments, *Fortschr. Phys.* **57**, 1153 (2009).
- [127] M. Aspelmeyer, Quantum mechanics: The surf is up, *Nature* **464**, 685 (2010). 79
- [128] D. A. Harrington and M. L. Roukes, *Caltech Technical Rep. No. CMP-106* (1994). 80
- [129] C. H. Metzger and K. Karrai, Cavity cooling of a microlever, *Nature* **432**, 1002 (2004). 80
- [130] G. Rempe, R. J. Thompson, H. J. Kimble, and R. Lalezari, Measurement of ultralow losses in an optical interferometer, *Opt. Lett.* **17**, 363 (1992). 82
- [131] R. Lalezari, Private communication. 82
- [132] S. D. Penn, P. H. Sneddon, H. Armandula, J. C. Betzwieser, G. Cagnoli, J. Camp, D. R. M. Crooks, M. M. Fejer, A. M. Gretarsson, G. M. Harry, J. Hough, S. E. Kittelberger, M. J. Mortonson, R. Route, S. Rowan, and C. C. Vassiliou, Mechanical loss in tantala/silica dielectric mirror coatings, *Class. Quantum Grav.* **20**, 2917 (2003). 82

- [133] G. M. Harry, H. Armandula, E. Black, D. R. M. Crooks, G. Cagnoli, J. Hough, P. Murray, S. Reid, S. Rowan, P. Sneddon, M. M. Fejer, R. Route, and S. D. Penn, Thermal noise from optical coatings in gravitational wave detectors, *Appl. Opt.* **45**, 1569 (2006). 82, 84
- [134] L. Sekaric, D. W. Carr, S. Evoy, J. M. Parpia, and H. G. Craighead, Nanomechanical resonant structures in silicon nitride: fabrication, operation and dissipation issues, *Sens. Actuat. A: Phys.* **101**, 215 (2002). 83
- [135] S. S. Verbridge, H. G. Craighead, and J. M. Parpia, A megahertz nanomechanical resonator with room temperature quality factor over a million, *Appl. Phys. Lett.* **92**, 013112 (2008).
- [136] D. R. Southworth, R. A. Barton, S. S. Verbridge, B. Ilic, A. D. Fefferman, H. G. Craighead, and J. M. Parpia, Stress and Silicon Nitride: A Crack in the Universal Dissipation of Glasses, *Phys. Rev. Lett.* **102**, 225503 (2009). 83
- [137] P. W. Anderson, B. I. Halperin, and C. M. Varma, Anomalous low-temperature thermal properties of glasses and spin glasses, *Philos. Mag.* **25**, 1 (1972). 84
- [138] G. M. Harry, A. M. Gretarsson, P. R. Saulson, S. E. Kittelberger, S. D. Penn, W. J. Startin, S. Rowan, M. M. Fejer, D. R. M. Crooks, G. Cagnoli, J. Hough, and N. Nakagawa, Thermal noise in interferometric gravitational wave detectors due to dielectric optical coatings, *Class. Quantum Grav.* **19**, 897 (2002). 84
- [139] I. Wilson-Rae, Intrinsic dissipation in nanomechanical resonators due to phonon tunneling, *Phys. Rev. B* **77**, 245418 (2008). 88, 89
- [140] G. D. Cole, I. Wilson-Rae, K. Werbach, M. R. Vanner, and M. Aspelmeyer, Minimization of phonon-tunneling dissipation in mechanical resonators, *arXiv:1007.4948* (2010). 88, 89, 93
- [141] C. Zener, Internal Friction in Solids. I. Theory of Internal Friction in Reeds, *Phys. Rev.* **52**, 230 (1937). 88
- [142] R. Lifshitz and M. L. Roukes, Thermoelastic damping in micro- and nanomechanical systems, *Phys. Rev. B* **61**, 5600 (2000).
- [143] A. Duwel, R. N. Candler, T. W. Kenny, and M. Varghese, Engineering MEMS resonators with low thermoelastic damping, *J. Microelectromech. S.* **15**, 1437 (2006). 88
- [144] G. D. Cole, S. Gröblacher, K. Gugler, S. Gigan, and M. Aspelmeyer, Monocrystalline  $\text{Al}_x\text{Ga}_{1-x}\text{As}$  heterostructures for high-reflectivity high-Q micromechanical resonators in the megahertz regime, *Appl. Phys. Lett.* **92**, 261108 (2008). 89
- [145] C. Wilmsen, H. Temkin, and L. A. Coldren (eds.), *Vertical-Cavity Surface-Emitting Lasers: Design, Fabrication, Characterization, and Applications* (Cambridge University Press, 1999). 89



- 
- [146] G. D. Cole, Y. Bai, M. Aspelmeyer, and E. A. Fitzgerald, Free-standing  $\text{Al}_x\text{Ga}_{1-x}\text{As}$  heterostructures by gas-phase etching of germanium, *Appl. Phys. Lett.* **96**, 261102 (2010). 89
- [147] A. D. O'Connell, M. Hofheinz, M. Ansmann, R. C. Bialczak, M. Lenander, E. Lucero, M. Neeley, D. Sank, H. Wang, M. Weides, J. Wenner, J. M. Martinis, and A. N. Cleland, Quantum ground state and single-phonon control of a mechanical resonator, *Nature* **464**, 697 (2010). 95
- [148] K. J. Bruland, J. L. Garbini, W. M. Dougherty, and J. A. Sidles, Optimal control of force microscope cantilevers. II. Magnetic coupling implementation, *J. Appl. Phys.* **80**, 1959 (1996). 95
- [149] A. Hopkins, K. Jacobs, S. Habib, and K. Schwab, Feedback cooling of a nanomechanical resonator, *Phys. Rev. B* **68**, 235328 (2003).
- [150] D. Kleckner and D. Bouwmeester, Sub-kelvin optical cooling of a micromechanical resonator, *Nature* **444**, 75 (2006). 95
- [151] D. Vitali, S. Gigan, A. Ferreira, H. R. Böhm, P. Tombesi, A. Guerreiro, V. Vedral, A. Zeilinger, and M. Aspelmeyer, Optomechanical Entanglement between a Movable Mirror and a Cavity Field, *Phys. Rev. Lett.* **98**, 030405 (2007). 111
- [152] A. Schliesser, R. Rivière, G. Anetsberger, O. Arcizet, and T. J. Kippenberg, Resolved-sideband cooling of a micromechanical oscillator, *Nature Phys.* **4**, 415 (2008). 112
- [153] G. Anetsberger, O. Arcizet, Q. P. Unterreithmeier, R. Rivière, A. Schliesser, E. M. Weig, J. P. Kotthaus, and T. J. Kippenberg, Near-field cavity optomechanics with nanomechanical oscillators, *Nature Phys.* **5**, 909 (2009). 112
- [154] M. Eichenfield, R. Camacho, J. Chan, K. J. Vahala, and O. Painter, A picogram- and nanometre-scale photonic-crystal optomechanical cavity, *Nature* **459**, 550 (2009). 112
- [155] M. Eichenfield, J. Chan, R. M. Camacho, K. J. Vahala, and O. Painter, Optomechanical crystals, *Nature* **462**, 78 (2009). 112
- [156] D. J. Wilson, C. A. Regal, S. B. Papp, and H. J. Kimble, Cavity Optomechanics with Stoichiometric SiN Films, *Phys. Rev. Lett.* **103**, 207204 (2009). 112
- [157] M. Li, W. H. P. Pernice, and H. X. Tang, Reactive Cavity Optical Force on Microdisk-Coupled Nanomechanical Beam Waveguides, *Phys. Rev. Lett.* **103**, 223901 (2009). 112
- [158] A. H. Safavi-Naeini, T. P. M. Alegre, M. Winger, and O. Painter, Optomechanics in an ultrahigh-Q slotted 2D photonic crystal cavity, *Appl. Phys. Lett.* **97**, 181106 (2010). 112
- [159] L. Ding, C. Baker, P. Senellart, A. Lemaitre, S. Ducci, G. Leo, and I. Favero, High frequency GaAs nano-optomechanical disk resonator, *arXiv:1007.3392* (2010). 112

- [160] S. Haroche and J.-M. Raimond, *Exploring the Quantum: Atoms, Cavities, and Photons* (Oxford University Press, 2006). [125](#)

# Acknowledgements

Writing the acknowledgments of a thesis is probably the hardest part. – During the more than 4 years of my doctorate I interacted with so many people that it is virtually impossible to remember all and to decide who I should thank for what. Of course I would like to thank every single one, as even the briefest encounters are often valuable or simply enjoyable, sometimes even more than the ones that I had continuously. Nonetheless, some people stick out of the crowd and those I would like to especially thank here and now:

Markus, I don't even know how to thank you. Without your help none of this here would have happened. The past years really were the time of my life! And this is almost completely thanks to you. You are just the best mentor I could have ever wished for. And you are so much more than just an advisor – you are a real friend! I hope you really know how grateful I am.

Anton, thank you for giving me the chance to work and learn in your group, an accumulation of so many bright and interesting people.

Sabine for being so kind and sharing Markus' time with me so long and patiently, especially during the early years of my PhD.

The mirror crew deserves very special thanks for creating this fantastic working environment in our group – I'm still always amazed by so much motivation. I'm also very grateful for everything we do that has nothing to do with physics (especially after lunch)! **DANKE** Sylvain, Hannes, Mauro, Kathrin, Garrett, Michael, Nikolai, Witlef, Alexey, Florian, Uros, Jonas, Rainer, Sebastian, Klemens, Katharina, Dilek, and of course Alexandra!!!

Keith for giving me the opportunity to work with his group and therefore providing us with the mechanical structures without none of the experiments in this thesis would have been possible. – I always felt very welcome!

Jared for (all the motivation to endure) the endless hours in the cleanroom, for everything I learned on microfabrication and the great chats.

Tchefor, Meredith, Mike and Rob for their helping hands and ideas in the cleanroom.

I would also like to thank those in the quantum group that have been good friends throughout all my years in Vienna and made it worth getting up every morning and go to work – Robert, Max, Johannes, Thomas, Alessandro, Tomek,

Tabi, Rupert, and Sven!

Of course I don't want to forget the people that rarely get the recognition they deserve but make the life of a physicist so much easier: Roland, Gerhard, Andreas, Waltraud, Aylin, Ursula, Dany, Canan, Verena, Elke, Martina, Alexander and Andrea – thank you so much!

Physics very often is not only true teamwork but also very expensive. Therefore I would also like to thank the Austrian Science Fund (FWF), the Austrian Academy of Sciences for my DOC stipend, the Vienna doctoral program on complex quantum systems (CoQuS) and also the IQOQI Vienna and the Cornell Nanoscale Facility (CNF) for the hospitality.

There are a lot of other people who made a big difference and who helped me to get through my dissertation: above of all my family. Mama, Papa, Hella, Klaus, Clara, Daniel, Judith, Julia, Agnes, Lucia, mãe, pai, Sidi, Jê, Lili, mano and Nachito. Thanks for supporting me and making me who I am today. I love you. And then there are those people I also truly love and that have always been there for me: Philipp, Chris, Sergio, Ingo, Leonie, Lauren, Nico, Hong, Caro, Kiki and needless to say Ju.

# Curriculum Vitae

**Place of Birth:** St. Pölten, Austria  
**E-mail:** [simon.groebbacher@quantum.at](mailto:simon.groebbacher@quantum.at)

## Educational History

- 02/2006 – PhD Thesis with Prof. Markus Aspelmeyer and Prof. Anton Zeilinger at the Austrian Academy of Sciences and the University of Vienna: *Experiments on "quantum mechanical" state engineering: combining quantum optics with nano-mechanics*
- 10/2004 – 12/2005 Diploma Thesis with Prof. Anton Zeilinger at the University of Vienna: *Experimental Investigation of Quantum Communication Protocols in Higher Dimensions*
- 01/2004 – 09/2004 Studies at the Universidade Federal do Rio de Janeiro, RJ, Brazil, in the quantum optics group of Prof. Paulo H. S. Ribeiro
- 10/2001 – 12/2005 Physics studies at the University of Vienna with distinction
- 10/2000 – Astronomy studies at the University of Vienna  
Portuguese & Spanish studies at the University of Vienna
- 06/1999 Matura at the Bundesrealgymnasium Krems a. d. Donau with distinction
- 07/1997 – 06/1998 Exchange year at the Colégio Sagrado Coração de Jesus, Ijuí, Rio Grande do Sul, Brazil, with AFS (American Field Service)
- 09/1991 – 05/1999 Bundesrealgymnasium Krems a. d. Donau

## Teaching Experience

- 09/2007 – 02/2008 Lab Courses in Quantum Optics

## Work Experience

- 08/2010 – 09/2010 Secondment at Caltech, CA, USA, with Prof. Oskar Painter
- 07/2010 Cleanroom work at Cornell University, NY, USA, hosted by Prof. Keith Schwab
- 12/2008 Cleanroom work at Cornell University, NY, USA, hosted by Prof. Keith Schwab
- 08/2007 Cleanroom work at Cornell University, NY, USA, hosted by Prof. Keith Schwab
- 08/2003 – 09/2003 *Investigation of the efficiency of the Skim-Programs at BELLE* for the Institute of High Energy Physics of the Austrian Academy of Sciences at the BELLE-Experiment, KEK, Tsukuba, Japan

## Other Work Experience

- 02/2006 – 10/2006    Civilian service at the environmental organisation Global 2000 as system administrator
- 04/2005 –            System administrator at the Faculty of Physics, University of Vienna and at the Institute for Quantum Optics and Quantum Information, Austrian Academy of Sciences
- 10/2004 – 12/2005    Photographer for Vienna Online
- 02/2001 – 09/2001    European Voluntary Service, Project: „Märjamaa Cultural House“, Raplamaa, Estonia
- 07/1998 – 07/2002    Volunteer for AFS Austria

## Scholarships & Awards

- 11/2010              Nano-Prize 2010 of the Erwin Schrödinger Society for Nanosciences
- 03/2010              Bank Austria Research Award 2010
- 01/2008 – 12/2009    DOC-fellowship of the Austrian Academy of Sciences
- 10/2007 –            Member of the FWF doctoral programme Complex Quantum Systems (CoQuS)
- 10/2006              3<sup>rd</sup> Prize at the INITS Award 2006 of the Founder Service of the Universities
- 01/2004 – 09/2004    Top-Stipendium Exchange Scholarship from the State of Lower Austria
- 06/2003              Top-Stipendium Scholarship from the State of Lower Austria

## Qualifications

<b>Languages:</b>	German:	mother tongue
	Portuguese:	fluent, written and spoken
	English:	fluent, written and spoken
	Spanish:	good knowledge
	French:	average knowledge
	Estonian:	basic knowledge

## Publications

### Peer-reviewed journals:

- M. Aspelmeyer, S. Gröblacher, K. Hammerer, and N. Kiesel, *Quantum optomechanics – throwing a glance*, J. Opt. Soc. Am. B **27**, A189 – A197 (2010)
- S. Gröblacher, K. Hammerer, M. R. Vanner, and M. Aspelmeyer, *Observation of strong coupling between a micromechanical resonator and an optical cavity field*, Nature **460**, 724 – 727 (2009)
- S. Gröblacher, J. B. Hertzberg, M. R. Vanner, S. Gigan, K. C. Schwab, and M. Aspelmeyer, *Demonstration of an ultracold micro-optomechanical oscillator in a cryogenic cavity*, Nature Phys. **5**, 485 – 488 (2009)
- G. D. Cole, S. Gröblacher, K. Gugler, S. Gigan, and M. Aspelmeyer, *Monocrystalline  $Al_xGa_{1-x}As$  heterostructures for high-reflectivity high-Q micromechanical resonators in the megahertz regime*, Appl. Phys. Lett. **92**, 261108 (2008)
- S. Gröblacher, S. Gigan, H. R. Böhm, A. Zeilinger, and M. Aspelmeyer, *Radiation-pressure self-cooling of a micromirror in a cryogenic environment*, Europhys. Lett. **81**, 54003 (2008)
- T. Paterek, A. Fedrizzi, S. Gröblacher, T. Jennewein, M. Żukowski, M. Aspelmeyer, A. Zeilinger, *Experimental Test of Nonlocal Realistic Theories Without the Rotational Symmetry Assumption*, Phys. Rev. Lett. **99**, 210406 (2007)
- M. Stütz, S. Gröblacher, T. Jennewein, and A. Zeilinger, *How to create and detect  $N$ -dimensional entangled photons with an active phase hologram*, Appl. Phys. Lett. **90**, 261114 (2007)
- S. Gröblacher, T. Paterek, R. Kaltenbaek, Č. Brukner, M. Żukowski, M. Aspelmeyer, and A. Zeilinger, *An experimental test of non-local realism*, Nature **446**, 871 – 875 (2007)
- S. Gröblacher, T. Jennewein, A. Vaziri, G. Weihs, and A. Zeilinger, *Experimental Quantum Cryptography with Qutrits*, New J. Phys. **8**, 75 (2006)

### Diploma Thesis:

- S. Gröblacher, *Experimental Investigation of Quantum Communication Protocols in Higher Dimensions*, University of Vienna (2005)

### Talks:

- S. Gröblacher, *Quantum opto-mechanics: how to use micromechanics in quantum experiments*, QFS 2010 (Grenoble, France, August 01-07, 2010) (2010)
- S. Gröblacher, *Quantum optical control of micro-mechanical resonators*, Lukin Group at Harvard University (Cambridge, MA, USA, April 02, 2010) (2010)
- S. Gröblacher, *An experimental test of non-local realism*, MIT LIGO (Cambridge, MA, USA, March 31, 2010) (2010)
- S. Gröblacher, *Experiments on strong coupling between a micromechanical oscillator and an optical cavity field*, Solid State and Optics Seminar, Yale University (New Haven, CT, USA, March 29, 2010) (2010)
- S. Gröblacher, *Quantum optics experiments with micromechanical oscillators*, NIST Ion Storage Group (Boulder, CO, USA, March 19, 2010) (2010)
- S. Gröblacher, *Observation of strong coupling between a micromechanical resonator and an optical cavity field*, DPG Frühjahrstagung (Hannover, Germany, March 08-12, 2010) (2010)
- S. Gröblacher, *An experimental test of non-local realism*, Caltech Applied Physics Seminars (Pasadena, CA, USA, October 28, 2009) (2009)
- S. Gröblacher, *Demonstration of strong coupling between a micromechanical resonator and an optical cavity field*, Universidade Federal do Rio de Janeiro (Rio de Janeiro, Brazil, October 26, 2009) (2009)

- S. Gröblacher, *Demonstration of Micromechanics in the Strong Coupling Regime*, Frontiers in Optics 2009 (San Jose, CA, USA, October 11-15 2009) (2009)
- S. Gröblacher, *Towards quantum mechanical resonators*, „Non local“ Seminars Vienna – Bratislava (Wien, Austria, July 01, 2009) (2009)
- S. Gröblacher, *Quantum optical control of micro-mechanical resonators*, CLEO/Europe-EQEC 2009 (München, Germany, June 14-19, 2009) (2009)
- S. Gröblacher, *Laser Cooling of Micromechanical Resonators in a Cryogenic Cavity*, Winter Colloquium on the Physics of Quantum Electronics (Snowbird, UT, USA, January 4-8, 2009) (2009)
- S. Gröblacher, *Quantum optical control of micro-mechanical systems*, Workshop on ‚Nanomechanical systems approaching the quantum regime‘ (München, Germany, September 15-17, 2008) (2008)
- S. Gröblacher, *Quantum-Optical Control of Micromechanical Systems*, Gordon Research Conference on ‘Mechanical Systems in the Quantum Regime’ (Ventura, CA, USA, February 17-22, 2008) (2008)
- S. Gröblacher, *Quantum physics with nano- and micro-mechanical systems: from quantum optics to quantum mechanics*, NanoForum (Linz, Austria, May 17-18, 2007) (2007)
- S. Gröblacher, *Radiation pressure cooling of a micro-mirror*, DPG Frühjahrstagung (Düsseldorf, Germany, March 19-23, 2007) (2007)
- S. Gröblacher, *Experiments on nonlocal hidden-variable theories*, SFB Colloquium (Vienna, Austria, February 01-02, 2007) (2007)
- S. Gröblacher and Robert Prevedel, *Recent Experiments on Quantum Communication and Computation*, Institute for Quantum Computing (Waterloo, Canada, August 24, 2006) (2006)
- S. Gröblacher and Robert Prevedel, *Multi-Partite and Higher-Dimensional Quantum Entanglement Experiments*, Quantum Optics Seminar, University of Toronto (Toronto, Canada, August 21, 2006) (2006)
- S. Gröblacher, *Experiments Towards Opto-Mechanical Quantum Entanglement*, Canadian Quantum Information Students’ Conference (Calgary, Canada, August 14-18, 2006) (2006)
- S. Gröblacher, *Experimental Quantum Cryptography with Entangled Qutrits*, SFB Colloquium (Innsbruck, Austria, April 06-07, 2006) (2006)
- S. Gröblacher, *Experimental Quantum Cryptography with Qutrits*, DPG Frühjahrstagung (Frankfurt, Germany, March 13-17, 2006) (2006)